

This meeting will be co-sponsored  
by The Electrochemical Society 



14<sup>th</sup>  
**ABAF**

BRNO 2013

Advanced Batteries, Accumulators  
and Fuel Cells

INTERNATIONAL CONFERENCE

September 1<sup>st</sup> - September 5<sup>th</sup> 2013

**Organised by:**

**Department of Electrical and Electronic Technology,**  
Faculty of Electrical Engineering and Communication,  
Brno University of Technology

**Organizing committee:**

Jiří Vondrák  
Marie Sedlaříková

**Honourary Scientific Committee:**

Arnaldo Visitin  
Jaromír Kadlec  
Petr Vanýsek  
Doron Aurbach  
Vito di Noto  
Jiří Kazelle  
Jiří Vondrák  
Marie Sedlaříková  
Ladislav Kaván  
Renata Oriňáková  
Pedro Gomez-Romero

**Organisation Committee:**

Jiří Vondrák  
Marie Sedlaříková  
Vítězslav Novák  
Jiří Wagner  
Miroslav Zatloukal  
Tomáš Kazda  
Lucie Šimonová  
Jiří Libich  
Josef Máca

**Program Committee:**

Jiří Vondrák  
Marie Sedlaříková  
Arnaldo Visitin  
Josef Máca  
Vítězslav Novák  
Petr Bača  
Tomáš Kazda  
Jiří Špínka  
Helena Polsterová  
Martin Frk  
Edita Hejátková  
Miroslav Zatloukal  
Jiří Šubarda  
Andrea Fedorková  
Jiří Libich

**ISBN 978-80-214-4767-7**

Conference is sponsored by:



INVESTMENTS IN EDUCATION DEVELOPMENT



Centre for Research  
and Utilization  
of Renewable Energy

This meeting will be co-sponsored  
by The Electrochemical Society



We would like to express our thanks to the Brno University of Technology, Faculty of Electrical Engineering and Communication for support and help with organising 13<sup>th</sup> ABAF conference.

Partners:



Media partners:



CZECHINVEST

## Contents

### Mineral resources of lithium

*Barraco, D.*

**From the salt mine to the battery projects in Argentina**.....9

### Materials for anhydrous batteries

*Amalraj, S. F., Talianker, M., Markovsky, B., Burlaka, L., Erikson, E., Haik, O., Zinigrad, E., Aurbach, D., Lampert, J. K., Schulz-Dobrick, M.*

**Studies on High Energetic Li Rich  $\text{Li}_x[\text{MnNiCo}]_2\text{O}_2$  Electrodes at 60 °C for Li-ion batteries**.....10

*Boyadzhieva, T., Koleva, V., Stoyanova, R., Zhecheva, E.*

**Ion Exchange Reactions for Synthesis of Nano-Sized Lithium and Sodium Manganese Phospho-Olivines as Cathode Materials in Lithium and Sodium Ion Batteries** .....11

*Manab Kundu, Lifeng Liu*

**Nanostructured metal oxide electrodes for electrochemical energy storage**.....14

*Czajka, B., Zieliński, M., Wojciechowska, M., Tomska-Foralewska, I., Osińska-Broniarz, M.*

**Modifying MgO as a binder agent applied in the molten electrolyte**.....17

*Danilov, M.O., Kolbasov, G.Y.*

**Catalytically Active Electrode Materials for Oxygen Electrodes Based on Tungsten - Modified Carbon Nanotubes**.....19

*Fedorková, A., Oriňáková, R., Sedlaříková, M., Gómez-Romero, P.*

**S-LiFePO<sub>4</sub>-PPy cathode material for Li/S batteries prepared by solid-state synthesis** .....23

*Vondrák, J., Sedlaříková, M.*

**Recent development in lithium batteries and related topics**.....26

*Cech, O., Fedorkova, A., Sedlarikova, M.*

**Sulfur based cathode materials for Li-ion batteries**.....29

*Frk, M., Maca, J., Rozsivalova, Z., Sedlarikova, M.*

**Properties of Solvents for Aprotic Electrolytes with Fire Retardant** .....32

*Kazda, T., Vondrák, J., Di Noto, V., Sedlaříková, M., Čudek, P.*

**Comparison of production processes of high-voltage cathode materials** .....36

*Libich, J., Sedlaříková, M., Vondrák, J. Frk, M.*

**New Approach to the Preparation of the Prelithiated Graphite Materials**.....40

*Maca, J., Frk, M., Vondrak, J., Sedlarikova, M.*

**The use of triethylphosphate as flame retardant in lithium ion batteries** .....44

<i>Peskov, R., Apostolova, R., Shembel, E., Danilov, M.</i> <b>Comparison study of LiMn<sub>2</sub>O<sub>4</sub> composites with graphite and carbon nanotubes in the electrodes for Li-ion batteries</b> .....	48
<i>Pleha, D., Musil, M., Cudek, P.</i> <b>Characterization of PVdF fibrous membrane separators for lithium-ion rechargeable batteries</b> .....	52
<i>Tulibaeva, G.Z., Yudina, A.V., Shestakov, A.F., Yarmolenko, O.V.</i> <b>Experimental and theoretical investigation of the conducting properties of ordered layers of crown ether complexes with Li<sup>+</sup> ions on the lithium anode surface</b> .....	56
<i>Vojtěch, L., Hájek, J., Neruda, M., Zatloukal, M.</i> <b>Monometallic Textile Electrodes for „Green“ Electronics</b> .....	61
<i>Yudina, A.V., Chernyak, A.V., Volkov, V.I., Kulova, T.L., Yarmolenko, O.V.</i> <b>Investigation of ion transport in the network polymer gel electrolytes, modified with ionic liquid BMIBF<sub>4</sub> for lithium-ion batteries</b> .....	65
<i>Musil, M., Pleha, D., Libich, J.</i> <b>Electrospun PVDF separators for lithium ion batteries</b> .....	68
<i>Haik, O., Amalraj, F. S., Hirshberg, D., Talianker, M., Markovsky, B., Zinigrad, E., Aurbach, D.</i> <b>Thermal Processes in Systems “Li-rich Cathode Materials - LiPF<sub>6</sub>-Based Organic Solutions”</b> .....	73
<b>Special simulations methods</b>	
<i>Vyroubal, P., Maxa, J., Kazda, T., Vondrák, J., Tichý, J.</i> <b>Numerical simulation of lithium ion battery</b> .....	77
<i>Maxa, J., Vyroubal, P., Vaněk, J., Hladká, K.</i> <b>Analysis of using the air for solar panel cooling with ANSYS systém</b> .....	81
<b>New materials for electrochemical power sources</b>	
<i>Gómez-Romero, P.</i> <b>Energy Storage: From Hybrid Devices to Hybrid Materials</b> .....	84
<i>Oriňáková, R., Škantárová, L., Filkusová, M., Oriňák, A.</i> <b>Electrocatalysis at nanoparticles and nanostructured surfaces</b> .....	86
<i>Cech, O., Moravkova, J., Sedlarikova, M., Vondrak, J.</i> <b>Nanofibrous Li<sub>4</sub>Ti<sub>5</sub>O<sub>12</sub> prepared by centrifugal force spinning and its lithium insertion properties</b> .....	88
<i>Polonský, J., Hnát, J., Paidar, M., Bouzek, K.</i> <b>Advanced materials for PEM water electrolysis</b> .....	90
<i>Komárek, M.</i> <b>Nanofibrous composite materials and their utilization potential for the electrochemical applications</b> .....	92

## Physical Method for Investigation

*Kavan, L.*

**Investigation of lithium insertion into TiO<sub>2</sub> by Raman spectroscopy supported by <sup>6/7</sup>Li and <sup>16/18</sup>O isotope substitutions** .....99

*Krtil, P.*

**Catalyst breathing in electrocatalytic processes** .....100

*Di Noto, V., Vezzù, K., Negro, E., Polizzi, S.*

**Morphology and Electrochemical Investigations on Multimetal Carbon Nitride Electrocatalysts Supported on Graphitized Polyketone Nanoballs** .....101

## Special Materials and Methods

*Chladil, L., Čudek, P., Musil, M.*

**Growth of zinc dendrites from the aqueous KOH solution** .....103

*Ivanova, Sv., Zhecheva, E., Stoyanova, R.*

**Enhancing of the electrochemical behavior of LiNi<sub>1/2</sub>Mn<sub>3/2</sub>O<sub>4</sub> by acid treatment** .....106

*Joska, Z., Kadlec, J., Klanica, O., Tomáščík, J., Svoboda, E.*

**Testing of DLC Coating on Plasma Nitrided Austenitic Stainless Steel** .....109

*Onderka, F., Klanica, O., Dobrocký, D., Kadlec, J.*

**Reasons of Total Endoprosthesis Failure** .....111

*Kalapsazova, M., Stoyanova, R., Zhecheva, E.*

**Structural Characterization and Electrochemistry of Layered Na<sub>0.65</sub>Ni<sub>0.5</sub>Mn<sub>0.5</sub>O<sub>2</sub> obtained by Freeze-Drying Method** .....115

*Kaválek, O., Chladil, L., Máca, J.*

**Effect of inhibitor on Zn-dendrite formation** .....118

*Křivík, P.*

**Pulse charging of lead acid batteries** .....121

*Kunovjánek, M., Musil, M., Trnková, L.*

**Alkali hydroxide doped PVA membranes** .....125

*Polsterová, H.*

**Temperature Dependence of the Electrical Properties of Nanocomposites** .....130

*Stojan, R., Vaněk, J., Malý, M., Gvritishvili, R., Šimonová, L., Frantík, O.*

**Analysis of luminescence radiation interact by silicon defects** .....134

*Tošer, P., Bača, P.*

**AGM separator in VRLA batteries** .....137

<i>Vaculík, S., Zimáková, J., Bača, P.</i> <b>The Influence of Temperature in Curing Processes in the Manufacturing of Electrodes of Lead-Acid Batteries</b> .....	139
<i>Vanek, J., Gvritishvili, R., Strnadel, J.</i> <b>Snail tracks phenomenon on photovoltaic modules</b> .....	142
<i>Danilov, M.O., Slobodyanyuk, I.A., Rusetskii, I.A., Kolbasov, G.A.</i> <b>Synthesis the graphene from carbon nanotubes, based on the electrochemical approach and the effects of oxidizing and reducing agents on its electrochemical performances in oxygen electrodes</b> .....	146
<i>Musil, M., Dvořák, P.</i> <b>Review on gel polymer electrolytes for lithium ion batteries and supercapacitors</b> .....	150
<i>Dvořák, P., Musil, M.</i> <b>Polymer gel PMMA based electrolytes containing Li<sup>+</sup> salts</b> .....	155
 <b>Application of batteries for electromobility and industry</b>	
<i>Kristl, P., Vaněk, M., Poupa, P.</i> <b>Operation of E-Octavia fleet</b> .....	160
<i>Hladík, M.</i> <b>Secondary cells and Energy Accumulation in Energetic Applications and Transportation</b> .....	164
<i>Vorel, P., Procházka, P., Huták, P., Pazdera, I., Červinka, D.</i> <b>Fast-charger for electric plane</b> .....	165
<i>Červinka, D., Knobloch, J., Klíma, B., Huták, P., Kadlec, J., Fajkus, P.</i> <b>Electric Drive of Propeller for Battery-Powered Aircraft</b> .....	169
<i>Kadlec, J., Cipin, R., Klíma, B., Cervinka, D., Vorel, P.</i> <b>Li-ion accumulators for propulsion system of electric Airplane VUT 051 RAY</b> .....	172
<i>Polnik, B., Miedziński, Z. B., Kozłowski, A.</i> <b>Possibility of using the advanced battery systems in the Polish mining industry</b> .....	174
<i>Prochazka, P., Cipin R., Pazdera, I., Knobloch, J., Fajkus, P</i> <b>Comparison of fuel cell and Li-ion accumulators for using in electrical airplane</b> .....	177

## **From the salt mine to the battery projects in Argentina**

Barraco, D.

FAMAF, Universidad de Córdoba, Av Medina Allende s/n, Ciudad Universitaria, CP: X5000HUA,  
Argentina

Argentine government's interest in exploiting large lithium deposits not only in the north of our country, but also in Bolivia and Chile, Lithium Triangle or Also called by Forbes "of the Saudi Arabian Lithium" According. During the last year and a half, a new lithium-ion doping materials and alloy materials have been studied at as a part of this big project. The project is based on international scientific cooperation with the group led by Professors Jiri Vondrak and Marie Sedlarikova, who have been working in the field of new electrochemical energy sources for over two Decades. Research in this group focuses on obtaining lithium battery cathodes. That should be safe and have a long service life. In the last years info we have been working, the above laboratories altogether, in traditional graphite anode and other nanotube structure based on coal, silicon material titanatus graphemes, fullerenes, etc. We have just, recently, researching began in organic electrolytes. Both placed focus is on the synthesis and characterization of materials suitable for the development of lithium-ion batteries, basically new cathodes and anodic materials, and on the design of a prototype lithium-ion battery. Based on a commercial battery, we are working on the design of a lithium battery powerful enough to drive an electric. In this short communication I will tell the Argentine National Project "from Salar to the Battery" and the status of our arts in the matter.

## Studies on High Energetic Li Rich $\text{Li}_x[\text{MnNiCo}]\text{O}_2$ Electrodes at 60 °C for Li-ion batteries

Amalraj, S. F.<sup>a\*</sup>, Talianker, M.<sup>b</sup>, Markovsky, B.<sup>a</sup>, Burlaka, L.<sup>a</sup>, Erikson, E.<sup>a</sup>, Haik, O.<sup>a</sup>, Zinigrad, E.<sup>a</sup>, Aurbach, D.<sup>a</sup>, Lampert, J. K.<sup>c</sup>, Schulz-Dobrick, M.<sup>c</sup>

<sup>a</sup>Department of Chemistry, Bar-Ilan University, Ramat-Gan 52900, Israel

<sup>b</sup>Department of Materials Engineering, Ben-Gurion University of the Negev, Beer-Sheva 84105, Israel

<sup>c</sup>BASF SE, GCN/E, Ludwigshafen am Rhein, 67056 Germany

In recent years, the studies on Li-rich layered materials composed of  $\text{Li}[\text{Li-Mn-Ni-Co}]\text{O}_2$  have become appealing, because they exhibit much higher capacities (~250 mAh/g) in the potential range from 2.0 V to 4.6 V [1]. However, this class of materials exhibits an accelerated capacity fade during cycling or storage at elevated temperatures as a result of the chemical reactions between the delithiated cathode and the electrolyte at high operating potential.

In this work, we aimed to study the electrochemistry of  $x\text{Li}_2\text{MnO}_3 \cdot (1-x)\text{LiMO}_2$  ( $x \sim 0.5$ ;  $M = \text{Mn, Ni, Co}$ ) electrodes at 60 °C in relationship with the structural changes of the active material due to the lithium extraction at high anodic potentials. The structure was considered on the basis of two-components model, namely monoclinic  $\text{Li}_2\text{MnO}_3$  ( $C2/m$ ) and rhombohedral  $\text{LiMO}_2$  ( $R-3m$ ) ( $M = \text{Mn, Ni, Co}$ ) that are structurally compatible and closely integrated phases. An emphasis on the effect of  $\text{AlF}_3$  coating on their electrochemical performance was also carried out. Based on TEM studies we concluded that the coating had a crystalline tetragonal structure  $t\text{-AlF}_3$  ( $P4nmm$  symmetry) and  $\text{AlF}_3$  nano-crystals were regularly distributed over the particles surface. It was shown that electrodes comprising the  $\text{AlF}_3$ -coated material exhibited higher reversible capacities of ~250 mAh/g at a C/5 rate, more stable cycling behavior, higher lithium storage capability at 60 °C, and lower impedance measured during Li-deintercalation comparing to electrodes prepared from the uncoated material. An important finding is that  $\text{Li}_x[\text{MnNiCo}]\text{O}_2 / \text{AlF}_3$  materials revealed much higher thermal stability both in the pristine (lithiated) and cycled (delithiated) states than their uncoated counterparts.

### Reference

1. Francis Amalraj, M. Talianker, B. Markovsky, D. Sharon, L. Burlaka, E. Zinigrad, O. Haik, D. Aurbach, J. Lampert, Martin Schulz-Dobrick, *J. Electrochem. Soc.*, 160, A324 (2013).

## Ion Exchange Reactions for Synthesis of Nano-Sized Lithium and Sodium Manganese Phospho-Olivines as Cathode Materials in Lithium and Sodium Ion Batteries

Boyadzhieva, T., Koleva, V., Stoyanova, R., Zhecheva, E.

Institute of General and Inorganic Chemistry, Bulgarian Academy of Sciences,  
Sofia 1113, Bulgaria

Nowadays phospho-olivines with compositions  $\text{LiMPO}_4$  ( $M = \text{Fe, Mn, Co and Ni}$ ) are attracted both research and technological interest as electrode materials for lithium ion batteries with potential application in the hybrid electric vehicles (1, 2). This interest is motivated by the many advantages of these compounds: reasonably high capacity ( $170\text{mAhg}^{-1}$ ) and cyclic stability, tolerance to overcharge, excellent safety and low cost. More recently, in response to the current requirements for the development of cheaper "green" batteries the replacement of lithium with sodium becomes very attractive (3). Since the thermodynamically stable  $\text{NaMPO}_4$  does not form the electrochemically active olivine-type structure, the synthesis of olivine-type  $\text{NaMPO}_4$  is a great challenge and requires original synthesis approaches. On the other hand, to improve the low rate capability of the phospho-olivines the research efforts have to be devoted to the development of new specific synthetic routes which enable to control the morphology and design  $M'MPO_4$  ( $M' = \text{Li, Na}$ ) in the nano-scale region.

The choice of the appropriate precursor is a crucial factor for the morphology control of the materials. In this contribution we provide data on the successful use of  $\text{KMnPO}_4 \cdot \text{H}_2\text{O}$  as a morphology-template agent for low temperature synthesis of both olivine-type  $\text{LiMnPO}_4$  and  $\text{NaMnPO}_4$ . Till now only one report in the literature deals with the preparation of olivine-type  $\text{NaMnPO}_4$ .

$\text{KMnPO}_4 \cdot \text{H}_2\text{O}$  is a representative of the dittmarite-type compounds having general formula  $M'M''\text{PO}_4 \cdot \text{H}_2\text{O}$ , where  $M' = \text{K, NH}_4$  and  $M'' = \text{Mg, Fe, Mn, Co, Ni}$ . They have a layer structure, where the  $M^{2+}\text{-PO}_4$  sheets are separated by the  $M^+$  ions. From structural point of view the dittmarite-type compounds are particularly suitable as precursors in the ion exchange reactions since the topology of the  $M^{2+}\text{-PO}_4$  layer in the *ac* plane of the dittmarites completely matches the topology of the  $M^{2+}\text{-PO}_4$  layer in the *bc* plane of the olivines. This remarkable structural similarity facilitates the transformation of the dittmarite-type to the olivine-type crystal structure which occurs without major structural rearrangements. More recently, Nazar et al. (4) have obtained  $\text{NaMnPO}_4$  from  $\text{NH}_4\text{MnPO}_4 \cdot \text{H}_2\text{O}$ , but no details on the preparation conditions were supplied. To our knowledge the present work is the first report on the preparation of olivine-type  $\text{NaMnPO}_4$  based on potassium manganese dittmarite. Using  $\text{KMnPO}_4 \cdot \text{H}_2\text{O}$  we expect more facile pathways for ion exchange between  $\text{K}^+$  and  $\text{Li}^+$  or  $\text{Na}^+$  ions since only electrostatic bonds between  $\text{K}^+$  and  $\text{PO}_4^{3-}$  are developed in the potassium dittmarite, while hydrogen bonds between  $\text{NH}_4^+$  and  $\text{PO}_4^{3-}$  exist in the ammonium analogue.

The ion exchange process into the  $\text{KMnPO}_4 \cdot \text{H}_2\text{O}$  host matrix is carried out using  $\text{LiCl-LiNO}_3$  mixtures and  $\text{NaCH}_3\text{COO} \cdot 3\text{H}_2\text{O}$  taken in excess. It is established that the ion exchange between  $\text{K}^+$  and  $\text{Li}^+$  occurs very fast and only 90 min at 270 °C, accordingly 180 min at 200 °C are enough for the synthesis of pure  $\text{LiMnPO}_4$  (5). However, the exchange between  $\text{K}^+$  and  $\text{Na}^+$  is hindered due to the larger ionic radii of the latter and a longer reaction time (more than 10 h) is needed for the complete transformation of the dittmarite into olivine. Thus prepared manganese olivines are stable during the further prolonged annealing at 400-500 °C.  $\text{LiMnPO}_4$  and  $\text{NaMnPO}_4$  are characterized by XRD powder diffraction, IR spectroscopy, SEM and TEM analyses. The reversible lithium

intercalation in manganese phospho-olivines is tested in model two-electrode lithium cells of the type Li | LiPF<sub>6</sub> (EC:DMC) | LiMnPO<sub>4</sub>.

The Rietveld analyses (Figure 1) evidence that well crystallized LiMnPO<sub>4</sub> and NaMnPO<sub>4</sub> (SG *Pnma*) are obtained. The olivine crystallites exhibit a preferred orientation along [100] which is more pronounced in LiMnPO<sub>4</sub> than in NaMnPO<sub>4</sub>. The preferred orientation is inherited from the precursor. No disorder between Li and Mn ions and Li deficiency are found in LiMnPO<sub>4</sub>. A very small antisite mixing between Na and Mn ions (below 1%) can be supposed for NaMnPO<sub>4</sub>.

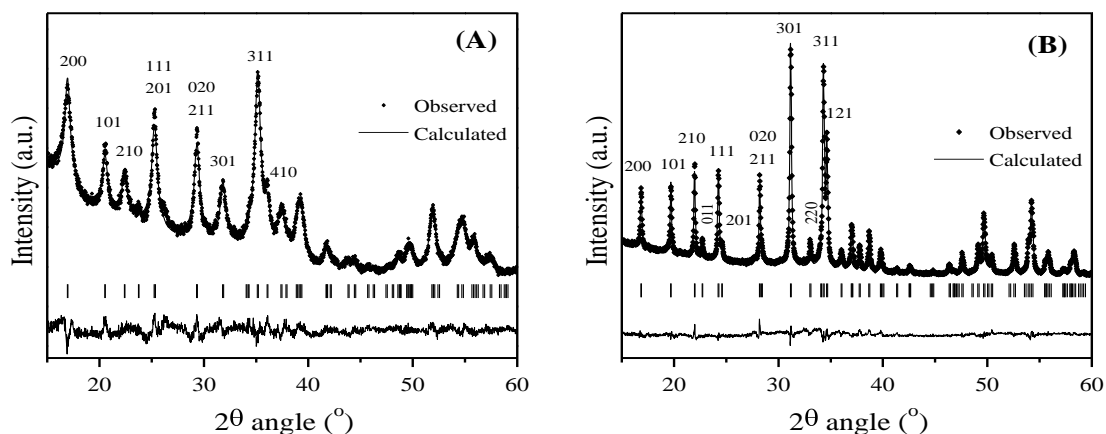


**Figure 1.** Rietveld refinement plots of LiMnPO<sub>4</sub> (A) and NaMnPO<sub>4</sub> (B) prepared from KMnPO<sub>4</sub>·H<sub>2</sub>O

The SEM images (Figure 2) show that the plate morphology of KMnPO<sub>4</sub>·H<sub>2</sub>O is preserved in the prepared LiMnPO<sub>4</sub> (plates with basal dimensions between 1 and 5 μm and thickness above 200 nm). TEM studies evidence that LiMnPO<sub>4</sub> is nanostructured and consists of particles smaller than 10 nm, which are closely packed in plate-like aggregates with dimensions of about 2 - 3 μm. In the case of NaMnPO<sub>4</sub> the SEM images (Fig. 2 (C)) reveal a transformation of the plate morphology of KMnPO<sub>4</sub>·H<sub>2</sub>O crystals to the rod like morphology (rods with length of about 1 μm and with 100-200 nm) of the prepared olivine. The formation of rods is probably caused by a high interface strain at the grain boundary between the KMnPO<sub>4</sub>·H<sub>2</sub>O and NaMnPO<sub>4</sub> which causes cleavage during the ion exchange thus creating rods.

The advance in using of LiMnPO<sub>4</sub> as a cathode material is a higher energy density in comparison with the conventional LiFePO<sub>4</sub>. This is a consequence of the chemical potential of the Mn<sup>2+</sup>/Mn<sup>3+</sup> redox-couple, which is higher than that of the Fe<sup>2+</sup>/Fe<sup>3+</sup> couple (4.1 V vs 3.4 V, respectively). Figure 3 gives the first charge/discharge curves for LiMnPO<sub>4</sub> prepared by us. The preliminary data outline the potential of low-temperature methods of Li/NaMnPO<sub>4</sub> cathode materials with controlled morphologies.

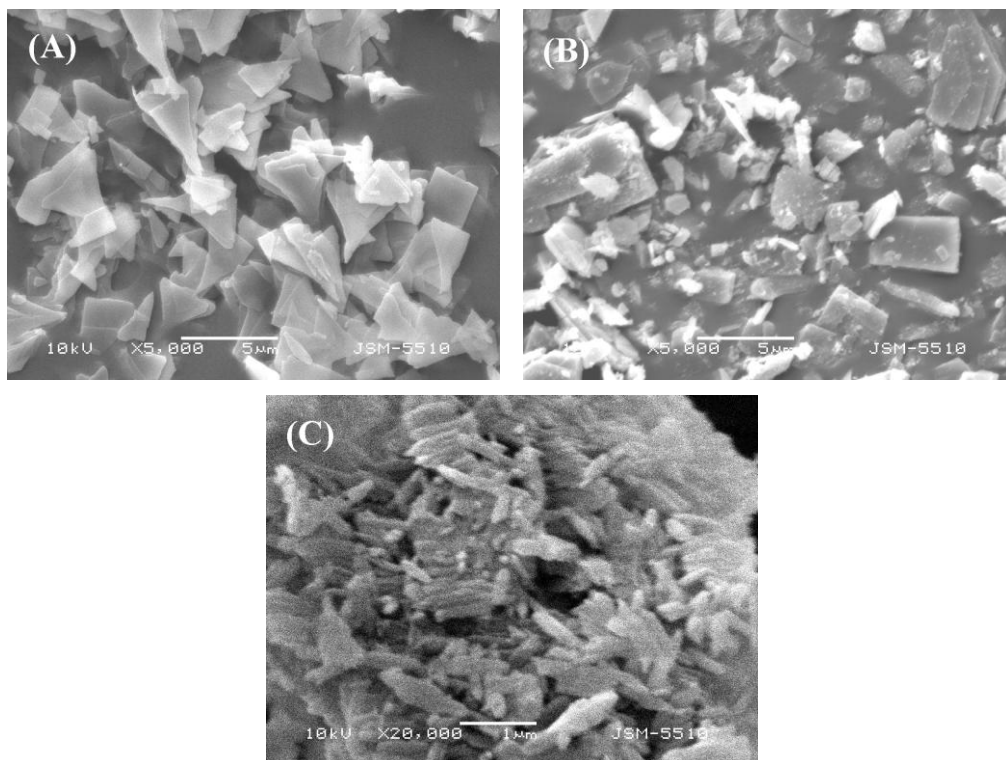


**Figure 2.** SEM images of  $KMnPO_4 \cdot H_2O$  (A),  $LiMnPO_4$  (B) and  $NaMnPO_4$  (C)

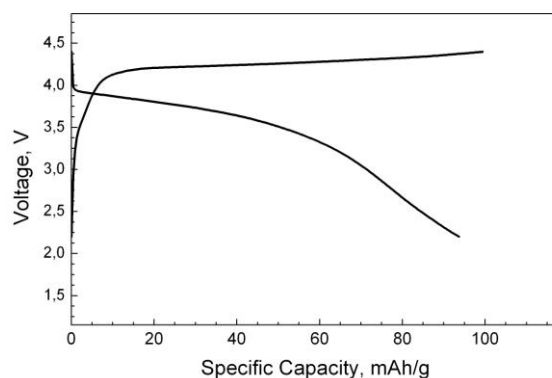


**Figure 3.** First charge/discharge curves of  $LiMnPO_4$ .

### Acknowledgments

Authors are grateful to the financial support from ESF (Grant BG051PO001-3.3.06-0050).

### References

1. M. S. Whittingham, *Chem. Rev.*, **104**, 4271 (2004).
2. B. L. Ellis, K. T. Lee and L. F. Nazar, *Chem. Mater.*, **22**, 1059 (2010).
3. B. L. Ellis, L. F. Nazar, *Curr. Opin. Solid State Mater. Sci.*, **16**, 168 (2012).
4. K. T. Lee, T. N. Ramesh, F. Nan, G. Botton, L. F. Nazar, *Chem. Mater.*, **23**, 3593 (2011).
5. V. Koleva, E. Zhecheva, R. Stoyanova, *Dalton Trans.*, **40**, 7385 (2012).

## Nanostructured metal oxide electrodes for electrochemical energy storage

Manab Kundu, Lifeng Liu\*

E-mail: lifeng.liu@inl.int

International Iberian Nanotechnology Laboratory (INL), Av. Mestre Jose Veiga, 4715-330 Braga, Portugal

In view of the current energy scenario, global warming and pursuit of alternative energy sources, lithium-ion batteries (LIBs) with high energy density and supercapacitors or electrochemical capacitors (SCs/ECs) with excellent power density have positioned themselves as the smartest choice for clean and efficient back up power sources and energy storage devices. In both cases, the performance depends very much on the properties of the electrode materials such as the microstructure, composition, surface area and so on. Generally, nanostructured transition metal oxides are very promising for use as electrode materials in both LIBs and SCs. Among various transition metal oxides, manganese dioxide ( $\text{MnO}_2$ ) and nickel oxide ( $\text{NiO}$ ), have received large research interest due to their low cost and toxicity, environmental friendliness and encouraging electrochemical performance than other metal oxides. In this work, we have synthesized mesoporous  $\text{MnO}_2$  nanosheets and porous  $\text{NiO}$  nanofibers by electrodeposition and electrospinning, respectively, and investigated their potential application in electrochemical supercapacitor as well as Li-ion battery electrode.

High density and vertically aligned  $\text{MnO}_2$  nanosheet arrays were directly grown very uniformly on nickel foam current collector by one-step electrodeposition method (Fig. 1a). A close inspection reveals that the deposited manganese oxide has a thickness of 20 – 30 nm, as shown in Fig. 1b. The TEM micrograph in Fig. 1c exhibits that, the nanosheets possess flexible silk-like morphology with a high degree of transparency, indicating that they are very thin. Upon a closer examination, it is observed that the sheets are actually porous with an average pore size of eight nanometers (Fig 1d). When used as electrodes in supercapacitors, the nanosheets exhibit specific capacitance of 201, 150, 122, 105 and 96  $\text{F g}^{-1}$  at current densities of 1, 5, 10, 15 and 20  $\text{A g}^{-1}$ , respectively. Upon cycling at 5  $\text{A g}^{-1}$ , the specific capacitance loses 35% of its initial value in the beginning 1800 cycles and then remains constant up to 3000 cycles, showing reasonably good cycling performance. This observed initial loss in specific capacitance might be due to the dissolution of Mn into the electrolyte, which is common for  $\text{MnO}_2$ -based electrodes (1, 2). Remarkably, it is found that the Columbic efficiency remains > 99% during the whole cycling test, suggesting that the charge/discharge processes are highly reversible. On the other hand, when the nickel foam supported  $\text{MnO}_2$  nanosheets are used as anodes in Li-ion batteries, they exhibit remarkably high capacity, which is around 1640  $\text{mAh g}^{-1}$  at a charge/discharge current density of 100  $\text{mA g}^{-1}$ . Even at a current density as high as 1000  $\text{mA g}^{-1}$ , the capacity of the nanosheets still remains 680  $\text{mAh g}^{-1}$ , much higher than the theoretical capacity (372  $\text{mAh g}^{-1}$ ) of graphite, the anode material currently being widely used in commercial lithium-ion batteries. It is also noted that the Columbic efficiency of the cell is very high (> 96%), indicating that the discharge happens very efficiently. The results suggest that the nickel foam supported  $\text{MnO}_2$  nanosheets are promising candidate for use in electrochemical supercapacitors as well as lithium-ion batteries.

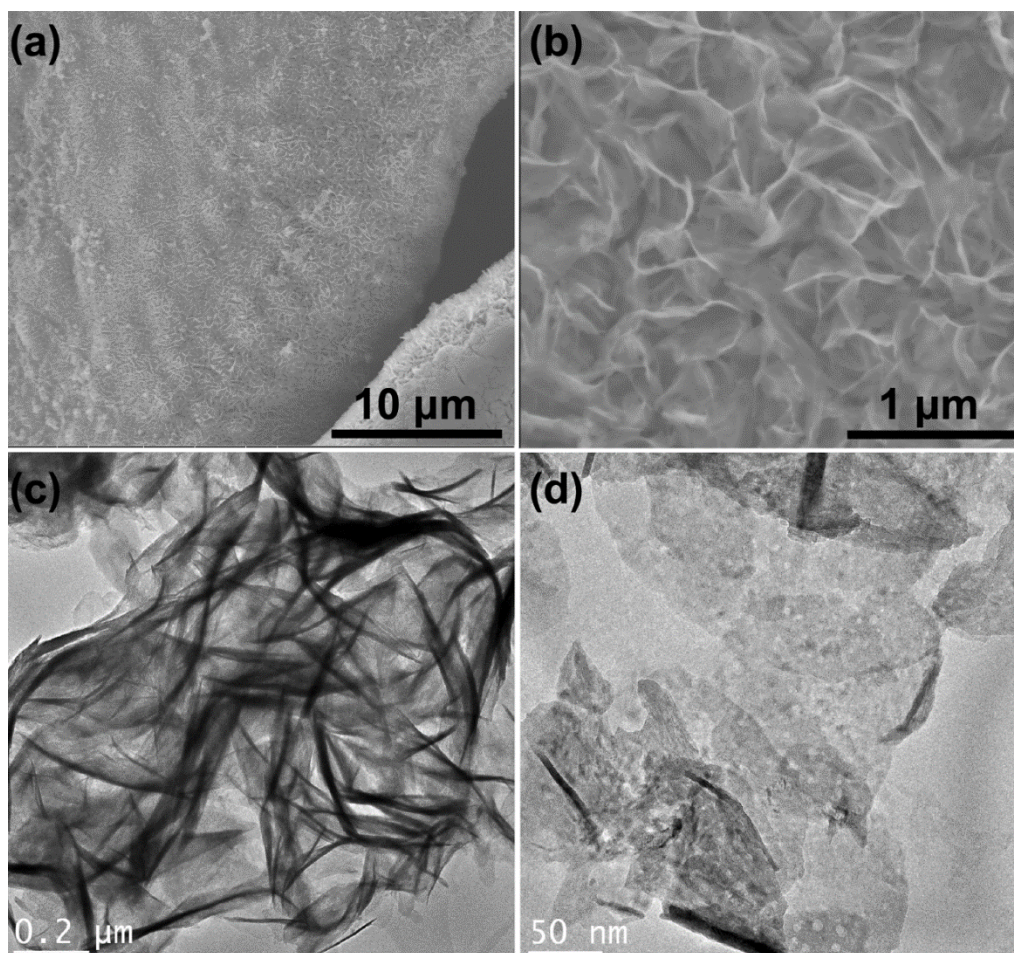


**Figure 1.** Microstructural characterization of the electrodeposited  $\text{MnO}_2$  nanosheets: (a) and (b) SEM, (c) and (d) TEM micrographs

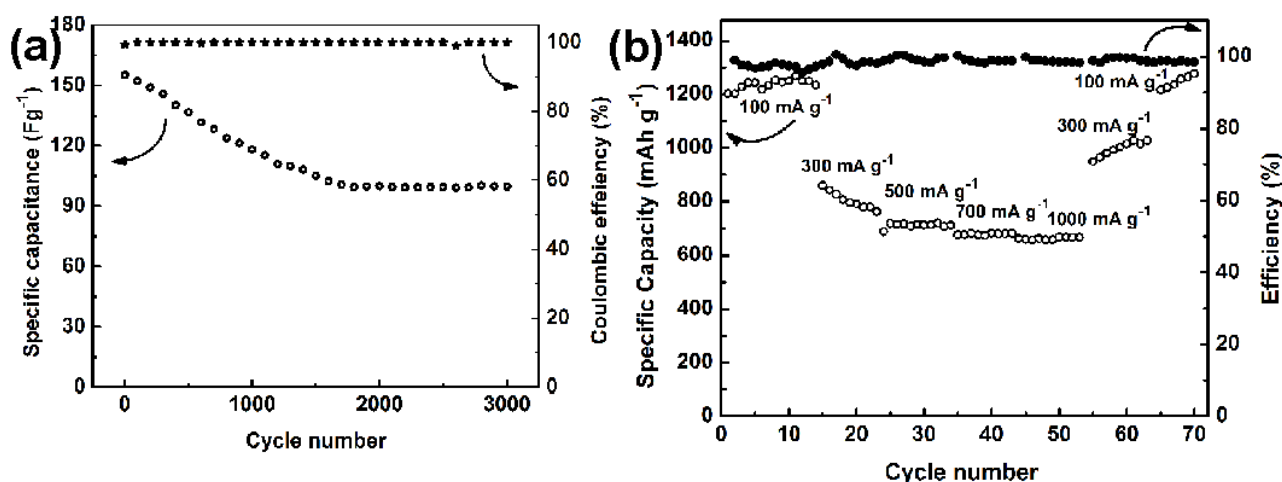


**Figure 2.** Electrochemical performance of the deposited  $\text{MnO}_2$  nanosheets for use as (a) supercapacitor and (b) lithium-ion battery electrode.

Porous NiO nanofibers have been synthesized by electrospinning precursor solution containing nickel acetate and PVA, followed by a thermal treatment at 700 °C. Microstructural characterization by SEM and TEM, confirms that the diameter of the as-synthesized NiO nanofibers ranges from 200 to 350 nm (Fig. 3a and Fig. 3b). The potential application of the as-synthesized NiO nanofibers in supercapacitors and LIB anodes are tested. When used as supercapacitor

electrodes, the NiO nanofibers are found to exhibit specific capacitance values of 738, 583, 569 and 561  $F g^{-1}$  at the current densities of 2.5, 5, 10 and 15  $A g^{-1}$  respectively (Fig. 3c), showing great potential for use in high-rate supercapacitors. In addition, the potential of using these porous NiO fibers as electrodes in lithium-ion batteries (LIBs) is also evaluated. The cycling test (Fig. 3d) shows at the 1C rate, the specific capacity drops at first upon cycling, and then gradually increases, reaching 620  $mAh g^{-1}$  after 80 cycles, close to the theoretical capacity of NiO and much higher than that of graphitic anodes. Furthermore, the Coulombic efficiency of the cell is found to be nearly 100 % during the whole cycling test. This suggests that the as-fabricated porous NiO nanofibers hold great promise for use as high-performance anode materials in lithium-ion batteries.

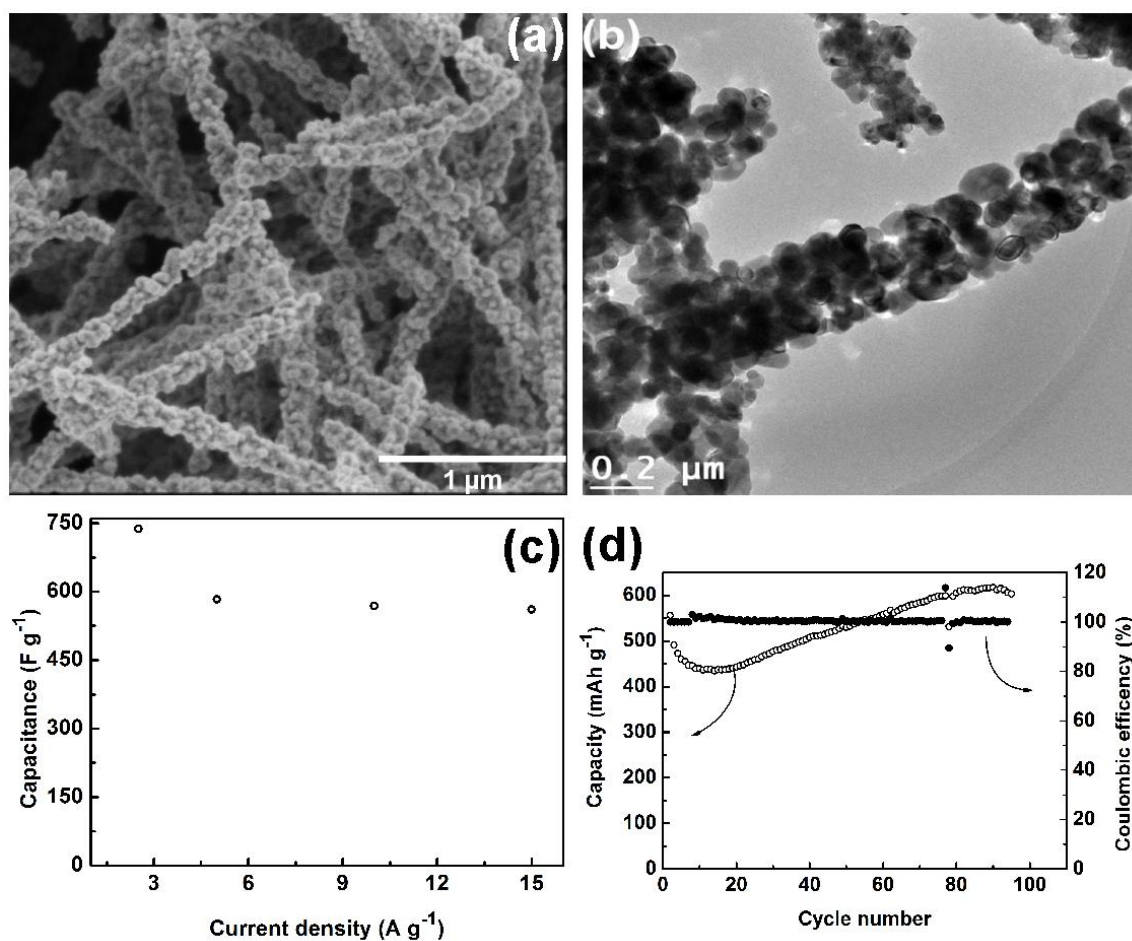


**Figure 3.** (a) SEM and (b) TEM micrographs of the electrospun NiO nanofibers. (c) Variation of the capacitance values with the charge/discharge current densities of the NiO nanofibers as electrodes in supercapacitors. (d) Cycling performance of the NiO nanofiber lithium-ion battery anodes.

### Acknowledgement

L. Liu acknowledges the financial support of the INL Start-up Funds.

### Reference

1. K. Naoi, P. Simon, *Electrochem. Soc. Interface*, **17** 34 (2008).
2. G. Yu, L. Hu, N. Liu, H. Wang, M. Vosgueritchian, Y. Yang, Y. Cui, Z. Bao, *Nano Lett.*, **11** 4438 (2011).

## Modifying MgO as a binder agent applied in the molten electrolyte

Czajka, B.<sup>1</sup>, Zieliński, M.<sup>2</sup>, Wojciechowska, M.<sup>2</sup>, Tomska-Foralewska, I.<sup>2</sup>, Osińska-Broniarz, M.<sup>1</sup>

<sup>1</sup> Institute of Non-Ferrous Metals Branch in Poznan, 61-362 Poznan, Poland

<sup>2</sup> Faculty of Chemistry, A. Mickiewicz University, 61-614 Poznan, Poland

Thermal batteries are primary chemical power sources designed for special applications. They are resistant to shocks, vibrations and g-forces. In a single cell, electrolyte is immobilized in a filler material (binder) to prevent leakage of the molten electrolyte while maintaining high ionic conductivity at the same time. For these reasons, filler material should be characterized by possibly low density, good wettability, chemical resistance to molten electrolyte and mechanical strength (1). Filler materials presently used include: SiO<sub>2</sub>, MgO, ZrO<sub>2</sub>, BN, Y<sub>2</sub>O<sub>3</sub> and TiO<sub>2</sub> (2,3). The most commonly used filler materials are SiO<sub>2</sub> -10-20 wt% or MgO -40 wt% in a mixture with electrolyte. The electrolyte itself is an eutectic mixture of alkali metal halogenides.

The aim of this work is the presentation of preliminary studies on the preparation and application of fluoride ions modified MgO as a filler material for a thermal battery cell containing electrolyte in form of an eutectic mixture of KCl-LiCl-RbCl ( $T_T = 302$  °C).

Filler material was obtained by introducing a definite amount of 20% aqueous HF solution into aqueous suspension of magnesium carbonate, followed by calcinations at range of temperature 400-900 °C.

The texture of modified and non-modified magnesium oxide preparations was investigated in order to determine their specific surface area, pore volume and the mean pore diameter. The obtained results were presented in the paper (4). MgO-MgF<sub>2</sub> mixture and the electrolyte were homogenized and pressed in form of pellets at 400 MPa pressure. Table 1 and 2 show the results of the measurements of electrolyte absorption expressed in % as the change of pellet thickness under 60 kPa pressure at the temperature of 400 °C. Binder was calcinated at 400-900 °C and added to the electrolyte in the amount of 20-50 wt%.

**Table I.** (left) Electrolyte absorption by tablet using MgO as a binder.

**Table II.** (right) Electrolyte absorption by tablet using 40% MgF<sub>2</sub>-60% MgO as a binder.

Calcinations temperature of the binder, °C	Concentration of the binder in the electrolyte, %mas.			
	20	30	40	50
400	58.1	1.9	1.3	-
500	75.3	8.7	7.6	1.3
600	87.9	14.1	17.6	8.0
700	86.7	31.9	6.2	1.4
800	84.4	30.7	4.4	4.9
900	74.0	26.4	2.3	1.4

Calcinations temperature of the binder, °C	Concentration of the binder in the electrolyte, %mas.			
	20	30	40	50
500	24.3	4.2	2.6	0.0
600	36.4	18.6	10.8	0.0
700	74.0	33.1	20.8	0.1
800	78.9	67.6	71.3	25.3
900	83.0	77.0	69.0	45.4

Conductivity of the electrolyte pellets containing 50wt% of binder was determined by subjecting them to 60 kPa pressure at the temperature of 400 °C during 300s. Conductivity of the mixture containing MgO as the electrolyte immobilizer and calcinated at the temperature of 400-900 °C, ranged from 0.03 - 0.09 Scm<sup>-1</sup>. Pellets with filler material of the same composition (60% MgO-40% MgF<sub>2</sub>) and investigated in the same test conditions revealed ionic conductivities in the range of 0.03-0.13 Scm<sup>-1</sup>, respectively

The above observations were verified experimentally by discharging the cell of Li/KCl-LiCl-RbCl/FeS<sub>2</sub> system which contained electrolyte immobilizer (40% MgF<sub>2</sub>-60% MgO) in the amount of 40 wt% and calcinated at 500 °C. The experiment consisted in the discharging of the cell through 1.32Ω resistor to 0.5 V at 400 °C and 60 kPa pressure.

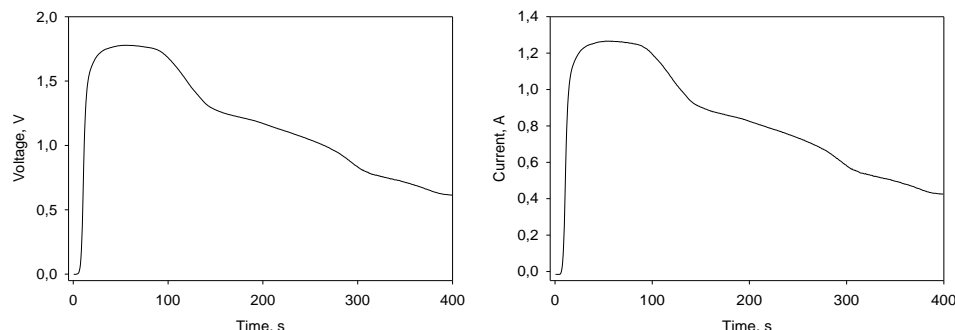


**Figure 1.** (left). Time dependence of the voltage of the cell during discharge at resistor 1.32Ω.

**Figure 2.** (right) Time dependence of the current of the cell during discharge at resistor 1.32Ω

Fig. 1 shows the changes of cell voltage in time, while Fig 2, the changes of cell current as a function of time. The cell under test was capable of delivering stable electrical energy for about 80s. The initial shape of the respective curves reflects the process of electrolyte melting when placed in the measuring device at the temperature of 400 °C. No leakage of electrolyte was observed after the completion of the electrical tests.

It was demonstrated that the use of electrolyte immobilizer in form of F<sup>-</sup> ions surface modified magnesium oxide allows obtaining a mixture which can efficiently protect the cell against uncontrolled electrolyte leakage.

### Acknowledgements

This study is financed within a grand No N N204 214140 by National Science Center Poland.

### References

1. D. Linden, T. Reddy, *Handbook of Batteries*, Mc Grow Hill, New York 2002.
2. S.M. White, *Molten Salts Techniques*, Vol. 1, Chap.2, eds. D. G. Lovering and R.J. Cale, New York 1983.
3. P. Masset, R.A. Guidotti, *J.Power Sources*, **44**, 397 (2007).
4. M. Zieliński, I. Tomska-Foralewska, M. Pietrowski, B. Czajka, M. Wojciechowska, *XLV Polish Annual Conference on Catalysis*, 2013, Kraków, Poland, Proceedings of the Conference p.206.

## Catalytically Active Electrode Materials for Oxygen Electrodes Based on Tungsten - Modified Carbon Nanotubes

Danilov, M.O.\*, Kolbasov, G.Ya.

V.I. Vernadskii Institute of General and Inorganic Chemistry of the Ukrainian National Academy of Sciences, prospekt Palladina 32/34, Kyiv 142, Ukraine

\*Corresponding author: Danilov M.O. E-mail: [danilovmickle@rambler.ru](mailto:danilovmickle@rambler.ru)

Studies on energy-transforming processes are relevant nowadays, because the total energy capacity of distributed power generation exceeds the energy generated by nuclear, thermal and hydroelectric power plants combined. This fact accounts for the increasing interest in fuel cells and in electrode materials for them. The use of air or oxygen electrode in the devices generating electrical energy is very promising because it does not create environmental problems and saves natural resources such as oil and gas. Air and oxygen electrode is a three-phase electrode-electrolyte-gas system, where the generation of electric current is localized at the phase boundary. The current magnitude generated at such gas diffusion electrode depends on the triple contact zone of these three phases. In its turn, the electrode itself is composed of catalyst and carrier. The interaction between them determines the quantity of generated current, which depends on catalyst being used. It is known that nowadays the most effective catalyst for oxygen recovering is platinum, which is a very expensive material. A great number of works is oriented towards the investigation of other effective but less costly catalysts. Another problem is catalytically active and stable carrier. A review article (1-4) displays the possibility of using multiwalled carbon nanotubes as electrode material for oxygen electrodes and also proves the stability of these materials over time for the various media. It was also noted that the use of multiwalled carbon nanotubes as catalyst supports enables no aggregation in contrasts to the use of activated carbons. In works (2-5) the benefits of carbon nanotubes used as the carrier are shown. The application of platinum on carbon nanotubes (CNT) enabled the characteristics of oxygen electrodes to be improved (4). Carbon nanotubes are characterized by high conductivity and large specific surface area. They also can form mesoporous three-dimension structures, which makes them promising as carriers. Tubular carbonic structure enables the extension of triple electrode-electrolyte-oxygen contact zone, where the process of current flow generation takes place. This leads to increasing in operating current density as compared to activated carbon. The advantages of the material also include small specific density of carbon nanotubes as compared to activated carbon. It follows from the data given in (6,7) that the composite consisting of tungsten oxide and platinum have electrocatalytic properties in the reactions of oxygen reduction. Therefore, the investigation of the catalytic activity of tungsten oxide deposited on carbon nanotubes by galvanic method was of special interest. This method of tungsten electrodeposition on carbon nanotubes allows regulating the current density and the time of electrolysis and hence controlling the amount and size of the deposited catalyst particles. The purpose of this study was to investigate the electrocatalytic characteristics of carbon nanotubes, with tungsten oxides applied on them by galvanic deposition, as the material of oxygen electrode for power cell.

Multi-walled carbon nanotubes (MWCNT) (8) were taken in our investigation as carriers and electrode material. The product was a black powder with a bulk density of  $25\text{-}35\text{ g} \cdot \text{dm}^{-3}$ . The outer diameter of nanotubes was about 10-30 nm, the specific surface area was  $230\text{ m}^2\text{ g}^{-1}$ . Two-layer oxygen electrodes were prepared by pressing. Hydrophobic layer contained  $0.07\text{ g} \cdot \text{cm}^{-2}$  acetylene black with 25% polytetrafluoroethylene. The active layer contained  $0.02\text{ g} \cdot \text{cm}^{-2}$  MWCNT, modified by tungsten oxide with 5% polytetrafluoroethylene. The research was conducted on a

power cell mock-up with zinc as the anode. The mock-up for gas diffusion electrodes testing is described in the works (9). A solution of 5M KOH with 1M LiOH was taken as an electrolyte. A silver chloride electrode connected via salt bridge was taken as the reference electrode. All potentials were measured with respect to standard silver chloride electrode. The characteristics were measured in the galvanostatic mode. The source of oxygen was a U-shaped electrolyzer with alkaline electrolyte. Oxygen was fed to the gas electrodes under surplus pressure of 0.01 MPa. Before the research the oxygen electrode was cleaned with oxygen. During the electrochemical research, the current at the electrolyzer exceeded by a factor of three the current generated at the gas electrode. The electron micrographs were obtained with the help of electron microscope JEM-100 CXII. The X-ray phase analysis was carried out with the help of "DRON – 4" X-ray diffractometer (XRD) with the emission of  $\text{CuK}\alpha$ .

The deposition of tungsten oxides was carried out by electrochemical method at different current densities of 10 and 20  $\text{mA}/\text{cm}^2$  from solutions containing equal amount of sodium tungstate  $\text{Na}_2\text{WO}_4 \cdot 2\text{H}_2\text{O}$  reagent grade, 20  $\text{g dm}^{-3}$  and boric acid of high purity with concentration 50  $\text{g dm}^{-3}$ . Conditions of electrolysis were the same: time of electrolysis of 0.25 hour and the temperature of 80 °C. As a result, by electrochemical method nanocomposites based on carbon nanotubes with deposited tungsten oxide compounds were obtained.

The tungsten content in the samples obtained at current densities of 10  $\text{mA}/\text{cm}^2$  and 20 was: 0.25 and 0.45 mass % respectively. Fig. 1 and Fig. 2 shows electron micrographs of the resulting formulations. The photographs show that increasing the applied amount of the tungsten oxide improves the distribution of particles on the surface of the nanotubes. To identify the deposited particles was carried out X-ray analysis of the composites. Fig. 3 show the XRD patterns of tungsten oxide (0.25 mass. % of elemental tungsten) deposited on carbon nanotubes (C- $\text{WO}_3$ ) and initial multiwalled carbon nanotubes (C). All the patterns match the characteristics of  $\text{WO}_3$  crystal (PDF#20-1324) by comparing JCPDS cards. The peak intensities of the  $\text{WO}_3$  are small, which related to the particle size.

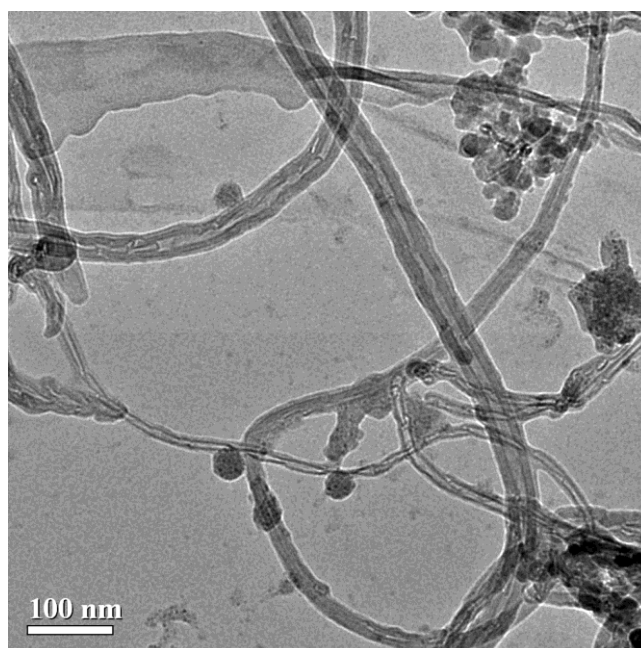


**Figure 1.** Electron micrograph of the tungsten oxide deposited on carbon nanotubes. Elemental tungsten content 0.25 wt %.

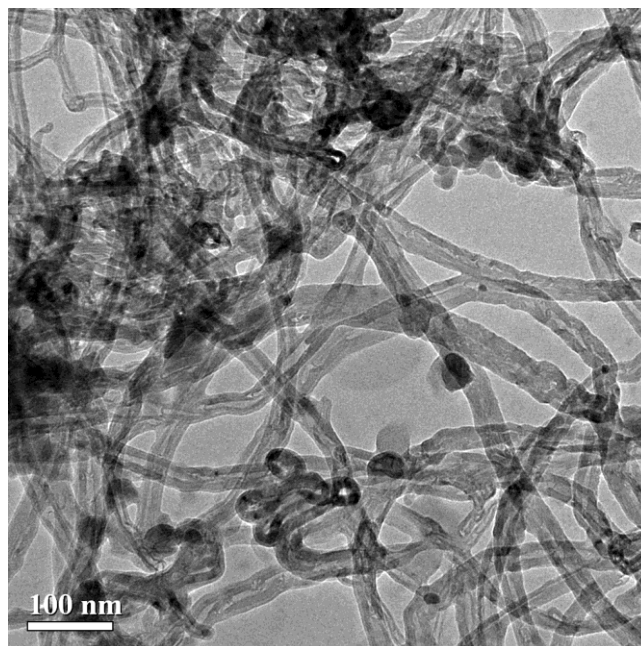


**Figure 2.** Electron micrograph of the tungsten oxide deposited on carbon nanotubes. Elemental tungsten content 0.45 wt %.

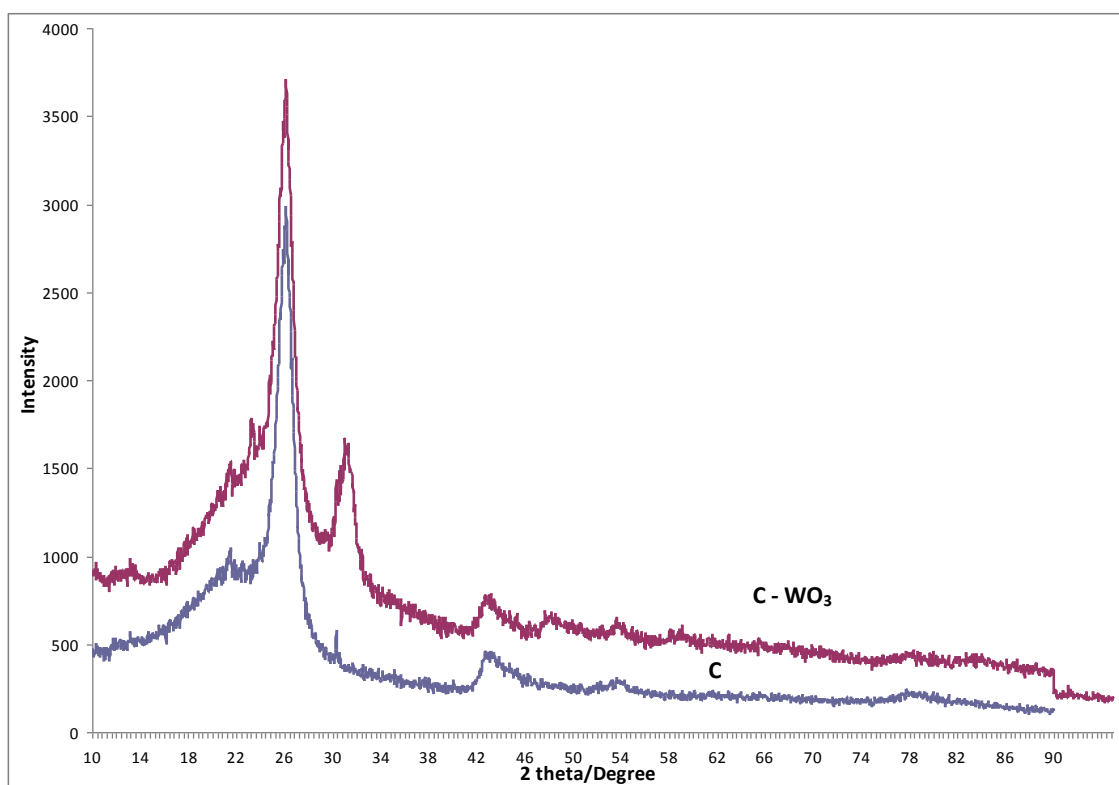


**Figure 3.** X-ray phase analysis of composite based on tungsten oxide deposited on carbon nanotubes ( $C - WO_3$ ) and initial carbon nanotubes (C).

The oxygen electrodes were made from the obtained composites. Fig. 4 shows the plots of potential against current density for oxygen electrode based on nanostructured composites from the nanotubes with tungsten oxide applied on them.

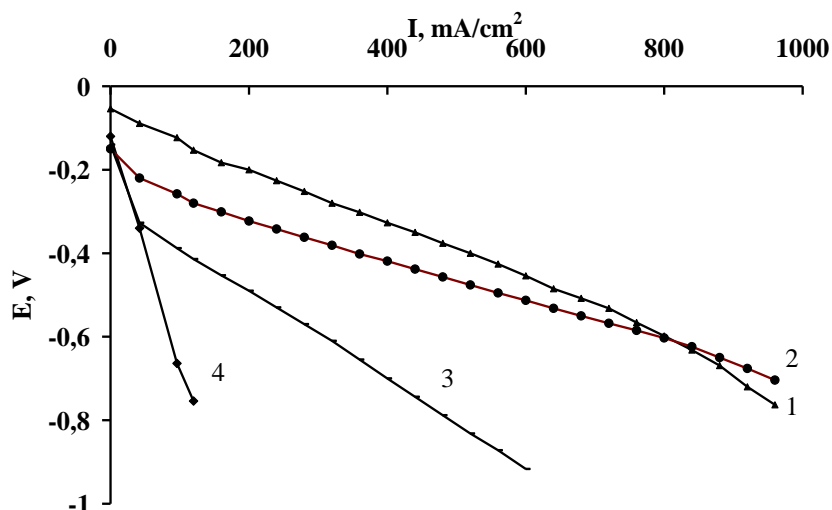


**Figure 4.** Dependence of potential on current density for an oxygen electrode based on  $0.02 \text{ g/cm}^2$  composites of nanotubes and deposited tungsten oxide with elemental tungsten content of (wt %): (2) 0.45, (3) 0.25, carbon nanotubes with deposited Pt (10 wt %) - (1) and pure carbon nanotubes (4).

It follows from the figure 4 that the electrode which contains 0.45 mass % of elemental tungsten has the best characteristics. Next to them, according to activity decrease, are the electrodes based on nanotubes composites with tungsten oxide containing 0.25 mass. % elemental tungsten. Such dependence of electrical characteristics of oxygen electrodes is determined by the relatively uniform deposition of the tungsten oxide compounds on the surface of the carbon nanotubes at the current density  $20 \text{ mA/cm}^2$ . It is also confirmed by electron micrographs of the composites contained elemental tungsten: Fig. 1- 0.25 mass. % (current density  $10 \text{ mA/cm}^2$ ), Fig. 2 for 0.45 mass. % (current density  $20 \text{ mA/cm}^2$ ). For comparison, the figure 4 shows a curve 4 for electrodes based on initial nanotubes and curve 1 for electrodes based on platinum (in an amount of 10 mass. %) deposited by electroplating on multi-walled carbon nanotubes. As seen from the figure 4 current - voltage curves for the tungsten oxide is not inferior to the parameters of electrodes from platinum deposited on the multi-walled carbon nanotubes.

An electrochemical method of production of nanostructured composites based on carbon nanotubes and tungsten oxide compounds is suggested. It is shown that the obtained electrode materials are promising catalysts for oxygen electrodes of power cells, which can substitute for catalysts containing platinum.

## References

1. E. Antolini, *Applied Catalysis B: Environmental*, **88** (1-2), 1 (2009).
2. X. Xie, L. Gao, *Carbon*, **45**, 2365 (2007).
3. S. Yang, X. Zhang, H. Mi, X. Ye, *J. Power Sources*, **175** (1), 26 (2008).
4. X. Wang, M. Waje, Y. Yan, *Electrochem. Solid-State Lett.*, **8** (1), A42 (2005).
5. M.O. Danilov, A.V. Melezhyk, *J. Power Sources*, **163** (1), 376 (2006).
6. Z. Yan, W. Wei, J. Xie, S. Meng, X. Lu, J. Zhu, *J. Power Sources*, **222**, 218 (2013).
7. C. K. Poh, S. H. Lim, Z. Tian, L. and et al, *Nano Energy.*, **2**(1), 28 (2013).
8. A. V. Melezhyk, Yu. I. Sementsov, V. V. Yanchenko, *Russian Journal of Applied Chemistry*, **78** (6), 917 (2005).
9. M.O. Danilov, G.Ya. Kolbasov, I.A. Rusetskii, I.A. Slobodyanyuk, *Russian Journal of Applied Chemistry*, **85**(10), 1536 (2012).

## S-LiFePO<sub>4</sub>-PPy cathode material for Li/S batteries prepared by solid-state synthesis

Fedorková, A.<sup>a,b</sup>, Oriňáková, R.<sup>a</sup>, Sedlaříková, M.<sup>b</sup>, Gómez-Romero, P.<sup>c</sup>

<sup>a</sup> Institute of Chemistry, Faculty of Science, P.J. Šafárik University, Moyzesova 11, SK-04154 Košice, Slovak Republic

<sup>b</sup> Department of Electrical and Electronic Technology, Faculty of Electrical Engineering and Communication, Brno University of Technology, Technická 10, 616 00 Brno, Czech Republic

<sup>c</sup> Centre d'Investigació en Nanociència i Nanotecnologia, CIN2 (CSIC-ICN), Campus UAB, E-08193 Bellaterra, Barcelona, Spain

### Abstract

S-LiFePO<sub>4</sub>-PPy cathode material was synthesized using a solid-state method in ball mill. Using this technique, the preparation of carbon-coated and MWCNTs coated S-LiFePO<sub>4</sub>-PPy nanoparticles were investigated. The S-LiFePO<sub>4</sub>-PPy cathode with MWCNTs additive showed an initial capacity of 1100 mAh/g at 0.1 C. Morphology of this sample is also very homogeneous and distribution of the pores and MWCNTs on the surface of the cathode particles is very well organized. The results suggest that the S-LiFePO<sub>4</sub>-PPy with MWCNTs additive can be used as a cathode material of lithium-ion batteries for large-scale application.

### Introduction

Elemental sulfur is considered to be one of the most promising candidates as a material for the positive electrode of a high-performance lithium secondary battery, because sulfur has a high theoretical specific capacity of 1672 mAh g<sup>-1</sup> for the reaction with lithium to form lithium sulfide (Li<sub>2</sub>S) [1,2]. Generally, the amount of energy which can be stored increases as the number of bound or inserted lithium ions increases. The higher energy density of the lithium-sulfur battery is due to the fact that each sulfur atom can bind two lithium ions, whereas, in the case of conventional battery types, less than one lithium ion is “captured” on average [3-5]. The advantage of lithium-sulfur batteries is primarily their superior storage capacity (energy density), but they also excel in economic and environmental terms. Sulfur is a relatively inexpensive and abundant raw material, unlike expensive elements, such as cobalt, which are used in lithium-ion batteries. This is important because material costs make up a very large proportion of the total cost of a battery. From an environmental perspective, lithium-sulfur batteries also make it possible to avoid the use of heavy metals.

Unfortunately, sulfur has not been sufficiently utilized in lithium secondary batteries with conventional liquid electrolytes because the batteries suffer from rapid capacity fading on cycling. The capacity fading during cycling was due to the fact that polysulfides, which were formed during a discharge process, were dissolved in liquid electrolytes. All-solid-state cells using a solid electrolyte instead of a liquid electrolyte have safety advantages such as nonleakage and nonflammability.

Polypyrrole (PPy) is one of the most extensively studied conducting polymers because it has good environmental stability, low toxicity, and higher conductivity than other conducting polymers; further, it can be synthesized via a facile route. PPy-based composites have been extensively

investigated in a variety of applications such as membranes, drug delivery, rechargeable batteries, super-capacitors, sensors, and electromagnetic interference shielding where the performance of the composites is governed by the high surface area and high average pore diameter of the porous host polymer.

## Experimental

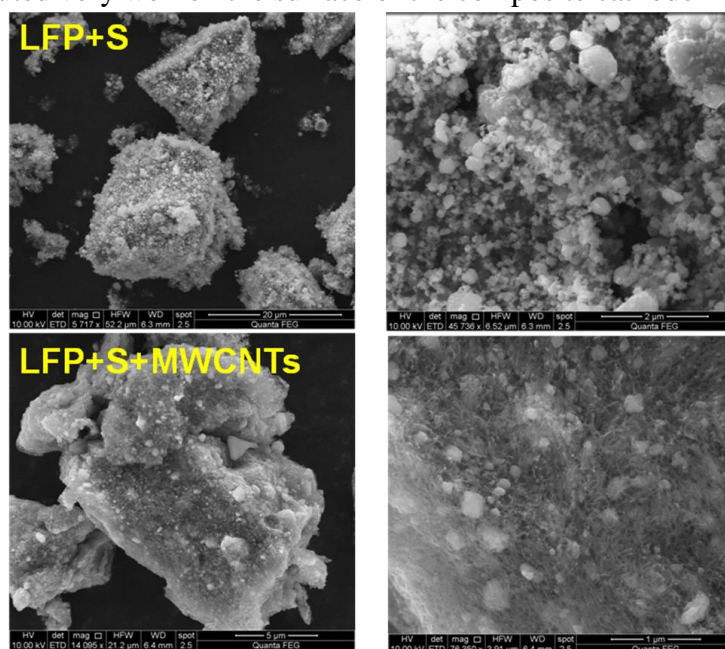
Sulfur and PPy were dried under vacuum at 60 °C for 24 h before use. Carbon-coated LiFePO<sub>4</sub> and MWCNTs were dried under vacuum at 110 °C for 24 h. The S-LiFePO<sub>4</sub>-PPy composite was prepared by processing the mixture of sulfur, LiFePO<sub>4</sub> and PPy (70:20:10 w/o) at 450 Hz for 1 hour using a COL-INT-TECH planetary ball mill.

Slurry was made by mixing the PPy-LiFePO<sub>4</sub> as the active material with Super P and polyvinylidene fluoride (PVdF) in *N*-methyl-2-pyrrolidone (NMP) with a weight ratio of 80:10:10. The slurry was then coated onto aluminium foil as current collector and carefully dried at 55 °C under mild vacuum. Circular electrodes with 12 mm diameter were cut out of the coated foil, with an area of 1.13 cm<sup>2</sup> and total mass of 1.5-2 mg on a substrate of Al foil. Test cells were assembled using these cathodes in a Swagelok cell together with a reference electrode made from lithium metal foil and a separator layer (SEPARION<sup>®</sup> and fibber glass separator Wattman GF/D). All handling was done in an argon filled dry glove box.

Electrochemical tests were performed at 25 °C using a VMP3 cyler (Bio-Logic SAS). Scanning electron microscopy (SEM) images were obtained using a field emission electron microscope (Hitachi model S-4700).

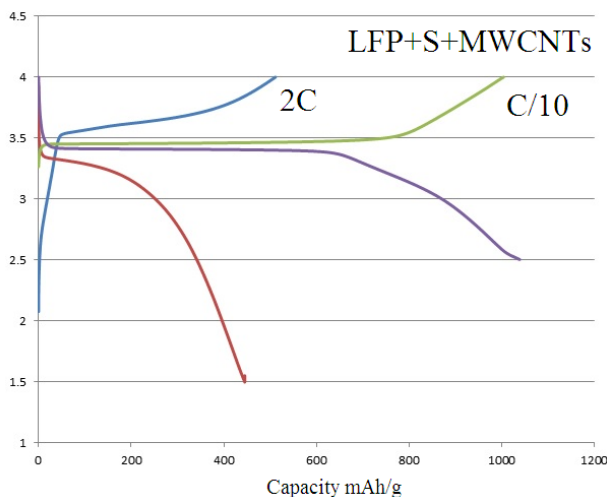
## Results and discussion

Fig. 1 shows the morphology of S-LiFePO<sub>4</sub> and the S-LiFePO<sub>4</sub>-MWCNTs cathode material. The sulfur is composed of loose agglomerates of 10–20 μm primary particles. During the mechano-chemical reaction, the sulfur particles are covered with the finer LiFePO<sub>4</sub> particles on the surface. MWCNTs are distributed very well on the surface of the composite cathode material.



**Figure 1.** SEM images showing the morphology of the S-LiFePO<sub>4</sub> sample (up) and S-LiFePO<sub>4</sub>-MWCNTs sample (down).

The initial discharge and charge profiles of S-LiFePO<sub>4</sub>-MWCNTs composite cathode material are presented in Fig. 2. The S-LiFePO<sub>4</sub>-MWCNTs composite cathode displays a higher discharge capacity (1100 mAh/g) voltage plateau at 3.4 V. The initial discharge capacity at 2C rate was about 440 mAh/g.



**Figure 2.** The first discharge and charge profiles at 0.1 C and 2 C for S-LiFePO<sub>4</sub>-MWCNTs composite cathode material.

### Acknowledgement

The authors wish to acknowledge financial support from the Grant Agency of the Ministry of Education of the Slovak Republic, Grant No. 1/0211/12, Center of Research and Utilization of Renewable Energy Sources, No. CZ.1.05/2.1.00/01.0014, and project CZ.1.07/2.3.00/30.0039 of Brno University of Technology.

### References

1. P. G. Bruce, S. A. Freunberger, L. J. Hardwick, J. M. Tarascon, *Nat. Mater.*, 11 (2012), p. 19
2. X. Ji, L. F. Nazar, *J. Mater. Chem.*, 20 (2010), p. 9821
3. A. Fedorkova, R. Orinakova, A. Orinak, I. Talian, A. Heile, H.-D. Wiemhofer, D. Kaniansky, H. F. Arlinghaus, *J. Power Sources*, 12 (2010) 3907.
4. Y. H. Huang, K. S. Park, J. B. Goodenough, *J. Electrochem. Soc.*, 153 (12) (2006), A2282.
5. B. Kang, G. Ceder, *Nature*, 458 (2009), pp. 190.

## Recent development in lithium batteries and related topics

Vondrák, J. \*, Sedlaříková, M.

Department of Electrotechnology, Faculty of Electrotechnical Engineering, Brno University of Technology

\* Corresponding author: vondrakj@feec.vutbr.cz

It would be useless to emphasize the importance of lithium secondary batteries for modern life.

We have studied the problems connected to lithium batteries and materials for them from a variety of viewpoints. They can be divided in several groups:

- a) The cathode materials, the improvement of their specific energy and contribution to the safety of the batteries
- b) The anode materials based on carbon, silicon or other materials able to intercalate lithium atoms
- c) Lithium cells with voltage approaching the limit 5 V
- d) Aprotic electrolytes for lithium systems

### Modifications of cathode materials

Lithium cobalt oxides are known to be extremely sensitive on improper charging and discharging. Attempts to improve the specific energy and charge by modification of their composition had to be done. The stability of these materials was increased by addition of potassium compounds in the process of their preparation. The capacity was decreased slightly, but the material was less vulnerable by overcharge (by complete removal of intercalated alkali ions) and its voltage during discharge did not sink so rapidly. The latter is caused by crystallographic and thermodynamic processes.

Also lithium ferrophosphate was found to be one of the best choices, thanks to its stability. Modifications of the basic material by doping or substitution of iron by other elements was checked.

### Modification of anode materials

Classical graphite was used as the anode material at first place. Treatment with butyl lithium was introduced for improvement of initial irreversible charging in first cycle of a new cell. Also the treatment by annealing in CO<sub>2</sub> was checked; it increased the reversible capacity closer to theoretical value. These experiments were performed with expanded graphite.

Recently, new anode materials have been introduced. We started to investigate SiC, silicon of various grain size and lithium titanium oxide. The testes were not entirely successful. We started to study electrodeposition of silicon and other metals from aprotic solution with the aim to find most efficient ones.

Lithiated cathode materials based on carbon are known to be strong reducing agents and their fire danger must be taken in account.

In cooperation with Technical Institute of Fire Protection in Prague, we have started to prepare greater amounts of lithiated graphite in a non – electrochemical way. Its flammability and

the possibility of fire extinguishing have been investigated. Apparently, these anode materials are virtually much less dangerous as metallic lithium itself.

### Lithium batteries with voltage approaching 5 V

There is a possibility to increase specific energy of a lithium cell by increasing its voltage. This is possible by the use of a new family of cathode materials, which contain compounds based on the substance  $LiNi_{0.5}Mn_{1.5}O_4$ . Lithium cells with voltage approaching the limit 5 V will offer by 20 – 25 % higher energy density than batteries used nowadays:

The changes of valence in the material were tested by EPR spectroscopy. The change of valence of manganese to +5 and that of nickel to +4 was identified and these values explain the unusually high potential of this material.

The composition of the cathode materials was tested by SEM / EDX mapping. Apparently, the distribution of all important components seems to be homogenous in all particles.

These materials require electrolytes sufficiently stable against high electrode potentials.

Electrolytes prepared from sulfolane fulfil this requirement and offer higher safety due to their lower flammability.

### Investigation of composite gel electrolytes

Gel polymer electrolytes prepared from methylmethacrylate and sodium perchlorate in suitable solvents were investigated. It was indicated clearly that these composites contain macromolecular chains “flowing” in liquid component. Relaxation time obtained by NMR and measurement of molar conductivities has shown that the ions of sodium are much more mobile in systems which contain more of free solvent.

### Investigation of liquid electrolytes

Modern lithium batteries need electrolytes which are stable at higher temperatures and less flammable. Moreover, the higher resistivity against oxidation is also important. We started to investigate the use of sulfolane as a solvent for this purpose. Its use increases the flash point by 30 – 50 degrees C, and the main disadvantage of rather high freezing point can be overcome by suitable additives. Sulfolane can be used as the constituent of gel polymer (composite) electrodes similarly to cyclic carbonates and similar substances. Lithium electrolytes (*e.g.*, lithium tetrafluoride or hexafluoride) prepared from sulfolane are electrochemically stable in contact with high voltage materials. Most recently we started the addition of other sulfones to dimethylsulfone. Finally, we have been interested in addition of triethylphosphate as flame retardant to these electrolytes. On contrary to expectation, amount up to 20% by vol. increased molar conductivity quite essentially. This phosphate would not interfere in lithium cells from conductivity reasons at least.

## **Other projects**

We are open to start the research of any further innovations in the electrochemistry of lithium. Just recently we started to perform experiments with the system lithium – sulphur, which is discussed vividly just now.

Another important effect will be preparation of thin layer systems for special purposes.

### **Acknowledgments**

Among others, our investigation has been supported by :

Center of Research and Utilization of Renewable Energy Sources CVVOZE project No.Cz.1.05/2.1.00/01.0014 and by a common research program No. 7AMB13AR008 based on cooperation between BUT and INIFTA, UNLP, Argentina.

## Sulfur based cathode materials for li-ion batteries

Cech, O.<sup>a</sup>, Fedorkova, A.<sup>a</sup>, Sedlarikova, M.<sup>a</sup>

<sup>a</sup> Department of Electrotechnology, Brno University of Technology, Brno, Czech Republic

<sup>b</sup> Centre of Research and Utilization of Renewable Energy, Brno, Czech Republic

The article deals with the properties of elemental sulfur and the polymeric sulfur compounds with respect to their utilization in li-ion cathodes. It aims to summarize fundamental differences between conventional and sulfur based electrodes and wants to show an easy and cheap method of preparation of sulfur electrode.

### Intercalation and conversion materials

Elemental sulfur together with sulfur compounds and sulfur-based polymers attracted attention of many researchers working in the field of li-ion batteries in past years. Undoubtedly, it is one of the most promising cathode materials. Sulfur is an available, cheap and harmless material with astonishing theoretical capacity of 1672 mAh/g and due to its low bulk density also astonishing energy density as high as 2600 Wh/kg(1).

All known commercially available lithium-ion batteries of today are fitted with active materials based on different types of intercalation compounds. Intercalation is a reversible process of incorporating of an ion into a crystallic structure without changing its crystallographic properties. One of the biggest advantages of this concept is a very low volume change during charge and discharge. On the other hand, the theoretical specific capacity of such materials is limited due to a small fraction of lithium in crystalline cell. Mostly used intercalation materials for li-ion batteries are  $\text{LiCoO}_2$  (274 mAh/g),  $\text{LiFePO}_4$  (165 mAh/g) and  $\text{Li}_4\text{Ti}_5\text{O}_{12}$  (296 mAh/g).

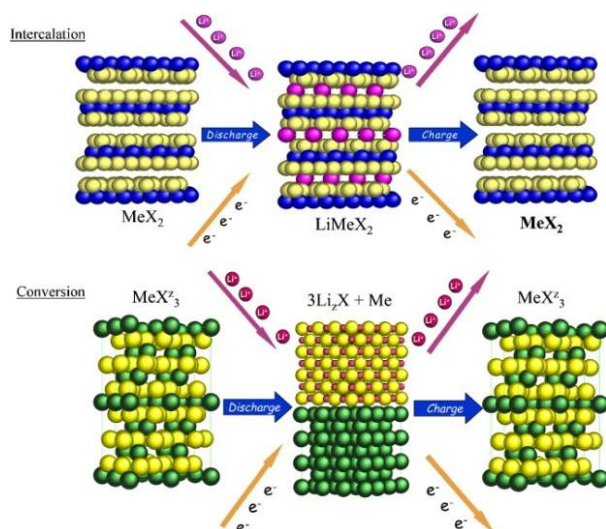


**Figure 1.** Illustrated difference between intercalation and conversion principle(2)

Utilization of conversion principle is a new approach to electrode active materials for rechargeable li-ion batteries. Conversion electrodes are based on materials which changes their phase structure during charge and discharge to form compounds with different properties from

starting material(3). Discharge capacity of electrode materials based on conversion principle is usually in order of magnitude higher compared with the intercalation materials. Unfortunately, massive utilization of such materials in batteries is still not possible due to three main drawbacks: a) very low intrinsic conductivity b) massive volume changes during cycling c) possible solubility of intermediate products in electrolyte. See Figure 1 for difference between intercalation and conversion materials(3).

### Sulfur cathode for li-ion cells

Sulfur is probably the most promising materials for li-ion cathodes in the present. Elemental sulfur itself has three basic allotropes. Orthorhombic  $\alpha$  is the most common one and it transforms to monoclinic  $\beta$  form at the temperature 94.4 °C which is still below the melting point of 112 °C. It is also possible to obtain another monoclinic allotrope at temperature about 200 °C which is heavier and decomposes at room temperature.

The conductivity of elemental sulfur corresponds to an insulator (approx.  $5 \cdot 10^{-30} \text{ S}\cdot\text{cm}^{-1}$  at 25 °C) with both types of charge carrier. In sulfur, mobility of electrons is  $10^{-4} \text{ cm}^2\text{V}^{-1}\text{s}^{-1}$  and mobility of holes is  $10 \text{ cm}^2\text{V}^{-1}\text{s}^{-1}$ .

### Electrode preparation and results

One of the perspective approaches to elimination of drawbacks arising from the electrochemical properties of sulfur is its encapsulation in pores of special conductive carbons for li-ion batteries (4, 5). It can be basically made by filling the carbon pores by melted sulfur or deposition of sulfur from a liquid solution. Encapsulation in the pores of carbon prevents sulfur intermediates from dissolution in electrolyte and makes conductive contact with small particles of active material.

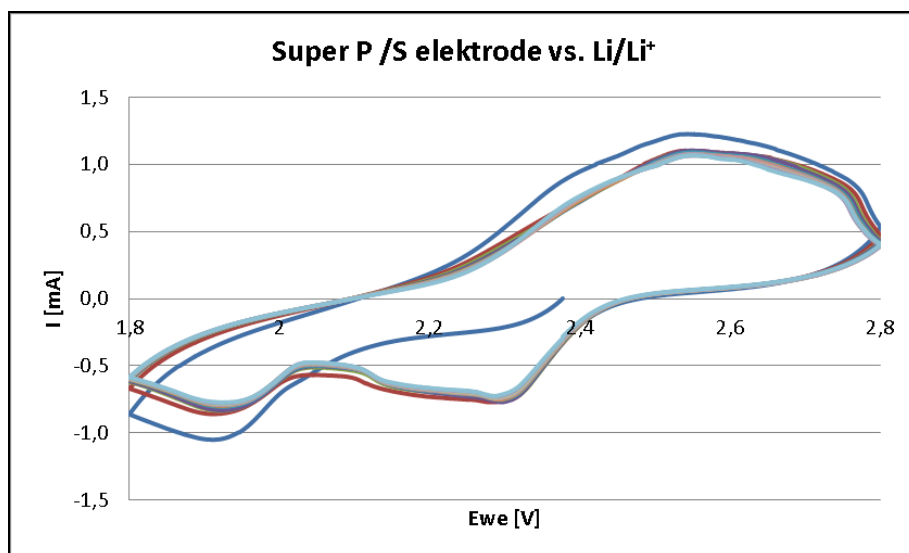


**Figure 2.** Cyclic voltamogram of electrode prepared by impregnation of Timcal Super P carbon by molten sulfur.

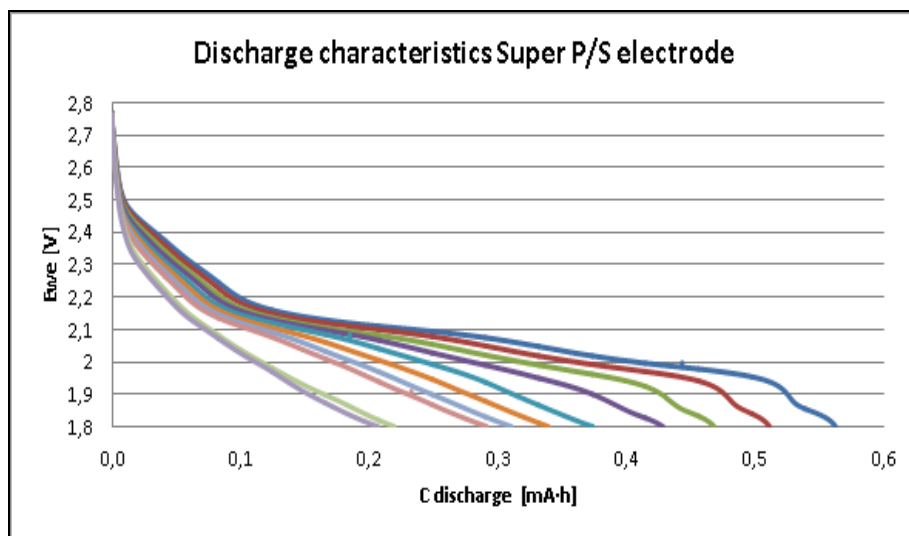


**Figure 3.** Discharge characteristics of Super P/S electrode. It is possible to see capacity fade during cycling.

### Acknowledgments

This work was made due to support of CVVOZE CZ.1.05/2.1.00/01.0014 and grant FEKT-S-11-7.

### References

1. J. Jin, Z. Wen, X. Liang, Y. Cui and X. Wu, *Solid State Ionics*.
2. G. G. Amatucci and N. Pereira, *Journal of Fluorine Chemistry*, **128**, 243 (2007).
3. J. Hassoun, J. Kim, D.-J. Lee, H.-G. Jung, S.-M. Lee, Y.-K. Sun and B. Scrosati, *Journal of Power Sources*, **202**, 308 (2012).
4. M. Rao, X. Song, H. Liao and E. J. Cairns, *Electrochimica Acta*, **65**, 228 (2012).
5. X. Ji, K. T. Lee and L. F. Nazar, *Nat Mater*, **8**, 500 (2009).

## Properties of Solvents for Aprotic Electrolytes with Fire Retardant

Frk, M., Maca, J., Rozsivalova, Z., Sedlarikova, M.

Brno University of Technology, Technická 10, Brno, Czech Republic

The question of battery safety is much discussed in these days. Batteries are used in almost mobile electronic devices. The main idea of our research is to use combination of commercial used solvent (propylene carbonate) with new low flammable solvents as sulfolane. To improve the temperature stability, we added a fire retardant triethylphosphate to reach even larger temperature use window.

### Introduction

The flame retardants are substances, with slow or stop the burn occurrences of materials, or the burning process itself (creation and spreading of flame). The flame retardants are used in all state of matter solid, liquid and gas. The flame retardants are working in specific phase of burning process e. g. temperature increasing, substances decomposition or formation of flames. In praxis there are used a combination of different flame retardants for synergistic effect of desired influence. There are two main possibilities of interaction of flame retardation in manufacturing process flame retardants additive and reactive. The additive retardants are part of the material but they are not connected to the base material on molecule bound level. Usually they are added to the material in end phase of material preparation or after the finishing of base material. The influence of this retardant kind is on physical base. The additive retardant is decomposed by the influence of temperature on factors with depressed the burning, limits burning and expansion of heat and flame. The fire retardants are substances with high temperature capacity and endothermic influence. The retarder cools the material in burning process so that it is absorbing part of the thermal energy and cools the material below the flash point temperature. Concurrently by decomposition of flame retardant are inert gas released and the flammable gases are diluted with prevents re-ignition. There exist inorganic mineral retardants (metal hydroxides), halogenated flame retardants *TBBPA* (*tetrabrom - bisfenol A*), *HDCD* (hexabrom - cykłododekan) *PDBE* (polybrom – difenyl - ether) and phosphor based retardands such as triethylphosphate with we are using. Triethylphosphate is a colourless liquid, the melting point and boiling point of which are -112 °C and 215 °C. Its viscosity is lower than that of sulfoane (10.65 mPa·s at 30 °C) and permittivity at room temperature is 13.

### Experimental method and instrumentation

The behaviour of solvents for aprotic electrolytes in an AC electric field is monitored using the method of dielectric relaxation spectroscopy in the frequency range 20 Hz - 2 MHz and in the temperature interval from ambient temperature to 90 °C. Dielectric relaxation spectroscopy represents widespread non-destructive diagnostic method using the frequency dependence of impedance characteristics or other suitable physical quantities ( $\underline{C}_s$ ,  $C_p$ ,  $R_p$ ,  $tg\delta$ ) for the analysis of the material properties. The principle of the method is monitoring of permanent and induced dipoles response in electric field. In an AC electric field, it represents measurement of frequency dependencies of the components of the complex permittivity or measurement of time dependencies of charging and discharging currents in the case of DC electric field.

The real and imaginary part of complex permittivity was calculated from measured values of parallel capacity  $C_p$ , dissipation factor  $tg\delta$  and dimension of sample respectively test fixture. Finally, the real part of complex permittivity is expressed as

$$\varepsilon' = \frac{C_p}{C_0} = \frac{C_p h}{\varepsilon_0 S_{ef}} \quad (1)$$

where  $C_p$  and  $C_0$  is capacity of sample resp. geometric capacity,  $h$  is thickness of the sample,  $\varepsilon_0 = 8,854.10^{-12} \text{ F m}^{-1}$  (permittivity of free space) and  $S_{ef}$  is effective area.

Imaginary part of complex permittivity is given by following formula

$$\varepsilon'' = \varepsilon' tg\delta \quad (2)$$

Fully automated laboratory workplace was designed and assembled for measurement of frequency dependencies of the complex permittivity components of liquid materials in temperature range. Workplace is comprised of precision LRC meters Agilent 4980A including dielectric liquid test fixture Agilent 16452A, bath thermostat Medingen KT40 and control computer. Frequency range of RLC meter is 20 Hz – 2 MHz and bath thermostat is usable in the temperature range (-40 – 200) °C with a sensitivity of  $\pm 0.1$  °C and temperature stability more than 0.05 °C. The liquid test fixture with solvent sample is immersed into a water bath which is heated to requirement temperature. Data communication between RLC meter, bath thermostat and is provided via LAN interface and LAN/RS232 gateway. Control of the measuring system is commanded by a software application programmed in graphical language environment Agilent VEE Pro and measured data is stored for further processing in MS Excel spreadsheet. The arrangement of laboratory workplace for measurement of electrical properties of liquid materials is shown in Fig. 1.

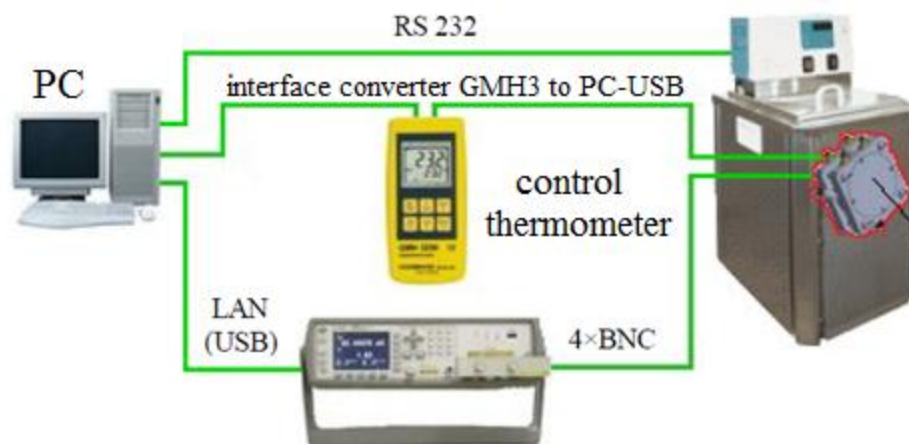


**Figure 1.** Schematic illustration of instruments connection for measuring electrical properties

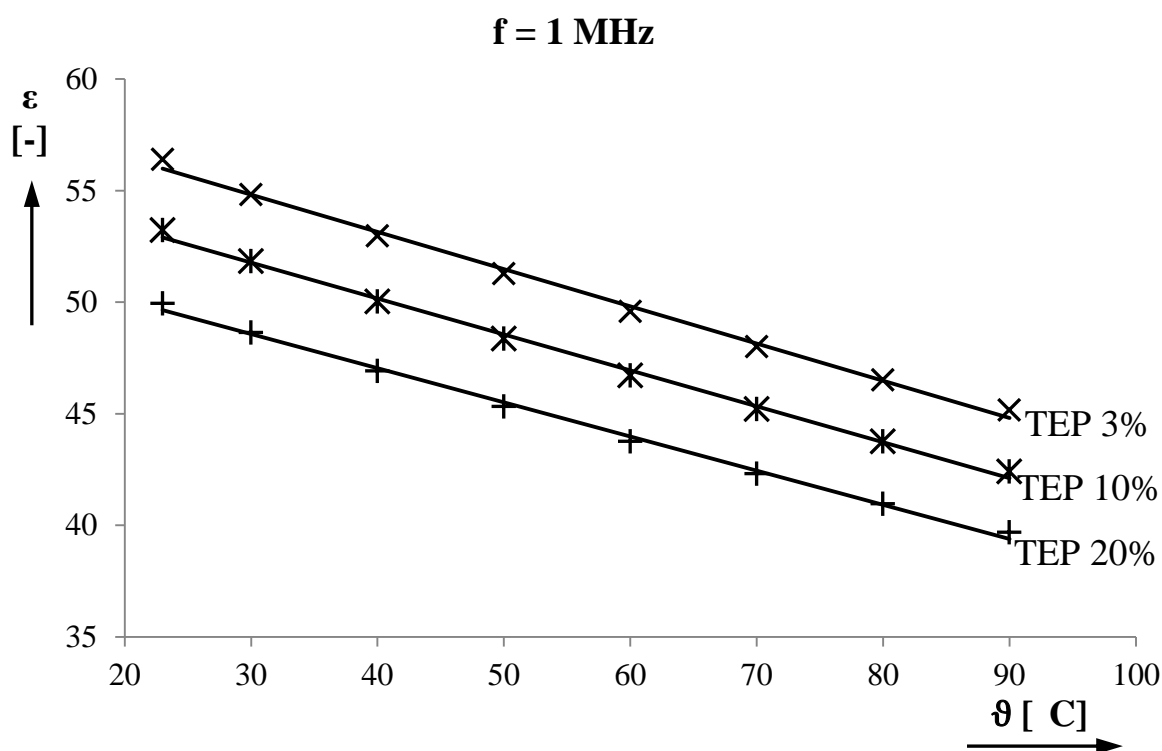
In our experiments were used solvents sulfolane (Sigma Aldrich) 99% and propylene carbonate (Sigma Aldrich) 99.7% and fire retardant triethylphosphate (Sigma Aldrich) with 99.8% purity. The samples were prepared by blending of sulfolane and second solvents in volume ratio determination. Above this volume was added the flame retardant in 3, 10 and 20% of the base volume. The samples were prepared in dry box without access of air humidity and oxygen.

## Results

In Table I are numeric listed the values of relative permittivity of measured solutions. The prepared samples were 25 vol.% of sulfolane, 75vol.% of propylene carbonate and 3%, 10% and 20% of triethylphosphate from basic volume. For higher clarity is on Fig. 2 shown the temperature dependence of permittivity for only one frequency and that 1 MHz.

**TABLE I.** Results of permittivity measurement

$f = 1 \text{ MHz}$			
$\vartheta [^{\circ}\text{C}]$	$\varepsilon [-]$ TEP 3%	$\varepsilon [-]$ TEP 10%	$\varepsilon [-]$ TEP 20%
23	56.39	53.22	49.95
30	54.82	51.83	48.63
40	52.97	50.03	46.91
50	51.27	48.36	45.33
60	49.59	46.71	43.75
70	48.01	45.20	42.31
80	46.51	43.75	40.96
90	45.16	42.41	39.69

**Figure 2.** The temperature dependence of permittivity

### Discussion

As shown in Fig. 2, the value of real permittivity varies from 56 for sample with 3% TEP at ambient temperature to 39 for sample with 20% TEP at 90 °C and is dependent on temperature as well as on frequency. It is obvious that the permittivity is decreased with increased concentration of triethylphosphate because the triethylphosphate has the lowest permittivity from all used compounds. The permittivity dependence will be compared with calculated values of permittivity obtained from Onsager - Debye - Hückel equation in further work. The decreasing of the permittivity with temperature is caused by higher thermal motion of molecules and the deviation position of molecules is less perfect alignment with the electric field and this caused the permittivity decreasing. From measured results it is shown that by adding the flame retardant, the main property for complete dissolving of salts in electrolytes ( $\varepsilon > 30$ ) is not violated.

### Acknowledgement

This work was supported by specific research FEKT-S-11-7 Materials and technologies for electronics and project CZ.1.07/2.3.00/20.0103 “Support for human resources and transfer of knowledge in conditions of international cooperation of research teams“.

### References

1. A. Abouimrane, I. Belharouak and K. Amine, Sulfolane-based electrolytes for high-voltage Li ion batteries, in *Electrochemistry- Communications* 11 (2009), pp. 1073–1076.
2. Y. Marcus, *The Properties of Solvents*, John Wiley & Sons Ltd, Chichester (1998), p. 399.
3. A. A. Amooey, Improved mixing rules for description of the permittivity of mixtures, *Journal of Molecular Liquids* 180 (2013), pp 31-33.
4. Types of chemical flame retardants, [online] <http://www.epa.gov/dfe/pubs/flameret/altrep-v1/altrep-v1a-sec2.pdf>

## Comparison of production processes of high-voltage cathode materials

Kazda, T.<sup>a</sup>, Vondrák, J.<sup>a</sup>, Di Noto, V.<sup>b</sup>, Sedlaříková, M.<sup>a</sup>, Čudek, P.<sup>a</sup>

<sup>a</sup> Department of Electrical and Electronic Technology, Faculty of Electrical Engineering and Communication, BUT, Technická 10, 616 00 Brno, Czech Republic

<sup>b</sup> Dipartimento di Chimica Inorganica, Metallorganica ed Analitica, Università di Padova, via Loredan 4, 35121 Padua, Italy

The first mentions of cathode materials for lithium-ion batteries have emerged around the year 1980 and since then these materials have undergone extensive development which continues until today. Lately high-voltage cathode materials attracted attention, those are materials with a voltage approaching 5 V. This enables a higher voltage while maintaining a similar capacity as that of conventional materials such as LiCoO<sub>2</sub> or LiFePO<sub>4</sub> and thus achieving higher power density obtained from the battery based on this type of cathode materials. This article compares the resulting properties of high-voltage cathode materials obtained by two preparation methods.

### Introduction

These materials are mostly based on LiMn<sub>2</sub>O<sub>4</sub> – it has spinel structure that makes it more stable than LiCoO<sub>2</sub> which means that these materials can operate at higher voltages than currently commonly used materials. This material is not very toxic and is thermally stable because of the use of Mn. Its specific capacity is ~ 120 mAh/g and the voltage against lithium 4 V [1][2]. If one fourth of manganese atoms is substituted by nickel, this material can be charged up to 5 V and the voltage against lithium is about 4.7 V. This voltage is therefore about 1 V more than other today's commonly used materials offer. The theoretical capacity of LiNi<sub>0.5</sub>Mn<sub>1.5</sub>O<sub>4</sub> material is ~ 147 mAh/g, due to its capacity and high voltage its energy density is 700Wh/kg which is approximately 20% higher than LiCoO<sub>2</sub> and 30% higher than LiFePO<sub>4</sub> [3][4]. Thanks to the spinel structure the material remains stable during cycling and handles higher load currents well. These properties are interesting for example for use in automotive applications. This cathode material reaches the high voltage using several oxidation steps at which there occurs conversion LiNi<sub>0.5</sub><sup>II</sup>Mn<sub>1.5</sub><sup>III</sup>O<sub>4</sub>/Ni<sub>0.5</sub><sup>IV</sup>Mn<sub>1.5</sub><sup>IV</sup>O<sub>4</sub>. At 4V vs Li this material oxidizes Mn<sup>3+</sup> to Mn<sup>4+</sup> and subsequently at the voltage range 4.7 – 4.8 V vs Li Ni<sup>2+</sup> it is oxidized to Ni<sup>3+</sup> and then to Ni<sup>4+</sup> [5]. With this successive change of the valence of nickel it is possible that two discharge plateaus can merge in one very stable discharge plateau. Cathode material LiNi<sub>0.5</sub>Mn<sub>1.5</sub>O<sub>4</sub> loses its capacity during cycling very slightly, even at higher temperatures, because of its stable spinel structure. The capacity decrease of the material during cycling at room temperature at 0.2 C is around 6% after 400 charge/discharge cycles, a similar decrease in capacity during cycling remains at the current of 1 C. Another advantage of this material is that it is very good at loading very high discharge currents of up to 20 C,[6] which is very important property for the use of lithium-ion batteries in the automotive industry.

## Experimental

The method of reaction in solid state was chosen for the production of this material. Precursors based on carbonates have been selected as basic materials for the production. We chose  $\text{Li}_2\text{CO}_3$  (lithium carbonate),  $\text{MnCO}_3$  (manganese carbonate) and  $\text{NiO}$  (nickel oxide). These three materials were mixed in a stoichiometric ratio 0.02M. Two types of production processes (a two-step annealing process and a three-step annealing process) were selected for the preparation. Both these processes are described in the literature but without any comparison. During the two-step annealing process precursors are weighed and crushed together in a ball mill for 4 hours for a good mixing and refining the structure. This is followed by annealing in an oven for 24 hours at 900 °C, and the next step is re-annealing at 700 °C for 8 hours. As a second method the method of reaction in solid state using a three-step annealing process was chosen. During this process, selected precursors are first milled together for 4h. In the first annealing step, the resultant mixture is annealed at 600 °C for 10h. The second step is annealing at 900 °C for 15h. Last – third - annealing step is annealing at 700 °C for 15h. Material which was prepared this way was then mixed into a mixture consisting of NMP (N-Methyl-2-pyrrolidone) (solvent), PVDF (Polyvinylidene fluoride) (binder) and carbon Super P. The weight ratio of materials was: 80%, Super P 10%, PVDF 10%. The resulting mixture was subsequently deposited on an Al foil, dried and pressed by the pressure of 3200 kg/cm<sup>2</sup>. A disk with a diameter of 18 mm was cut out of the coated aluminium foil and inserted into the electrochemical test cell El-Cell<sup>®</sup> ECC-STD. Assembly was done in glove box filled with argon atmosphere. As an anode material metal lithium was used and as an electrolyte 1M  $\text{LiPF}_6$  impregnated in the glass fibre separator, ratio of solvents in the mixture was: EC:DMC 1:1 w/w.

Galvanostatic cycling was used for measuring; the potential window was set from 3 to 5.1 V versus lithium. Two cycles of charging and discharging have always been carried out during which the used charging and discharging currents were 0.5 C (calculated from the weight of the deposited material provided that the capacity of the material is 120 mAh/g). The real value of capacity of the sample has been deducted from these two cycles and the sample was then submitted to long term cycling, during which it was cycled four times by current 1C, then subsequently cycled ten times by current 0.5 C, then again four times by current 1C, and finally there were four cycles by current 0.5 C. The samples produced by the two-step annealing process were identified as  $\text{LiNi}_{0.5}\text{Mn}_{1.5}\text{O}_4$  No1 and samples created by three-step annealing process  $\text{LiNi}_{0.5}\text{Mn}_{1.5}\text{O}_4$  No2.

**TABLE I.** The capacity of the  $\text{LiNi}_{0.5}\text{Mn}_{1.5}\text{O}_4$  No1 and  $\text{LiNi}_{0.5}\text{Mn}_{1.5}\text{O}_4$  No2 in the first two discharging cycles

Capacity in cycle [mAh/g]	$\text{LiNi}_{0.5}\text{Mn}_{1.5}\text{O}_4$ No1	$\text{LiNi}_{0.5}\text{Mn}_{1.5}\text{O}_4$ No2
1st	41.3 mAh/g	61.1 mAh/g
2nd	34.4 mAh/g	58.6 mAh/g

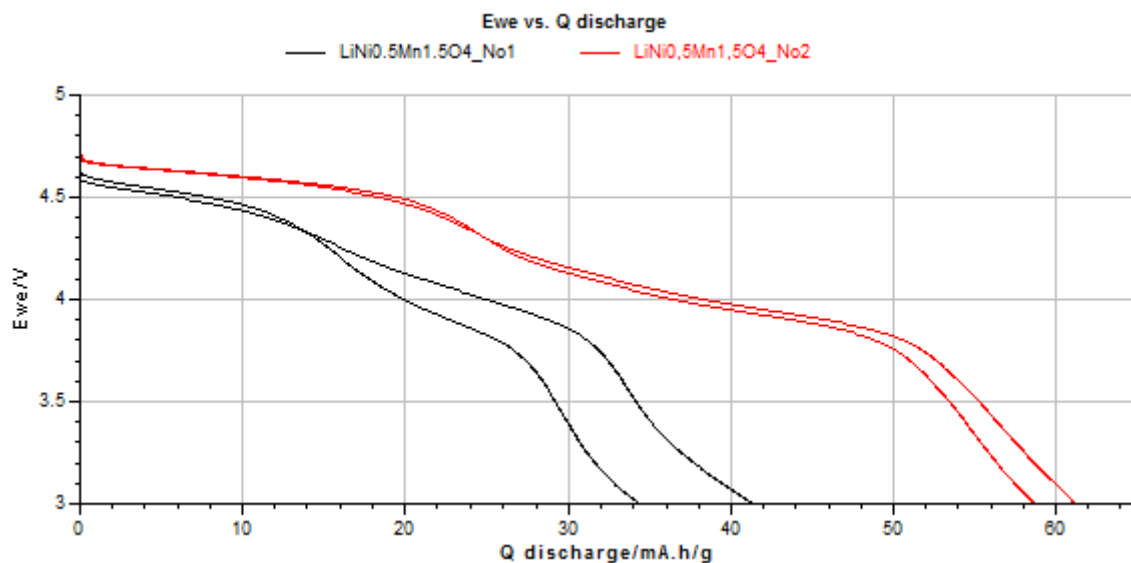


**Figure 1.** Comparisons of capacity in the first two cycles of the samples of LiNi<sub>0.5</sub>Mn<sub>1.5</sub>O<sub>4</sub> No1 and LiNi<sub>0.5</sub>Mn<sub>1.5</sub>O<sub>4</sub> No2

From the measured values during the first two cycles shown in Figure 1 and listed in Table 1 were determined by the capacity of these two materials. According to these two capacities were determined discharging currents for the next measurement.

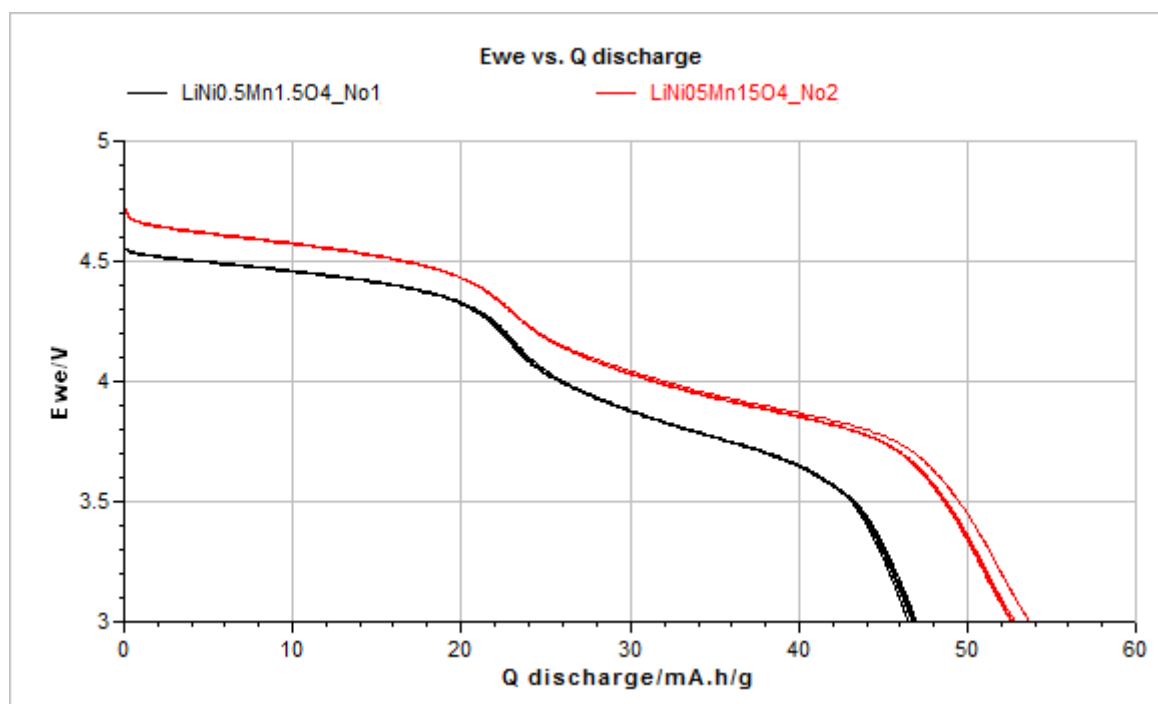


**Figure 2.** Comparisons of during second four cycles by 1 C of the samples of LiNi<sub>0.5</sub>Mn<sub>1.5</sub>O<sub>4</sub> No1 and LiNi<sub>0.5</sub>Mn<sub>1.5</sub>O<sub>4</sub> No2

**TABLE II.** The capacity of  $\text{LiNi}_{0.5}\text{Mn}_{1.5}\text{O}_4$  No1 and  $\text{LiNi}_{0.5}\text{Mn}_{1.5}\text{O}_4$  No2 the during long term cycling

Name of discharge cycle	$\text{LiNi}_{0.5}\text{Mn}_{1.5}\text{O}_4$ No1	$\text{LiNi}_{0.5}\text{Mn}_{1.5}\text{O}_4$ No2
1C - cycle No.1	48.8 mAh/g	58.8 mAh/g
1C - cycle No.4	47.7 mAh/g	57.3 mAh/g
0.5C - cycle No.1	58.3 mAh/g	62.4 mAh/g
0.5C - cycle No.10	56.0 mAh/g	58.2 mAh/g
Repeat 1C - cycle No.1	46.5 mAh/g	53.7 mAh/g
Repeat 1C - cycle No.4	46.8 mAh/g	52.9 mAh/g
Repeat 0.5C - cycle No.1	54.9 mAh/g	57.8 mAh/g
Repeat 0.5C - cycle No.4	54.3 mAh/g	58.2 mAh/g

### Conclusions

In comparison the measured results show that both samples have lower capacity than the theoretical capacity and capacity quoted in the articles, this may be due to natural cooling of cooling controlled instead, which is recommended for proper crystallization of the material. Furthermore, it is apparent that the materials exhibit discharge plateau at 4.7 V as disclosed in the literature. Both materials exhibit generally very stable capacity even at high loads. However, when compared to each other materials, we can see that the material  $\text{LiNi}_{0.5}\text{Mn}_{1.5}\text{O}_4$  No2 made whit using the three-step annealing method achieves higher capacity vis. Table 1 and Figure 1. This is evident from Fig.2. Furthermore, we see that the material  $\text{LiNi}_{0.5}\text{Mn}_{1.5}\text{O}_4$  No2 has a smaller decline in capacity depending on the load than  $\text{LiNi}_{0.5}\text{Mn}_{1.5}\text{O}_4$  No1 vis Table 2.

### Acknowledgments

This work was supported by FEKT-S-11-7 and Project Center of Research and Utilization of Renewable Energy Sources CVVOZE No. CZ.1.05/2.1.00/01.0014.

### References

1. D. Linden and T. B. Reddy, *Handbook of Batteries*, McGraw-Hill (2002).
2. W. A. Van Schalkwijk and B. Scrosati, *Advances in Lithium-Ion Batteries*, Kluwer Academic/Plenum Publishers (2002).
3. T. Ohzuku and R. J. Brodd, *Journal of Power Sources*, **174**, 449 (2007).
4. J. Xiao, X. Chen, P. V. Sushko, M. L. Sushko, L. Kovarik, J. Feng, Z. Deng, J. Zheng, G. L. Graff, Z. Nie, D. Choi, J. Liu, J.-G. Zhang and M. S. Whittingham, *Advanced Materials*, **24**, 2109.
5. B. Markovsky, Y. Talyossef, G. Salitra, D. Aurbach, H.-J. Kim and S. Choi, *Electrochemistry Communications*, **6**, 821 (2004).
6. S. b. Patoux, L. Daniel, C. Bourbon, H. l. n. Lignier, C. Pagano, F. d. r. Le Cras, S. v. Jouanneau and S. b. Martinet, *Journal of Power Sources*, **189**, 344 (2009).

## New Approach to the Preparation of the Prelithiated Graphite Materials

Libich, J.<sup>1</sup>, Sedlaříková, M.<sup>1</sup>, Vondrák, J.<sup>1</sup>, Frk, M.<sup>1</sup>

<sup>1</sup>Department of Electrical and Electronic Technology, Brno University of Technology, Faculty of Electrical Engineering and Communication, Technická 3058/10 616 00 Brno, Czech Republic.

In this paper are presented two different lithiation methods of graphite. Lithiation methods are a process during which we are able to build lithium ions into graphite structure. These graphite ions should be intercalated among graphite sheets like in case of charging in lithium-ions batteries. Our goal is to prepare lithiated graphite material that we will use as a material precursor for preparing negative electrode material. According with our assumption, this way prepared negative electrode for lithium-ion battery should have very small irreversible capacity. The irreversible capacity of graphite reduces a potential capacity of lithium-ion battery, it comprises in conventional batteries from 15 % up to 45 % of entire capacity.

### Introduction & Experiments

The capacity losses arise between the first and second charge – discharge cycle on negative electrode (anode) interface in lithium-ions battery. These losses are caused by formation SEI layer on the electrode interface. It is already known that the SEI layer (Solid Electrolyte Interface) is made by decomposition product of electrolyte for example salt  $\text{Li}_2\text{CO}_3$ , oxide  $\text{LiO}_2$  and captured gases  $\text{CO}$ ,  $\text{C}_2\text{H}_4$  and the other kinds of carbonaceous molecules which origin from electrolyte solvents. This polymer film is very important for correct function of lithium-ions battery. It is ions conductive but electron nonconductive, this property ensures to battery very low self-discharge effect. On Figure 2 is drawn a process steps of SEI layer creation.

In the first part of our work we started with our first work results with n-Butyllithium, when it was shown as a too feeble reduction agent for graphite. On the base of these results we used ionic halogen compound  $\text{FeCl}_3$ , it works like a lithium ions attractor. This idea was taken over R. Yazami and his work with ionic compounds, namely manganese chloride ( $\text{MnCl}_2$ ), iron chloride ( $\text{FeCl}_3$ ), cobalt chloride ( $\text{CoCl}_2$ ) and nickel chloride ( $\text{NiCl}_2$ ). From these compounds was chosen iron chloride, R. Yazami used to prepare the mixtures of ionic compound and graphite powder in the molar ratio four carbon atoms per one molecule of ionic compound. In our case we used  $\text{FeCl}_3$  in different molar ratios to find the most appropriate one.

Second part of the work used the different kind of lithiation that is based on electrical potential. The concept is represented by electrical potential as a result of the connection of two different conductive materials in electrolyte (conductor of second class), see an illustration on Figure 1. This kind of lithiation, is called electroless lithiation, because the potential do not arise from external power supply but it evolves as the potential in galvanic cell. [1, 3, 4]

The transfer of lithium atoms and electrons is shown on Figure 1 below.

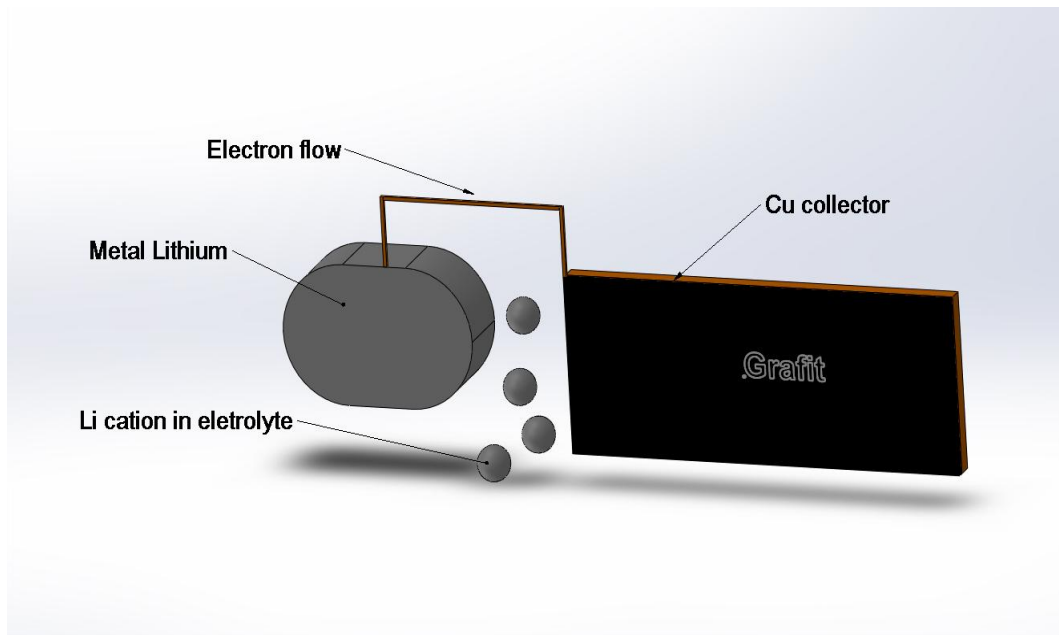


**Figure 1.** Draft of electrode arrangement in 1 mol  $\text{LiClO}_4$  electrolyte.

Electrons pass through external circuit which conductive wires metal lithium with copper collector. The copper collector is coated by active electrode material (graphite). Lithium cations are pulled out from metal lithium and go toward to the graphite electrode and collector. The external circuit, which is above the electrolyte thus is not dipped in it, conduct the electrons to the copper collector and graphite material. The lithium cations which was extract from metal lithium are reduced via intercalation process in graphite by the electrons from external circuit. The potential of this reaction is around 2 volts, this potential going down, proportionally to the amount of intercalated lithium ions. Electroless lithiation process is very slowly process which takes 48 hours. In the end of the lithiation process is the reaction potential dropped in around 0 volts.

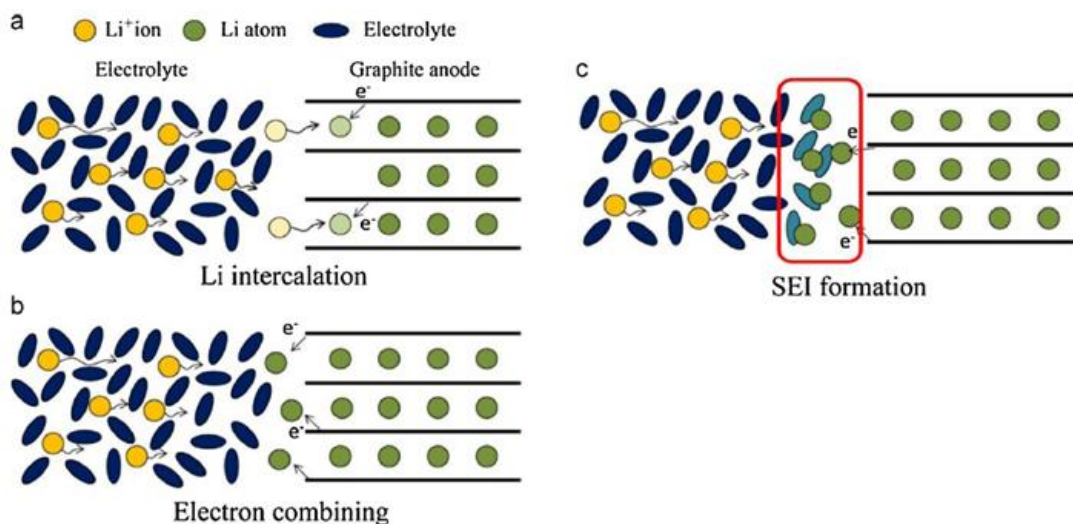


**Figure 2.** The concept of the SEI layer forming during the first charge-discharge cycles.[7]

As the electrolyte was used mixture of solvents, ethylene carbonate (EC) and diethyl carbonate (DC) with lithium salt  $\text{LiClO}_4$  in 1 mol concentration. This aprotic electrolyte type was chosen like the most widely spread one in commercial area, among its advantages belongs its price too.

### Lithiation with help of FeCl<sub>3</sub> compound

As was written previously we used ionic compound FeCl<sub>3</sub> like Li cations attractor, perhaps it can be called catalyst. Addition of this ionic compound to mixture made by graphite and n-butyllithium, changing the system potential energy. Was used natural graphite class COND CR 5995 for its capacity characteristics, high stability and low irreversible capacity. The n-butyllithium (next n-BuLi) reagent, which we used, was dissolve at n-hexane with 2.5 mol concentration. As is written in the work of R. Yazami [3], was used the atom ratio 4:1 i.e. four carbon atoms per one molecule FeCl<sub>3</sub>, besides these ratios, we used next ones. In the base of the ratio changes, was followed the influence of FeCl<sub>3</sub> to the amount of lithium atoms which passing to graphite. The ratios and the electrode parameters which were measured are listed in TABLE I below.

**TABLE I.** Graphite dopped by ironchloride catalyst.

Ratio	Capacity 1st charging	Capacity 1st discharging	Irreversible capacity [%]	Coulomb efficiency [%]
2:1	93	15	83	17
4:1	94	27	70	29
6:1	161	135	15	84
10:1	171	70	52	41

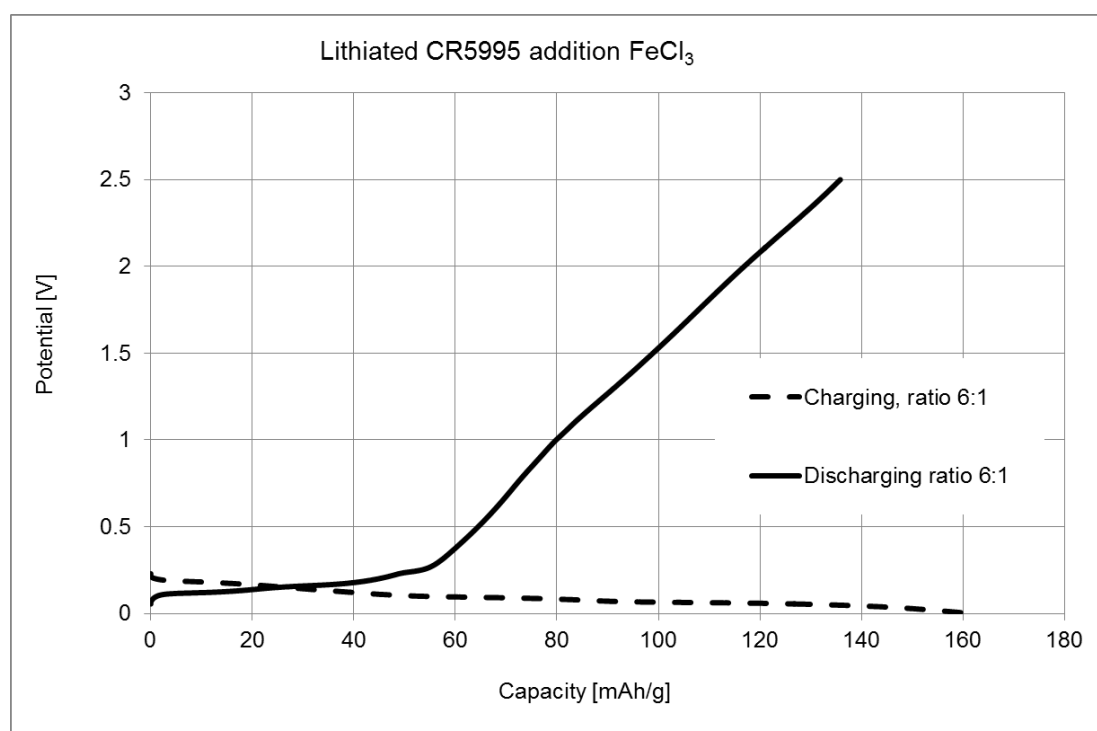


**Figure 3.** Charge-discharge characteristics for ratio „6:1”.

As can be seen, the ratio with the lowest irreversible capacity is 6:1 i.e. six carbon atoms per one molecule of FeCl<sub>3</sub>. Characteristic of this ratio are depicted on Figure 3 above.

### Conclusion

First stage of our experiments with lithiation process was reach improvement at irreversible capacity. Electrode made from natural graphite (CR 5995) has initial irreversible capacity around

24 % in first cycle. Adding one molecule of iron chloride per six carbon atoms we reached irreversible capacity in first cycle around 15 %. It supports our hypothesis about ionic compounds and gives us interesting results in the form of ratio 6:1. The ratio 6:1 corresponds with hexagonal structure of graphite and lithium placing during intercalation process between graphite sheets.

### Acknowledgement

This work was supported by project Support for human resources and transfer of knowledge in conditions of international cooperation of research teams CZ.1.07/2.3.00/20.0103 and specific research FEKT-S-11-7 (Materials and technologies for electronics).

### References

1. R. Yazami, Generateurs electrochimiqu lithium/composes d'insertion du graphite avec FeCl<sub>3</sub>, CuCl<sub>2</sub>, MnCl<sub>2</sub> et CoCl<sub>2</sub>, *Synthetic Metals*, Volume 7, Issue 3, May 1983, Pages 169-176.
2. M. C. Smart, B. V. Ratnakumar, S. Surampudi, Y. Wang, X. Zhang, S. G. Greenbaum, A. Hightower, C. C. Ahn, B. Fultz, Irreversible Capacities of Graphite in Low Temperature Electrolytes for Lithium-Ion Batteries, *Journal of the Electrochemical Society*, April 1999, Pages 3963-3969.
3. R. Yazami, New chemical reduction of transition metal chloride-GICs with nbutyllithium, *Synthetic Metals*, Volume 20, Issue 3, July 1987, Pages 383-386.
4. Anode based on prelithiated carbonaceous material for secondary lithium battery, *Fuel and Energy Abstracts*, Volume 38, Issue 3, May 1997, Page 160.
5. Yang, J.-l. Wang, SECONDARY BATTERIES – LITHIUM RECHARGEABLE SYSTEMS – LITHIUM-ION | Negative Electrodes: Lithium Alloys, In: Editor-in-Chief: Jürgen Garche, Editor(s)-in-Chief, *Encyclopedia of Electrochemical Power Sources*, Elsevier, Amsterdam, 2009, Pages 225-236.
6. Yangxing Li, Brian Fitch, Effective enhancement of lithium-ion battery performance using SLMP, *Electrochemistry Communications*, Volume 13, Issue 7, July 2011, Pages 664-667.
7. SANG-PIL, K., ADRI, C.T. VAN, D., VIVEK, B. S. Effect of electrolytes on the structure and evolution of the solid electrolyte interphase (SEI) in Li-ion batteries: A molecular dynamics study, *Journal of Power Sources*, Volume 196, Issue 20, 15 October 2011, Pages 8590-8597, ISSN 0378-7753.

## **The use of triethylphosphate as flame retardant in lithium ion batteries**

Maca, J., Frk, M., Vondrak, J., Sedlarikova, M.

Brno University of Technology, Technická 10, Brno, Czech Republic

The safety of lithium batteries has been discussed recently in connection to prospective use in a variety of high power applications such as electric cars, reserve batteries in huge aircrafts and similar objects. We have decided to add some contribution to this problem. One way to increase the fire safety of electrolytes is to use a new low flammable solvents and materials. For further increase the safety is possible to add some kind of flame retardant into the electrolyte. We are describing the influence of flame retardant triethylphosphate on main properties of electrolytes in this article.

### **Introduction**

Lithium accumulators (secondary cells) contain negative electrodes with strong reduction action and flammability, positive electrode the composition of which is quite opposite as strong oxidants, and aprotic electrolyte based on solvents with high permittivity and possibly also high point of ignition. In general, there are several methods how to reduce the safety of incineration. First, we have to use solvents with high boiling point and possibly high flash point. Further, we can use additives known as fire retardants. These additives should not worsen the properties of the solvent for the purpose to be used in lithium battery electrolytes. For this purposes we have used triethylphosphate as the simplest fire retardant commercially available. Our research has included investigation of flash point and conductivity of mixed electrolytes containing sulfolane, propylene carbonate and other solvents suitable for lithium batteries. Triethylphosphate is a colourless liquid, the melting point and boiling point of which are -112 °C and 215 °C. Its viscosity is lower than that of sulfoane (10.65 mPa·s at 30 °C) and permittivity at room temperature is 13.

### **Instrumentation**

#### 2.1 Flash point determination

Device for evaluation of flash point SETFLASH SERIES 3 Model 31000-0 according to Cleveland was used. On the beginning of the measurement was the temperature set 3 – 5 °C below the expected flashpoint, after tempering was the test flame initiated. In the case of no initiation was the temperature increased by 1 °C or in dependence of false effect of ignition (halo effects) by 0.5 °C until the flash point was determined. This way was the lowest temperature of flash point determined.

#### 2.2 Conductivity measurements

The two electrode conductivity cell and electrochemical impedance spectroscopy was used for the specific conductivity determination. The measurement was performed in frequency range from 1 MHz to 100 Hz. The measurements were carried out in ambient conditions in a sealed vessel to prevent the humidity contamination of the sample.

## Experimental

In our experiments were used solvents sulfolane (Sigma Aldrich) 99% and propylene carbonate (Sigma Aldrich) 99.7%. Used fire retardant was triethylphosphate (Sigma Aldrich) with 99.8% purity. Added salt was lithium perchlorate  $\text{LiClO}_4$  also from Sigma Aldrich company. The samples were prepared by blending of sulfolane and second solvents in volume ratio determination and added a salt in 1 mol/l concentration. Above this volume was added the flame retardant in 3, 10 and 20% of the base volume.

## Results

As a main safety parameter was the flash point measured and as main electric parameter was the specific conductivity of the electrolytes measured.

### 4.1 Flash point results

In Table I is visible that adding of fire retardant increased the flashpoint and that in all samples with is also clear shown on Fig. 1. The flashpoint increases with the triethylphosphate concentration. The largest increase of flash point temperature was in sample 50%SL – 50%PC and 20%TEP and that of 10.5% in compare with sample without a fire retardant.

**TABLE I.** Results of flash point measurement

Sulfolane [%]	+ PC			
	0% TEP	3% TEP	10% TEP	20% TEP
0	132.0	142.4	142.7	143.6
25	139.3	148.0	150.0	150.6
50	142.0	149.7	153.7	156.9
75	151.8	156.2	158.6	163.2
100	165.0	167.6	168.8	170.4

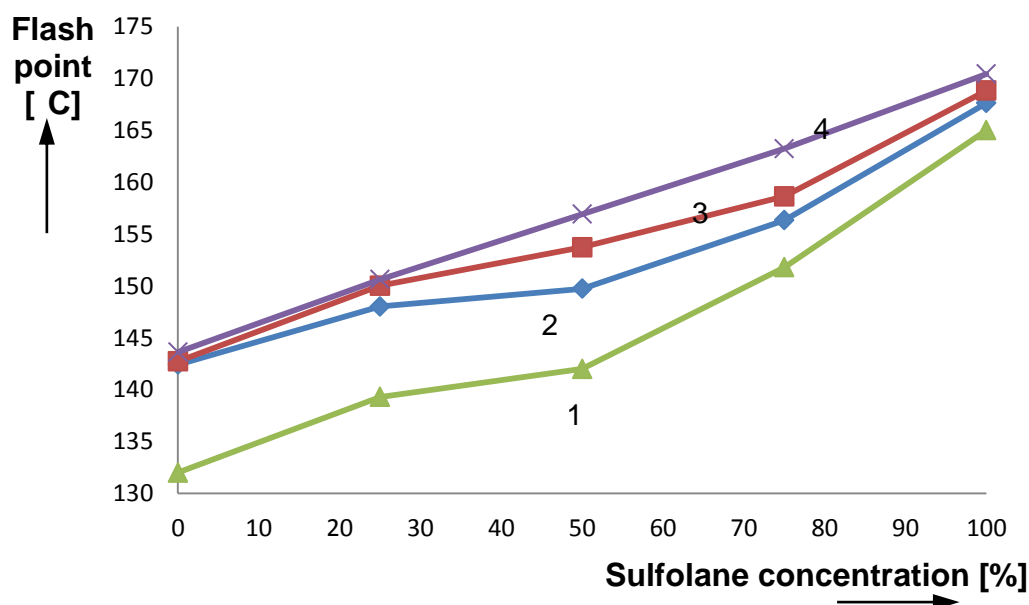


**Figure 1.** The flash point temperature dependence of sulfolane and propylene carbonate electrolytes with different ratio of TEP, curve 1 0% TEP, curve 2 3% TEP, curve 3 10% TEP and curve 4 20% TEP

## 4.2 Conductivity

In Table II is shown the benefit of fire retardant on specific conductivity. The increase of specific conductivity compared to the sample without the fire retardant with is not negligible. The increase is most visible on sample containing 75%SL – 25%PC and 20%TEP with was 45.6%. The increase of specific conductivity is shown on Fig. 2 and that by shift on y axis to higher values.

**TABLE II.** Results of specific conductivity measurement

Sulfolane [%]	+ PC			
	$\gamma$ [ $\text{mS}\cdot\text{cm}^{-1}$ ]			
	0% TEP	3% TEP	10% TEP	20% TEP
0	7.81	8.09	8.23	9.35
25	5.49	6.63	6.68	7.73
50	4.21	5.56	5.73	6.13
75	3.31	4.91	4.90	4.82
100	3.19	3.36	3.36	3.71

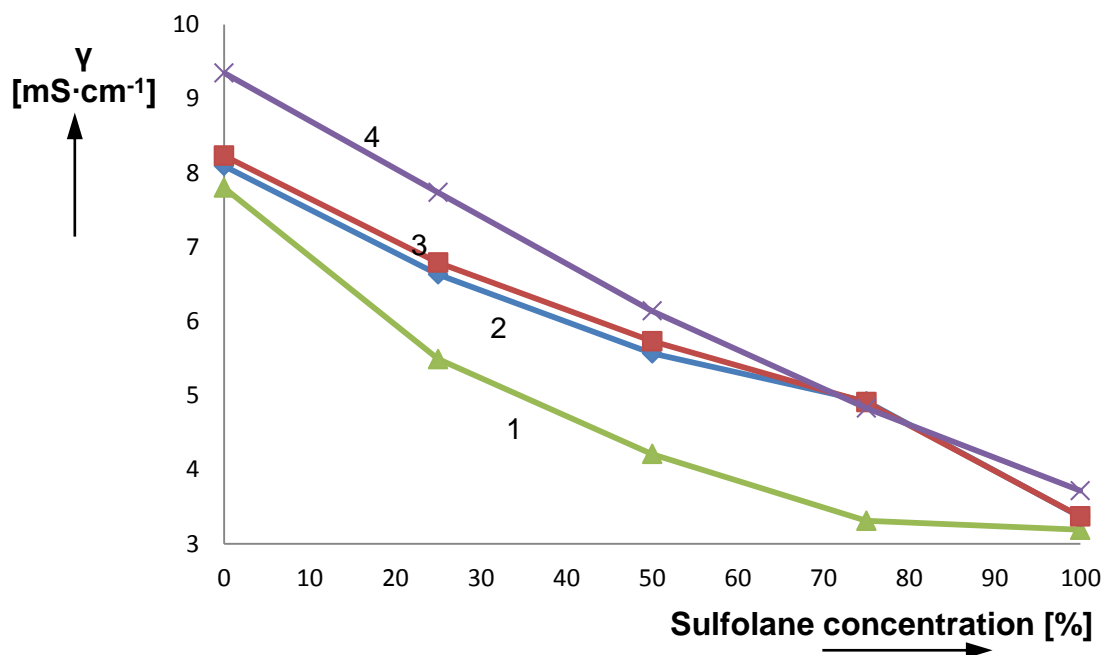


**Figure 2.** The specific conductivity dependence of sulfolane and propylene carbonate electrolytes with different ratio of TEP, curve 1 0% TEP, curve 2 3% TEP, curve 3 10% TEP and curve 4 20% TEP at room temperature

## Discussion

This work was focused on determination of fire retardant influence on selected properties of aprotic electrolytes. The samples of sulfolane and second solvent (propylene carbonate) with different ratio of fire retardant triethylphosphate (3%, 10% and 20%) were made. From measured results is clear that fire retardant additive increased the flash point temperature up to 10% in mixtures with propylene carbonate. This was caused due the activation of fire retardant and its decomposition on gas and free radical of phosphate which displaces the hydrogen radicals. By adding of fire retarder also increased the specific conductivity up to 45% by use of sulfolane and propylene carbonate compared to the same sample without the retardant. The specific conductivity

increase is probably caused due the lower viscosity of the electrolytes. The specific conductivity decrease with increased concentration of sulfolane which has 10 times higher dynamic viscosity in compare to the second solvent by the same temperature. The relative permittivity is also lower than the permittivity of second solvent.

### Acknowledgement

This work was supported by specific research FEKT-S-11-7 Materials and technologies for electronics and project CZ.1.07/2.3.00/20.0103 “Support for human resources and transfer of knowledge in conditions of international cooperation of research teams“.

### References

1. D. Brouillette, G. D. Brouillette, G. Perron, J. Desnoyers. Effect of viscosity and volume on the specific conductivity of lithium salts in solvent mixtures, in *Electrochimica Acta* 44 (1999), pp. 4721-4742.
2. Y. Marcus, *The Properties of Solvents*, John Wiley & Sons Ltd, Chichester (1998), p. 399.
3. R.C. Lance, A.J. Barnard Jr., J.E. Hooyman, “Measurement of flashpoints: Apparatus, methodology, applications”, in *Journal of Hazardous Materials*, Vol. 3, pp. 107-119
4. Monica M. D., Jannelli L., Lamanna U. Physicochemical Properties of Sulfolane, *Journal of Physical Chemistry* 1967, p. 1068-1071
5. Bajer, M. Aprotic electrolytes for lithno-ion accumulators with higher temperature stability. Brno: Vysoké učení technické v Brně, Fakulta elektrotechniky a komunikačních technologií, 2013. 69 p.
6. Xianxia Y. Hansan L., Zhang J., *Lithium-Ion Batteries: Advanced Materials and Technologies*. CRC Press, 2011. ISBN-10: 1439841284, 420p.
7. Yao X., Xie S., Chen Ch., Wang Q. Comparative study of trimethylphospite and trimethylphosphate as electrolyte additves in lithium ion batteries. 2005. [online] <http://www.sciencedirect.com/science/article/pii/S0378775304012017>

## Comparison study of $\text{LiMn}_2\text{O}_4$ composites with graphite and carbon nanotubes in the electrodes for Li-ion batteries

Peskov, R.<sup>1</sup>, Apostolova, R.<sup>1</sup>, Shembel, E.<sup>1,2</sup>, Danilov, M.<sup>3</sup>

<sup>1</sup> Ukrainian State University of Chemical Technology, 49005, Gagarina prospect, 8, Dnepropetrovsk, Ukraine, shembel@onil.dp.ua

<sup>2</sup>Enerize Corporation, Coral Springs, FL, USA

<sup>3</sup>V.I. Vernadskyi Institute of General and Inorganic Chemistry NAS Ukraine, 03680, Palladina prospect 32/34, Kiev-142, Ukraine

### Introduction

On consider spinel  $\text{LiMn}_2\text{O}_4$  as alternative to  $\text{LiCoO}_2$  oxide in commercial Li-ion batteries because of its low cost, low toxicity, high potential vs. lithium electrode and theoretic capacity of 148 mAh/g. The loss of the discharge capacity at cycling is the disadvantage of spinel  $\text{LiMn}_2\text{O}_4$ . It prevents from the series industrial output of Li-ion power-consuming batteries on the base of  $\text{LiMn}_2\text{O}_4$  spinel. The probleme of the achievement of high specific characteristics and the ensuring of the stability of Li-ion system was increased, after Li accumulators were considered as power sources for the consumers of cosmic and military engineering, vehicles. Degradation processes in Li-ion system depend on many factors (nature and structure of electrode material, structure stability during cycling and the storage, nature and temperature of the electrolyte, the depth of the electrode discharge, discharge and charge current values). One of key factors determining the working ability of  $\text{LiMn}_2\text{O}_4$  spinel in the redox reaction with Li is the presence of conductive additive in its composition.

In the present work the studies of cycling performance of  $\text{LiMn}_2\text{O}_4$  spinel as a function of such conductive additives as graphite and carbon nanotubes were reported.

### Experimental

Thin-layer  $\text{LiMn}_2\text{O}_4$  spinel electrodes ( $\text{LiMn}_2\text{O}_4/\text{Al}$ ) have been prepared by mechanical embedding of  $\text{LiMn}_2\text{O}_4$  powder in Al matrix (1.0x1.0x0.1 cm; mass of 0.1–0.5 mg/cm<sup>2</sup>) by method (1). Volume composite  $\text{LiMn}_2\text{O}_4$  spinel electrodes contain  $\text{LiMn}_2\text{O}_4$  spinel powder, F4 teflon binder, graphite or multiwall carbon nanotubes (MCNT) as conductive additives at a ratio of (80:10:10 % mass) prepared as a slurry in N-methyl-pyrrollidone that was pasted on stainless steel sheet (1.0x1.0 cm). MCNT were synthesized by catalytic ethylen pyrolysis (2). The graphite was EUZ-M trademark (GOST 10274-79).

Electrochemical measurements were conducted in two-electrode coin-type cell (model 2325) and in three-electrode pouch cell. The solutions containing PC, DME, 1 M  $\text{LiClO}_4$  and EC, DMC, 1 M  $\text{LiClO}_4$  were used as electrolytes in Li model accumulator.

Discharge-charge characteristics of spinel were obtained in galvanostatic mode using programm tester and analytical radiometer VoltaLab PJZ 301.

The  $\text{LiMn}_2\text{O}_4$  spinel structure was examined by X-ray diffraction analysis (DRON-2).

The electron micrograph have been obtained with the aid of a JEM-100 CXII electron microscope.

### Results and discussion

The initial  $\text{LiMn}_2\text{O}_4$  spinel powder does not contain any admixture. In the X-ray spectrum can be seen only the reflex of  $\text{LiMn}_2\text{O}_4$  spinel (fig.1). Its crystallite size is about 70 nm,  $M=6.25 \cdot 10^{-4}$ . The unit cell lattice parameter (a) of the  $\text{LiMn}_2\text{O}_4$  powder sample is found to be 8.2371 Å.

Diameter of MCNT is equals 10 nm (fig. 2); specific surface – 230  $\text{m}^2/\text{g}$ .

The cycling stability of ballastless thin-layer  $\text{LiMn}_2\text{O}_4/\text{Al}$ -electrode is high. Its discharge capacity reaches of 70-80 mAh/g (fig. 3) during more than 100 cycles.

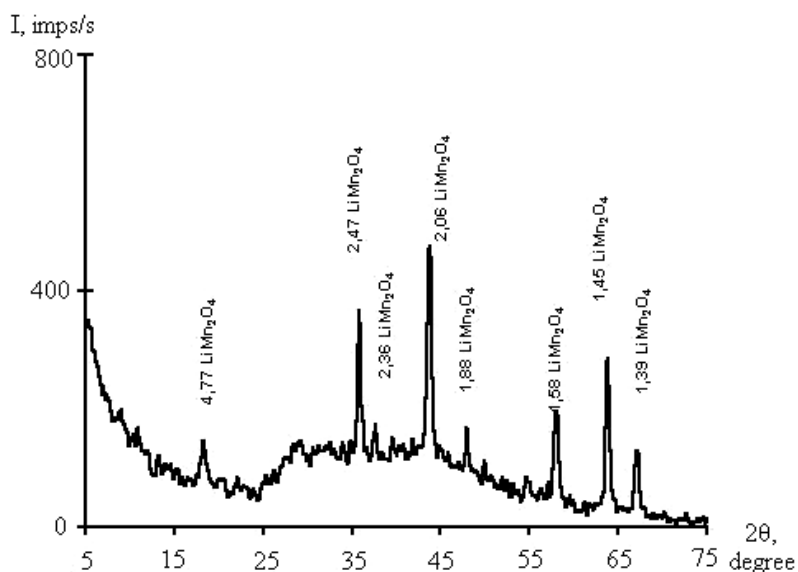


**Figure 1.** XRD-pattern of  $\text{LiMn}_2\text{O}_4$  spinel powder.

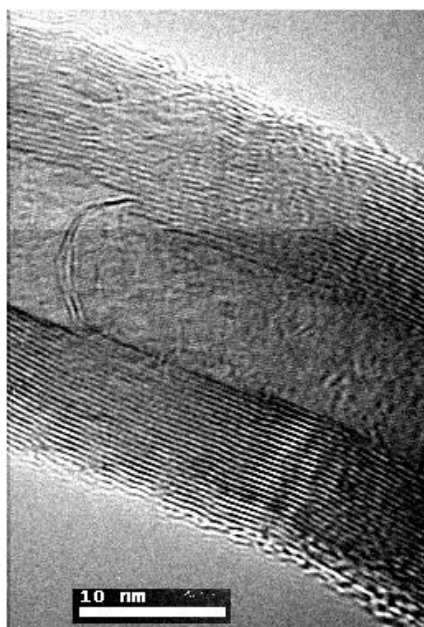


**Figure 2.** SEM micrograf of a multiwall carbon nanotubes.

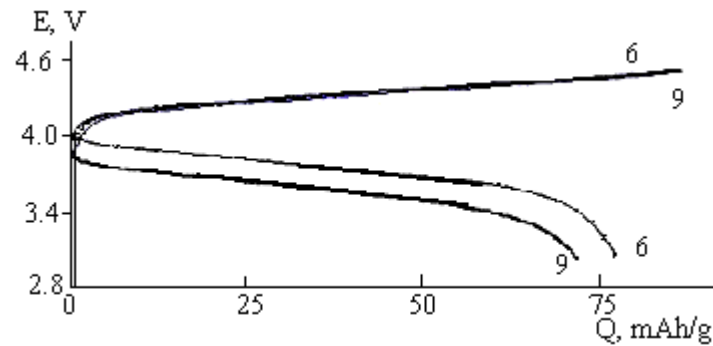


**Figure 3.** Discharge-charge curves of  $\text{LiMn}_2\text{O}_4/\text{Al}$ -electrode during the 6-th and 9-th cycles versus current density ( $i$ ),  $\mu\text{A}/\text{cm}^2$ : 6)  $i_1=5$ ; 9)  $i_2=16$ .

Resistance of  $\text{LiMn}_2\text{O}_4/\text{Al}$ -electrode defined as  $(R_c)=dE/di$  ( $18 \text{ k}\Omega/\text{cm}^2$ ) exceeds resistance order of  $\text{LiMn}_2\text{O}_4$ , MCNT/ $\text{Al}$ -electrode ( $1 \text{ k}\Omega/\text{cm}^2$ ) and characterizes the contact resistance between spinel particles. Here  $dE=E_2-E_1$ , when  $di=i_2-i_1$  (fig. 3).

Electrode without the conductive additive which show long-term stability during the cycling has potentiality for the application of the spinel in commercial Li-ion batteries at the condition of increasing capacity in spinel composites.

Conductive additives play key role in effective cyclic performance of  $\text{LiMn}_2\text{O}_4$  spinel in model lithium accumulator. It is shown undoubted superiority of the characteristics of  $\text{LiMn}_2\text{O}_4/\text{MCNT}$  composites over those  $\text{LiMn}_2\text{O}_4/\text{graphite}$  composites in redox reaction with Li in EC, DMC, 1 M  $\text{LiClO}_4$  and PC, DME, 1 M  $\text{LiClO}_4$  electrolytes.

Discharge capacity of  $\text{LiMn}_2\text{O}_4/\text{Al}$ -electrode is low because of high contact resistance between spinel particles and it grows in the presence of MCNT in thin-layer  $\text{LiMn}_2\text{O}_4/\text{Al}$ -electrode (fig. 4).

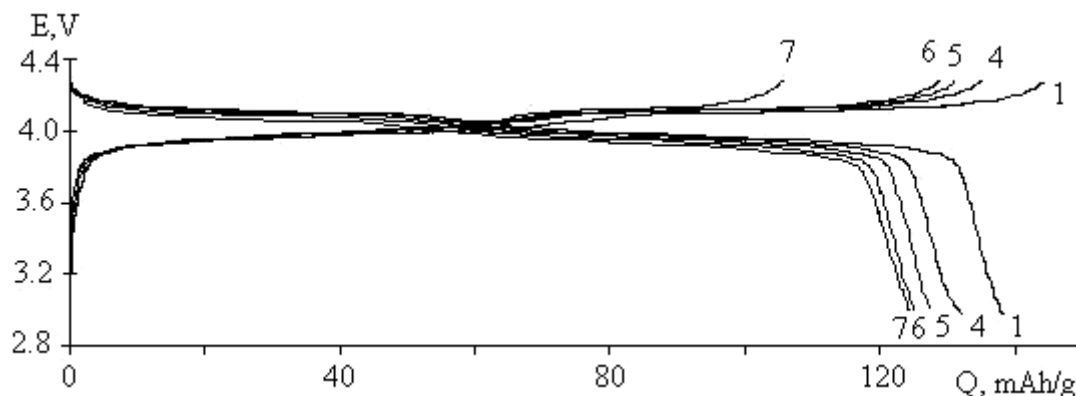


**Figure 4.** Discharge-charge characteristics of  $\text{LiMn}_2\text{O}_4$ , MCNT/EC, DMC, 1 M  $\text{LiClO}_4/\text{Li}$  system.  $i$  ( $\mu\text{A}/\text{cm}^2$ ): 5 (cycles 1<sup>st</sup>-4<sup>th</sup>), 16 (5<sup>th</sup> cycle), 64 (6<sup>th</sup> cycle), 105 (cycles 7<sup>th</sup>-8<sup>th</sup>). Composite mass –  $0.5 \text{ mg}/\text{cm}^2$ . Figure near the curves is the number of the cycle.

The rate discharge characteristics of  $\text{LiMn}_2\text{O}_4$  have also been improved under MCNT influence in volume  $\text{LiMn}_2\text{O}_4$ , MCNT/ electrodes (fig. 5).  $\text{LiMn}_2\text{O}_4$  discharge capacity in the MCNT presence stabilizes at the level higher than  $100 \text{ mAh}/\text{g}$  in the current density range of  $0.1\text{-}3.0 \text{ mA}/\text{cm}^2$  in the model Li accumulator.

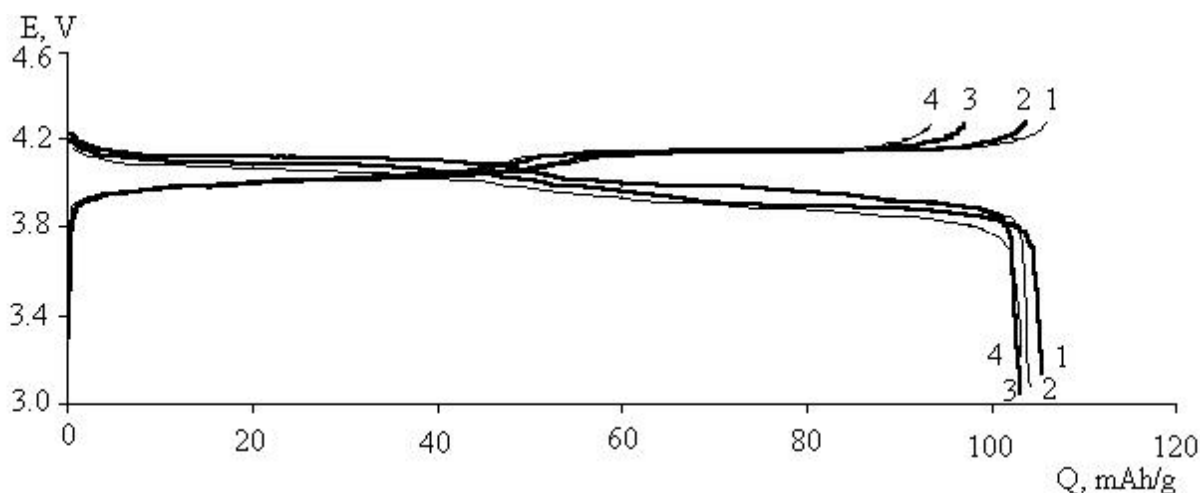


**Figure 5.** Discharge-charge characteristics of volume  $\text{LiMn}_2\text{O}_4$ , MCNT / electrode.  $i_{\text{disch}}$  ( $\mu\text{A}/\text{cm}^2$ ): 200-1000 (cycles 1<sup>th</sup>-4<sup>th</sup>). Mass  $\text{LiMn}_2\text{O}_4$  44.9  $\text{mg}/\text{cm}^2$ . Figure near the curves is the number of the cycle.

Comparison discharge rate characteristics of  $\text{LiMn}_2\text{O}_4$  composites with graphite and carbon nanotubes are shown in figure 6.

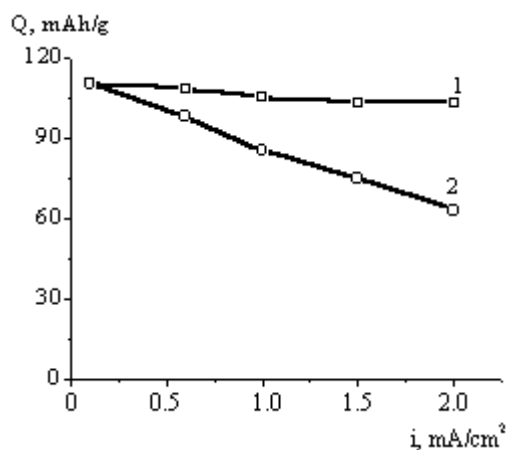


**Figure 6.** Discharge capacity versus current density,  $i$  ( $\text{mA}/\text{cm}^2$ ): 1)  $\text{LiMn}_2\text{O}_4$ , MCNT/Al-electrode, 2)  $\text{LiMn}_2\text{O}_4$ , graphite /Al-electrode.

The obtained results show the need of correct choice of the conductive additive and its further optimization in spinel composites.

### References

1. B. Markovsky, D. Kovacheva, Y. Talyosef, M. Gorova, J. Grinblat, D. Aurbach: *Electrochim. Acta*, **50**, 5553 (2006).
2. A. Melezhik, Yu. Sementsov, V. Yanchenko: *J. of Appl. Chem. (Russian)*, **78**, 917 (2005).

## **Characterization of PVdF fibrous membrane separators for lithium-ion rechargeable batteries**

Pleha, D., Musil, M., Cudek, P.

Institute of Electrotechnology, Brno University of Technology, Faculty of Electrical Engineering and Communication, Technická 3058/10 616 00 Brno, Czech Republic.

Separators play the key role in all types of commercially available batteries. Main role of these is to prevent from short circuit between positive and negative electrode. Simultaneously, separators have to allow current of ion carriers spread in the bulk of electrolyte, and moreover, demonstrate good isolating properties, ionic conductivity and electrolyte uptake in the same time. Battery separators must not take part in any electrochemical reaction. Material selection depends on chemical composition and application of accumulator. Separators in Li-ion batteries are mostly made from polypropylene (PP), polyvinylidene fluoride (PVDF) and polyethylene (PE). In this paper are given global properties of non-commercial PVDF nanofibrous separators produced by Nafigate Corporation stock company.

### **Introduction**

Microporous separators are usually applied nowadays. These have good mechanical strength, convenient thickness and excellent chemical stability. Disadvantages of separators are low porosity, inconvenient thermal stability, bad wettability and electrolyte uptake ability. These disadvantages may cause high resistance of the battery cell. Unconventional separator production methods ensure elimination of mentioned disadvantages. Electrospinning seems to be the most prospective method of separators production.

Electrospinning is new, widely spreading method of separators production nowadays. In this range is electrospinning mainly used to produce nano fibres formed into separators, which are usually applied in the aprotic battery cells with electrolytes based on carbonate solvents. Separators prepared by this method prove high porosity, high chemical stability and ability to uptake electrolyte. Thanks to mentioned properties, ions dissolved in electrolyte are enabled to easily move in the whole bulk between cathode and anode. Hand in hand are better electrochemical properties of the battery cell.

Electrospinning method is applicable to all polymer materials, that are meltable or soluble. In li-ion accumulators are usually used materials like Polyacrylonitrile (PAN), Polyethylene oxide (PEO), polymethyl methacrylate (PMMA), Polyvinylidene fluoride (PVdF) or polyvinyl alcohol (PVA). The most convenient in Li-ion batteries with carbonates based electrolytes is from the previously listed materials PVdF. The main reasons are both very high chemical and thermal stability.

### **Experimental**

Our team aimed on determination properties of nano fibred separators (from the Nafigate Corporation stock company) designated for Li-ion batteries. Selected separators were subsequently

measured in the real operative cell. Determined properties were compared with parameters of commercially available separators. Five separator types from the Nafigate (labeled AM, 5409, 7209, 13L and 43L) and one comparative separator type Celgard 3401 from the Celgard LLC were analyzed. Celgard is currently one of the most used separators in Li-ion battery cells.

#### Nano fibre production in the Nafigate Corporation stock company

Samples pieces of nano fibred separators are produced in the laboratory machine Nanospider™ NS LAB 500 equipped with EMW (Endless Motion Wire) technology. This EMW technology is based on spinning by the string electrode with usage of a small amount of polymer solution. Polymer solution is applied (the rate of application is set) on the string (spin electrode).

Intensive electrostatic field, which results from potential difference between spin and collecting electrodes, forms Taylor's cone. This cone is fibre source. Drawn fibre is subsequently elongated, surface area increases and solvent evaporates simultaneously. Properly adjusted Nanospider (electrodes position, solvent selection) produces sub-micron wide dry fibres. Electric charge carried by the produced fibres has the same polarity as the spin electrode. This charge is drained onto collector and usually grounded (1).

#### Ageing in the liquid aprotic electrolyte

Materials suitable for li-ion batteries must be resistant to carbonate aprotic solvents without limits, and must not lose neither its tensile strength nor its toughness. Analyzed samples were long period aged in 1 mol/l LiBF<sub>4</sub> in EC/DMC electrolyte. Samples were checked on mechanical properties and structural changes dependent on time.

#### Electrolyte uptake

Electrolyte uptake is one of the most important parameters. Separators should have high ability to uptake and retain electrolyte in long-term. Each of the Nafigate samples was measured on this property. Separators were measured in 1 mol/l LiBF<sub>4</sub> in EC/DMC (1:1 wt.) electrolyte at 20 °C.

**TABLE I.** Electrolyte uptake

Sample	Electrolyte uptake [%]
3401	157,2
AM	62,1
5409	233,8
7209	73,7
13L	188,7
43L	154,3

#### Dielectric properties of separators

Furthermore, samples were measured on relative permittivity and loss tangent. Values of permittivity at frequency 100 Hz correspond to tabulated values (samples 3401 and 13L). Separator 43, which is mainly made from polyethersulfone (PES), practically corresponds to tabulated value

( $\epsilon' = 3.5$  at frequency 100 Hz). Differences are caused by non-homogeneous surface of the separator's surface.

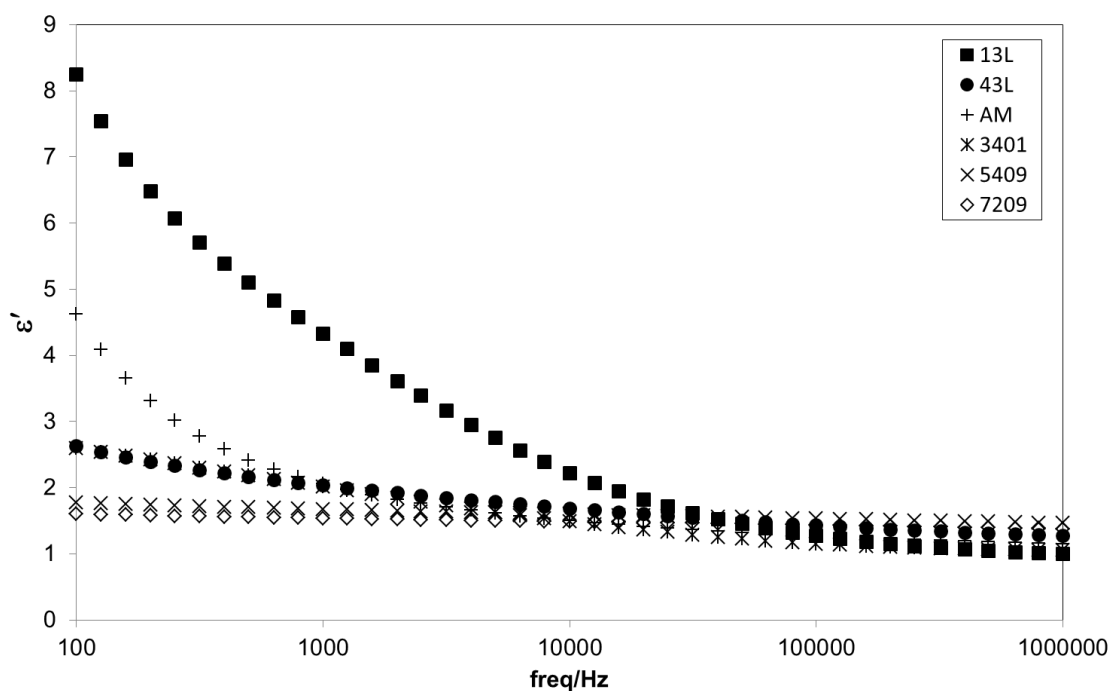


**Figure 1.** Relative permittivity frequency dependence

### Morphology

Navigate microporous separators were observed by the SEM microscope Tescan VEGA3 XM. Small samples (area 1 sq. cm) were cleaned with compressed air duster before observation. Micrographs were taken at resolutions 5 000x and 20 000x at 30 kV in the inert argon atmosphere (low pressure set to 100 Pa). As you can see on figure below, fibres are approx. 0,2  $\mu\text{m}$  thick.

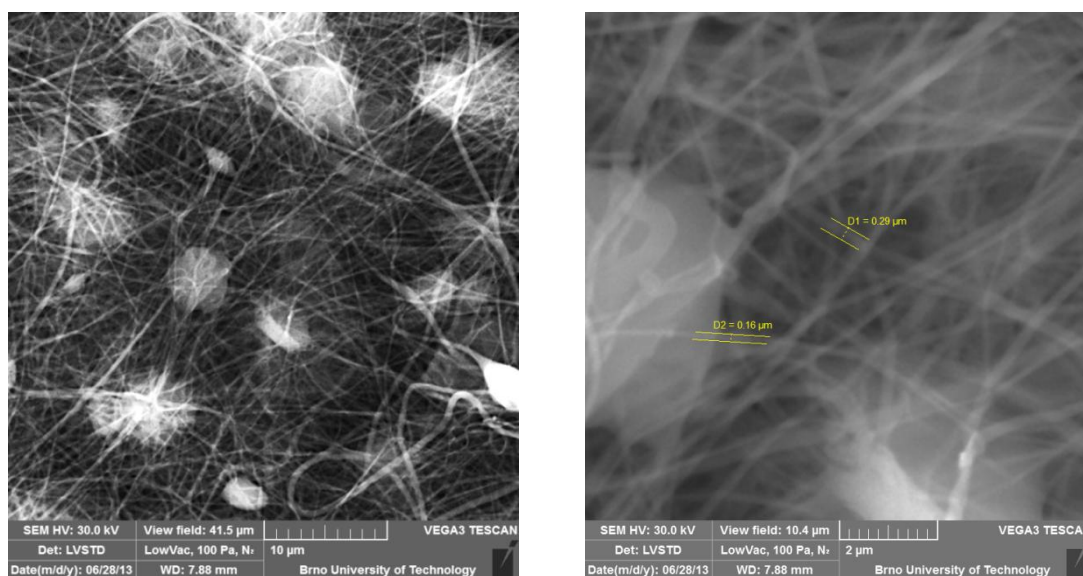


**Figure 2.** SEM images of PVDF fibrous membrane

## Conclusion

This work is focused on measuring properties of non-commercial separators from the Nafigate Corporation stock company. Properties of separators are compared with on the market available separator Celgard 3401. Nafigate separators were prepared by electrospinning. These nafigate separators (especially AM model) have all the parameters comparable with the world production.

## Acknowledgements

This work was supported by the grant FEKT-S-11-7 and project CVVOZE CZ.1.05/2.1.00/01.0014.

## References

1. Nanospider: Electrospinning technology. [online]. [cited 2013-05-06]. Available from: <http://old.elmarco.com/obsah.php?id=27&s=25>
2. Agilent 16008B Bias RESISTIVELY CELL Operation and Service Manual. [online]. [cited 2013-05-06]. Available from: <http://cp.literature.agilent.com/litweb>
3. LIANG Y, CHENG S, ZHAO J, et al. Heat treatment of electrospun Polyvinylidene fluoride fibrous membrane separators for rechargeable lithium-ion batteries. *Journal of Power Sources*. 2013, 240, 204-211.
4. SHENG SHUI Z, A Review on the separator of liquid electrolyte Li-ion batteries. *Journal of Power Sources*. 2007, 164, 351-364
5. COSTA C.M., NUNES-PEREIRA J., RODRIGUES L.C et al. Novel poly(vinylidene fluoride-trifluoroethylene)/poly(ethylene oxide) blends for battery separators in lithium-ion applications. *Electrochimica Acta* 88, 2013, 473-476

## Experimental and theoretical investigation of the conducting properties of ordered layers of crown ether complexes with Li<sup>+</sup> ions on the lithium anode surface

Tulibaeva, G.Z., Yudina, A.V., Shestakov, A.F., Yarmolenko, O.V.

Institute of Problems of Chemical Physics RAS, Chernogolovka, Russian Federation

Li<sup>+</sup>-conducting properties of ordered layers of crown ethers on the modified lithium anode surface were studied by experimentally and theoretically. The layers were grown from crown ethers, contained in network polymer gel electrolyte based on polyester diacrylate and 1M LiBF<sub>4</sub> in gamma-butyrolactone at -16 °C. The method of quantum-chemical modeling showed that the growth of such layers on lithium nitride surface is better than on metallic lithium surface. Theoretically calculated that the diffusion of Li<sup>+</sup> ions in ordered layers of crown ethers isn't difficult.

Lithium power sources with polymer electrolyte is a promising alternative to lithium-ion batteries (LIB) with liquid electrolyte, in which scientific and technological problems of LIB's operating at low temperatures from 0 to -70 °C aren't resolved. It is well known that the operating temperature of the best compositions of liquid electrolytes is limited to -40 °C, therefore, to obtain workable electrolytes necessary reduce their freezing temperature. This can be achieved by using the polymer gel electrolyte having glass transition temperature (T<sub>g</sub>) below -100 °C. Previously, we obtained gel electrolyte based on polyester diacrylate PEDA (20 wt.%) and 1M LiBF<sub>4</sub> in gamma-butyrolactone (GBL) with T<sub>g</sub> = -117 °C (1).

LIB's operating is also strongly influenced by characteristics of electrode/electrolyte interface. The current exchange on this interface according to Arrhenius's equation for the rate of elementary electrochemical reactions (electrode reaction of Li<sup>+</sup>+e<sup>-</sup>↔Li<sup>0</sup>) changing an order with changing temperature on 30 °C. In addition with decreasing temperature the diffusion of charged particles slows, which also worsens the performance of the chemical power source at lower temperatures.

In this work proposed to combine the polymer gel electrolyte with T<sub>g</sub> below -100 °C and highly conductive layer of crown ethers on electrode/electrolyte interface.

### Experimental

The polymer gel electrolyte was obtained by radical polymerization reaction of 20 wt.% polyester diacrylate PEDA in 1M LiBF<sub>4</sub> in GBL using benzoyl peroxide at 80 °C for 3 hours. The conductivity of gel electrolyte with decreasing temperature varied little and was 4.12×10<sup>-3</sup> S/cm at 25 °C, 1.67×10<sup>-3</sup> S/cm at 0 °C and 1.47×10<sup>-3</sup> S/cm at -16 °C.

For the formation of ordered layers of 1,6-dioxo-14-crown-4 which are in composition PEDA (up to 30 wt.%) lithium metal surface coated Li<sub>3</sub>N was used. Previously, we have shown that the formation of layers of crown ethers on the example of 15-crown-5 on pure lithium doesn't happen (2).

Results of the study of growth layers of crown ethers by electrochemical impedance are presented in Fig. 1. Cell area is 0.2 cm<sup>2</sup>.

Two equivalent circuits for the calculation of impedance hodographs were offered (Fig. 2). In the case of ordered layers of crown ethers the kinetics of charge transfer is completely controlled by the diffusion of the particles to the interface (Fig. 2 b). Therefore we introduce new element of the circuit – Warburg element.

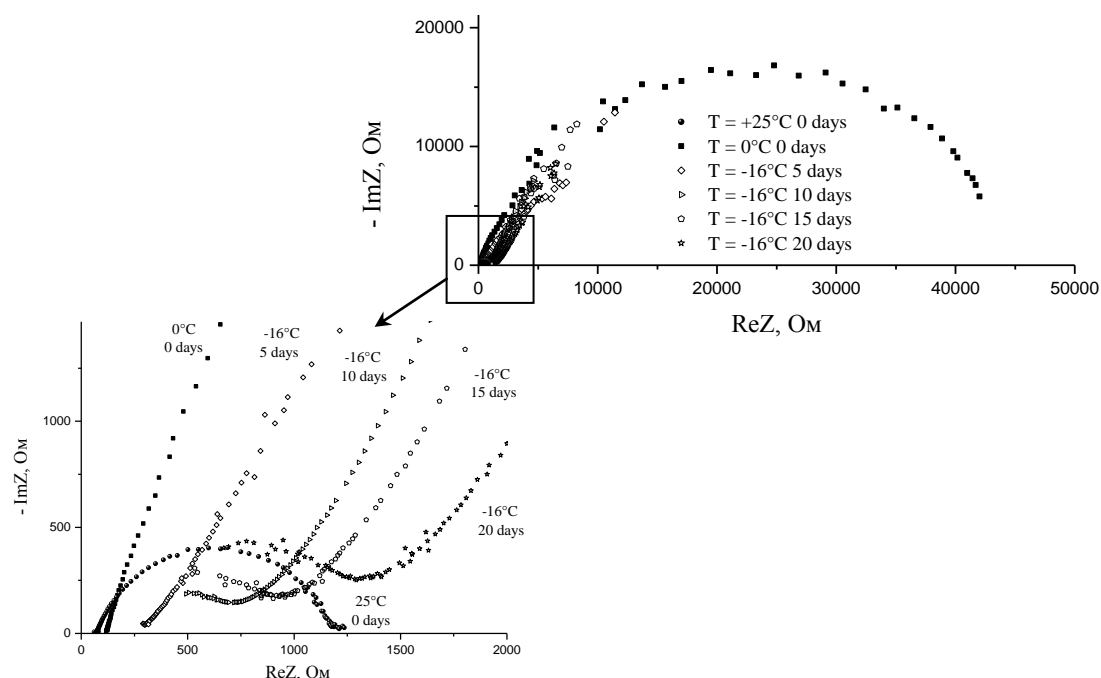


**Figure 1.** Hodographs impedance symmetrical cell  $\text{Li}(\text{Li}_3\text{N})/\text{PE} + \text{crown ether}/(\text{Li}_3\text{N})\text{Li}$



**Figure 2.** Equivalent circuits for the room temperature and 0 °C (a) and -16 °C (b)

The results of the hodographs calculation according to the equivalent circuits for the three temperatures are presented in Table I.

**TABLE I.** The results of calculation of the impedance hodographs of cell  $\text{Li}(\text{Li}_3\text{N})/\text{PE} + \text{crown ether}/(\text{Li}_3\text{N})\text{Li}$  for equivalent circuits (Fig. 2)

Element of equivalent circuit	Value (error, %)		
	25 °C	0 °C	-16 °C, 15 days
R1	70 (0.2%)	110 (0.8%)	110 (1.0%)
R2	1120 (0.2%)	45570 (0.8%)	1220 (0.6%)
CPE1-T	$1.8 \times 10^{-6}$ (1.0%)	$7.6 \times 10^{-7}$ (1.5%)	$6.4 \times 10^{-9}$ (10%)
CPE1-P	0.8 (0.1%)	0.8 (0.2%)	0.73 (0.9%)
W1-R	-	-	8210 (2.7%)
W1-T	-	-	$1.4 \times 10^{-3}$ (3.6%)
W1-P	-	-	0.58 (0.6%)

Figure 1 and Table I shown that the initial resistance at electrolyte/electrode interface at 25 °C is about 1100 Ohms. By lowering temperature to 0 °C this resistance increases to ~ 45000 Ohms. The crystallization the crown ether complexes with the lithium salt begin at -16 °C and electrolyte/electrode interface resistance is reduced by two orders. Increase in resistance from 300 Ohms to 1400 Ohms for 20 days at -16 °C shows an increase in the thickness of this layer.

### Quantum-chemical modeling

To understand the nature of the interaction between the lithium electrode surface and crown ether quantum-chemical study of the interaction of 15-crown-5 molecule with lithium cluster  $\text{Li}_{20}$  was carried out by density functional theory. We used ab initio density functional PBE (3) and extended basis H [6s2p/2s1p], C, O [10s7p3d/3s2p1d], Li, N [10s7p3d/4s3p1d], Cl [14s11p3d/4s3p1d]. All calculations were performed by the software package PRIRODA (4) using the computational capabilities of Joint Supercomputer Center of RAS. This approach provides a satisfactory description of the structures and relative energies of the cluster isomers  $\text{Li}_6$ , for which are known high-precision data analysis (5).

### Modeling the interaction of lithium metal with 15-crown-5

To simulate the interaction of 15-crown-5 molecules with lithium electrode surface was used defective regular tetrahedral cluster lithium  $\text{Li}_{19}$ , which is a fragment of the lattice Li. This cluster is completed to a regular tetrahedral positively charged cluster  $\text{Li}_{20}^+$  (Fig. 3) using  $\text{Li}^+$  ion from complex  $\text{Li}(15\text{-crown-5})^+$ . This reaction proceeds with energy gain 22.5 kcal/mol. In this case, the crown ether molecule is coordinated by three lithium atoms cluster. Probably for this reason, the binding energy of the crown ether in the complex is quite high - 65.1 kcal/mol.

However, when supplying additional electron the binding energy of crown ether in neutral complex  $\text{Li}_{20}(15\text{-crown-5})$  is reduced to 49.3 kcal/mol. In the case of negatively charged complex  $\text{Li}_{20}(15\text{-crown-5})^-$  the energy of the crown ether is 37.6 kcal/mol.

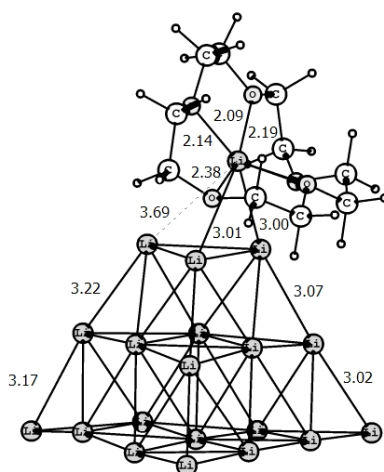


**Figure 3.** Structure 15-crown-5 on  $\text{Li}_{\text{metal}}$  surface

Therefore we can expect that when supplying additional electrons on the  $\text{Li}_{20}$  (model anode) binding energy of the donor molecule 15-crown-5 will be reduced and the result will be thermodynamically favorable process of splitting the crown ether by the entropy gain.

### Modeling the interaction of lithium nitride with 15-crown-5

To understand the mechanism of the influence of lithium nitride thin layer and crown ether on the lithium electrode surface the quantum-chemical modeling of  $\text{Li}_3\text{N}(15\text{-crown-5})$  was performed.

The lithium nitride surface simulated hexagonal cluster  $\text{Li}_n\text{N}_m$ . The calculated unit cell parameters  $\text{Li}_3\text{N}$  ( $a = 3.58 \text{ \AA}$ ,  $a = 3.84 \text{ \AA}$ ) are in good agreement with the experimental data

( $a = 3.65 \text{ \AA}$ ,  $a = 3.87 \text{ \AA}$ ) (6). In coordination molecule of 15-crown-5 is formed 5 bonds Li-O (Fig. 4). The average bond length Li-O =  $1.98 \text{ \AA}$ . The binding energy of the neutral complex is  $55.3 \text{ kcal/mol}$ , which is strong attaching crown ether to nitride. Deformation of the surface layer structure of  $\text{Li}_3\text{N}$  is small: Li-N distances for the atoms Li, coordinating crown ether molecule are reduced by an average  $0.01 \text{ \AA}$ .

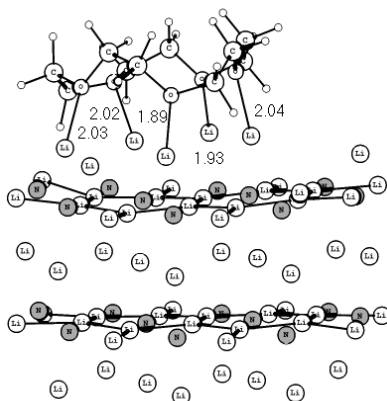


**Figure 4.** Structure  $\text{Li}_3\text{N}(15\text{-crown-5})$

The obtained data show that the binding energy for the complex  $\text{Li}_3\text{N}(15\text{-crown-5})$  and  $\text{Li}_{20}(15\text{-crown-5})$  are sufficiently large and comparable. However, the chemisorption of crown ether molecule to the lithium nitride doesn't result in destruction of its structure. While reacting of cluster  $\text{Li}_{20}$  with 15-crown-5 molecule leads to a deformation of it, which can then result in the destruction of the cluster.

#### Modeling $\text{Li}^+$ ion diffusion in the 15-crown-5 cavity

To simulate the lithium ion transport in the surface layer the structure of  $(15\text{-crown-5})_2\text{Li}^+(\text{ClO}_4^-)_2$  complexes with lithium ion starting position (Fig. 5a) and transient state to move  $\text{Li}^+$  from one equilibrium state to another (Fig. 5b) were calculated. The calculated energies of the complexes are very similar. This suggests that the  $\text{Li}^+$  diffusion isn't difficult. Since  $\text{ClO}_4^-$  anion models defectives on  $\text{Li}^+$  ions the negatively charged lithium nitride layer, it can be assumed that the barrier to entry of  $\text{Li}^+$  in the layer  $\text{Li}_3\text{N}$  cluster is also small. Modeling of this process is the subject of further study.

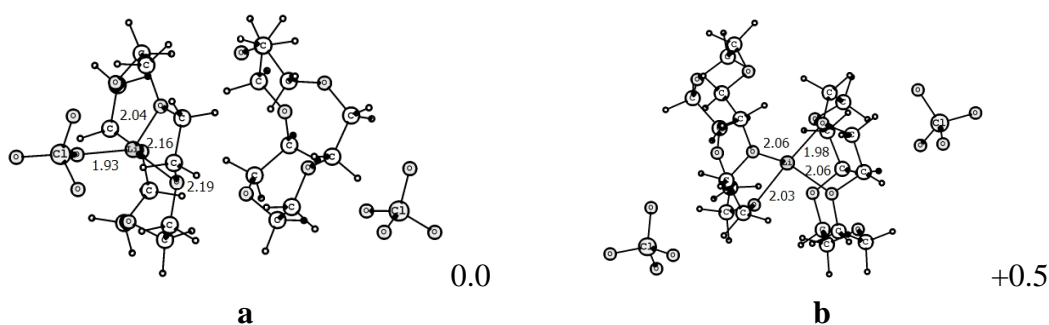


**Figure 5.**  $\text{Li}^+$  complex structure with two 15-crown-5 molecules and two  $\text{ClO}_4^-$  counterions. The bond lengths are in  $\text{Å}$ . Under the structure indicated energy difference in  $\text{kcal/mol}$  (taking into account the contribution of zero-point energy)

Thus, on the basis of experiments and theoretical calculations it is possible to draw conclusions about the formation of  $\text{Li}^+$ -conducting ordered crown ethers layers on the modified lithium anode surface. Electrochemical system with such crown ethers transition layer on the

protected lithium anode surface is perspective to develop a low-temperature lithium-polymer power sources.

### Acknowledgments

The work was supported by Russian Foundation for Basic Research (grant 12-03-31453).

### References

1. O.V. Yarmolenko, Yu.V. Baskakova, G.Z. Tulibaeva, L.M. Bogdanova, E.A. Dzhavadyan, B.A. Komarov, N.F. Surkov, B.A. Rozenberg, O.N. Efimov, *Rus. J. of Electrochemistry*, **45**, 101 (2009).
2. Yu.V. Baskakova, O.V. Yarmolenko, N.I. Shuvalova, G.Z. Tulibaeva, O.N. Efimov, *Rus. J. of Electrochemistry*, **42**, 949 (2006).
3. P. Perdew, K. Burke, M. Ernzerhof, *Phys. Rev. Lett.*, **77**, 3865 (1996).
4. D.N. Laikov, *Chem. Phys. Lett.*, **281**, 151 (1997).
5. B. Temelso, C.D. Sherrill, *J. Chem. Phys.*, **122**, 064315 (2005).
6. H. Schulz, K. Schwarz, *Acta Crystallogr., Sect. A: Cryst. Phys., Diffr., Theor. Gen. Crystallogr.*, **34**, 999 (1978).

## Monometallic Textile Electrodes for „Green“ Electronics

Vojtěch, L.<sup>a</sup>, Hájek, J.<sup>a</sup>, Neruda, M.<sup>a</sup>, Zatloukal, M.<sup>b</sup>

<sup>a</sup> Department of Telecommunication Engineering, Czech Technical University in Prague, Prague 166 27, Czech Republic

<sup>b</sup> Centre for Research and Utilization of Renewable Energy Sources, Brno University of Technology, Brno 601 90, Czech Republic

Modern trends in the development of new, rapidly applicable, electrical engineering technology have increasingly focused on environmentally friendly elements. The result is the new "green" electrical engineering in agreement with EU by 2020 - Horizon 2020 (1). The aim is implementation of not only modern organic components and circuit structures, but also environmentally friendly and therefore "green" electrochemical sources (2). In the analysis of the current situation in the development of electrode and battery separators it is obvious that especially new types of textile fibers (i.e. linear fabric) are promising direction of development (3). Planar electrically conductive fabrics remain for many years used to produce protective clothing, which evenly distribute electric charge on their surface. Therefore they realize the protection against ESD (Electro Static Discharge), but only if properly conductive structure of such materials is selected (i.e. the desired electrical conductivity is obtained) (4). In recent years, the electrical conductivity of the materials was managed to increase and applications can thus be found in the implementation of flexible electrically conductive elements or electromagnetic shielding (5). Thanks to the significant surface of textile materials, which is determined by the structure of the material and the used fibers, it seems advisable to use these materials also as carriers of electrodes with a maximum surface, as it is required in the implementation of electrochemical cells - batteries. Such applications can be found in foreign sources, particularly in the implementation of supercapacitors using nanotextiles (6).

The paper focuses on implementation of "green" electrodes of electrochemical sources by preparation technology of monometallic layers of tin with a maximum area on the PP textile substrate. The technology is verified in laboratory conditions and further research is discussed.

The use of nanotextiles is not possible in the case of strongly alkaline electrolytes because they are made of PVDF (polyvinylidene difluoride) materials, PVDF copolymers and PAN (polyacrylonitrile) (7), which do not withstand such electrolytes (8). In the development of new types of environmentally friendly, electrochemical sources, it is taken into account using of environmentally friendly metals (zinc, tin, copper) and strong alkaline electrolyte in the form of gels (9).

Especially PP (Polypropylene) has a high resistance against strong alkaline and acidic chemicals. The PP is widely used in the construction of chemical technologies and components. It is necessary to make conductive the textile based on PP fibers, in order to use it as electrode.

It can be performed by several technologies:

- Coating of metal powder
- Physical methods of coating in a vacuum
- Chemical coating
- Electroplating

The analysis of the above-mentioned requirements and the analysis of available technologies show, it is not possible to secure required properties of the described procedures. The solution however lies in a combination of several procedures (Fabric Pretreatment - Vacuum Deposition - Reinforcement of Tin Layer).

Electroformed tin layer, which reinforces the primary vapor deposited film of tin, is realized by alkaline tinning bath, because the electrode will be operated in an alkaline environment. Moreover, alkaline tinning baths have higher depth effect. Nevertheless, the alkaline electrolyte will be based on KOH, it is possible to use tinning bath with NaOH. The basis of both baths is  $\text{Na}_2\text{SnO}_3$  or  $\text{K}_2\text{SnO}_3$  and appropriate hydroxide.

Anodes are not covered by the standard yellow greenish layer indicating anodes polarization. In contrast, they turn dark grey under these conditions and therefore tin passes to the bath in the form of divalent ions. As a result, tough coating is formed with higher surface than conventional decorative glosses, which are realized by tetravalent ions (4). The primary reason for this is a small anode area compared with the cathode. It also results in strong evolution of oxygen in the electrolyte.

The proposed technological processes were verified in laboratory conditions with good results, Fig. 1 – 4. In addition, electroforming procedures enabled to coat salient fibers not only from the front side toward the anode, but also on the sides, which is not possible in most electrolytes due to the depth effectiveness.  $0.72 \text{ g/cm}^2$  of tin was excluded in the implementation of unilateral electrode. Tests of the cyclic stress of conductive felt structure (3D structure) as a collector and carrier of electrode materials for alkaline battery showed good results and stability of excluded monometallic layer. The main criteria for the evaluation of the collector were evolution of hydrogen under cyclic stress (charging and discharging of battery), encompassment of application of active material to the collector and not least comparison with other materials - nets, pocket electrodes etc.

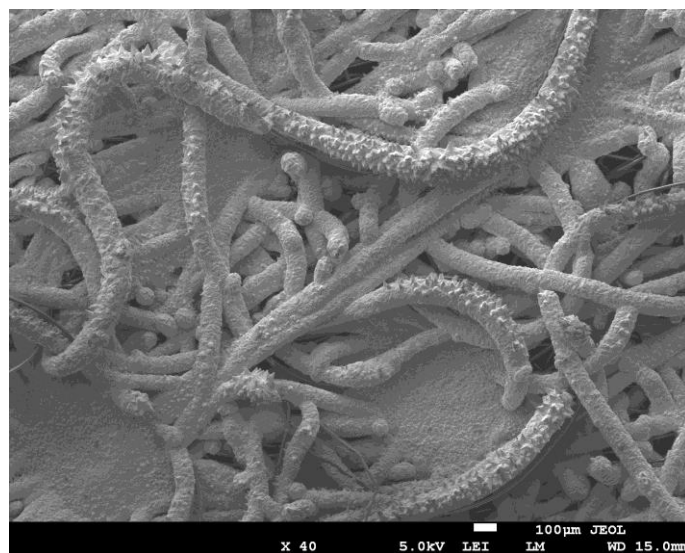


**Figure 1.** Monometallic tin electrode realized on needled PP.

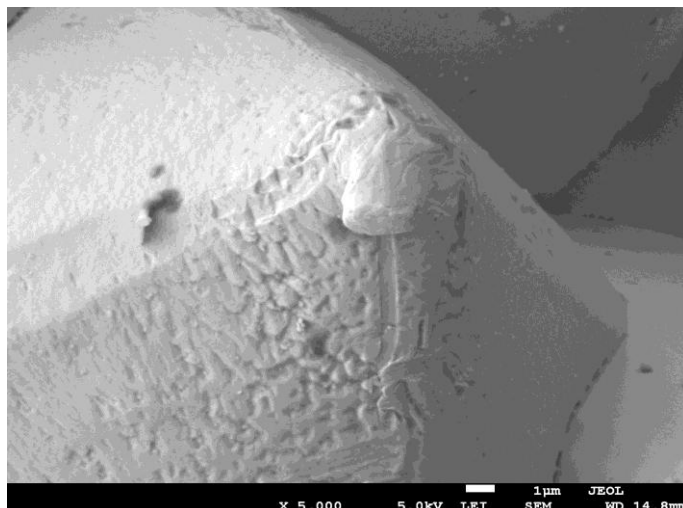


**Figure 2.** Detail of the crystal surface of divalent tin of realized monometallic tin electrode.

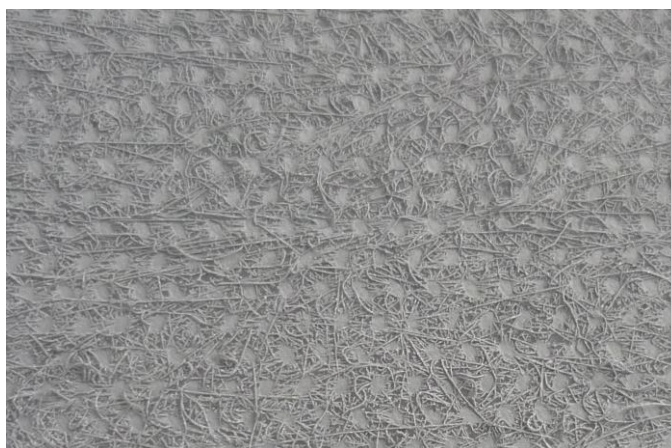


**Figure 3.** Macrophotography of monometallic tin electrode realized on heat reinforced PP.



**Figure 4.** Monometallic tin felt electrode ready for filling (non-woven PP textile carrier realized by needling).

The aim of the development project was to design and validate in laboratory conditions the preparation technology of monometallic layers of tin with a maximum area on the PP textile substrate for implementation of "green" electrodes of electrochemical sources. The paper describes several procedures and results confirm the project goals. The used technologies simultaneously enable mass manufacturing. During the work a promising path for continued research in this area was also found. Laboratory tests were carried out on one or both sides coated samples in different types of PP substrates, both variously reinforced fabrics, and different planar densities. Realized

samples also passed by laboratory verification for cyclic stress in the measuring cell of electrochemical cell between cycles of charging and discharging.

### Acknowledgments

The paper was supported by the project Kompozitex FR–TI4/202 - Composite textile materials for humans and technology protection from the effects of electromagnetic and electrostatic fields and Center for Research and Utilization of Renewable Energy, CZ.1.05/2.1.00/01.0014 (CVVOZE).

### References

1. Green Paper - From Challenges to Opportunities: Towards a Common Strategic Framework for EU Research and Innovation funding, web Horizon 2020, 2011. [http://ec.europa.eu/research/horizon2020/pdf/com\\_2011\\_0048\\_csf\\_green\\_paper\\_en.pdf#page=2](http://ec.europa.eu/research/horizon2020/pdf/com_2011_0048_csf_green_paper_en.pdf#page=2)
2. Towards Green Electronics in Europe: Strategic Research Agenda Organic & Large Area Electronics, 2009.
3. [http://cordis.europa.eu/fp7/ict/photonics/docs/reports/olae-sra\\_en.pdf](http://cordis.europa.eu/fp7/ict/photonics/docs/reports/olae-sra_en.pdf)
4. L. Ji and X. Zhang, "Fabrication of porous carbon/Si composite nanofibers as high-capacity battery electrodes," *Electrochemistry Communications*, vol. 11, pp. 1146-1149, June 2009.
5. M. Neruda and L. Vojtěch, "Verification of Surface Conductance Model of Textile Materials," *Journal of Applied Research and Technology*, vol. 10, pp. 579-585, 2012.
6. L. Vojtěch and M. Neruda, "Application of Shielding Textiles for Increasing Safety Airborne Systems - Limitation of GSM Interference," in *The Ninth International Conference on Networks*, Los Alamitos: IEEE Computer Society, p. 157-161, April 2010.
7. A. Laforgue, "All-textile flexible supercapacitors using electrospun poly(3,4-ethylenedioxythiophene) nanofibers," *Journal of Power Sources*, vol. 196, pp. 559–564, January 2011.
8. Elmarco. Battery separators, Elmarco nano for life, 2013.
9. <http://www.elmarco.com/application-areas/battery-separators/>.
10. Chemical Resistance Chart, Zeus, 2013.
11. <http://www.zeusinc.com/technicalservices/technicalbulletins/chemicalresistanceofpolymers/chemicalresistancechartpvdf.aspx>.
12. K. Yuri, Y. Mototani and J. Asaoka, "Alkaline battery having a gelled negative electrode," U.S. Patent No. 5,587,254. 24 Dec. 1996.

## Investigation of ion transport in the network polymer gel electrolytes, modified with ionic liquid BMIBF<sub>4</sub> for lithium-ion batteries

Yudina, A.V.<sup>a</sup>, Chernyak, A.V.<sup>a</sup>, Volkov, V.I.<sup>a</sup>, Kulova, T.L.<sup>b</sup>, Yarmolenko, O.V.<sup>a</sup>

<sup>a</sup> Institute of Problems of Chemical Physics RAS, Chernogolovka, Russian Federation

<sup>b</sup> A.N. Frumkin Institute of Physical Chemistry and Electrochemistry, Moscow, Russian Federation

Gel polymer electrolytes based on polyethylene glycol diacrylate, salts LiBF<sub>4</sub>, ethylene carbonate and the ionic liquid 1-butyl-3-methylimidazolium tetrafluoroborate were synthesized and investigated. The conductivity reached a value of  $2.5 \times 10^{-3}$  S/cm at 20 °C and  $1.1 \times 10^{-2}$  S/cm at 100 °C. The resulting network polymer gel electrolyte tested in an electrochemical cell Li//the amorphous Si-SiO<sub>x</sub> composite.

The replacement of carbonate solvents on the ionic liquid (IL) is the one way to increase the conductivity and improve the properties of polymer electrolytes for lithium-ion batteries (LIB). Incorporating ionic liquid into the polymer electrolyte leads to increase electrochemical and thermal stability over a wide temperature range.

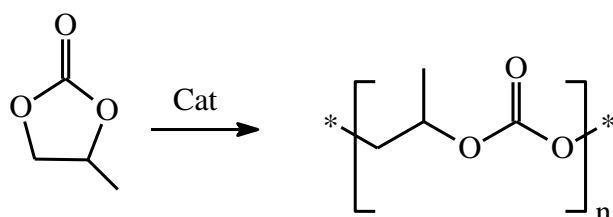
Previously (1) we investigated features of the synthesis and properties of the polymer electrolyte based on polyethylene glycol diacrylate (PEGDA), LiBF<sub>4</sub> salt and ionic liquid 1-butyl-3-methyl imidazolium tetrafluoroborate (BMIBF<sub>4</sub>). Incorporating BMIBF<sub>4</sub> up to 63 wt.% did not increase the ionic conductivity of polymer electrolyte at room temperature. The ionic conductivity reaches about  $10^{-3}$  S/cm, only at 50 °C.

This paper proposed a polymer gel electrolyte with partial replacement solvent (propylene carbonate, PC and ethylene carbonate, EC) on BMIBF<sub>4</sub>. Synthesis network polymer electrolyte was carried out by radical polymerization of PEGDA in the presence of benzoyl peroxide (BP) at 80 °C for 3 hours.

The method of thermal analysis shows that the loss of solvent in the resulting gel electrolytes based on IL for propylene carbonate begins at 83 °C (for the composition of PE with 31 wt.% PC), and this temperature indicator almost independent of the solvent concentration in the range of 15-31 wt.%. For PE with ethylene carbonate initial weight loss temperature is strongly dependent on the concentration and is 107 °C at 27 wt.%.

By isothermal calorimetry, DSC analysis and NMR spectroscopy on nuclei <sup>1</sup>H and <sup>13</sup>C, followed by quantum chemical modeling showed that propylene carbonate during radical polymerization in BMIBF<sub>4</sub> environment is changing its structure.

We suppose that on the basis of PB and IL arises catalytic center, which accelerates the reaction of polymerization of the PC:



In addition to changing the chemical shifts in both nuclei  $^1\text{H}$  and  $^{13}\text{C}$  NMR spectra in propylene carbonate are also observed slight chemical shifts changes for the ionic liquid. This change in the structure of the polymer electrolyte system PEGDA-LiBF<sub>4</sub>-BMIBF<sub>4</sub>-PC has negative effect on the transport of ions Li<sup>+</sup>.

However, in the case of a partial replacement of ethylene carbonate by BMIBF<sub>4</sub> is no changes in the structure of the solvents and IL molecules.

In the compositions of the polymer electrolyte with partial replacement of the organic solvent on BMIBF<sub>4</sub> the presence of two states of the lithium ions, with high (~ 20% of the ions Li<sup>+</sup>) and low self-diffusion coefficient that differ by 1-2 orders was revealed by NMR (2). Appearance of the mobile state of the Li<sup>+</sup> ions is due to the formation of a new coordination environment consisting of solvation molecules of solvent. In PC addition in the range from 15 to 31 wt.% the conductivity rises to 10<sup>-4</sup> S/cm at 20 °C, but it is an extreme character as the proportion of Li<sup>+</sup> ions with high-mobility is reduced from 24 to 7%. This is due to the effect of the polymerization PC.

Due to the fact that the structure of ethylene carbonate in the synthesis of the network polymer electrolyte is stable better results of conductivity were achieved in this electrolyte system.

High conductivity of 2.5×10<sup>-3</sup> S/cm at 20 °C and 1.1×10<sup>-2</sup> S/cm at 100 °C was achieved in the electrolyte composition (wt.%) PEGDA -19, LiBF<sub>4</sub> -10, BMIBF<sub>4</sub> -44, EC-27, where the Li<sup>+</sup> ions of both types have the same order of diffusion coefficients - 4.1×10<sup>-11</sup> and 1.2×10<sup>-11</sup> m<sup>2</sup>/s. This indicates the preferential replacement of units of the polymer matrix in the coordination environment of the ion Li<sup>+</sup> by ethylene carbonate molecules. In polyester diacrylate systems in the absence of ionic liquid the similar process we observed earlier (3,4).

For the above electrolyte composition with a high conductivity cycling tests were carried out in an electrochemical cell Li//(*Si-SiO<sub>x</sub>*). Test results are presented in Figure 1.

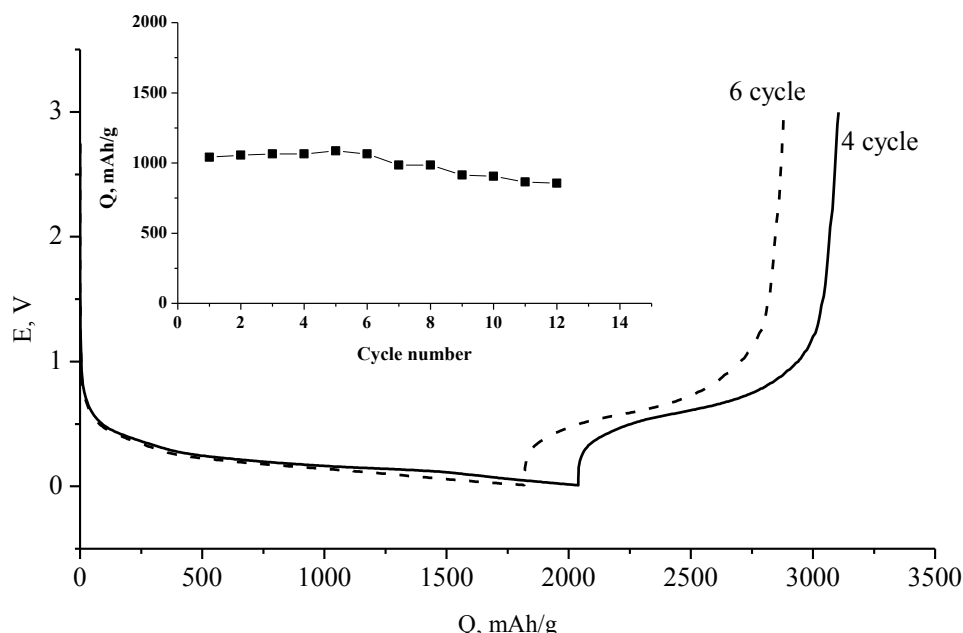


**Figure 1.** Charge-discharge curves and capacity fading of LIB's anode based on amorphous composite (*Si-SiO<sub>x</sub>*). Current density of 75 mA/g *Si-SiO<sub>x</sub>*.

Figure 1 shows that the electrochemical cell with a polymer gel electrolyte was cycled well, though with a slight drop in capacity. The specific discharge capacity of amorphous *Si-SiO<sub>x</sub>*

composite amounted about 1000 mAh/g, which is 3 times exceeds the discharge capacity of traditional carbon anode material.

Thus, the highly conductive polymer gel electrolytes were obtained based on PEGDA, LiBF<sub>4</sub>, ethylene carbonate and the ionic liquid 1-butyl-3-methylimidazolium tetrafluoroborate. It is promising for use in lithium-ion batteries with the anode based on amorphous Si-SiO<sub>x</sub> composite.

### Acknowledgments

This work was supported by Russian Foundation for Basic Research, grants 13-03-00698 and 12-03-31453.

### References

1. E. Y. Evschik, M. L. Bubnova, E. A. Dzhavadyan, O. V. Yarmolenko, *Bulletin of Bashkir University*, **17**, 51 (2012).
2. O. Yarmolenko, E. Evschik, A. Marinin, V. Volkov, A. Shestakov, *40 International conference on coordination chemistry*, Valencia, Spain (2012).
3. A.A. Marinin, K.G. Khatmullina, V.I. Volkov, and O.V. Yarmolenko, *Rus. J. Electrochemistry*, **47**, 717 (2011).
4. O.V. Yarmolenko, K.G. Khatmullina, G.Z. Tulibaeva, L.M. Bogdanova, A.F. Shestakov, *Rus.Chem.Bulletin*, **61**, 539 (2012).

## Electrospun PVDF separators for lithium ion batteries

Musil, M., Pleha, D., Libich, J.

Institute of Electrotechnology, Brno University of Technology, Faculty of Electrical Engineering and Communication, Technická 3058/10 616 00 Brno, Czech Republic.

The main reason for using nano fibred materials for separators are their both high porosity and relative surface area. These requirements are important to improve ionic conductivity of separators and ensure sufficient electrolyte volume in battery. These advantages makes electrospinning very promising method of nanofibred separators production. In this paper are described electrospinning fabrication process and discussed results of separator's properties measurements. Furthermore, electric and electrochemical properties of non-commercial nanofibrous separators produced by Nafigate Corporation stock company are compared with properties of Celgard 3401 (standard on the market).

### Introduction

Microporous separators based on polypropylene and polyolefine are the most used ones in contemporary commercial li-ion batteries. The reason is it's properties suitable for this purpose. These separators demonstrate high chemical stability, appropriate thickness, tensile strenght and toughness. As a negative properties of commercial separators occur low porosity, low thermal stability, wettability and ability to uptake electrolyte. Low wetability and ability to uptake electrolyte are both caused by polarity difference between non-polar separator (polyolefine) and highly polar electrolyte containing solvent [1]. This fact may lead to increase in battery cell resistance and subsequently to battery capacity lowering [2, 3]. Several fabrication methods improving overall properties of separators were introduced. It is possible to apply one of these methods: spinning - monomer liquid is jetted from the rotary source on to the target, or melt blowing method [4]. Alternative to these methods is electrospinning. Electrospinning enables producers to lower separator's thickness preserving mechanical properties at high level.

Main advantages of such separators fabricated as mentioned above are high porosity and chemical stability. Moreover, thanks to porous structure, ability to uptake sufficient amount of electrolyte. Thanks to mentioned preperities, ions dissolved in electrolyte are enabled to easily move in the whole bulk between cathode and anode. Hand in hand are better electrochemical properties of the battery cell. Electrospinning method is applicable to all polymer materials, that are meltable or soluble.

### Experimental

#### Separator fabrication

Experimental samples of nano fibred separators are fabricated in the laboratory machine Nanospider™ NS LAB 500 equipped with EMW (Endless Motion Wire) technology. This EMW technology is based on spinning by the string electrode with usage of a small amount of polymer

solution. Polymer solution is applied (the rate of application is set) on the string (spin electrode). Intensive electrostatic field, which results from potential difference between spin and collecting electrodes, forms Taylor's cone. This cone is fibre source. Drawn fibre is subsequently elongated, surface area increases and solvent evaporates simultaneously. Properly adjusted Nanospider (electrodes position, solvent selection) produces sub-micron wide dry fibres. Electric charge carried by the produced fibres has the same polarity as the spin electrode. This charge is drained onto collector and usually grounded [6].

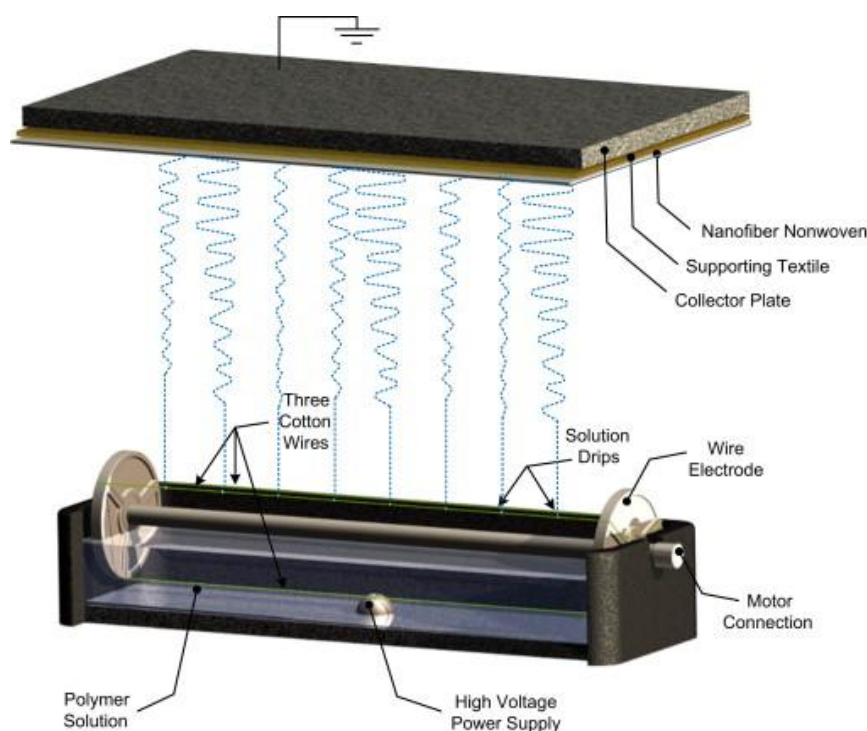


**Figure 1.** Nanospider scheme with main parts description [8]

### Electric volume and surface resistance measurement

Electric resistance measurements run in three electrode cell with stainless steel working electrodes (26 millimeters diam.) and thrust set on 5000 grams. Measurement at potential set on 100 V took 60 and 600 seconds respectively. All separator samples underwent this process.

**TABLE 1.** Volume and surface separator resistances at time  $t = 60$  s and 600 s.

Sample	Volume resistance $R_v$ [ $\Omega$ ]		Surface resistance $R_p$ [ $\Omega$ ]	
	60 s	600 s	60 s	600 s
3401	$3.80 \times 10^7$	$7.12 \times 10^7$	$7.62 \times 10^{11}$	$4.67 \times 10^{11}$
AM	$1.61 \times 10^{11}$	$2.95 \times 10^{10}$	$2.93 \times 10^{14}$	$2.53 \times 10^{12}$
5409	$1.16 \times 10^{11}$	$1.03 \times 10^{11}$	$4.84 \times 10^{13}$	$3.80 \times 10^{13}$
7209	$1.13 \times 10^{11}$	$1.17 \times 10^{11}$	$1.27 \times 10^{14}$	$9.75 \times 10^{13}$
13L	$2.26 \times 10^7$	$1.23 \times 10^8$	$4.39 \times 10^{10}$	$1.01 \times 10^{11}$
43L	$1.59 \times 10^8$	$2.73 \times 10^7$	$3.94 \times 10^8$	$3.97 \times 10^9$

### Ionic conductivity

Impedance spectroscopy was run on potentiostat VSP Biologic. All samples were immersed in 1 mol . l-1 LiBF<sub>4</sub> in EC/DMC electrolyte and tempered in the climate chamber with temperature set at 20 °C simultaneously. Separator circles (16 millimeters in diam.) were measured in electrochemical test cells EL-CELL at frequency range 0.5 Hz – 1 MHz with amplitude 10 mV. All the process took place in the inert argon atmosphere. Ionic conductivity ( $\sigma$ ) was calculated according to the equation below:

$$\sigma = \frac{d}{R_b \times S}, \quad (1)$$

where  $R_b$  is the bulk resistance,  $d$  and  $S$  are thickness and area of the sample [2].

Ionic conductivity measurement results are shown in the Nyquist plot (see Figure 2 below).

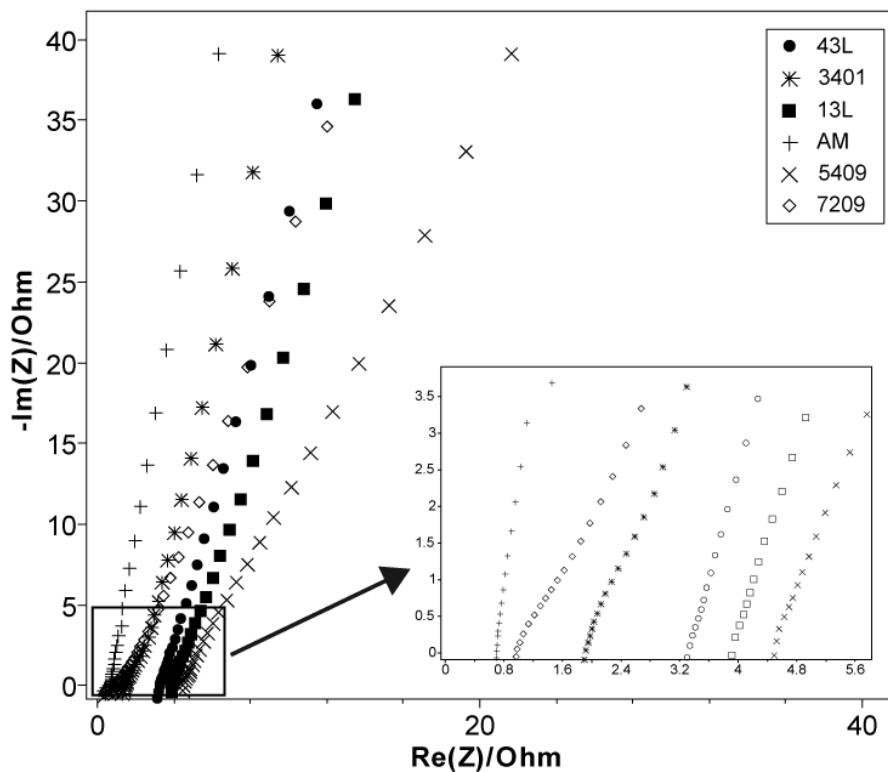


**Figure 2.** Separator impedance spectras, 1 mol . l-1 in EC/DMC electrolyte, 20 °C.

**TABLE 2.** Thickness and relative conductivity of separators. Frequency rance 0.5 Hz - 1 MHz.

Sample	Thickness [mm]	Relative conductivity $\sigma$ [mS cm <sup>-1</sup> ]
3401	0.155	1.97
AM	0.195	2.90
5409	0.019	1.36
7209	0.025	0.68
13L	0.064	0.70
43L	0.082	4.17

### Ionic conductivity measurement in half-cell

Separator influence on battery performance was measured in three electrode electrochemical test cell EL-CELL. Test cells representing lithium ion half-cell consisted of metallic lithium counter (CE) and reference (RE) electrodes. As a working electrode (WE) was chosen anode. Negative electrode in commercial lithium ion batteries is made from materials based on carbon. We prepared our WE from graphite COND CR 5995. Test cells were assembled in the inert argon atmosphere. We employed common liquid electrolyte  $1 \text{ mol} \cdot \text{l}^{-1} \text{ LiPF}_6$  in EC/DMC (50:50 wt. %) in test cells. Test process consisted of several steps:

- Assembling test cell embedded with separator #1
- Characteristics measuring on potentiostat / galvanostat
- Disassembling test cell embedded with separator #1, assembling test cell embedded with separator #2
- Characteristics measuring on potentiostat / galvanostat

Half-cell was measured on Galvanostatic Cycling with Potential Limitation (GCPL). This method enabled us to control electrochemic half-cell potential at cycled charge and discharge. In first two cycles was half-cell formatted (double layer on the interface electrode-electrolyte was stabilised). Formatting is linked to electrode characteristics changes – irreversible capacity of the half-cell, impedance of both electrode and electrode material; coulombic efficiency. During sequent cycles was evaluated electrode stability and power characteristics. Half-cell (embedded with commercial separator Celgard 3401) formatting cycle is shown in figure 3.

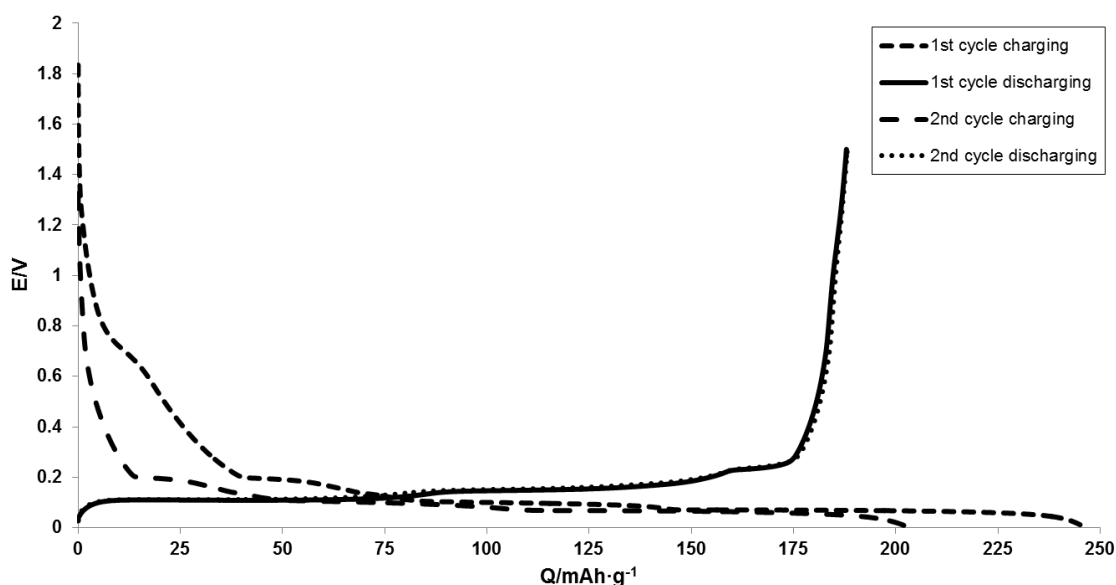


**Figure 3.** Half-cell formatting cycle, celgard 3401 separator.

In figure 3 are shown first two cycles of SEI layer formatting on the graphite electrode interface. SEI layer formatting is represented by the capacity loss (in this case 24 %). Separator influence on the formatting and stability of this polymer layer was examined during characteristics measurement. The SEI layer is essential for lithium ion batteries. Instead of this, separators influence on cyclic stability, capacity loss, Coulombic efficiency, capacity stability and power characteristics will be interpreted.

## Conclusion

This report is focused on measuring properties of non-commercial separators from the Nafigate Corporation stock company. Properties of separators are compared with on the market widely pread separator Celgard 3401. Nafigate separators were prepared by electrospinning. Samples were tested on ionic conductivity and influence on characteristic of lithium ion half-cell. These nafigate separators (especially AM model) have all the important parameters comparable with the world production.

## Acknowledgements

This work was supported by the grant FEKT-S-11-7 and project CVVOZE CZ.1.05/2.1.00/01.0014.

## References

1. S.S. Zhang, Journal of Power Sources 164 (2007) 351–364.
2. H. Choaz, T. Sakaia, S. Tanasea, K. Kimurab, Y. Kondob, T. Taraob, M. Tanakab,
3. Electrochemical and Solid-State Letters 10 (2007) A159–A162.
4. K.M. Abraham, M. Alamgir, Journal of Electrochemical Society 142 (1995) 683.
5. Yang, C., Jia, Z., Guan, Z., & Wang, L. (2009). Polyvinylidene fluoride membrane by novel electrospinning system for separator of Li-ion batteries: Journal of Power Sources, vol. 189 (issue 1).
6. Nanospider: Technologie electrospinningu. [online]. [cit. 2013-05-06]. Available from: <http://old.elmarco.com/obsah.php?id=27&s=25>
7. Agilent 16008B Bias RESISTIVELY CELL Operation and Service Manual. [online]. [cit. 2013-05-06]. Available from: <http://cp.literature.agilent.com/litweb>
8. Sambaer, Wannes, Martin Zatloukal, and Dusan Kimmer. "3D air filtration modeling for nanofiber based filters in the ultrafine particle size range." Chemical Engineering Science vol. 82 (2012): 299-311.

## Thermal Processes in Ssystems ‘Li-rich Cathode Materials – LiPF<sub>6</sub>-Based Organic Solutions’

Haik, O., Amalraj, F. S., Hirshberg, D., Talianker, M., Markovsky, B., Zinigrad, E., Aurbach, D.\*

### Introduction

Lithiated transition metal oxides Li<sub>x</sub>MO<sub>y</sub> (M – transition metal) of layered and spinel structures are used as positive electrodes (cathodes) in Li-ion batteries. These materials are thermodynamically unstable in air as well as in lithium battery solutions comprising LiPF<sub>6</sub> in mixtures of ethylene carbonate (EC) and dimethyl carbonate (DMC). It was established that lithium carbonate can be formed on the surface of the above lithiated oxides, being exposed to humid air. Even at ambient temperatures, oxides react with solution species, like HF, PF<sub>5</sub>, EC and DMC resulting in inorganic and organic products. In the present study, we investigated thermal behavior of the following cathode materials: monoclinic Li<sub>2</sub>MnO<sub>3</sub> (layered monoclinic structure), xLi<sub>2</sub>MnO<sub>3</sub>·(1-x)Li(NiMnCo)O<sub>2</sub> (the so called Li-rich integrated compounds), and LiNi<sub>1/3</sub>Mn<sub>1/3</sub>Co<sub>1/3</sub>O<sub>2</sub> (NCM 111, layered rhombohedral structure) that were heated in EC-DMC/LiPF<sub>6</sub> electrolyte solutions. We assign these electrode powders as being in "pristine state" in contrast to similar powders in the "charged state" that were scratched from the delithiated electrodes.

### Results and Discussion

#### i. Thermal responses of different cathode materials and their correlation with the morphology

We have found that in the pristine state, the above electrode powders indicate the existence of two minor peaks in the temperature range of 60-140 °C that are not always separated, and from one to three major (much intensive) exothermic peaks, in the temperature range of 200-400 °C. The I-st minor peak between 65 and 100 °C belongs to the reactions of the electrolyte solution with surface Li<sub>2</sub>CO<sub>3</sub> [1]:

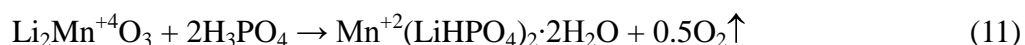


The disproportionation of POF<sub>3</sub> as it is being liberated might begin with processes conjectured as [2]:



Based on the Raman spectroscopy, XRD, EDAX, and HRSEM results we suggest that the second minor exotherm that begins at ~ 90 -100 °C is related to the cathode-solution interaction:





The Li-rich integrated materials show highly inhomogeneous morphology. The spherical particles have different size and roughness and their diameter varies from 3 to 15  $\mu$ . Two types of morphology can be distinguished. The first, the spheres with high roughness compose of well-defined flattened small fractions of irregular shape, about 0.5  $\mu$  in size, that are not tightly adjoined. Some of those small fractions are faceted. The second morphological type is characterized by less rough spheres compose of similar small particles, but very tightly packed.

The amount of exothermic heat is associated with appropriate degradation level of reactive materials. In our DSC tests the critical heat amount was about 10-40 J/g. If exothermic heat at low temperature is higher than this critical value, the exothermic processes that appear after 200 °C change significantly. The new endothermic peak appears in the temperature range 200-300 °C, and no peaks are observed at  $T > 300$  °C. We suppose that the endothermic process relates to thermal decomposition of  $\text{LiPF}_6$ . The salt can precipitate because of substantial consumption of solvents at temperature higher than 200 °C. XRD patterns of the samples that were heated up to 400 °C are strongly dependent on the type of DSC response. The cathode that was partially chemically delithiated during aging in solution at 60 °C as well as the pristine one are stable only to  $\sim 80$  °C in fresh solution. Nevertheless, the heat evolved at  $\sim 80 - 100$  °C was 4.5 times lower for the aged cathode in aged solution,  $\sim 7$  J/g, than that for the pristine one in the pristine solution, 45 J/g. Such a difference is explained considering that the aged cathode was already partially delithiated at 60 °C during aging, and the additional delithiation at higher temperature is only part of the entire process. The delithiated Li-rich compound has significantly higher thermal stability, and in opposite to pristine materials does not react with electrolyte solution up to 180 °C. Importantly to note that the minor exotherms in low temperatures interval are never observed for samples that were fully electrochemically delithiated.

## ii. Post-mortem analysis of heated and aged cathode materials

XRD spectra collected from Li-rich pristine electrode after heating up to 140 °C in 1M  $\text{LiPF}_6/\text{EC}:\text{DMC}$  electrolyte solutions in hermetically sealed Swagelok cells, demonstrates significant structural changes. Namely a new XRD peak appears at 18.8, which can be associated with the  $\text{Mn}(\text{LiHPO}_4)_2 \cdot 2\text{H}_2\text{O}$  phase. In addition, the characteristic weak peak (020)<sub>M</sub> within the  $2\theta$  range of 20–24° related to the  $\text{Li}_2\text{MnO}_3$  component almost completely disappeared. The unit cell parameter  $c$  of the rhombohedral structure decreased from 14.19 Å (pristine state) to 14.09 Å after thermal reactions in solutions. The unit cell parameter  $c$  increases to 14.44 Å after electrochemical delithiation, which occurs with increasing of the oxidation states of cations. The opposite change of  $c$  value may indicate the lithium extraction from the rhombohedral structure without changes of the oxidation states of cations. The pattern collected from the material heated up to 400 °C shows significantly decreased (about 3 times) the intensity of all the peaks related to both monoclinic and rhombohedral structures while their width increased. In addition, the (015)<sub>R</sub> peak at 48.9° disappeared. These changes can be attributed to structural changes and lattice strain effects, which accompany the decomposition of the monoclinic  $\text{Li}_2\text{MnO}_3$  and rhombohedral  $\text{Li}[\text{NiMnCo}]\text{O}_2$  components and, probably, to chemical delithiation. Moreover, two new peaks appear at 35.6 ° and 41.5 °, we assume that those peaks are attributed to a new phase of the following composition  $\text{NiO}_{0.25}\text{MnO}_{0.75}$  (01-078-0427).[3] The Raman spectrum of the pristine material shows two main peaks at about 600 and 485  $\text{cm}^{-1}$  related to the  $A_{1g}$  and  $E_g$  modes, respectively. The Raman peaks below 485  $\text{cm}^{-1}$  are attributed to the monoclinic  $\text{Li}_2\text{MnO}_3$  component. The Raman spectrum of the

heated sample up to 400 °C shows the disappearance of the bands below 485 cm<sup>-1</sup> and a blue-shift in the position of two main Raman peaks to about 630 and 500 cm<sup>-1</sup> that can be correlated to the lithium extraction and formation of a spinel-type structural ordering (layered-to-spinel-type transition) [4, 5]. Similar structural transformations take place during aging of the Li-rich material in solution and during its heating up to 140 and 400°C. The observed splitting of the main Raman peak into two peaks positioned at 600 cm<sup>-1</sup> and 625 cm<sup>-1</sup> in spectrum related to the heated sample up to 140°C can be explained by coexistence of the layered and a newly formed cubic spinel structures. In addition, the spectrum of the aged material shows the appearance of a peak at 945cm<sup>-1</sup> associated with the PO<sub>4</sub> band, this is in correlation with the results of XRD studies. We suggest that species containing PO<sub>4</sub> groups can be developed according to reactions (9) – (11) in solutions. After heating to 140 °C the amount of fluorine on the surface increases twice for both of them that obviously is a result of formation of LiF according to reactions (1) – (8). The contours of the heated particles become less pronounced and blurred that may be a result of the formation of surface layer comprising polymeric species, LiF, LiMn<sub>2</sub>O<sub>4</sub>, Mn (LiHPO<sub>4</sub>)<sub>2</sub>·2H<sub>2</sub>O.

### Conclusions

1. Upon exothermic reactions of cathode materials and surface lithium carbonate with solution species in the temperature range of 60 - 140 °C, Li<sub>2</sub>CO<sub>3</sub> disappears by transformation to LiF, and cathode materials undergo partial chemical delithiation accompanied with formation of a cubic spinel phase and MnHPO<sub>4</sub>·3H<sub>2</sub>O, as was detected by XRD and Raman measurements.

2. Exothermic reactions at 60 - 140 °C lead to decomposition of both cathode material and electrolyte solution, and to forming the secondary passive layer that consists of organic and inorganic components like polymeric species, LiF, LiMn<sub>2</sub>O<sub>4</sub>, Mn (LiHPO<sub>4</sub>)<sub>2</sub>·2H<sub>2</sub>O. The high level of decomposition can cause fast batteries degradation (failing) at T> 60 °C. Partially delithiated cathode materials that are covered by newly formed species are stable up to 180 °C.

3. The heat evolved during thermal reaction between cathode materials and solution in the temperature range of 60 - 140 °C is strongly dependent on the nature of the material, particles morphology, the amount of surface Li<sub>2</sub>CO<sub>3</sub>, and can vary from a few to tens or even hundreds Joules per gram.

4. The products formed are identical in both cases, namely in a dynamic DSC heating and in an isothermic aging. Therefore, DSC tests can be used for estimating the thermal stability of electrodes in battery solutions since they allow getting the results in a relatively short time (1 h) in contrast to prolonged aging experiments.

5. The extensive exothermic decomposition of both solution and cathode material at relatively low temperatures of 60 - 140 °C can affect significantly the thermal processes in the high temperature range.

6. The total irreversible destruction of both the cathode material and the electrolyte solution takes place in the temperature range of 180 – 400 °C. The total heat evolved during thermal reactions in the range of 70 – 400 °C was estimated in our tests as 400 - 600 J/g.

### References

1. G. V. Zhuang, G. Chen, J. Shim, X. Song, P. N. Ross, and T. J. Richardson , *J. Power Sources*, 134, 293 (2004).
2. E. Markevich, R. Sharabi, O. Haik, V. Borgel, G. Salitra, D. Aurbach, G. Semrau, M.A. Schmidt, N. Schall, C. Stinner, *J. Power Sources*, 196, 6433 (2011).
3. C. A. Barrett, E. B. Evans, *J. Am. Ceramic Soc.*, 47, 533 (1964).
4. S. F. Amalraj, D. Kovacheva, M. Talianker, L. Zeiri, J. Grinblat, N. Leifer, G. Goobes, B. Markovsky and D. Aurbach, *J. Electrochem. Soc.*, 157, A1121 (2010).
5. C.M . Julien, M. Massot, *Material Science and Engineering*, B100, 69 (2003).

## Numerical simulation of lithium ion battery

Vyroubal, P.<sup>1</sup>, Maxa, J.<sup>1</sup>, Kazda, T.<sup>1</sup>, Vondrák, J.<sup>1</sup>, Tichý, J.<sup>1</sup>

<sup>1</sup>Department of Electrical and Electronic Technology, Faculty of Electrical Engineering and Communication, BUT, Technická 10, 616 00 Brno, ČR

### Abstract

This article deals with the possibilities of numerical simulations of lithium ion batteries. The real battery datasheet will be compared with simulation results and with real measurements. For numerical study of the lithium-ion battery Comsol Multiphysics and MatLab Simulink will be used.

### Introduction

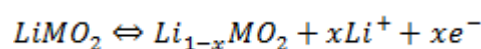
Comsol Multiphysics is tool for modeling and simulating engineering tasks. The problems we want to solve in real life are always based on multiphysics phenomena. Thus it's required to take into account interaction between two or more physics domains at one time. Comsol Multiphysics is defined for solving these complex problems [11].

In chemical modules you can find predefined physical interface for analysis of chemical reactions, transport of diluted species or species transport in porous media. Electrochemistry modules provide interface for design and simulation of battery or fuel cell life cycle. Comsol Multiphysics includes also option to model process of galvanization or corrosion [11].

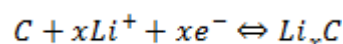
MatLab Simulink is a block diagram environment for multi-domain simulation and Model-Based Design. It supports system-level design, simulation, automatic code generation, and continuous test and verification of embedded systems [10].

Lithium-ion batteries are used as a primary and a secondary power source. This article focuses on the use of secondary sources of power. This type of batteries gains more and more importance due to their higher specific capacity, longer life and lower self-discharge compared with conventional batteries such as NiCd or NiMH. These properties are based on the use of lithium and intercalation materials from which the electrodes are formed. These substances are characterized by the ability to release and then incorporate lithium ions in their structure, thereby these batteries differ from the conventional ones, in which chemical conversion of anode and cathode material takes place. Another advantage is that these accumulators use only a small amount of electrolyte, which serves only as ion conductor, thus again goes to reducing the size of these batteries. The following equations describe the function of lithium-ion batteries. In these equations  $\text{LiMO}_2$  metal oxide is used as a cathode material such  $\text{LiCoO}_2$  or  $\text{LiNiO}_2$ . C is typically used as the anode material [2].

Reaction at the positive electrode of Li-Ion cells:



Reaction at the negative electrode of Li-Ion cells:



Summary reaction:

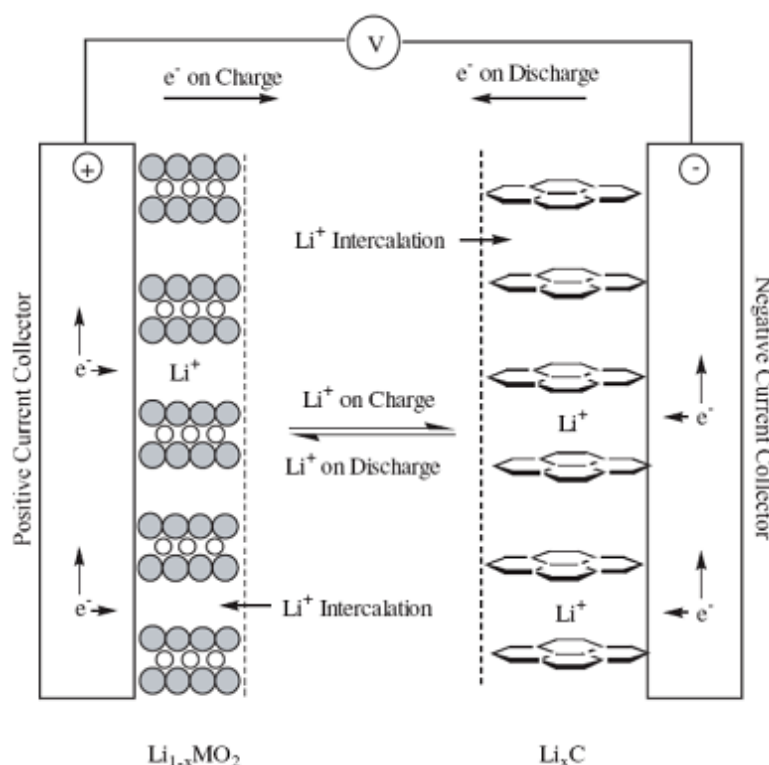
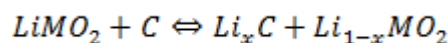


**Figure 1.** The principle of function of Li-ion accumulators [2].

Currently the most used material for positive electrode in lithium-ion cells is  $\text{LiCoO}_2$  and its modification. This type of material was used in the first commercial lithium-ion batteries made by Sony in 1991. It is a material with a layered structure, which voltage against lithium in pure form is 3.88V and capacity  $\sim 155\text{mAh/g}$ . Its disadvantage is worse temperature and cycling stability. A modification by using Ni is very common. Material  $\text{LiNi}_{1-x}\text{Co}_x\text{O}_2$  shows better stability and higher capacity than the default material, but it is slightly less thermally stable. The final properties depend on the content of Co. Specific capacity of the material is from  $190\text{mAh/g}$  to  $220\text{mAh/g}$ . Similarly voltage against lithium varies from 3.72 V to 3.78 V depending on the content of Co.  $\text{LiFePO}_4$  was created as its possible replacement. The first notes about the material  $\text{LiFePO}_4$  are dated from 1997.  $\text{LiFePO}_4$  material is the latest of a group of materials for lithium-ion cells and is characterized by olivine structure, high stability and shelf life. It is composed of ecological and cheap materials and shows the voltage 3.3 V versus lithium and capacity of  $170\text{mAh/g}$ . This material gradually begins to replace older types of cathode materials [1], [2].

The cylindrical cell continues to be one of the most widely used packaging styles for primary and secondary batteries. The advantages are ease of manufacture and good mechanical stability. The tubular cylinder has the ability to withstand internal pressures without deforming. Figure 2 shows a cross section of a cell [12].

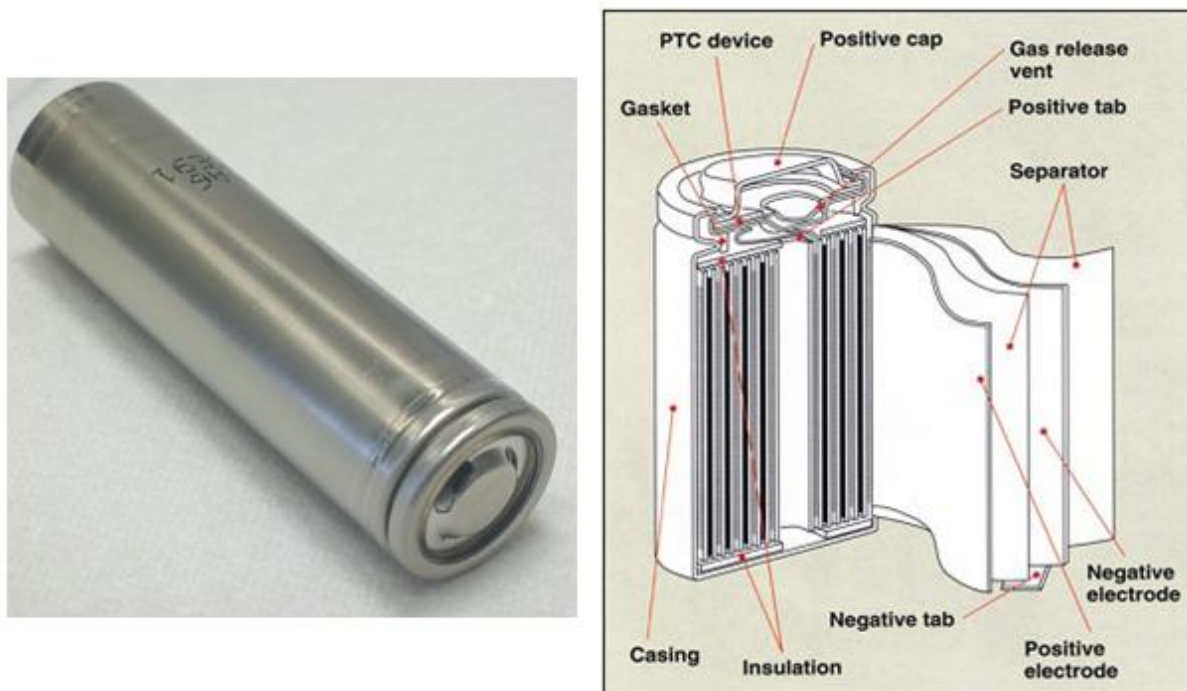


**Figure 2.** Cross section of a lithium-ion cylindrical cell [4].

A Samsung battery with capacity 3000mAh and a nominal voltage 3.7V was selected as the sample for real measurement.

The VMP3 potentiostat (Biologic) with attached VMP3B-20 booster was used for the measuring of discharge curves. The measurement procedure was set accordingly to the datasheet. Two discharging currents were selected - namely 0.2C and 0.5C. Charging was done using the CC-CV method. For the first measurement charging current was set to 0.2C (600mA) and the maximum charging potential was set to 4.2V. This was followed by CV charging until current dropped to 0.05C (150mA). Discharging was done by discharging current 0.2C (600mA), cut-off potential was set to 2.75V. Charging current for the second measurement was set to 0.5C (1500 mA) and the maximum charging potential was set to 4.2V. This was followed by CV charging until current dropped to 0.05C (150mA). After that discharging by discharging current 0.5C (1500 mA) was used. Cut-off potential was set to 2.75V.

### Conclusion

For the modelling of electro-chemical processes it is necessary to know their mathematical interpretation and how the simulation software proceeds during the solution. It is important to respect the geometry of the model and generated computational mesh. The quality of the computational mesh has the greatest influence on the actual computational time. The simulation will be more accurate if the computational mesh is finer and better quality.

### Acknowledgment

This work was supported by the grant CVVOZE CZ.1.05/2.1.00/01.0014 and by the specific graduate research of the Brno University of Technology No. FEKT-S-11-7

### References

1. D., Linden, T. B., Reddy, Handbook of Batteries. McGraw-Hill Prof Med/Tech, 2002 ISBN 0-07-135978-8.
2. P., Vyroubal, J., Maxa, J., Vondrák, T., Kazda, Modeling and Numerical Simulation of Lithium Ion Battery. In Advanced Batteries Accumulators and Fuel Cells - 13th ABAF Book of Proceedings. Brno: Brno University of Technology, 2012. p. 118-124. ISBN: 978-80-214-4610- 6.
3. W. A., Van Schalkwijk, B., Scrosati, Advances in Li-ion Batteries. Kluwer Academic, Plenum Publishers, NY, London, Moscow, 2002, ISBN 0-306-47356-9.
4. [http://batteryuniversity.com/learn/article/is\\_lithium\\_ion\\_the\\_ideal\\_battery](http://batteryuniversity.com/learn/article/is_lithium_ion_the_ideal_battery)
5. R., Spotnitz, J., Franklin, Abuse behavior of high-power, lithium-ion cells. Journal of Power Sources, 2003. 113(1): p. 81-100.
6. M. A., Colclasure, R. J., Kee, Thermodynamically consistent modeling of elementary electrochemistry in lithium-ion batteries, Electro-chemica Acta, Volume 55, Issue 28, 1 December 2010, Pages 8960–8973.
7. <http://www.comsol.com/products/batteries-fuel-cells/>
8. <http://www.humusoft.cz/produkty/comsol/>
9. L., Cai, R. E., White, Mathematical modeling of a lithium ion battery with thermal effects in COMSOL Inc. Multiphysics (MP) software. Journal of Power Sources. 2011, Volume 196.
10. <http://www.comsol.com/products/multiphysics/>
11. <http://www.humusoft.cz/produkty/comsol/>
12. [http://batteryuniversity.com/learn/article/types\\_of\\_battery\\_cells](http://batteryuniversity.com/learn/article/types_of_battery_cells)

## **Analysis of using the air for solar panel cooling with ANSYS system**

Maxa, J.<sup>1</sup>, Vyroubal, P.<sup>1</sup>, Vaněk, J.<sup>1</sup>, Hladká, K.<sup>1</sup>

<sup>1</sup>Department of Electrical and Electronic Technology, Faculty of Electrical Engineering and Communication, BUT, Technická 10, 616 00 Brno, Czech Republic

### **Introduction**

Photovoltaic concentrators are systems which use lenses or mirrors to concentrate sunlight on the photovoltaic cell.

The reason for their use is to reduce the size of the cell in order to achieve the desired performance. It is also possible to use more powerful photovoltaic cells, which would have been without using a concentrator too expensive in relation to the generating output. Concentration of solar radiation also causes disadvantages associated with greater warming [1]. Light radiation is converted into electrical energy only partially, the remaining greater part is converted into thermal energy. Provided that the heat with additional cooling components is removed, it can occur in systems with high concentration the total destruction [2].

The temperature has a significant impact on the position of the operating point. At high temperatures there is a change in the electrical properties of the cell, which leads to a reduction in terminal voltage. A decrease in the temperature in terminal voltage will reduce the power supplied to the load [3].

The most useful cooling medium from the aspect of price and upkeep is the air. The air has got a lower ability for the heat dissipation which is its disadvantage against the cooling liquids.

The Ansys Fluent system with the setting of transient analysis of the convection of cooling medium and the heat transfer in combination of convection, conduction and radiation was used to the analysis. The Discrete Ordinates module including a fluid area had been used as the radiation module.

The first results show a possibility of cooling down a solar panel under 100 °C (Fig. 1), when the temperature limit is 120° C.

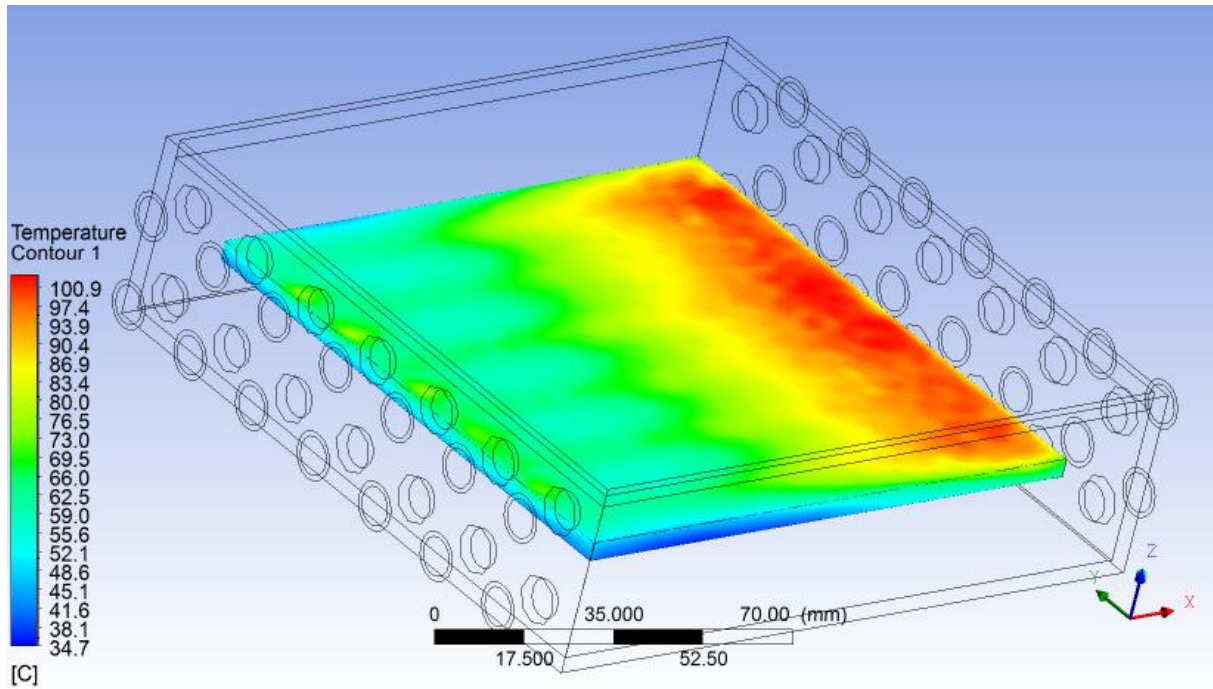


**Figure 1.** The temperature field displaying.

During next optimization of the cooling cabinet will be necessary to focus on the upper distant part of the panel (Fig.2).

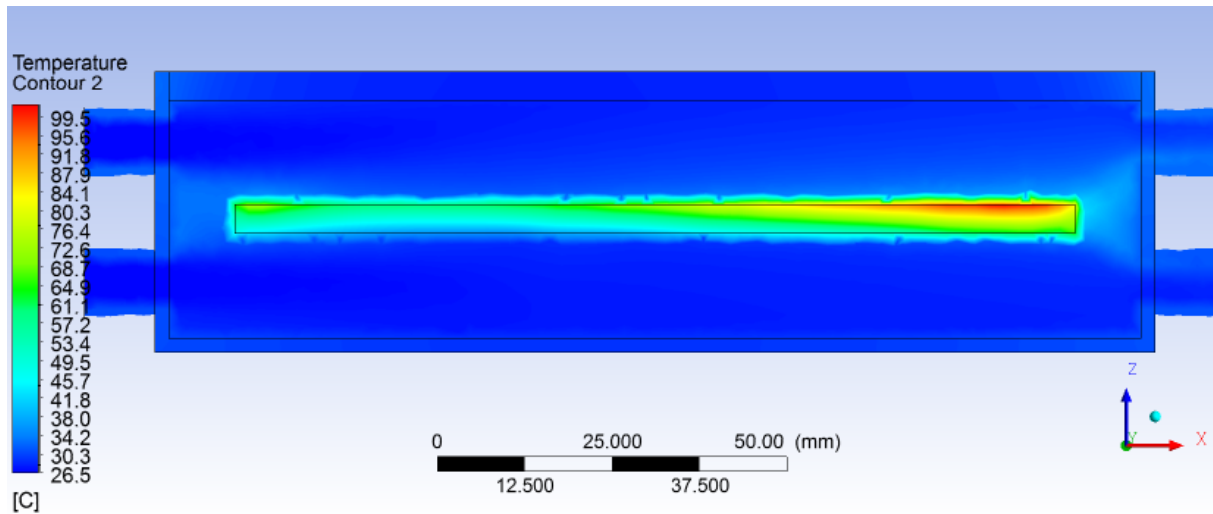


**Figure 2.** The temperature field displaying.

The image of vector field of speed of the medium demonstrates, that it is necessary to choose the conception of the cooling cabinet in such way that leads to a steady speed flow for cooling down even the distant parts of the panel. It will regard the reduction of whirls and the optimization of outlet of the cooling medium.

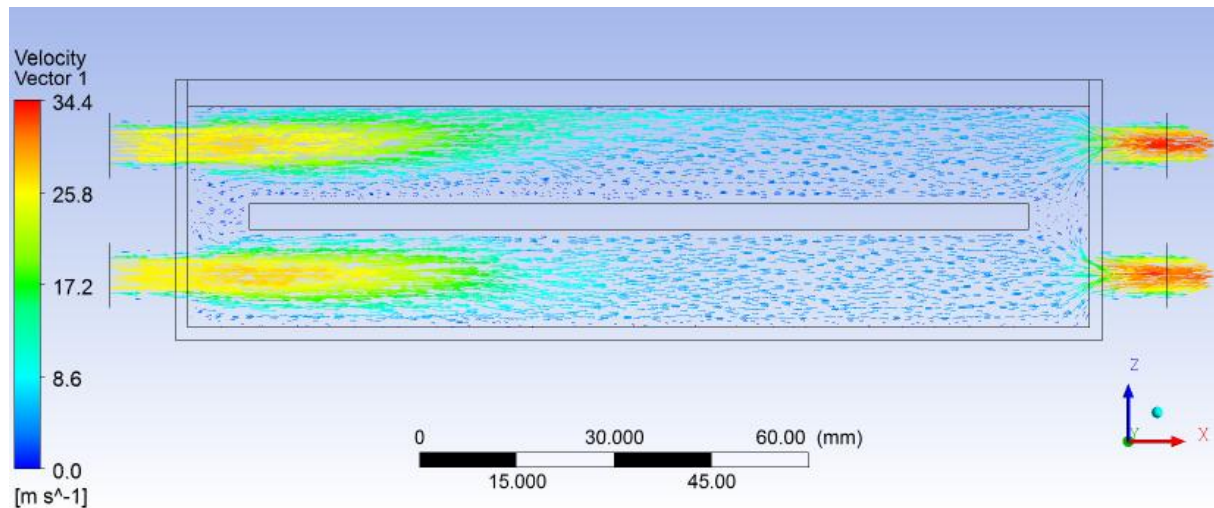


**Figure 3.** The vector image of the speed field.

### Conclusion

The first analysis with help of ANSYS Fluent system proved a theoretical possibility of using the air as a cooling medium, but there is big entitled to the optimization of the cooling cabinet's construction there. Above all it will be about an optimization of the cooling medium's outlet from the cooling cabinet so that it would reduce the formation of whirls in the distant part of the solar panel and the high outlet speed because of the pressure increase in front of the orifices (output slots).

### Acknowledgment

This work was supported by the grant CVVOZE CZ.1.05/2.1.00/01.0014 and by the specific graduate research of the Brno University of Technology No. FEKT-S-11-7

### References

1. DUFFIE, J., BECKMAN, A., WILLIAM A. Solar engineering of thermal processes. *University of Wisconsin. New York, Wiley-Interscience, 1980. 775 p.* New York, 2006
2. VESELÝ, A., VANĚK, J., STOJAN, R. Concentrator Photovoltaic Systems. *ECS Transactions.* 2012. 40(1). p. 161 - 165. ISSN 1938-5862.
3. SOLČANSKÝ, M., VANĚK, J. Influence of quinhydrone concentration on chemical passivation in solar cell technology. In *Elektrotechnika a informatika 2010 - elektrotechnika.* Nečtiny: 2010. p. 1-4. ISBN: 978-80-7043-913- 5.

## Energy Storage: From Hybrid Devices to Hybrid Materials

Gómez-Romero, P. <sup>1,2</sup>,

<sup>1</sup>Centro de Investigación en Nanociencia y Nanotecnología, CIN2, ICN2 (CSIC-ICN), Campus UAB, E-08193 Bellaterra, Barcelona, Spain.

<sup>2</sup>MATGAS Research Center, Campus UAB, E-08193 Bellaterra, Barcelona, Spain.

The end of cheap oil and the compulsion for energy security are decisively adding to climate change concerns to finally boost a long overdue change towards a sustainable model of generation and consumption of energy. In this new model, energy storage will be a key player and a wide variety of energy storage devices and approaches are being reinstated as R+D priorities, from thermal energy storage to redox flow batteries to Li batteries to supercapacitors. The latter two are in a continuous race to increase their power and energy densities respectively (at lower and lower costs) in order to improve their chances to play a central role in a variety of emerging markets, and especially in the Electric Vehicle sector. Yet, the track along the diagonal of the Ragone Plot (Figure 1) is no easy feat.

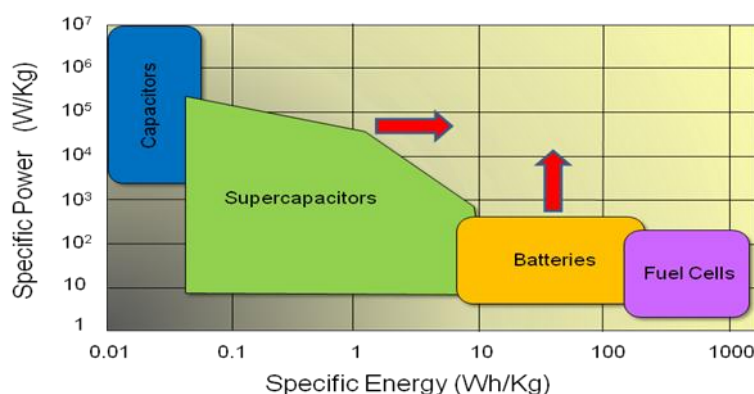


**Figure 1** Ragone plot showing a qualitative landscape of electrochemical (batteries, fuel cells) versus electrophysical (capacitors) energy storage devices. Forefront research on Li batteries, for instance, aims at fast-charging high power and low cost devices, whereas electrochemical supercapacitors represent a new hybrid land but still in need of (energy) improvement.

The hybrid approach constitutes a very valuable tool to get the best properties of different materials or components integrated in a synergic device. There are many levels at which hybridization can take place: device, electrode, or material. A recent review by Cericola and Kötz[1] makes a systematic analysis of the different possibilities, including the consideration of series or parallel coupling of individual devices. Yet, the widest field for improvement rests at the materials design landscape. Hybrid materials allow for synergic combinations which we will analyze in this presentation, with emphasis on, though not limited to our work on asymmetric and hybrid supercapacitors[2,3] and nanocomposite electrodes for batteries.[4] Efforts to design complex materials allowing for fast-charging Li batteries and high-energy density supercapacitors are converging at the nanoscale with chemically and functionally hybrid combinations in an approach which is just beginning to show its potential.[5]

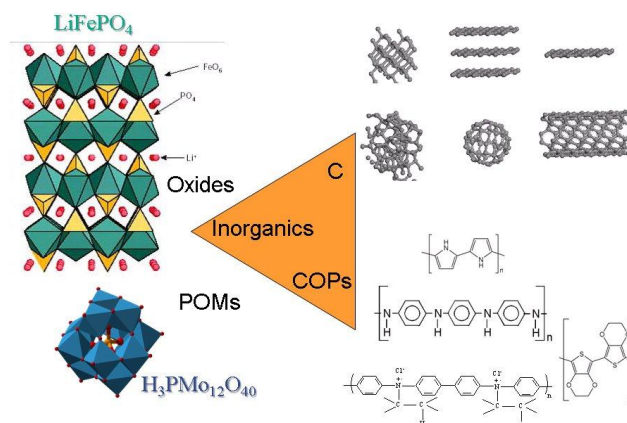


**Figure 2** Schematic view of our main components for the design of electroactive hybrid materials: Inorganics, from oxides to phosphates to polyoxometalate clusters, carbon materials and conducting organic polymers (COPs).

In our group we have developed a whole line of work dealing with the prospective research of hybrid combinations of electroactive and conductive materials for energy storage applications. Among electroactive components we have used a wide variety of inorganic species, from oxides (or phosphate) [4] to polyoxometalate (POM) clusters,[3] but also conducting organic polymers (COPs) or carbon materials (See Figure 2), the later two also providing suitable conducting properties. As a matter of fact we have prepared hybrids along the three sides of the triangle shown, [3-4, 6-8] as will be discussed in this presentation.

## References

1. D. Cericola, R. Koetz, *Electrochimica Acta*, **2012**, 72, 1-17
2. P. Gomez-Romero, O. Ayyad, J. Suarez-Guevara and D. Muñoz-Rojas, *J. Solid State Electrochem.* **2010**, 14(11), 1939-45,
3. V. Ruiz, J. Suárez-Guevara, P. Gomez-Romero, *Electrochem. Commun.* **2012**, 24, 35-38 .
4. A. Fedorkova, A. Nacher-Alejos, P. Gomez-Romero, R. Orinakova, D. Kaniansky. *Electrochimica Acta.* **2010**, 55(3), 943-947.
5. P. Gomez-Romero, V. Ruiz, O. Ayyad , sent to *Chem. Soc. Rev.*
6. J. Vaillant, M. Lira-Cantu, K. Cuentas-Gallegos, N. Casañ-Pastor and P. Gómez-Romero *Progress in Solid State Chemistry*, **2006**, 34, 147-159.
7. M. Baibarac and P. Gómez-Romero, *Journal of Nanoscience and Nanotechnology*, 6(2) **2006**, 289-302.
8. M. Baibarac, M. Lira-Cantú, J. Oró Solé, N. Casañ-Pastor and P. Gomez-Romero *Small* **2006**, 2(8-9), 1075-1082.

## Electrocatalysis at nanoparticles and nanostructured surfaces

Oriňáková, R. \*, Škantárová, L., Filkusová, M., Oriňák, A.

Department of Physical Chemistry, Institute of Chemistry, Faculty of Science,  
P.J. Šafárik University, Moyzesova 11, SK-041 54 Košice, Slovak Republic

\*Corresponding author. Tel.: +421 55 2342328; fax: +421 55 6222124.

E-mail address: Renata.Orinakova@upjs.sk

Hydrogen as the cleanest and ideal energy carrier for the transition to a “hydrogen based economy” has been increasingly considered as the fuel of the future [1, 2]. The most desirable source of hydrogen is water. Electrochemical production of hydrogen from water or “hydrogen evolution reaction” (HER) is one of the most promising methods where the pure hydrogen can be supplied by environmentally friendly energy sources, without evolution of the green-house gas [3, 4]. Electrochemical systems, such as fuel cell and water splitting devices, represent some of the most efficient and environmentally friendly technologies for energy conversion and storage.

The main operating cost of the hydrogen evolution is the cost of electricity. Hence, research and development efforts have been recently focused on the minimizing ohmic resistance, lowering overpotential through improving cell and electrode design and using electrode material with higher electrocatalytic activity [3].

Two properties play an important role in selecting the catalytically active materials for the HER: the actual electrocatalytic effect of the material, which is directly dependent on the overpotential used to operate the electrolytic cell at significant current densities and the catalyst stability. A required decrease in overpotential can be acquired by selecting of an electrode material of a high intrinsic catalytic activity for the HER and/or by increasing the active surface area of the electrode [2, 4].

Today, the most efficient HER catalysts are those made from platinum-group metals, but these are expensive. It remains challenging to develop highly active HER catalysts based on materials that are more abundant at lower costs. Effective electrocatalysts are now routinely prepared by the modification of conducting polymers by electrodeposition and dispersion of catalyst particles on a preformed polymer [2, 5] or by incorporation of metal crystals or crystal aggregates in conducting polymer films during monomer polymerization [6, 7].

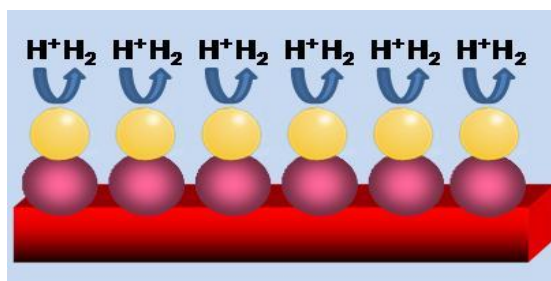


**Figure 1.** HER on nanostructured catalyst surface.

The current generated at an electrode is proportional to the active surface of catalyst on the electrode surface (Fig. 1), so higher power density fuel cells can be formed from nanomaterials, because nanomaterials have a higher surface area to volume ratio. The applications of highly active nanomaterials in the field of catalysis for fuel cells reactions such as methanol oxidation and

hydrogen and oxygen evolution reactions have attracted the attention of many scientific researchers and became one of the most important topics. The electrocatalytic activity and the stability of the nanomaterials during the course of a reaction are a concern for nearly all electrodes. Recently, shape-control of the nanoparticles has become an imperative task due to the fact that most of the reactions in fuel cells are sensitive to the surface structure of the catalysts.

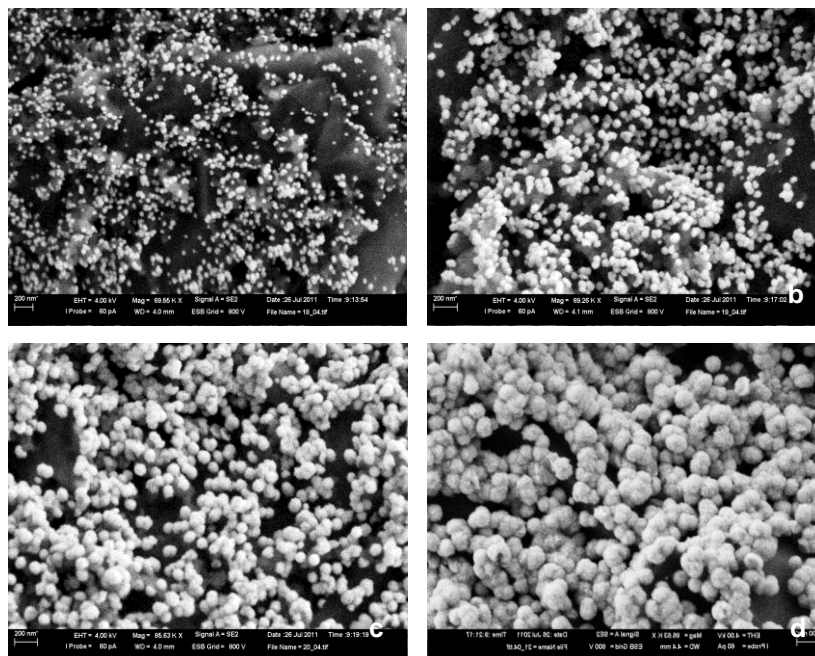


**Figure 2.** Electrocatalytic active nickel nanoparticles for HER electrodeposited on the electrode surface at potential  $-2.0$  V with different deposition time: a) 5s, b) 10s, c) 30s, d) 50s.

Electrocatalysts play key roles in the chemical processes but often limit the performance of the entire systems due to insufficient activity, lifetime, or high cost. It has been a long-standing challenge to develop efficient and durable electrocatalysts at low cost. The scope of our work includes the use of the electrochemically deposited nickel (Fig. 2) and silver particles, in the submicro/nano scale and nanostructured layers, as catalysts for hydrogen evolution reaction. The electrocatalytic activity of such catalysts can be enhanced by the use of conducting polymers as substrates.

### Acknowledgments

The authors wish to acknowledge the financial support from the Grant Agency of Ministry of Education of the Slovak Republic (Grant No. 1/0211/12).

### References

1. R. Aydin, F. Köleli, *Progr. Org. Coat.*, **56**, 76 (2006).
2. E. Navarro-Flores, S. Omanovic, *J. Mol. Catal. A: Chem.*, **242**, 182 (2005).
3. X. Mo, J. Wang, Z. Wang, S. Wang, *Synth. Met.*, **142**, 217 (2004).
4. P.R. Zabinski, R. Kowalik, M. Piwowarczyk, *Arch. Metall. Mater.*, **52**, 627 (2007).
5. V.M. Jovanovic, S. Terzic, A. Dekanski, *J. Serb. Chem. Soc.*, **70**, 41 (2005).
6. K. Bouzek, K.M. Mangold, K. Juttner, *Electrochim. Acta*, **46**, 661 (2000).
7. Z. Peng, E. Wang, S. Dong, *Electrochem. Commun.*, **4**, 210 (2002).

## Nanofibrous $\text{Li}_4\text{Ti}_5\text{O}_{12}$ prepared by centrifugal force spinning and its lithium insertion properties

Cech, O., Moravkova, J., Sedlarikova, M., Vondrak, J.

<sup>1</sup>Faculty of Electrical Engineering and Communication, Department of Electrical and Electronic Technology, Brno University of Technology

<sup>2</sup>Pardam s.r.o., Pardubice, Czech Republic

Interest in ceramic materials as active electrode materials for lithium-ion batteries has been increased during past decade. Especially  $\text{Li}_4\text{Ti}_5\text{O}_{12}$  has attracted a lot of attention as an anode material because of its high capacity, very good lithium ion intercalation and deintercalation reversibility and mainly its stability during deep cycling and cycling with high rates.[2] Very low volume changes during cycling, absence of SEI layer and electrolyte decomposition should be also mentioned. Spinel  $\text{Li}_4\text{Ti}_5\text{O}_{12}$  material has a discharge plateau at 1.55V which is high enough to avoid electrolyte decomposition and low enough to be usable together with some of high voltage cathodes based on  $\text{LiCoO}_2$  or  $\text{LiMnO}_4$ .

Despite of all mentioned positive characteristics, pure titanate materials suffer by poor intrinsic electronic conductivity and low  $\text{Li}^+$  diffusion coefficient[4], which limits the practical use of this material.

There are many approaches to improve the properties of ceramic electrode materials. Nanoscaling of its structure can improve diffusion of  $\text{Li}^+$  ions due to shorter diffusion pathways[1; 2] and  $\text{Li}_4\text{Ti}_5\text{O}_{12}$  nanoparticles, nanotubes, nanowires and nanosheets were successfully prepared and tested. With decrease of particle size, the capacity loss may increase due to higher specific surface area[3]. Several strategies have been taken in order to improve the low electronic conductivity of intrinsic  $\text{Li}_4\text{Ti}_5\text{O}_{12}$ , including mixing with conductive carbons, coating by different conductive compounds (carbons, conductive polymers, and conductive ceramic materials), incorporating a conducting second phase and doping with anti-valent metal ions such. Another successful method is treating the material in reduced or low-oxygen partial pressure atmosphere.

The centrifugal force spinning is a simple and effective method for preparation of micro and nanoscale fibers. It allows producing not only polymer, but also metallic and ceramic nanofibres. Its composition often depends on the post-processing treatment.

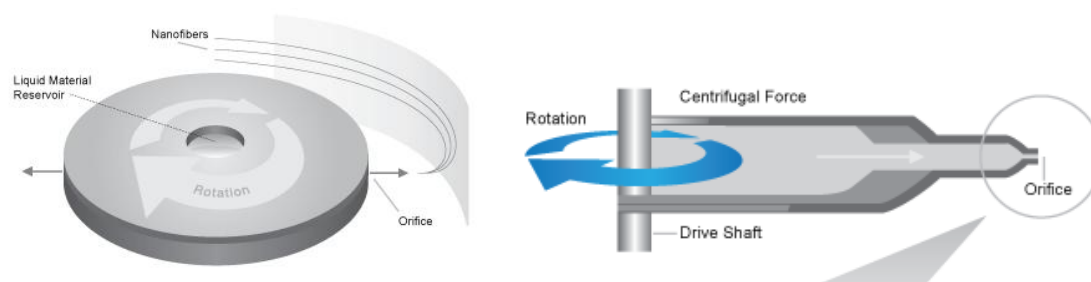


**Figure 1.** The principle of centrifugal force spinning. Scheme of spinning head.

In lab scale, centrifugal force spinning when comparing with electrospinning needs less parameters to control and thus is more straightforward and can be much faster than electrospinning. Due to effect of centrifugal force, the liquid polymeric solution is pressed from rotating spinning head through thin nozzles, stretched and dried in turbulent flowing air.

In this study, we would like to introduce a novel method of preparation nanofibrous ceramic  $\text{Li}_4\text{Ti}_5\text{O}_{12}$  via centrifugal force spinning method and show its electrochemical properties. Electrochemical characterization via cyclic voltammetry, charge-discharge cycling and impedance spectroscopy will be made and structural characterization by SEM, EDS and XRD will be provided.

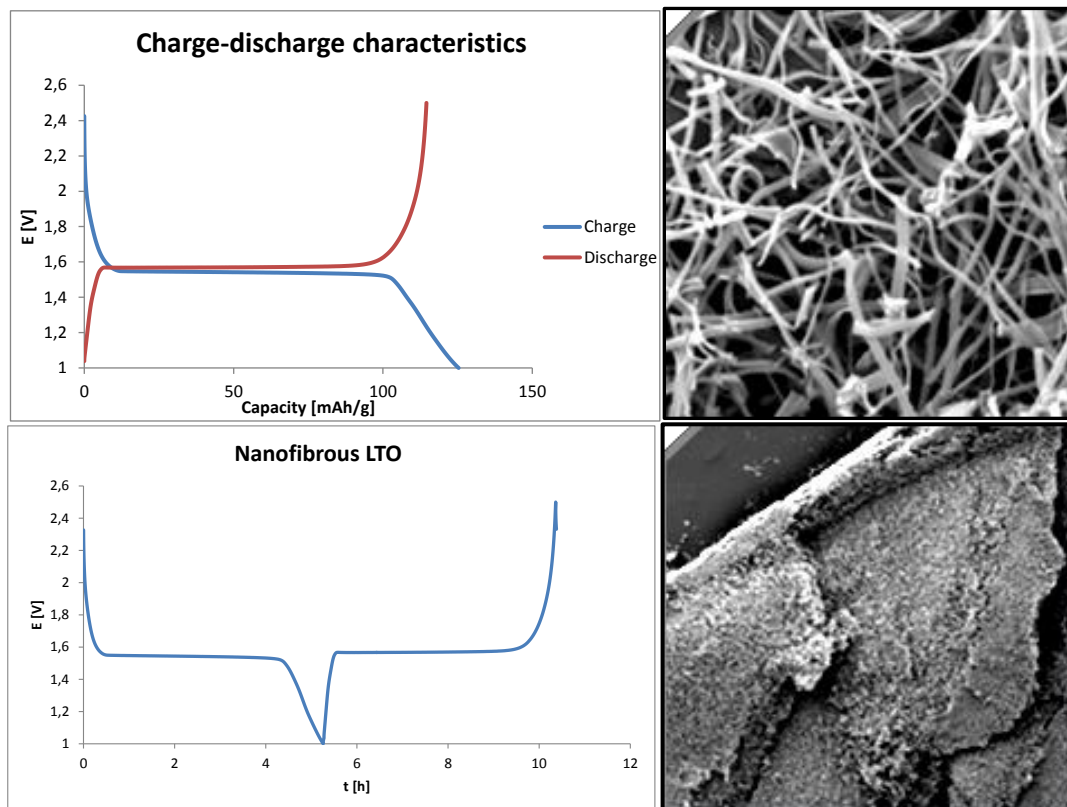


**Figure 2.** Charge-Discharge characteristics and structure of nanofibrous  $\text{Li}_4\text{Ti}_5\text{O}_{12}$

### Acknowledgments

This work was made due to support of CVVOZE CZ.1.05/2.1.00/01.0014 and grant FEKT-S-11-7.

### References

1. FANG, W. Nano- $\text{Li}_4\text{Ti}_5\text{O}_{12}$  Pore Microspheres: A High Power Electrode Material for Lithium Ion Batteries 2012.
2. FERGUS, J.W. Recent developments in cathode materials for lithium ion batteries. *Journal of Power Sources*, 2010, vol. 195, no. 4, p. 939-954.
3. GUO, B., LI, Y., YAO, Y., LIN, Z., JI, L., XU, G., LIANG, Y., SHI, Q. AND ZHANG, X. Electrospun  $\text{Li}_4\text{Ti}_5\text{O}_{12}/\text{C}$  composites for lithium-ion batteries with high rate performance. *Solid State Ionics*, 2011, vol. 204-205, p. 61-65.
4. LI, B. Synthesis and Characterization of Long Life  $\text{Li}_4\text{Ti}_5\text{O}_{12}/\text{C}$  Composite Using Amorphous  $\text{TiO}_2$  Nanoparticles 2011.

## Advanced materials for PEM water electrolysis

Polonský, J., Hnát, J., Paidar, M., Bouzek, K.

Department of Inorganic Technology, Faculty of Chemical Technology, Institute of Chemical Technology Prague, Technická 5, 166 28 Prague, Czech Republic

Hydrogen can be used to store substantial amounts of chemical energy. This energy can be converted to electricity in fuel cells or other suitable devices. The process of storing energy in hydrogen is usually achieved by water electrolysis. This cycle of electrical-chemical-electrical energy conversion is the core principle of a concept known as the *Hydrogen economy*. Vehicles, portable devices, uninterruptible power sources or large-scale energy storage systems are all examples where hydrogen can be used (1).

Alkaline route of water electrolysis represents technology established in industry already for decades. It utilizes concentrated potassium hydroxide solution as the electrolyte and the electrodes are based mainly on nickel. An alternative process is the polymer electrolyte membrane (PEM) water electrolysis (2). It offers several advantages over the conventional alkaline process: i) the interelectrode distance can be lower due to the zero gap design, increasing the process efficiency; ii) the current density can be higher, increasing the process intensity and iii) there is no corrosive liquid electrolyte, simplifying construction. Although more progressive than the alkaline process, the PEM water electrolysis is not yet widely employed industrially, because it has some still unresolved issues: The PEM water electrolyser (PEMWE) requires precious-metal catalysts on both its electrodes (3) and an expensive polymer electrolyte membrane. Although the efficiency is higher than in the alkaline process, the higher capital costs and durability issues prohibit a more-widespread application of this technology.

We focused on improving the anode of the PEMWE as one of the most challenging part of the system. Unlike in the PEM fuel cells, the anode in PEMWE is subjected to highly oxidative and acidic environment, where only very few materials can endure for sufficiently long time. The most commonly used materials for PEMWE's anode are titanium felt for the body of the electrode and iridium dioxide as the catalyst. The iridium dioxide is deposited onto the titanium felt by a spraying of a catalytic ink including besides the catalyst also a certain amount of bonding ionomer, most commonly Nafion. Because titanium felt is inherently porous, a substantial amount of the small catalyst particles penetrate deep into the electrode structure and thus have inferior contact with the membrane. Because only those particles in contact with both the membrane and the felt can be utilised in the reaction, a way to keep the particles on top of the felt is needed (4, 5). The common approach in PEM fuel cells is to make use of a microporous layer between the bulk electrode and the catalyst layer. Carbon-based microporous layers are routinely used in PEM fuel cells. But this solution is not suitable for application in a PEMWEs technology. It is because carbon in the anode would corrode quickly under the conditions of the electrode reaction.

We have synthesized two conductive ceramic materials that could be used for such an intermediate layer formation, namely titanium suboxides (6) and antimony-doped tin oxide (ATO) (7). Titanium suboxides is a group of conductive ceramic materials with a general formula  $Ti_xO_{2x-1}$ , where  $x = 4-9$ . Our in-house material consisted predominantly of the most conductive suboxide –  $Ti_4O_7$ . Antimony-doped tin oxide is a conductive ceramic material being currently researched for use in low and medium temperature PEM technology. It is very stable in oxidative environment and highly conductive. Both in-house ATO and a commercial ATO (Alfa Aesar) were studied. The materials were characterised using X-ray diffraction, scanning electron microscopy and

conductivity measurement. Subsequently, microporous layers were prepared (Figure 1) and their properties assessed.

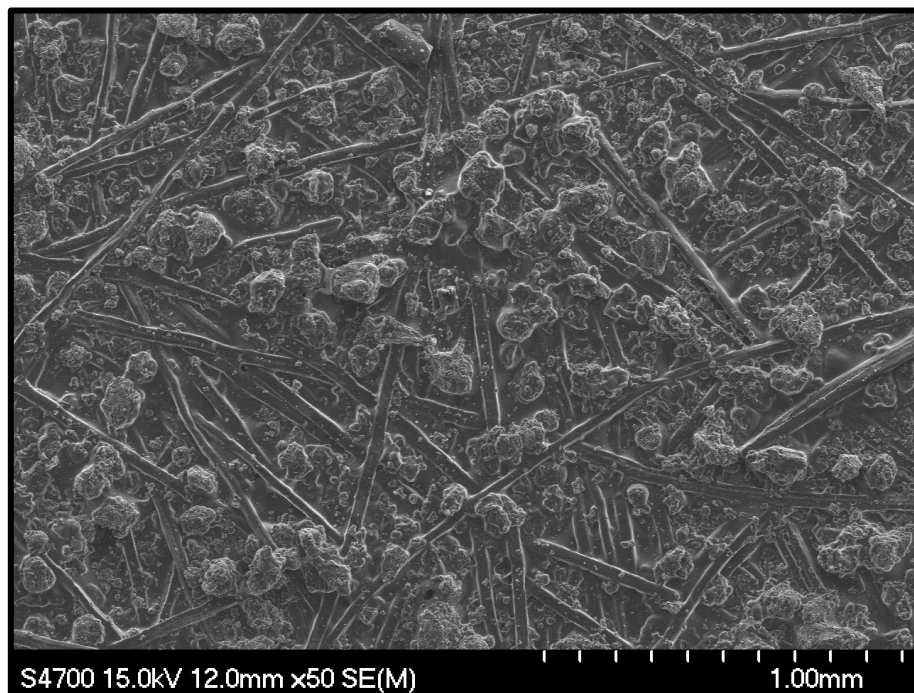


**Figure 1.** Scanning electron micrograph of a titanium felt anode with a microporous layer ( $Ti_4O_7$ , 63–125  $\mu\text{m}$ ).

The microporous layer could vastly enhance catalyst utilization and thus decrease the capital costs of PEMWEs, bringing this technology closer to a more-widespread application.

### Acknowledgements

Financial support from specific university research (MSMT No 21/2013) is gratefully acknowledged.

### References

1. M. F. Mathias, R. Makharia, H. A. Gasteiger et al., *Electrochem. Soc. Interface*, **14**, 24–35 (2005).
2. M. Carmo, D. L. Fritz, J. Mergel, D. Stolten, *Int. J. Hydrogen Energy*, **38**, 4901–4934 (2013).
3. P. Millet, N. Mbemba, S. A. Grigoriev, V. N. Fateev, A. Aukauloo, C. Etiévant, *Int. J. Hydrogen Energy*, **36**, 4134–4142 (2011).
4. J. Polonský, I. M. Petrushina, E. Christensen et al., *Int. J. Hydrogen Energy*, **37**, 2173–2181 (2012).
5. P. Mazúr, J. Polonský, M. Paidar, K. Bouzek, *Int. J. Hydrogen Energy*, **37**, 12081–12088 (2012).
6. S. Siracusano, V. Baglio, C. D'Urso, V. Antonucci, A. S. Aricò, *Electrochim. Acta*, **54**, 6292–6299 (2009).
7. J. Xu, Q. Li, M. K. Hansen et al., *Int. J. Hydrogen Energy*, **37**, 18629–18640 (2012).

## **Nanofibrous composite materials and their utilization potential for the electrochemical applications**

Komárek, M.

Laboratory of nanomaterial applications; Center for the Nanomaterials, Advanced Technologies and Innovation

Technical University of Liberec, Studentská 2, 461 17 Liberec, Czech Republic

[michal.komarek@tul.cz](mailto:michal.komarek@tul.cz), +420485353819

### **Abstract**

The aim of the publication is to introduce the scope of the research activities focused on the preparation, functionalization and the final applications of the nanofibrous materials at the Technical university of Liberec. Various types of the nanofibrous composite materials developed for the different final applications, such as filtration, catalysis, or the water cleaning are promising to show the application potential in the electrochemical systems, e.g. dye sensitized solar cells, battery electrodes and separators, fuel cells and supercapacitors. The elementary improvement of the state of the art technologies can be seen in the nanostructuring of the functional elements, especially electrodes. Benefits of such structuring are the increase of the reaction surface area, relative mechanical stability and the versatility of the modification possibilities.

### **Technologies for the nanofiber production**

Various methods of the nanofiber preparation were published in the scientific publications and patents over the last decades [1], [2], [3]. The most renowned methods include the template synthesis [4], drawing [5], self-assembly [6], [7], phase separation, spinning of the “island in the sea” fibers with subsequent dissolution of the matrix, melt-blown fibers prepared by the extremely fine orifices [8], centrifugal spinning [9] and the electrospinning. The melt-blown, centrifugal spinning and electrospinning has reached the commercial production levels for the preparation of the organic and inorganic nanofibrous layers [10].

### **Electrospinning technology**

The electrospinning process is a method of fine fiber preparation based on the application of the electrostatic field on the liquid containing the macromolecular component. In the general concept the effect can be explained as the encounter between the electrostatic force (pressure) and the capillary force (pressure), see the fig. 1 left. The fiber creation is usually divided into four regions when the process's physics is being described. The Taylor cone is the region associated with the onset of the electrohydrodynamic atomization. The study of the jet thinning in the stable region was studied by [11]. The instability region is important part of the nanofiber creation,

because in this part the most of the solvent evaporates and the fiber diameter decreases substantially [12]. The detailed description of the physics behind the electrostatic spinning can be found in [13].

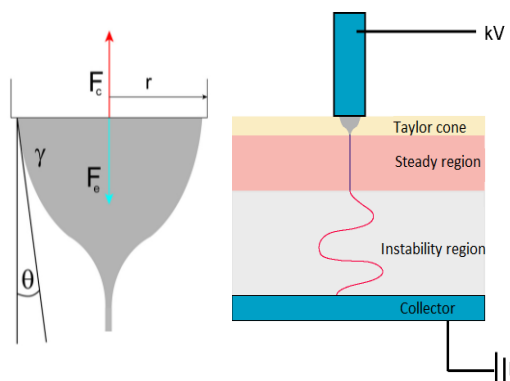


**Figure 1.** General description of the electrostatic nanofiber preparation process

The electrospinning method has been promoted into the industrial scale process mainly by the invention of the needleless roller based process [14]. This process has been further developed by the Elmarco co. under the “Nanospider” trademark.

### Chemical composition of the electrospun materials

The electrospun nanofibers are produced prevalently from the polymeric solutions. Therefore the prepared nanofibers are mainly made of the organic polymers. This category includes the natural polymers, synthetic polymers and polymer blends. Nanofiber layers from the natural polymers such as gelatin, chitosan, collagen, cellulose etc. are prepared frequently for the biochemical or medical applications [15]. The group of synthetic polymers include the polyamides, polyimides, polyurethanes, polyacrylonitrile, fluorinated polymers e.g. polyvinylidene fluoride, polyvinylalcohol and many others. The used polymer type is selected in accordance with the desired application. The special type of the nanofibers are materials prepared by the electrospinning of polymer melts [16], [17]. The advantage of the melt-electrospun materials is the ability to process thermoplastic polymers which have the substantial resistibility to solvents, e.g. polyethylene and polypropylene. Another specialty is the group of the inorganic nanofibrous materials prepared by the spinning of the suitable precursor, i.e. dispersion of the inorganic particles in the polymer solution. After the spinning process, the material is calcinated in the high temperature furnaces in order to remove the organic part of the fiber and sinter the inorganic part [18].

### Morphology types of the nanofiber products

The most common nanofiber structure is the nanofiber web with the non-oriented fiber distribution. The example of can be seen on the fig. 2. On the same figure are shown the possible irregularities of the nanofibrous layers. These defects include beaded fibers, fiber bunches, holes in the layer and irregular thickness of the layer. Special morphologies include the aligned anisotropic layers [19], porous nanofibers [20], nanofiber containing yarns [21], core-shell nanofibers [22] and hollow nanofibers [23].

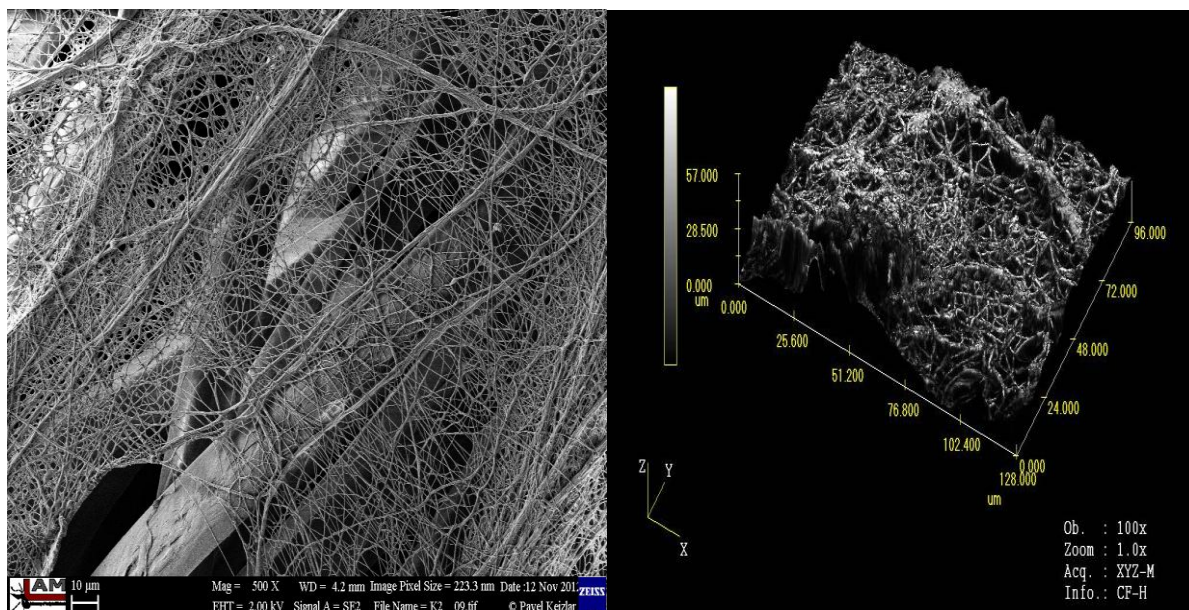


**Figure 2.** SEM comparison of the nanofibers and standard fibers (left), irregularities in the nanofiber layer thickness (right)

### Modifications (functionalization) of the nanofibers

In many application fields the nanofibrous layers work as the active substance carrier. An example could be the medical field, where the nanofibers are studied as the drug delivery material. On the fig. 3 the application of the thermally resistant polyimide nanofibers as a carrier of the combined heterogeneous catalyst particles is shown. The left part of the figure shows the particles immobilized in the nanofiber mass. The particles are observable only as small bulges on the nanofiber surface. On the right part of the picture, the same catalyst particles are immobilized on the top of the nanofibers.

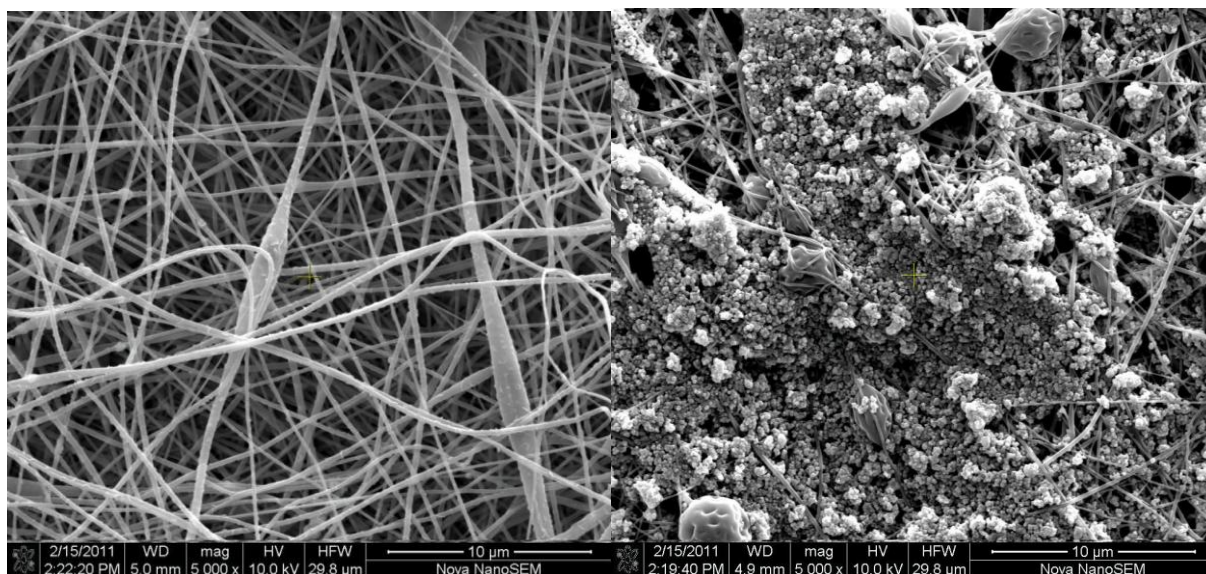


**Figure 3.** Nanofibers with immobilized catalyst particles

The figure 4 shows the organic nanofibers covered with the homogenous layer of inorganic  $\text{TiO}_2$  layer. The layer was prepared for the photo-catalytic application and in this case is well observable, because the sol tends to seal the inter fiber areas. By the precise variation of the sol parameters it is possible to obtain the nanofibrous layer perfectly coated by the inorganic material. Such type of material could be potentially utilized in the electrochemical applications, especially in the dye sensitized solar cells [24].

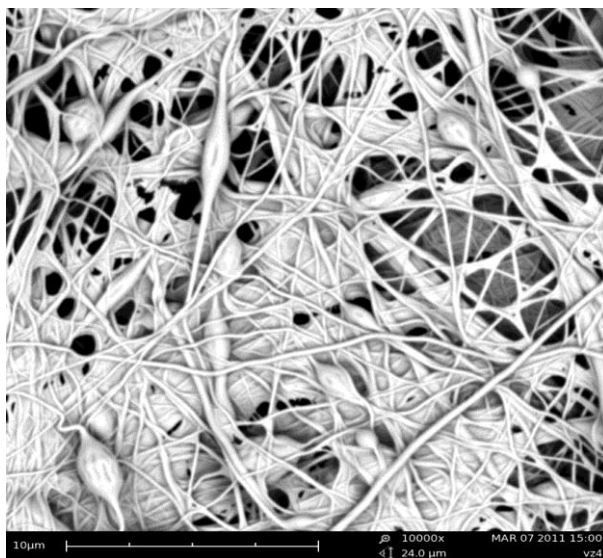


**Figure 4.** The nanofibers covered with the  $\text{TiO}_2$  sol-gel layer

### Electrochemical applications of nanofibers

Nanofiber materials are currently finding their way also in the electrochemical applications. The most straightforward application is the utilization of nanofibrous layers as battery separators in the lithium ion batteries. Typical polymers in this category are polyimides and fluorinated polymers, e.g. PVDF. The main advantages of the nanofibrous separators are the lower thermal shrinkage, higher mechanical strength and higher ionic conductivity at higher temperatures compared to the standard polypropylene or polyethylene separators. These properties implicate the stable charge-discharge profiles and overall electrochemical performance of the battery cell [25], [26], [27]. The nanofibrous materials found the application potential in the electrodes of the electrochemical devices. In the case of the lithium batteries the carbon nanofibers (CNF) doped with the lithium salts. Compared with commercial graphite, PAN/PPy bicomponent-based carbon nanofibers have improved electrochemical performance, especially high capacities. In addition, these fibrous structures carbonaceous materials also can alleviate the large structural changes and accommodate the strains related to the large transformation upon charge/discharge processes. As a result, relatively good electrochemical performance, such as large reversible capacity, improved cycle ability, and good rate capability, can be obtained [28]. In several works also the carbon – silica [29] and carbon-titanium [18] nanofibrous composites are studied for the battery anodes. The silicon coating of the surfaces of a hollow carbon nanofiber improves the capacity of the Si/CNF composite during cycling. The hollow core of the CNF effectively moderates the degradation of the Si negative electrode [29].

The similar function i.e. increase of the specific surface and improvement of the mechanical stability is utilized in the electrodes of the fuel cells [30] and supercapacitors [31]. The PAN/Au/PVDF materials shown a specific capacitance of  $235 \text{ F g}^{-1}$  and discharge capacitance of

245 F g<sup>-1</sup> at 100 mV s<sup>-1</sup> [32]. Carbon nanofibers composites prepared from PAN/V<sub>2</sub>O<sub>5</sub> in an aqueous electrolyte, exhibited a promising energy density of 18.8 Wh kg<sup>-1</sup> [33]. Simultaneously this type of materials exhibited excellent capacity retention.

The important research is being conducted also in the photovoltaic applications, especially the dye sensitized solar cells. These material require the usually the inorganic nanofibers with low residues of the organic component after the calcination. The prevalent materials are represented by titanium dioxide [24], [34], zinc oxide [35], or copper oxide [36]. Dye-sensitized solar cells (DSSC) based on the AZO nanofiber photoelectrodes give a total energy conversion efficiency of 0.54–0.55% under irradiation of AM 1.5 simulated sunlight with a power density of 100 mW/cm<sup>2</sup> [35]. The dye sensitized solar cell with a photoanode of Ag nanoparticle doped TiO<sub>2</sub> nanofibers exhibited the short circuit current density of the Ag doped DSSC sample was improved by 26% resulting in a conversion efficiency improvement of 25% when compared with the raw DSSC samples [37].

### Conclusions

Functionalized nanofibrous materials prepared by the relative simple process of electrospinning have already been proven to have the innovative and enhancement potential in the wide application range including various electrochemical methods of the energy transformation and storage. Most of the work to the present day has been done in the laboratories over the world. This work is documented by the significant number of the published research papers. The main goal of the future research work remains in the transfer of the edge laboratory experiments to the industrial scale production and the possible risk assessment in order to take advantage of these new approaches in everyday life and improve the energy management rationalization.

### References

1. Ramakrishna, S. *An Introduction to Electrospinning and Nanofibers*; World Scientific, 2005.
2. Andradý, A. L. *Science and Technology of Polymer Nanofibers*; John Wiley & Sons, 2008.
3. Haghi, A. K. *Electrospinning of Nanofibers in Textiles*; CRC Press, 2011.
4. Martin, C. R. Membrane-Based Synthesis of Nanomaterials. *Chem. Mater.* **1996**, *8*, 1739–1746.
5. Tong, L.; Zi, F.; Guo, X.; Lou, J. Optical microfibers and nanofibers: A tutorial. *Optics Communications* **2012**, *285*, 4641–4647.
6. Pal, J.; Sanwaria, S.; Srivastava, R.; Nandan, B.; Horechyy, A.; Stamm, M.; Chen, H.-L. Hairy polymer nanofibers via self-assembly of block copolymers. *J. Mater. Chem.* **2012**, *22*, 25102–25107.
7. Kim, J. K.; Yang, S. Y.; Lee, Y.; Kim, Y. Functional nanomaterials based on block copolymer self-assembly. *Progress in Polymer Science* **2010**, *35*, 1325–1349.
8. Ellison, C. J.; Phatak, A.; Giles, D. W.; Macosko, C. W.; Bates, F. S. Melt blown nanofibers: Fiber diameter distributions and onset of fiber breakup. *Polymer* **2007**, *48*, 3306–3316.
9. Lu, Y.; Li, Y.; Zhang, S.; Xu, G.; Fu, K.; Lee, H.; Zhang, X. Parameter Study and Characterization for Polyacrylonitrile Nanofibers Fabricated via Centrifugal Spinning Process. *European Polymer Journal*. 2010, 2050-2056.
10. Fang, J.; Niu, H.; Lin, T.; Wang, X. Applications of electrospun nanofibers. *Chinese Science Bulletin* **2008**, *53*, 2265–2286.

11. He, J.-H.; Wu, Y.; Zuo, W.-W. Critical length of straight jet in electrospinning. *Polymer* **2005**, *46*, 12637–12640.
12. Shin, Y. M.; Hohman, M. M.; Brenner, M. P.; Rutledge, G. C. Experimental characterization of electrospinning: the electrically forced jet and instabilities. *Polymer* **2001**, *42*, 09955–09967.
13. Lukáš, D.; Sarkar, A.; Martinová, L.; Vodsed'áková, K.; Lubasová, D.; Chaloupek, J.; Pokorný, P.; Mikeš, P.; Chvojka, J.; Komárek, M. Physical principles of electrospinning (Electrospinning as a nano-scale technology of the twenty-first century). *Textile Progress* **2009**, *41*, 59–140.
14. A method of nanofibres production from a polymer solution using electrostatic spinning and a device for carrying out the method.
15. Agarwal, S.; Wendorff, J. H.; Greiner, A. Use of electrospinning technique for biomedical applications. *Polymer* **2008**, *49*, 5603–5621.
16. Method of electrostatic spinning of polymer melt involves supplying polymer melt into electric field induced between spinning electrode and collecting electrode, where conducting agent is added to the polymer.
17. Nayak, R.; Kyrtzis, I. L.; Truong, Y. B.; Padhye, R.; Arnold, L. Melt-electrospinning of polypropylene with conductive additives. *J. Mater. Sci.* **2012**, *47*, 6387–6396.
18. Yang, X.; Teng, D.; Liu, B.; Yu, Y.; Yang, X. Nanosized anatase titanium dioxide loaded porous carbon nanofiber webs as anode materials for lithium-ion batteries. *Electrochemistry Communications* **2011**, *13*, 1098–1101.
19. Ionescu, L. C.; Lee, G. C.; Sennett, B. J.; Burdick, J. A.; Mauck, R. L. An anisotropic nanofiber/microsphere composite with controlled release of biomolecules for fibrous tissue engineering. *Biomaterials* **2010**, *31*, 4113–4120.
20. Lubasova, D.; Martinova, L. Controlled morphology of porous polyvinyl butyral nanofibers. *Journal of Nanomaterials* **2011**, *2011*.
21. Jirsak, O.; Sanetnik, F.; Chaloupek, J. Nanofiber-covered yarns. *Chemical Fibers International* **2011**, *61*, 84–86.
22. Wang, J.; Pan, K.; He, Q.; Cao, B. Polyacrylonitrile/polypyrrole core/shell nanofiber mat for the removal of hexavalent chromium from aqueous solution. *Journal of Hazardous Materials* **2013**, *244–245*, 121–129.
23. Donmez, I.; Kayaci, F.; Ozgit-Akgun, C.; Uyar, T.; Biyikli, N. Fabrication of hafnia hollow nanofibers by atomic layer deposition using electrospun nanofiber templates. *Journal of Alloys and Compounds* **2013**, *559*, 146–151.
24. Jung, W. H.; Kwak, N.-S.; Hwang, T. S.; Yi, K. B. Preparation of highly porous TiO<sub>2</sub> nanofibers for dye-sensitized solar cells (DSSCs) by electro-spinning. *Applied Surface Science* **2012**, *261*, 343–352.
25. Jiang, W.; Liu, Z.; Kong, Q.; Yao, J.; Zhang, C.; Han, P.; Cui, G. A high temperature operating nanofibrous polyimide separator in Li-ion battery. *Solid State Ionics* **2013**, *232*, 44–48.
26. Hwang, K.; Kwon, B.; Byun, H. Preparation of PVdF nanofiber membranes by electrospinning and their use as secondary battery separators. *Journal of Membrane Science* **2011**, *378*, 111–116.
27. Choi, S.-S.; Lee, Y. S.; Joo, C. W.; Lee, S. G.; Park, J. K.; Han, K.-S. Electrospun PVDF nanofiber web as polymer electrolyte or separator. *Electrochimica Acta* **2004**, *50*, 339–343.
28. Ji, L.; Yao, Y.; Toprakci, O.; Lin, Z.; Liang, Y.; Shi, Q.; Medford, A. J.; Millns, C. R.; Zhang, X. Fabrication of carbon nanofiber-driven electrodes from electrospun polyacrylonitrile/polypyrrole bicomponents for high-performance rechargeable lithium-ion batteries. *Journal of Power Sources* **2010**, *195*, 2050–2056.

29. Howe, J. Y.; Burton, D. J.; Qi, Y.; Meyer III, H. M.; Nazri, M.; Nazri, G. A.; Palmer, A. C.; Lake, P. D. Improving microstructure of silicon/carbon nanofiber composites as a Li battery anode. *Journal of Power Sources* **2013**, *221*, 455–461.
30. Kanninen, P.; Borghei, M.; Ruiz, V.; Kauppinen, E. I.; Kallio, T. The effect of Nafion content in a graphitized carbon nanofiber-based anode for the direct methanol fuel cell. *International Journal of Hydrogen Energy* **2012**, *37*, 19082–19091.
31. Jang, J.; Bae, J.; Choi, M.; Yoon, S.-H. Fabrication and characterization of polyaniline coated carbon nanofiber for supercapacitor. *Carbon* **2005**, *43*, 2730–2736.
32. Kim, B. C.; Kwon, J. S.; Ko, J. M.; Park, J. H.; Too, C. O.; Wallace, G. G. Preparation and enhanced stability of flexible supercapacitor prepared from Nafion/polyaniline nanofiber. *Synthetic Metals* **2010**, *160*, 94–98.
33. Kim, B.-H.; Kim, C. H.; Yang, K. S.; Rahy, A.; Yang, D. J. Electrospun vanadium pentoxide/carbon nanofiber composites for supercapacitor electrodes. *Electrochimica Acta* **2012**, *83*, 335–340.
34. Li, J.; Chen, X.; Xu, W.; Nam, C.-Y.; Shi, Y. TiO<sub>2</sub> nanofiber solid-state dye sensitized solar cells with thin TiO<sub>2</sub> hole blocking layer prepared by atomic layer deposition. *Thin Solid Films* **2013**, *536*, 275–279.
35. Yun, S.; Lim, S. Improved conversion efficiency in dye-sensitized solar cells based on electrospun Al-doped ZnO nanofiber electrodes prepared by seed layer treatment. *Journal of Solid State Chemistry* **2011**, *184*, 273–279.
36. Sahay, R.; Sundaramurthy, J.; Suresh Kumar, P.; Thavasi, V.; Mhaisalkar, S. G.; Ramakrishna, S. Synthesis and characterization of CuO nanofibers, and investigation for its suitability as blocking layer in ZnO NPs based dye sensitized solar cell and as photocatalyst in organic dye degradation. *Journal of Solid State Chemistry* **2012**, *186*, 261–267.
37. Li, J.; Chen, X.; Ai, N.; Hao, J.; Chen, Q.; Strauf, S.; Shi, Y. Silver nanoparticle doped TiO<sub>2</sub> nanofiber dye sensitized solar cells. *Chemical Physics Letters* **2011**, *514*, 141–145.

### Acknowledgement

The paper was supported in part by the Project OP VaVpI Centre for Nanomaterials, Advanced Technologies and Innovation CZ.1.05/2.1.00/01.0005 and by the Project Development of Research Teams of R&D Projects at the Technical University of Liberec CZ.1.07/2.3.00/30.0024.

## Investigation of lithium insertion into TiO<sub>2</sub> by Raman spectroscopy supported by <sup>6/7</sup>Li and <sup>16/18</sup>O isotope substitutions

Kavan, L.

J. Heyrovsky Institute of Physical Chemistry, v.v.i. Academy of Sciences of the Czech Republic, Dolejskova 3, 18223 Prague 8 (kavan@jh-inst.cas.cz)

Six representative O-isotope labeled samples of titanium dioxide were synthesized: Ti<sup>16</sup>O<sub>2</sub>, Ti<sup>17</sup>O<sub>2</sub> and Ti<sup>18</sup>O<sub>2</sub>, each in anatase and rutile forms. Furthermore, titania labeled by Ti isotopes 46, 48 and 49 were also obtained. The Raman spectra of all isotopologues were analyzed with the aid of DFT simulation. The found/calculated isotopic shifts elucidated various still open questions about the second-order Raman scattering in rutile, and about the overlapping features in the anatase spectrum [1, 2]. Electrochemistry of titania [3] is highlighted by the effects of Li-insertion, which allows sensitive tracing of phase composition and transitions. Analysis of cyclic voltammograms of Li insertion into TiO<sub>2</sub>(B) and anatase provided information about capacitive contributions to overall charge of Li-storage. The enhancement of 30% was found in capacitive contributions (normalized to the total stored charges) in TiO<sub>2</sub>(B) and anatase, in spite of ca. three times smaller surface area of the former. Different charging mechanism explained facilitated Li<sup>+</sup> insertion in TiO<sub>2</sub>(B). The difference is caused mainly by pseudocapacitive Li-storage in the bulk TiO<sub>2</sub>(B). Deconvolution of cyclic voltammograms also indicated different capacitive contributions of the two voltammetric peaks of TiO<sub>2</sub>(B). These results provide novel insight into the Li-storage in TiO<sub>2</sub>(B) and its difference from that in anatase [4]. Electrochemical and chemical (with n-butyllithium) insertion of Li into TiO<sub>2</sub> (anatase) was studied by Raman spectroscopy and by in-situ Raman spectroelectrochemistry. Four isotopologue combinations in the system, viz. <sup>6/7</sup>Li<sub>x</sub>Ti<sup>16/18</sup>O<sub>2</sub> (with x being the insertion coefficient), were prepared and studied. The reversible transition of tetragonal/orthorhombic phases of anatase/Li-titanate was thus analyzed in detail. The combination of experimental and theoretical (DFT) Raman frequencies with the corresponding isotopic shifts brings new inputs for several still open questions about the Li-insertion into TiO<sub>2</sub> (anatase).

### Acknowledgement

This work was supported by the Grant Agency of the Czech Republic (contract No. 13-07724S).

### References

1. L. Kavan, M. Zukalova, M. Ferus, J. Kürti, J. Koltai S. Civis, Phys. Chem. Chem. Phys. 13 (2011) 11583.
2. O. Frank, M. Zukalova, B. Laskova, J. Kürti, J. Koltai L. Kavan, Phys. Chem. Chem. Phys. 14 (2012) 14567.
3. L. Kavan, Chem. Rec. 12 (2012) 131.
4. B. Laskova, M. Zukalova, A. Zukal, M. Bousa, L. Kavan, J. Power Sourc. in press.

## Catalyst breathing in electrocatalytic processes

Krtil, P.

J. Heyrovský Institute of Physical Chemistry, Academy of Sciences of the Czech Republic,  
Dolejskova 3,18223 Prague, Czech Republic  
Petr.Krtil@jh-inst.cas.cz

Catalytically active alloys for processes such as hydrogen evolution, oxygen reduction, or oxidation of small organic molecules are of key importance in electrochemical electric energy generation or synthesis of chemicals.

The traditional approach in electrocatalysis builds on the assumption that the catalytic activity is confined to relatively small active sites, local structure of the which (coordination numbers and chemical nature of bonding partners in the 1<sup>st</sup> and 2<sup>nd</sup> coordination shells) does not change during the electrocatalytic reaction. It anticipates that the structural arrangements of the characteristic reaction centers are stable and present on the catalyst's surface at all times. This concept has been challenged by both theoretical as well experimental studies describing selective reaction triggered segregations of the alloy components in the surface.

The presented paper will focus on the possibility to describe the catalytic reaction driven surface structure changes using in-situ X-ray absorption spectroscopy (XAS). The extended X-ray fine structure (EXAFS) based local information will be used to address the effect of the specific adsorption of a) hydrogen, b) oxygen adsorption on the surface composition of model bimetal catalysts based on Au-Pd, Pt-Ni systems. The EXAFS data will be also used to visualize the active species transfer in bi-functional catalysis on Pt-Ru. based catalysts (see Fig. 1).

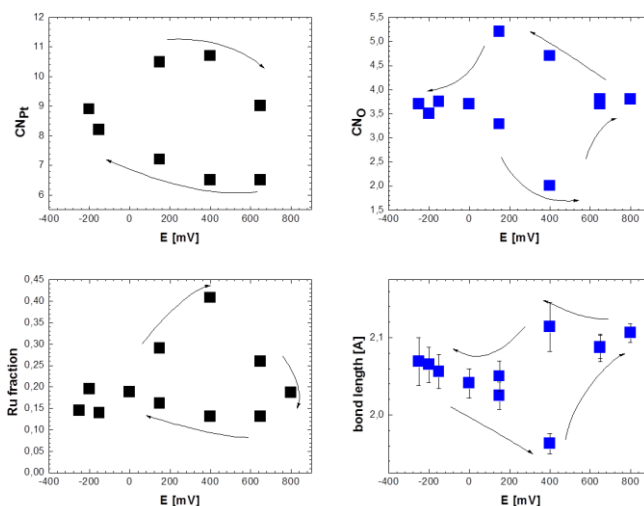


**Figure 1.** Local structure visualization of the oxygen transfer on PtRu electrocatalysts extracted from XAS spectra of a Pt<sub>2</sub>Ru nanoparticulate electrode polarized to different potentials in acid media. Figure shows Pt average coordination number (top left), Ru fraction in the Pt vicinity (bottom left), average number of oxygen bonded to Ru (top right) and average Ru-O bonding distance (bottom right).

### Acknowledgement

This work was supported by the European Commission within ITN ELCAT under the contract 214936.

## Morphology and Electrochemical Investigations on Multimetal Carbon Nitride Electrocatalysts Supported on Graphitized Polyketone Nanoballs

Di Noto, V.<sup>1\*</sup>, Vezzù, K.<sup>2</sup>, Negro, E.<sup>1</sup>, Polizzi, S.<sup>3</sup>

<sup>1)</sup> Department of Chemical Sciences, University of Padova, Via Marzolo 1, 35131 Padova (PD), Italy

<sup>2)</sup> Veneto Nanotech S.C.p.A, Via San Crispino 106, 35129 Padova (PD), Italy

<sup>3)</sup> Department of Chemistry, University of Venice “Ca’ Foscari”, Dorsoduro, Calle Larga S. Marta 2137, 30123 Venezia (VE), Italy

One of the most severe bottlenecks in the operation of proton exchange membrane fuel cells (PEMFCs) is the sluggish kinetics of the oxygen reduction reaction (ORR); suitable ORR electrocatalysts are required in order to obtain PEMFCs able to yield a sufficiently high performance. State-of-the-art ORR electrocatalysts for application in PEMFCs are obtained by distributing Pt nanocrystals on active carbon supports characterized by a very large surface area (1). A new preparation protocol has been proposed recently to obtain electrocatalysts with a well-controlled chemical composition, based on the pyrolysis and activation of hybrid inorganic-organic precursors (2); the resulting carbon nitride electrocatalysts are able to show an outstanding ORR performance both in “ex-situ” studies and in single-cell configuration (3). In this work, the morphology and “ex-situ” electrochemical performance of a new family of multimetal carbon nitride electrocatalysts is described. The materials are obtained as described elsewhere (4) by the pyrolysis of a hybrid inorganic-organic precursor including Pt and Ni atoms impregnating an innovative support. The latter is prepared by a three-step process: a) growth of polyketone nanofibers on graphite nanoparticles; b) chemical treatment to make the nanofibers infusible; and c) pyrolysis process under an inert atmosphere. An aliquot of each of the final electrocatalysts is treated with H<sub>2</sub>O<sub>2</sub>. The resulting samples undergo an extensive characterization by HR-TEM (see Fig. 1).

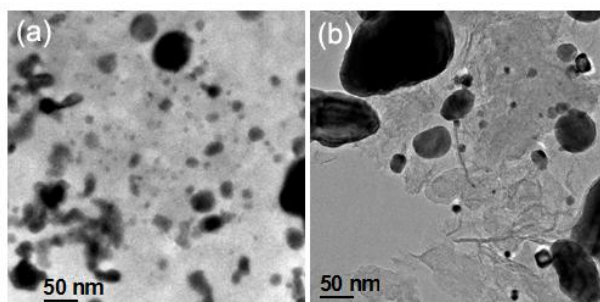


**Figure 1.** Effect of the H<sub>2</sub>O<sub>2</sub> treatment on the morphology of a multimetal carbon nitride ORR electrocatalyst as determined by HR-TEM. (a) Pristine sample; (b) after treatment with H<sub>2</sub>O<sub>2</sub>.

Finally, the “ex-situ” electrochemical performance in the ORR is determined by the CV-TF-RRDE method. These studies allow to obtain the correlations between the morphology and “ex-situ” electrochemical performance of these high-performing multimetal carbon nitride ORR electrocatalysts.

### Acknowledgments

This research is funded by project “PRAT 2011” financed by the University of Padova, and by the Italian MURST project PRIN2008 Prot. 2008SXASBC\_002. E. Negro thanks Regione del Veneto (SMUPR n. 4148, Polo di ricerca del settore fotovoltaico) for financial support.

### References

1. H. A. Gasteiger, S. S. Kocha, B. Sompalli, F. T. Wagner, *Appl. Catal. B-Environ.*, **56**, 9 (2005).
2. V. Di Noto, E. Negro, *Electrochim. Acta*, **55**, 7564 (2010).
3. V. Di Noto, E. Negro, *Fuel Cells*, **10**, 234 (2010).
4. V. Di Noto et al., submitted to IJHE.

## Growth of zinc dendrites from the aqueous KOH solution

Chladil, L.<sup>1,2</sup>, Čudek, P.<sup>1,2</sup>, Musil, M.<sup>1,2</sup>

<sup>1</sup> Institute of Electrotechnology, Brno University of Technology, Faculty of Electrical Engineering and Communication, BUT, Technická 10, 616 00 Brno, Czech Republic

<sup>2</sup> Centre for Research and Utilization of Renewable Energy, Faculty of Electrical Engineering and Communication, BUT, Technická 10, 616 00 Brno, Czech Republic

### Introduction

Ni-Zn alkaline accumulators have the big advantages in comparison with Ni-Cd or Ni-MH thanks to their high energy density, higher output voltage and thanks to ecological aspect. One of the biggest problems which limits the battery's life is dendritic growth, which proceeds during electro-deposition of dissolved zinc ions on the negative electrode. Suppression of growth of dendrites is possible mainly by usage of special additives in the electrolyte, which cause a homogenous distribution of current density or by choosing a suitable pulse charging mode. This article deals with the influence of pulse frequency on dendrites growth.

### Experimental

The working micro-electrode was made from 2,5 mm thick (active area is 4.9 mm<sup>2</sup>) zinc wire which was soldered to the copper belt. The whole working electrode was embedded into the epoxy resin and then a microsection was made perpendicularly to the soldered wire (Figure 1). As a reference electrode was used Zn wire coated by polyolefin insulation tube. Therefore all measured potentials are versus Zn ref. el. As a counter electrode was used Ni mesh 2 x 2 cm. Working electrode was cleaned and polished before measurement (using Al<sub>2</sub>O<sub>3</sub> nanoparticles paste). The whole electrode system was inserted into the 25 ml vial, which was filled with 15 ml of 6M KOH electrolyte saturated by ZnO. The working electrode was placed directly into opposition to the counter electrode and pulse electrode deposition were performed. Four different frequencies of pulse deposition were selected (1 kHz, 100 Hz, 10 Hz and 1 Hz) and charging current of pulse was 2 mA, which is equivalent to the current density 40 mA/cm<sup>2</sup>. The mark-space ratio was 1. For comparison with the DC charging mode, next electrode was loaded by current 1 mA during 1 hour. In this case the charge of deposition was 1 mAh and the time of deposition was 1 h.

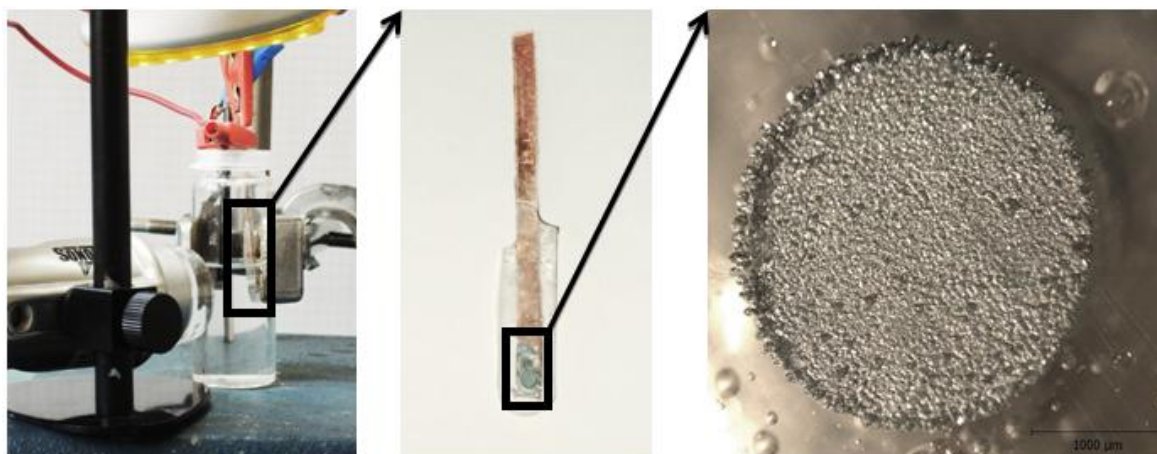


**Figure 1.** System for measuring of Zn dendrite growth and detailed view of working electrode

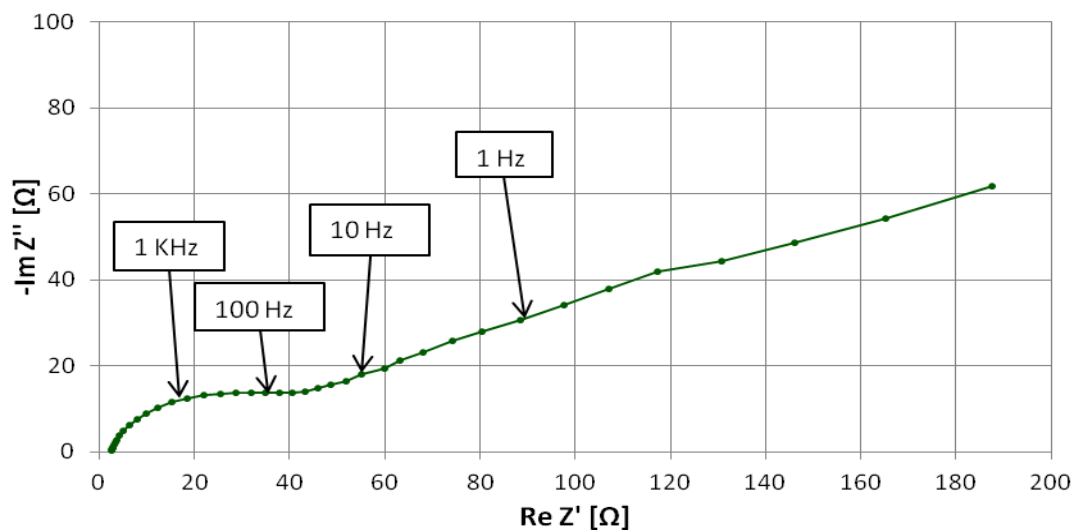


**Figure 2.** Nyquist diagram of pure Zn electrode before deposition with marked frequencies of pulse deposition

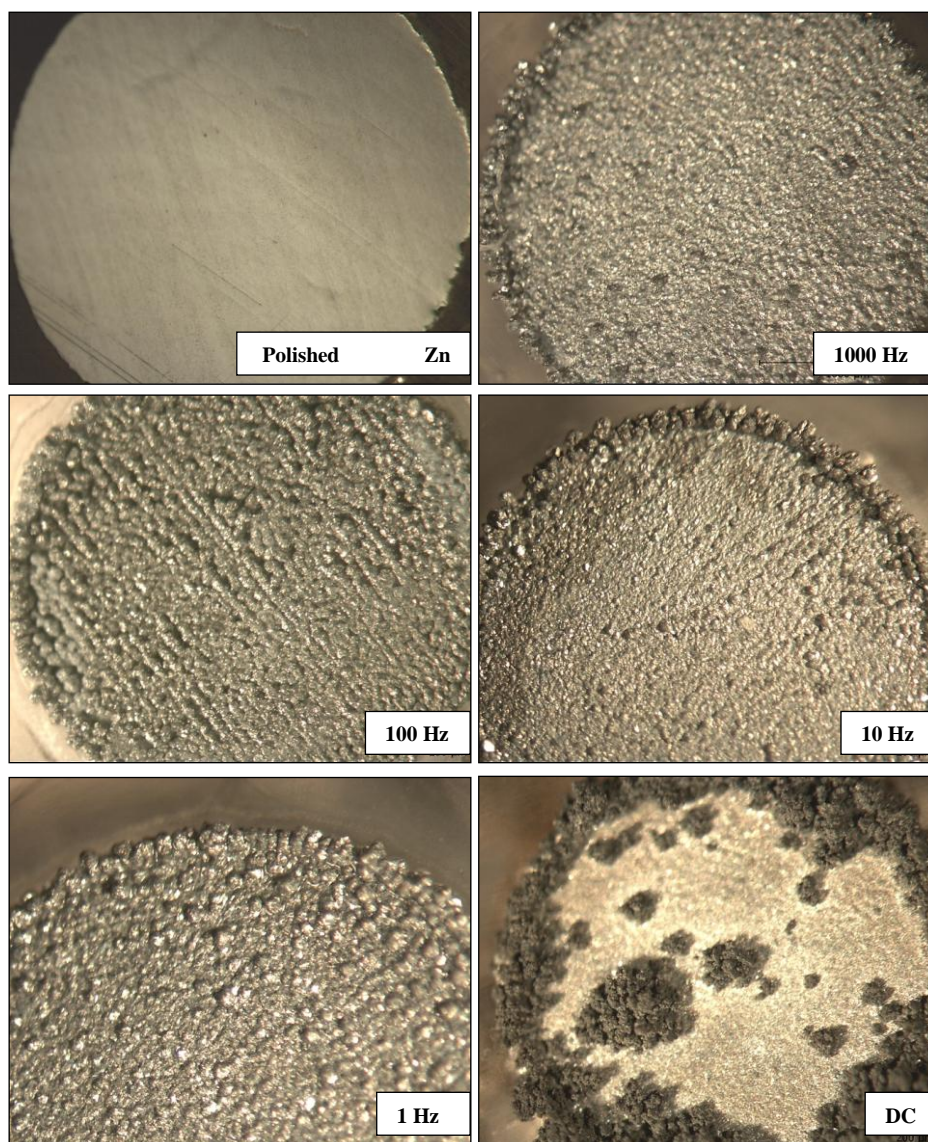


**Figure 3.** Effect of deposition frequency on the dendrite growth

## Results

Figure 2 show the typical nyquist diagram of pure Zn electrode before deposition with marked frequencies of pulse deposition. The resulting images of zinc deposited layer at various pulse frequencies are shown on figure 3. From images, it is obvious, that even a low frequency pulses have a great influence on deposition uniformity. At high frequency 1 kHz the dendrites grow in compact grey layer, with good adhesion. Nevertheless the rate of dendrites growth is slightly increased at the edges of the electrode. The best results were achieved at frequency 100 Hz when dendrites grow in groups (circular diameter about 50  $\mu\text{m}$ ) and no more significant growth at the edges of the electrodes is observed. With a decrease in the frequency from 10 Hz to 1 Hz dendrites clusters with accelerated growth are gradually formed and preferred growth at the edges is also obvious.

## Acknowledgement

This work was supported by the project CVVOZE CZ.1.05/2.1.00/01.0014 and by the internal grant FEKT-S-11-7.

## References

1. J. Jindra, *Journal of Power Sources*, **37**,(1992), pp. 297-313
2. J. Jindra, *Journal of Power Sources*, **66**, (1997), pp.15-25
3. Z. Liu, S. Zein El Abedin, F. Endres, *Electrochimica Acta*, **89**, (2013), pp. 635-643
4. G.N.K. Ramesh Babu, G. Devaraj, J. Ayyapparaj, *Journal of Solid State Electrochemistry*, **3**, (1998), p. 48

## Enhancing of the electrochemical behavior of $\text{LiNi}_{1/2}\text{Mn}_{3/2}\text{O}_4$ by acid treatment

Ivanova, Sv., Zhecheva, E., Stoyanova, R.

Institute of General and Inorganic Chemistry – Bulgarian Academy of Sciences, Sofia, Bulgaria

The increasing demands on high energy and high power Li-ion batteries lead the researchers to explore the high voltage cathode materials.  $\text{LiNi}_{1/2}\text{Mn}_{3/2}\text{O}_4$  is a promising cathode material for new generation lithium-ion batteries. The most remarkable property of spinel  $\text{LiNi}_{1/2}\text{Mn}_{3/2}\text{O}_4$  is its discharge voltage plateau at around 4.7 V delivering high energy density. In this study, the effect of acid treatment on the lithium intercalation in high-voltage  $\text{LiNi}_{1/2}\text{Mn}_{3/2}\text{O}_4$  spinel is examined by the application of diffraction and spectroscopic techniques. Acid treatment of ordered submicrometer  $\text{LiNi}_{1/2}\text{Mn}_{3/2}\text{O}_4$  modifies the particle size distribution without change of the cationic distribution. The synergetic effect between nano- and microparticles has an impact on the rate capability.

Nanosized spinels were synthesized using acetate-oxalate precursors, which were obtained mechanochemically at room temperature from metal acetates and oxalic acid. This method has been reported to be suitable for the preparation of nanosized spinels with close particle size distribution (1, 2). XRD and TEM analysis were employed for structural and morphological characterization of the spinel oxides. The electrochemical performance of pristine and acid treated  $\text{LiNi}_{1/2}\text{Mn}_{3/2}\text{O}_4$  is evaluated in model lithium cells using a galvanostatic mode with lithium as an anode and the examined spinel oxide as a cathode. One of the factors affecting the electrochemical performance of spinels is their stability in electrolyte solutions. The interactions between electrolyte and spinels are examined by X-ray photoelectron spectroscopy (XPS).

At 600 °C a stoichiometric nanosized spinel oxide  $\text{LiNi}_{1/2}\text{Mn}_{3/2}\text{O}_4$  with ordered structure is obtained. The mean particle size is between 10-30 nm with relatively close particle size distribution. With increasing the temperature, the particles start to grow reaching submicron dimensions (150-300 nm). The electrochemical performance of  $\text{LiNi}_{1/2}\text{Mn}_{3/2}\text{O}_4$  can be optimized by rational manipulation of its structure. Another approach to achieve a better performance for  $\text{LiNi}_{1/2}\text{Mn}_{3/2}\text{O}_4$  is by engineering its particle size. By decreasing the particle dimensions, the lithium ion transport path becomes shorter, and the contact area with the electrolyte increases, thus contributing to a high rate capability of the electrodes (3). Contrary, micrometer-sized  $\text{LiNi}_{1/2}\text{Mn}_{3/2}\text{O}_4$  (with a particle size of 3-5  $\mu\text{m}$ ) has recently been reported to display a high rate capability and excellent capacity retention (4). In order to stabilize the surface of the spinel oxides and to improve their electrochemical behavior acid treatment has been performed. According to the literature data, the acid treatment of  $\text{Mn}^{4+}$ -containing spinels takes place by an exchange of  $\text{Li}^+$  with protons from the acidic solution and sample dissolution. To check for possible  $\text{H}^+/\text{Li}^+$  exchange reactions, thermogravimetric (TG) experiments are undertaken. TG analysis shows that the acid-treated spinels release the  $\text{H}_2\text{O}$  after heating up to 250 °C. After acid treatment the only parameter that changes is the particle size distribution. The size of the particles after treatment for the obtained at 600 °C oxide remain of the same order while three-modal particle size distribution is formed for the high temperature oxide. This has an impact on the electrochemical properties of the oxides. The use of nanosized electrodes favors also the side reaction of  $\text{LiNi}_{1/2}\text{Mn}_{3/2}\text{O}_4$  with the organic-based electrolyte. However, nanosized  $\text{LiNi}_{1/2}\text{Mn}_{3/2}\text{O}_4$  shows good electrochemical behavior.

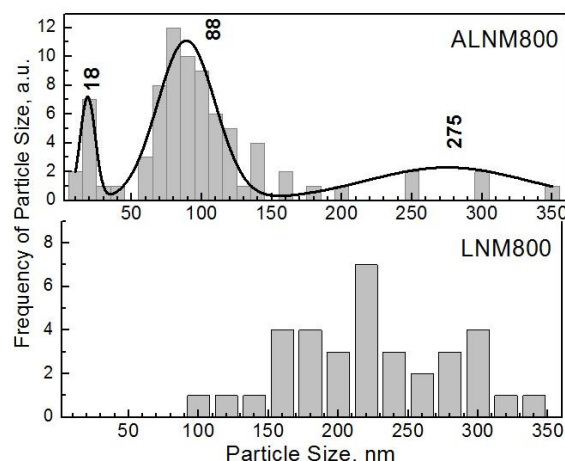


**Figure 1.** Particle size distribution of pristine (LNM) and acid treated high temperature spinel (ALNM).

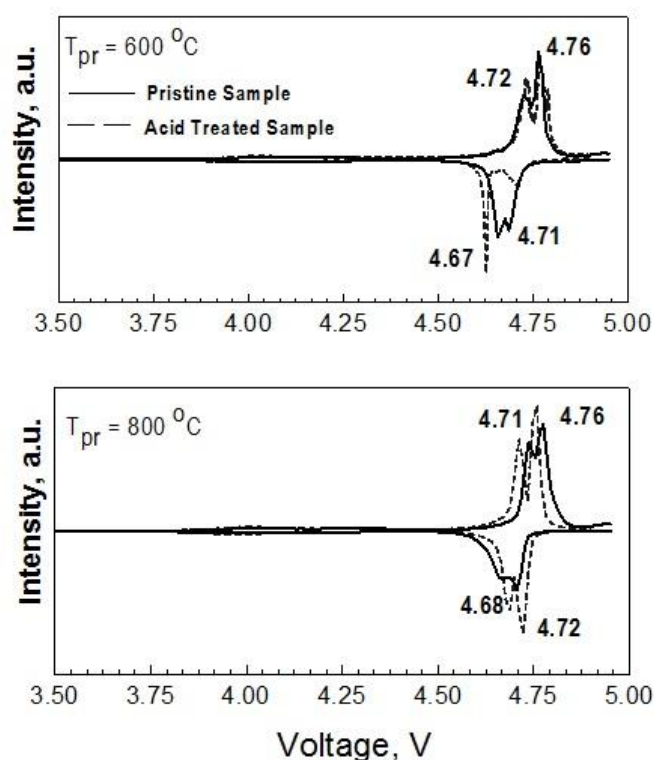


**Figure 2.** First derivative of the capacity-voltage curves for the pristine and acid-treated spinels, quenched at 600 and 800 °C.

Acid treatment is a way to modify the particle size distribution as a consequence of the partial dissolution of the spinel oxides (fig. 1). As a result, a 1:3 Ni/Mn ordered spinel with three-modal particle distribution encompassing the nano- and submicrometer range is formed for the high temperature spinel oxide (5). Local and long-range Ni, Mn distribution is maintained after acid treatment for both nano- and submicron-sized oxides. Cationic 1:3 order in the spinel affects the potential of  $\text{Li}^+$  extraction/insertion from/into the spinel with  $\text{Ni}^{2+}/\text{Ni}^{4+}$  oxidation/reduction reaction (fig. 2). Acid-treated  $\text{LiNi}_{1/2}\text{Mn}_{3/2}\text{O}_4$  having a three-modal particle size distribution that encompasses the nano and submicrometer range bears the characteristic reactivity of nano- and submicrometer-sized spinels.

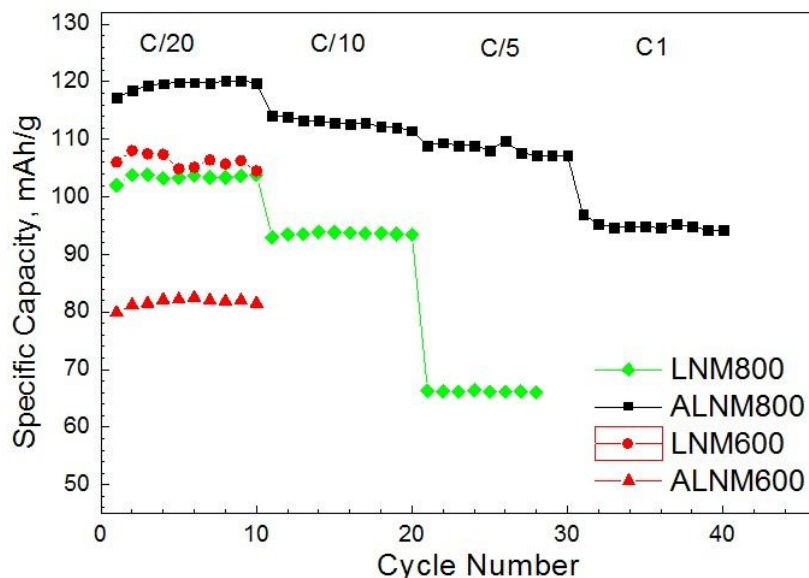


**Figure 3.** Rate capability of pristine (LNM) and acid treated (ALNM) spinels synthesized at 600 and 800 °C.

In conclusion the best electrochemical performance is for ordered spinel  $\text{LiNi}_{1/2}\text{Mn}_{2/3}\text{O}_4$  with three-modal particle size distribution (fig. 3).

### Acknowledgments

This work was supported by ESF (Grant BG051PO001-3.3.06-0050).

### References

1. X. R. Ye, D. Z. Jia, J. Q. Yu, X. Q. Xin, Z. Xue, *Adv. Mater.*, **11**, 941 (1999).
2. Sv. Ivanova, E. Zhecheva, D. Nihtianova, R. Stoyanova, *J. Mater. Sci.*, **46**, 7098 (2011).
3. E. Stura, C. Nicolini, *Anal. Chim. Acta*, **568**, 57 (2006).
4. K. Shaju, P. Bruce, *Dalton Trans.*, 5471Q (2008).
5. Svetlana Ivanova, Ekaterina Zhecheva, Radostina Stoyanova, Diana Nihtianova, Sebastian Wegner, Pavleta Tzvetkova, and Svetlana Simova, *J. Phys. Chem. C*, **115**, 25170 (2011).

## Testing of DLC Coating on Plasma Nitrided Austenitic Stainless Steel

Joska, Z.<sup>1\*</sup>, Kadlec, J.<sup>3</sup>, Klanica, O.<sup>1</sup>, Tomáščík, J.<sup>2</sup>, Svoboda, E.<sup>1</sup>

<sup>1</sup> Department of Mechanical Engineering, University of Defence in Brno, Kounicova 65, 602 00 Brno, Czech Republic

<sup>2</sup> Joint Laboratory of Optics of Palacky University and Institute of Physics of Academy of Sciences of the Czech Republic, 17. listopadu 12, Olomouc, 772 07, Czech Republic

<sup>3</sup> Department of Mechanical Engineering, Institute of Technology and Business in České Budějovice, Okružní 517/10, 370 01 České Budějovice, Czech Republic

(\*) Corresponding author. Tel: +420 723668071. E-mail address: joska.zdenek@email.cz

Keywords: Stainless steel, duplex coating, nanohardness, adhesion, surface morphology

### Introduction

Austenitic stainless steel AISI 304L is one of the most spread austenitic stainless steel, due to excellent corrosion resistance, superior cryogenic properties, good high-temperature strength, for this properties, it is used in the food and chemical industry and in medicine for surgical instruments (1). But strong limitation as low wear resistance and poor hardness defend their applications. Duplex surface system was applied to improve surface and subsurface properties. The combination of both plasma nitriding and subsequent deposited thin film DLC were used as duplex treatment. Plasma nitriding is very universal treatment process which was used for creation of supersaturate austenite layer (2, 3, 4). This layer is non magnetic, it has very high hardness and good corrosion resistance. High hardness, chemical inertness and excellent tribological properties of amorphous carbon coatings often called diamond-like carbon (DLC) coatings are of great interest for technological applications (5, 6). When these coatings are deposited on soft substrate material due to their very thin thickness, further increase in the wear and especially in the load-bearing resistance is limited by plastic deformation of the substrate, which results in the eventual collapse of the coating. In case of austenitic stainless steel plasma nitrided layer can create very useful transition layer between soft substrate and very hard thin coating (7, 8, 9). The duplex treatment consisted of plasma nitriding at 470 °C for 4 hours and subsequent coating with DLC layer was applied on AISI 304L stainless steel. The article is concerned to a study of the chemical composition and mechanical properties of duplex system.

### Experimental material, methods and surface treatment

Samples of an AISI 304L stainless steel in the untreated state was sized 30 x 15 mm and had thickness of 2 mm. The substrate had a microhardness of about 230 HV. Before the plasma nitriding process, the samples were wet ground using silicon carbide paper from 120 down to 4000 grit and finally polished with 1 µm diamond paste. Plasma nitriding was carried out in PN 60/60 Rübige equipment with these parameters: temperature of 470 °C, duration 6 h, pressure 320 Pa, gas mixture of H<sub>2</sub> flow 8 l/min and N<sub>2</sub> flow 24 l/min, pulse length 100 µm, voltage 520 V. The pre-nitrided samples were afterwards coated with DLC coatings in PVD industrial equipment Platit Pi 300. Depth profiles of plasma nitrided layers and PVD coatings were measured by GDOES/QDP method. GDOES measurements were performed in a LECO SA-2000. Calibration of

nitrogen: JK41-1N and NSC4A standards. Confocal laser microscope LEXT OLS 3000 was used for observation of the cross section morphology of duplex coatings and craters after adhesion Rockwell tests. The surface hardness of duplex systems was evaluated by a Vickers microhardness test in a LECO automatic microhardness tester LM 247 AT. Surface microhardness was measured in range of load 0.1N to 9.81N. For each load, there were carried out 5 measurements and the resulting value is the average of these. Adhesion test was performed on the duplex coatings as a standard Rockwell test, while using a load of 1471N and a diamond Rockwell indenter of 0.2 mm in diameter to assess the vertical adhesion of the coatings.

### Experimental results

The plasma nitriding process created a nitrided layer of 25  $\mu\text{m}$  thickness. The DLC coatings subsequently deposited by PVD have the thickness of 1.5  $\mu\text{m}$ . Indentation adhesion tests were performed by Rockwell indentation test. The sample shows good adhesion in range HF1, without any delamination of coatings. The surface hardness of duplex treated samples showed that the highest values 3400  $\text{HV}_{0.01}$  were found in the duplex treated sample with the DLC coating. The single coated sample reached only 1700  $\text{HV}_{0.01}$ .

### Conclusion

Duplex surface treatment consisted of deposition of a plasma nitrided layer and subsequently deposition of a DLC coating. The analysis carried out by using GDOES/QDP method was in a good agreement with observation of the metallographic cross-section and microhardness measurement. The thickness of the nitrided layer was 25  $\mu\text{m}$  and microhardness values were around 1150  $\text{HV}_{0.05}$ . The surface hardness of duplex coatings reached 3400  $\text{HV}_{0.01}$ . Rockwell adhesion test shows that the plasma nitrided layer contributes to good adhesion of the DLC coating, which has better adhesion than on a non-nitrided substrate.

### References

1. Lo K.H., Shek C.H., Lai J.K.L.: *Materials Science and Engineering: R: Reports*. **65**, 4-6 (2009)
2. Kadlec J., Dvorak M.: *Strength of Materials*. **40**, 118 (2008).
3. T. Czerwicz, N. Renevier and H. Michel, *Surf. Coat. Technol.* **131**, **267-277** (2000).
4. Pokorny Z., Kadlec J., Hruby V., et al.: *Advances in Military Technology*, **6**, 1 (2011)
5. Jelinek M., Kocourek T., Kadlec J., Bulir J.: *Laser Physics*. **19**, 2 (2009).
6. Jelinek M., Kocourek T., Bulir J., Novotny M., et al.: *Laser Physics*. **15**, 2 (2005).
7. Joska Z., Kadlec J., Pospichal M., et al.: *Chemicke Listy*. **105**, S (2011).
8. Heras E. De Las, Egidi D.A., Corengiea P., et al: *Coatings Technology*. **202**, 1 (2008).
9. Joska Z., Kadlec J., Hruby V., et al.: *Chemicke Listy*. **106**, S (2012).

## Reasons of Total Endoprosthesis Failure

Onderka, F.<sup>1</sup>, Klanica, O.<sup>1</sup>, Dobrocký, D.<sup>1</sup>, Kadlec, J.<sup>2\*</sup>

<sup>1</sup> Department of Mechanical Engineering, University of Defence in Brno, Kounicova 65, 602 00 Brno, Czech Republic

<sup>2</sup> Department of Mechanical Engineering, Institute of Technology and Business in České Budějovice, Okružní 517/10, 370 01 České Budějovice, Czech Republic

(\*) Corresponding author. Tel: +420 737425014, +420 973442355. Email: jaromir.kadlec@unob.cz

The aim of this work is to present the main reasons of failure of total endoprosthesis.

Keywords: total joint replacement, osteointegration, wear and corrosion resistance, mechanical properties of total endoprosthesis

### Introduction

Total joint replacement (TJR) is one of the most efficacious and cost effective procedures in surgery (1). It is applied to replace part of joint or all joint and must be secured the maintenance of absolute joint function. The functionality and lifetime of artificial joints *in vivo* are influenced by material properties, the shape of the implant, a combination of materials and also the reaction of the organism to a foreign object. The materials chosen must be biocompatible (both the material itself and any breakdown products), strong, resistant to fatigue, wear and corrosion, easily accessible and reasonably priced. Worldwide OECD statistics shows that 10% of men and 18% of women over the age of 60 years suffer from osteoarthritis. In 2011, the Czech Republic performed 166 primary implantations of the hip and 111 primary knee implants per hundred thousand patients. Between 2000 and 2009 in OECD countries, the total number of hip implantations are increased about 25%, the knee joints are increased by almost 100%. Another study published in England and Wales says, that in these countries is conducted annually one hundred and sixty thousand primary implantations of the knee and hip joints. The same number cases to reimplantation. Reimplantations of joint replacement is relatively frequent, 10 – 20% must be reoperated 15 to 20 years after the primary implantation (2, 3). It is expected that the number of reimplantations between years 2005 – 2030 of the knee joint increased by 607% and the hip joint by 137% (4). Because arthritis still affects younger patients and length of life extends, the development of endoprostheses is focused on extending the lifetime, especially improvement fixation of prostheses and abrasion reduction.

### Osteointegration.

Lack of primary stability (initial post-operative care) is considered as one of the main consequences of aseptic loosening of cementless orthopedic replacements. Physiological load increases the possibility of relative micromovements (100 – 200  $\mu\text{m}$ ) at the interface implant/bone, which then prevents the ingrowth of bone into the implant. A poor integration into the bone resulting in the formation of a fibrous tissue layer around the prosthesis, and eventually promoting loosening of the implant. To measure the micromovements at the interface bone/implant is necessary to use the

method with an accuracy at least 10 to 20  $\mu\text{m}$ . It is also difficult to determine what point is the largest movement, so the method must be able to measure the relative movement at any point of the interface (5). Total joint replacement materials should be ideally bioactive, that is osteoconductive (the growth of bony tissue into the structure of an implant) or better osteoinductive (acceleration of new bone formation by chemical means)- these two properties are especially important for materials that are implanted directly into the bone. The ideal bone ingrowth into the material is suitable porosity at least 100  $\mu\text{m}$  (6), another literature indicates the value 150 – 400  $\mu\text{m}$  (7). Inability integration of the implant with the surrounding tissue results in a micromovements and releases implant. In 1981, Albrektsson defined six factors affecting successful osseointegration:

- Implant material,
- Implant design,
- Surface conditions,
- Status of the bone,
- Surgical technique,
- Implant loading conditions (6).

#### Wear/corrosion resistance.

Wear is known as a removal process and thus a damage of a surface originated by the motion of two surfaces in close contact. The rate of lost material depends on the hardness of the material, the intensity of the load and the surface roughness. (8) Low wear resistance and low corrosion resistance of implants in body fluids lead to the release of metal ions into the surrounding tissues and body fluids, in addition low wear resistance leads to loosening of the implant. Typical differences between the biological response of the organism is polyethylene (UHMWPE – ultra-high-molecular-weight polyethylene). While a volume implant as an acetabular cup of hip joint in the human body behaves inert, polyethylene wear debris caused by abrasion femoral head and acetabular cup are today considered as a major factor in the process of aseptic osteolysis leading to the release of total hip arthroplasty (9). For metallic components, the first size of wear debris is 10 – 50 nm (10). Clinical significant debris size is in the range 0,1 – 10  $\mu\text{m}$ . Thus, for human organism wear debris are not biocompatible. Wear debris can cause metallosis (the putative medical condition involving deposition and build-up of metal debris in the soft tissues of the body). Direct reaction of the organism to these debris is phagocytosis of macrophages. Macrophages are monocytes - type of leukocytes, which grow and settle in tissues where it is involved in the immune system. Macrophages then producing inflammatory mediators (cytokines) IL-1, IL-6, TNF- $\alpha$  and PGE<sub>2</sub>. (11) Cytokines in the body affecting the ratio of bone formation - bone resorption toward superiority degradation. The clinical exhibition of the process is the formation of abrasive granuloma and periprosthetic osteolysis which lead to the release and failure of the prosthesis. Body fluids are solutions containing chloride (interstitial and synovial fluid contains about 5 g·l<sup>-1</sup> chlorides, saliva approximately five times less), the pH is in the range 5.6 – 9, oxidation ability is determined mainly oxygen (during inflammation the oxidation capability significantly increases), the temperature is usually about 37°C. Each metal implant corrodes in the human body at different speeds. Ions released as a product of the corrosion reaction contaminating tissue predominantly in the trochanteric area of the joint, which may cause subsequent allergic and toxic effects. The rate of corrosion of metal implants is influenced by the size of the first wear particles – with increasing size the corrosion rate is increased (10). Because the lifetime of implant is affected mainly by these two properties; the development of implants is aimed to prolong the life of the material in the body (4, 8). It is clear that different combinations of different materials carry the risk of wear. Using Al<sub>2</sub>O<sub>3</sub> as a head of the hip in combination with acetabular cup of UHMWPE is used because of the

relatively low friction coefficient. It was found that the combinations of Al<sub>2</sub>O<sub>3</sub>/Al<sub>2</sub>O<sub>3</sub> and CoCrMo/CoCrMo carry the lowest risk of release wear debris (8) – see Tab.I. However, it was shown that failure articulating metal/metal is common and is therefore not recommended as a pair (12). If the metallic hip joint head is not damage, it will produce up to 40% more wear debris in comparison with Al<sub>2</sub>O<sub>3</sub>, damaged head even up to 200 – 300% more (13).

**TABLE I.** comparison of abrasion material release during one year for different articulating pairs (14)

Friction pair	The amount of friction pair wear debris [ $\mu\text{m}/\text{year}$ ]
CoCrMo/UHMWPE	200
Al <sub>2</sub> O <sub>3</sub> /UHMWPE	20 – 130
Al <sub>2</sub> O <sub>3</sub> /Al <sub>2</sub> O <sub>3</sub>	1 – 10
CoCrMo/CoCrMo	4 – 8

### Other mechanical properties.

Besides the biocompatibility and other mentioned requirements, the material for replacement of hard tissue has to fulfill the mechanical characteristics. Appropriate choice of material is linked to the mechanical properties such as modulus of elasticity, ductility, tensile strength, fracture strength, yield strength and fatigue strength. These parameters are not only define the processability of the material, but they are also the key to the success of the implant in the area of hard tissue. The goal should be equivalent modulus of elasticity of the material very close to modulus of elasticity of human bone. The human bone modulus is between approximately 10 to 30 GPa. If the difference is too large, the mechanical strength of bone is not ideal (reduced or missed) - absence of the normal stress in the bone is due to the fact that the supporting element takes the implant. It occurs in osteoporosis of inactivity controlled according to Wolff's law (stress shield effect), which is characterized by tissue resorption – reduction of bone density (osteopenia), degradation of bone lamellas and the loss of calcium that is excluded by the kidneys and the bone weakens (8, 15). For highly loaded implants, especially hip and knee, it is necessary to take into account the amount of cyclic load, so the implant has to be throughout the operation without failure or fracture. Beside a large number of cyclic loading, fatigue failure may occur when a tensile stress is high enough. The titanium prosthesis fatigue is considered one of the main reasons of failure. Cyclic load in the joint can lead to deformation of articulating plastic acetabular cup in the form of a groove or other structural inhomogeneities. In these zones, the stress increases and it can lead to crack initiation, its spread and eventually rupture due to prolonged cyclic loading. (8, 14, 16, 17). Long-term cyclic loading of UHMWPE may cause softening leading to a change of Young's modulus and yield stress.

Besides the mechanical properties the implant geometry must be assessed as well. Diameter of the hip joint head affects the life of the implant. The risk of failure increases with increasing diameter in metal/metal combinations (12). Although the development of artificial joint replacements have been going on for decades (the oldest attempt of a human joint is from 1840 (9)) on the market today endless amount of products from different manufacturers (De Puy, Johnson & Johnson, Lima, Stryker, Smith & Nephew, Zimmer, B. Braun ...). Nevertheless it can be said that the most of the existing prosthesis do not fully comply with these conditions and especially the implants with a heavy load such as a hip replacement or knee replacement lead to the release implants.

## References

1. S. Santavirta, Y. T. Konttinen, R. Lappalainen, A. Anttila, S. B. Goodman, M. Lind, L. Smith, M. Takaqi, E. Gomez-Barena, L. Nordsletten, J. W. Xu, Materials in total joint replacement, *Current Orthopaedics*, **12**, 51-57 (1998).
2. National Joint Registry, *Joint replacement statistics* [online], 2012 [cit. 2013-07-06].
3. OECD Indicators, *Health Care Activities: Hip and knee replacement* [online], 2011 [cit. 2013-07-06].
4. M. Geetha, A. K. Singh, R. Asokamani, A. K. Gogia, Ti based biomaterials, the ultimate choice for orthopaedic implants – A review, *Progress in Materials Science*, **54**, 397-425 (2009).
5. M. Viceconti, R. Muccini, M. Bernakiewicz, M. Baleani, L. Cristofolini, Large-sliding contact elements accurately predict levels of bone-implant micromotion relevant to osseointegration, *Journal of Biomechanics*, **33**, 1611-1618 (2000).
6. A. Wennerber, The importance of surface roughness for implant incorporation, *Int. J. Mach. Tools Manufact*, **38**, 657-662 (1998).
7. V. J. Hetherington, J. S. Kawalec, B. Bhattacharyya, Enhancement of the Fixation of Pyrolytic Carbon Implants by Using Atomic Oxygen Texturing, *The Journal of Foot & Ankle Surgery*, **43** (1), 16-19 (2004).
8. S. Bauer, P. Schmuki, K. von der Mark, J. Park, Engineering biocompatible implant surfaces - Part I: Materials and surfaces, *Progress in Materials Science*, **58**, 261-326 (2013).
9. *Biomechanika lidského skeletu a umělých náhrad jeho částí* [online, ucebnice euromise], Ústav informatiky AV ČR, Praha, 2000 [cit. 2013-07-08].
10. A. Sargeant and T. Goswami, Hip implants – Paper VI – Ion concentrations, *Materials and Design*, **28**, 155-171 (2007).
11. A. Sargeant and T. Goswami, Hip implants: Paper V. Physiological effects, *Materials and Design*, **27**, 287-307 (2006).
12. A. J. Smith, P. Dieppe, K. Vernon, M. Porter, A. W. Blom, Failure rates of stemmed metal-on-metal hip replacements: analysis of data from the National Joint Registry of England and Wales, *The Lancet*, **379**, 1199-1204 (2012).
13. A. L. Galvin, S. Williams, H. Peter, J. Thompson, G. Isaac, M. Stone, E. Ingham, J. Fisher, Comparison of wear of ultra high molecular weight polyethylene acetabular cups against alumina ceramic and chromium nitride coated femoral heads, *Wear*, **259**, 972-976 (2005).
14. M. Long, H. J. Rack, Titanium alloys in total joint replacement - a materials science perspective, *Biomaterials*, **19**, 1621-1639 (1998).
15. S. Gross, E. W. Abel, A finite element analysis of hollow stemmed hip prostheses as a means of reducing stress shielding of the femur, *Journal of Biomechanics*, **34** (8), 995-1003 (2001).
16. S. H. Teoh, Fatigue of biomaterials: a Review, *International Journal of Fatigue*, **22**, 825-837 (2000).
17. M. Long, R. Crooks, H. J. Rack, High-cycle fatigue performance of solution – treated metastable beta titanium alloys, *Acta Metallurgica*, **47** (2), 661-669 (1999).

## Structural Characterization and Electrochemistry of Layered $\text{Na}_{0.65}\text{Ni}_{0.5}\text{Mn}_{0.5}\text{O}_2$ obtained by Freeze-Drying Method

Kalapsazova, M., Stoyanova, R., Zhecheva, E.

Institute of General and Inorganic Chemistry – Bulgarian Academy of Sciences, 1113 Sofia, Bulgaria

Recent progress in design of cathode materials for lithium ion batteries is closely related with the systematic exploration of the relationships between the intercalation properties and the crystal structure of solids. Among several groups of compounds, layered lithium–nickel–manganese oxides,  $\text{LiNi}_{1/2}\text{Mn}_{1/2}\text{O}_2$ , are considered as the next generation of cathode materials, which are capable to displace the widely used layered  $\text{LiCoO}_2$  oxides (1). This is a consequence of the flexibility of their structures to accommodate nickel and manganese ions in different oxidation states.

Irrespective of the improved performance of lithium ion batteries based on  $\text{LiNi}_{1/2}\text{Mn}_{1/2}\text{O}_2$  cathodes, they are still expensive, resulting in the limitation of their application in large scale electrochemical energy storage systems. Searching for cheaper energy storage, sodium ion batteries have been recently advanced (2). The main advantages of sodium ion batteries are the high abundance and low cost for sodium, as well as the very suitable redox potential ( $E^\circ(\text{Na}^+/\text{Na}) = -2.71$  V versus standard hydrogen electrode; only 0.3 V above that of lithium). Although much research works have been done on the cathode materials for lithium ion batteries, the studies on electrode materials for sodium ion batteries remain scarce.

In this contribution, new data on the structure and intercalation properties of sodium nickel–manganese oxides as electrode materials are provided. The studies comprise the preparation and structural characterization of novel nickel–manganese oxides with compositions  $\text{Na}_{0.65}\text{Ni}_{0.5}\text{Mn}_{0.5}\text{O}_2$ . These compounds are different from the proposed  $\text{NaNi}_{1/2}\text{Mn}_{1/2}\text{O}_2$  compositions as electrodes in sodium-ion batteries (3). For the synthesis of  $\text{Na}_{0.65}\text{Ni}_{0.5}\text{Mn}_{0.5}\text{O}_2$ , a simple soft-chemical method is adopted. The method consists of freeze-drying of the acetate solution of  $\text{Na}^+$ ,  $\text{Ni}^{2+}$ ,  $\text{Mn}^{2+}$  ions leading to the formation of mixed Na–Ni–Mn–acetates. The thermal decomposition is examined by differential thermal and thermo-gravimetric analyses in different atmosphere – air and oxygen. The structure and morphology of  $\text{Na}_{0.65}\text{Ni}_{0.5}\text{Mn}_{0.5}\text{O}_2$  are determined by powder X-ray diffraction and SEM analysis. The lithium intercalation in  $\text{Na}_{0.65}\text{Ni}_{0.5}\text{Mn}_{0.5}\text{O}_2$  is carried out in model two-electrode lithium cells of the type  $\text{Li}|\text{LiPF}_6(\text{EC}:\text{DMC})|\text{Na}_{0.65}\text{Ni}_{0.5}\text{Mn}_{0.5}\text{O}_2$ .

Thermal decomposition of freeze-dried  $\text{Na}_{0.65}\text{Ni}_{0.50}\text{Mn}_{0.50}$  acetates yields a mixture of sodium carbonate, nickel oxides and sodium-deficient nickel–manganese oxides. The formation of target  $\text{Na}_{0.65}\text{Ni}_{0.5}\text{Mn}_{0.5}\text{O}_2$  compound starts at 400 °C by the reaction between the products of thermal decomposed acetates. The solid state reaction proceeds at a nano-scale region, as a result of which well-crystallized  $\text{Na}_{0.65}\text{Ni}_{0.5}\text{Mn}_{0.5}\text{O}_2$  with three-layered type structure (*P3*-type) is formed at 500 and 700 °C. It is worth to mention that the stable structural form experimentally established for  $\text{Na}_{2/3}\text{MnO}_2$  belong to the *P2*-type structure (4). The difference between *P3* and *P2*-structures comes from the number of the transition metal layers in the unit cell. In the *P3*-modification all  $\text{Na}^+$  ions occupy one prismatic site that shares face on the one side and edges on the other side with the surrounding  $\text{MnO}_6$ -octahedra. In *P2*-modification two prismatic sites, where one of them is sharing only faces and the second one is sharing only edges, are available for  $\text{Na}^+$  ions. The *P3*-type structure for  $\text{Na}_{0.65}\text{Ni}_{0.5}\text{Mn}_{0.5}\text{O}_2$  deviates from the well known *O3*-type structure for  $\text{NaMn}_{0.5}\text{Mn}_{0.5}\text{O}_2$  and  $\text{LiNi}_{0.5}\text{Mn}_{0.5}\text{O}_2$  analogues in respect of Na site symmetry occupancy: at *P3*-type structure  $\text{Na}^+$  occupies a prismatic site, while  $\text{Na}^+$  and  $\text{Li}^+$  are in the octahedral site at the *O3*-type structure. The lattice parameters for  $\text{Na}_{0.65}\text{Ni}_{0.5}\text{Mn}_{0.5}\text{O}_2$  seem insensitive towards the

annealing temperature varying between 500 and 700 °C:  $a = 2.8826$  and  $c = 16.8353$  for the oxide heated at 500 °C;  $a = 2.8864$  Å and  $c = 16.7664$  Å for the oxide heated at 700 °C.

$\text{Na}_{0.65}\text{Ni}_{0.5}\text{Mn}_{0.5}\text{O}_2$  oxide displays a reversible lithium intercalation. Figure 1 gives the electrochemical curves for  $\text{Li}^+$  intercalation in  $\text{Na}_{0.65}\text{Ni}_{0.5}\text{Mn}_{0.5}\text{O}_2$  at the potential range of 2.5-4.6 V. When the cell starts by a discharge, a capacity of 78 mAh/g is obtained. During the subsequent charge and discharge cycles, the cell delivers a reversible capacity of 133 mAh/g. The charge/discharge curves shows several plateau at  $\sim 3.00$  and  $\sim 3.85$  V, indicating a formation of distinct phases during lithium insertion and extraction in  $\text{Na}_{0.65}\text{Ni}_{0.5}\text{Mn}_{0.5}\text{O}_2$ . The electrochemical reaction of  $\text{Li}^+$  intercalation takes place thanks to the participation of  $\text{Ni}^{2+}/\text{Ni}^{4+}$  and  $\text{Mn}^{3+}/\text{Mn}^{4+}$  ionic couples. Before the electrochemical reaction,  $\text{Na}_{0.65}\text{Ni}_{0.5}\text{Mn}_{0.5}\text{O}_2$  oxides interact with the electrolyte leading to the partial exchange of  $\text{Na}^+$  by  $\text{Li}^+$ . It is suggested that small amount of sodium in ionic exchanged nickel-manganese phase stabilizes the layered structure during the electrochemical intercalation of Li. To outline the different intercalation mechanism of  $\text{Li}^+$  in  $\text{LiNi}_{0.5}\text{Mn}_{0.5}\text{O}_2$  and  $\text{Na}_{0.65}\text{Ni}_{0.5}\text{Mn}_{0.5}\text{O}_2$ , Figure 1 gives also the electrochemical curves for  $\text{Li}^+$  intercalation in  $\text{LiNi}_{0.5}\text{Mn}_{0.5}\text{O}_2$ .

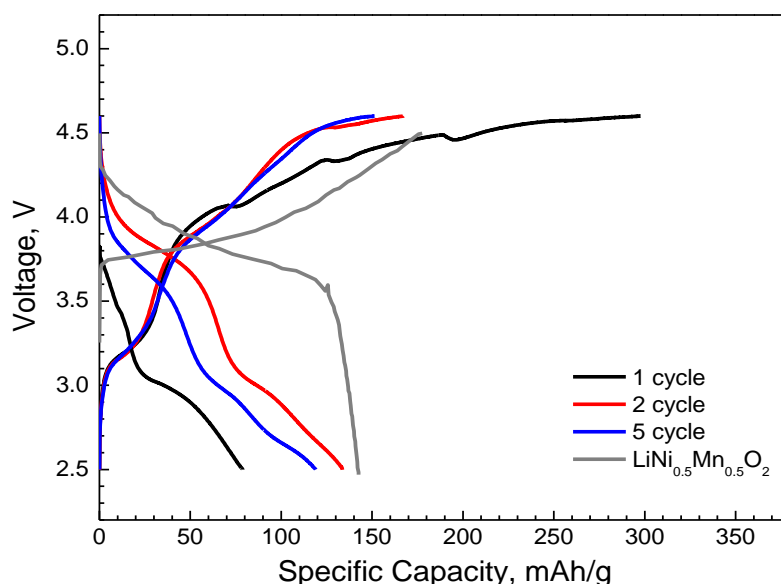


**Figure 1.** Charge/discharge curves for  $\text{Na}_{0.65}\text{Ni}_{0.5}\text{Mn}_{0.5}\text{O}_2$  in the model lithium ion cell. Grey lines correspond to reference  $\text{LiNi}_{0.5}\text{Mn}_{0.5}\text{O}_2$ .

In conclusion, the capability of  $\text{Na}_{0.65}\text{Ni}_{0.5}\text{Mn}_{0.5}\text{O}_2$  to intercalate reversibly lithium in high amount determines their potential for practical applications in lithium (or sodium) rechargeable batteries.

### Acknowledgment

This work was supported by ESF (Grant BG051PO001-3.3.06-0050).

### References

1. M. Yoncheva, R. Stoyanova, E. Zhecheva, R. Alcántara, G. Ortiz, J.L. Tirado, *Electrochimica Acta*, **54**, 1694 (2009)
2. Ellis BL, Nazar LF, *Curr. Opin. Solid State Mater. Sci.*, **16** (4), 168 (2012)
3. S.Komaba, N. Yabuuchi, T. Nakayama, A. Ogata. T. Ishikawa, I. Nakai, *Inorg. Chem.*, **51**, 6211 (2012)
4. M. Yoncheva, R. Stoyanova, E. Zhecheva, E. Kuzmanova, M. Sendova-Vassileva, D. Nihtianova, D. Carlier, M. Guignard and C. Delmas, *J. Mater. Chem.*, **22**, 23418 (2012)

## Effect of inhibitor on Zn-dendrite formation

Kaválek, O.<sup>1</sup>, Chladil, L.<sup>1,2</sup>, Máca, J.<sup>1</sup>

<sup>1</sup> Institute of Electrotechnology, Brno University of Technology, Faculty of Electrical Engineering and Communication, Technická 10, 616 00 Brno, Czech Republic

<sup>2</sup> Centre for Research and Utilization of Renewable Energy, Faculty of Electrical Engineering and Communication, BUT, Technická 10, 616 00 Brno, Czech Republic

E-mail: [ondrej.kavalek@phd.feec.vutbr.cz](mailto:ondrej.kavalek@phd.feec.vutbr.cz)

### Introduction

Ni-Zn alkali accumulators have the big advantages in comparing with Ni-Cd or Ni-MH thanks to their high energy density, higher voltage and thanks to ecological aspect. But now many unsolved problems as shape changes during cycling, poisoning of positive electrodes by zinc and dendrite growth still exist and thus reduces the battery lifetime and thereby preventing commercial using. Therefore, we have focused on dendrite growth in this contribution. Not only suppressing abilities of dendrite are needed but also we must ensure low charging potential which hinder to hydrogen generation [1.-3.]. There were studied effects of TEPA, Lugalvan P, Slovasol on inhibition of Zn-dendrite growth in Zn-Ni batteries.

### Experimental



**Figure 1.** System for measuring Zn dendrite growth

The working electrode was made by molding of 3 mm thick zinc wire. All electrodes had size 1 x 2 cm. As reference electrode were used Zn wire coated by polyolefin insulation tube. Therefore all measured potentials are versus Zn ref. el. There were used Ni meshes counter electrode and separator Toray PS0100S to prevent access of evolving gas to the measuring electrode. Before measurement working electrode were cleaned and polished by sandpaper with 3 000 grain/cm<sup>2</sup>. All electrodes with separator were inserted into 25ml vial which were filled by 20ml of 6M KOH electrolyte saturated by ZnO with 40µl appropriate additives. Large excess of electrolyte accelerate the dendrite growth because all charging current is consumed to Zn deposition.

Measurements were performed by  $\mu$ -Autolab (Figure 1) and Biologic potentiostat/Galvanostat. We applied charging and discharging current 20 mA for 2 hour. The five cycles were performed and formation of dendrites was monitored by Olympus microscope, which takes one picture every 6 minutes. After that we created the movie from acquired images.

### Result and discussion

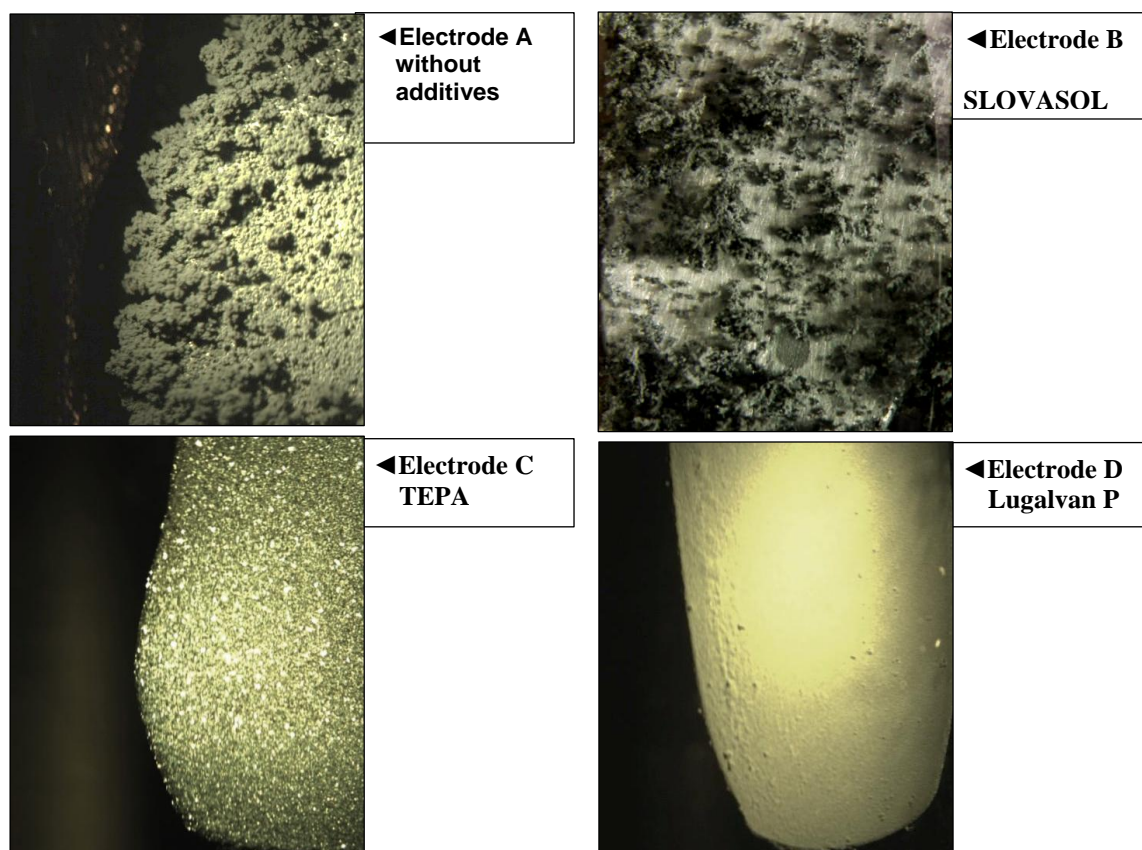


**Figure 2.** Effect of additives on dendrite growth

On figure 2 we can see the comparison of surface images of electrodes after cycling.

From comparison of surfaces is obvious that all additives have the essential effect on dendrite creation. Electrode A which was cycling in electrolyte without any additive has a large non-uniformly distributed dendrites which preferred grow on the edges of electrode. Moreover created movie shows that dendrites are gradually redistributed towards to the bottom side during cycling. This leads to creation of typical pear-shaped electrodes.

Addition of TEPA eliminated all dendrites and created layer is without porosity. This additive is useful for galvanic application, but for battery isn't suitable, because we need the slightly porous electrodes which have larger active area and allow using higher currents. Moreover charging potential is stable on value -100 mV vs. Zn ref. el. Observable gassing takes place on electrode at this value of potential.

Dendrites incurred in the electrolyte with the additive Slovasol have a specific shape and their growth occurs only in certain locations that are evenly distributed over the surface of the electrode. Dendrites don't grow preferentially on the edges of the electrodes and mechanically not much

coherent with the electrode and easily fall off. Charging potential is again relatively high and is about - 80mV vs. Zn el ref.

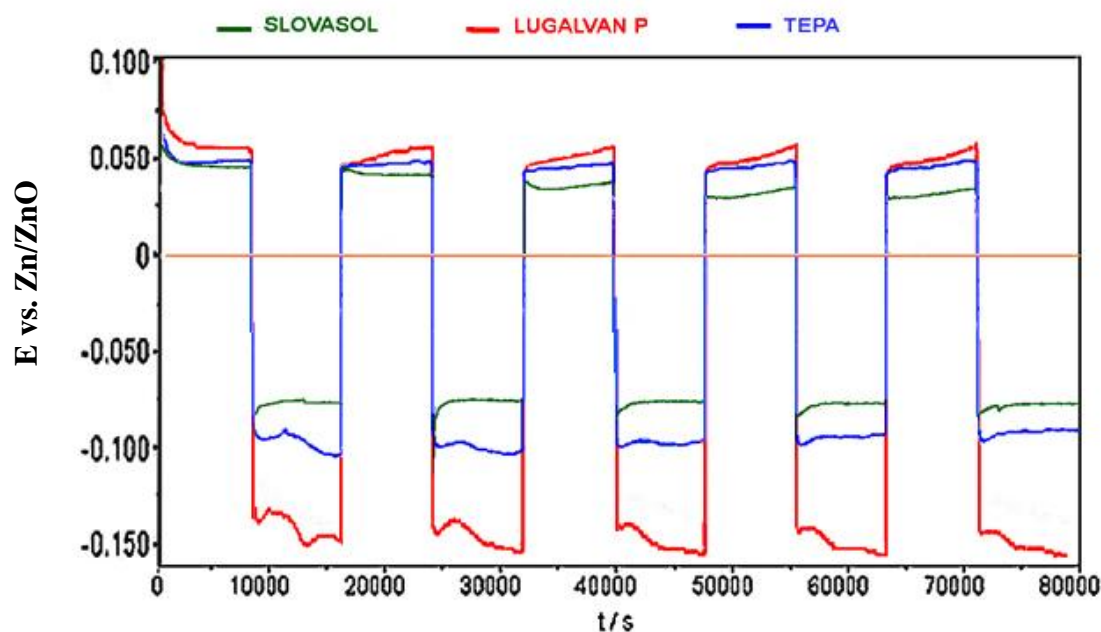


**Figure 3.** Charging and discharging potential of electrode in electrolyte with different additives

Lugalvan P help created homogeneous and compact slightly porous layer without significant dendrites. But from figure 3 is obvious that this required the highest overvoltage at charging from all comparison samples.

### Conclusion

Influence of additives on Zn dendrite grow were measured. It was found that many additives aren't suitable for battery application because these additives can created non-porous Zn layer or can created porous layer but with higher overvoltage at charging cycle. From the studied additives, Lugalvan P it might be an appropriate additive for dendrite inhibition, because help created uniform porous layer without dendrite.

### Acknowledgement

This work was supported by the grant MPO FR-TI3/198 and project FEKT-S-11-7.

### References

1. Lan, C.J., C.Y. Lee, and T.S. Chin, Tetra-alkyl ammonium hydroxides as inhibitors of Zn dendrite in Zn-based secondary batteries. *Electrochimica Acta*, 2007. **52**(17): p. 5407-5416.
2. Kan, J.Q., H.G. Xue, and S.L. Mu, Effect of inhibitors on Zn-dendrite formation for zinc-polyaniline secondary battery. *Journal of Power Sources*, 1998. **74**(1): p. 113-116.
3. Yang, Z.H., et al., Effects of dispersant on performance of Ni-Zn batteries. *Journal of Central South University of Technology*, 2010. **17**(5): p. 930-935.

## Pulse charging of lead acid batteries

Křivík, P.

Department of Electrotechnology, Faculty of Electrical Engineering and Communication, Brno University of Technology, Technická 10, 616 00 Brno, Czech Republic

### Abstract

For charging of lead acid batteries it can be used several different methods - from constant current charging to constant voltage charging, or a combination of these methods (constant current charging with voltage limitation). Nowadays there is an increasing development of charging method based on current pulses (1-2).

Pulse charging has an advantage by shortening of the charging time (compared to the constant current charging with voltage limitation) and extension of the lead acid battery cycle life (compared to the constant current charging without voltage limitation). Generally, the charging cycle comprises the charging current pulses and the standing time, and between them can or cannot still be short discharge pulses. The cycle is repeated until the battery is fully charged. During charging can be reduced the height or length of pulses, depending on the battery state of charge. This method of charging can prevent overheating of the battery, which can extend the battery life. Another advantage is the reduction of gassing, because of decreasing the amount of charge delivered during the pulse (3-4).

Although the constant current charging method is recommended for the majority of producers of lead acid batteries, it causes the capacity reduction and the cycle life decreasing. The capacity reduction of cells is associated with progressive changes in the positive active mass arising as a result of charging. In addition, the effectiveness of pulse charging is about 15-30% higher than during constant current charging. The pulse current method of charging can be used at higher current (compared with constant current charging) without damaging the electrode active materials. Pulse charging, however, due to the increased charge current can cause the elevated temperature of the lead acid battery.

### Experiment

For the experiment investigating influence of pulse charging on the functional characteristics of lead acid battery, we selected two test cells with a capacity of about 1 Ah, each with a different method of charging. Cells were composed of one positive and one negative electrode separated by a separator made of glass fibres of 1 mm thick, immersed into the sulphuric acid solution electrolyte with a concentration of 1.24 g/cm<sup>3</sup>, inserted into PVC vessel. After assembling the cells were first subjected to 16 cycles of formation, where one formation cycle included charging with constant current of 0.2 A for 4 hours and then 2 hours of standing. After the formation the cells were subjected to the first experiment.

Discharge was carried out at constant current of 0.4 A to the final voltage of 1.6 V.

The first cell was subjected to pulse charging a second cell was charged by constant current with voltage limitation.

Discharge was carried out at constant current of 0.4 A to the final voltage of 1.6 V.

Pulse charging was composed of two parts - the charging current of 0.4 A for a period of 7 s and standing for a period of 3.5 s. The voltage at the end of the charging interval ( $U_{ch}$ ), the voltage at the end of the standing interval ( $U$ ), voltage during discharge ( $U$ ) and total charge during charging and discharging ( $Q$ ) were recorded. Charging was completed at 110% of the capacity obtained from the previous discharge.

In the first charging stage (Fig. 1) in the range of 0-70% of supplied charge, the voltage at the end of the charging period is slowly increasing from about 2.2 to 2.4 V, as a result of charging reactions at the both electrodes. In the second stage of charging, since about 70% of supplied charge, the voltage at the end of the charging interval rapidly increases approximately from 2.8 to 3 V and dominantly begins the gassing reaction (electrolysis). The voltage measured at the end of the standing period grows during charging from approximately 2.05 V to 2.35 V.

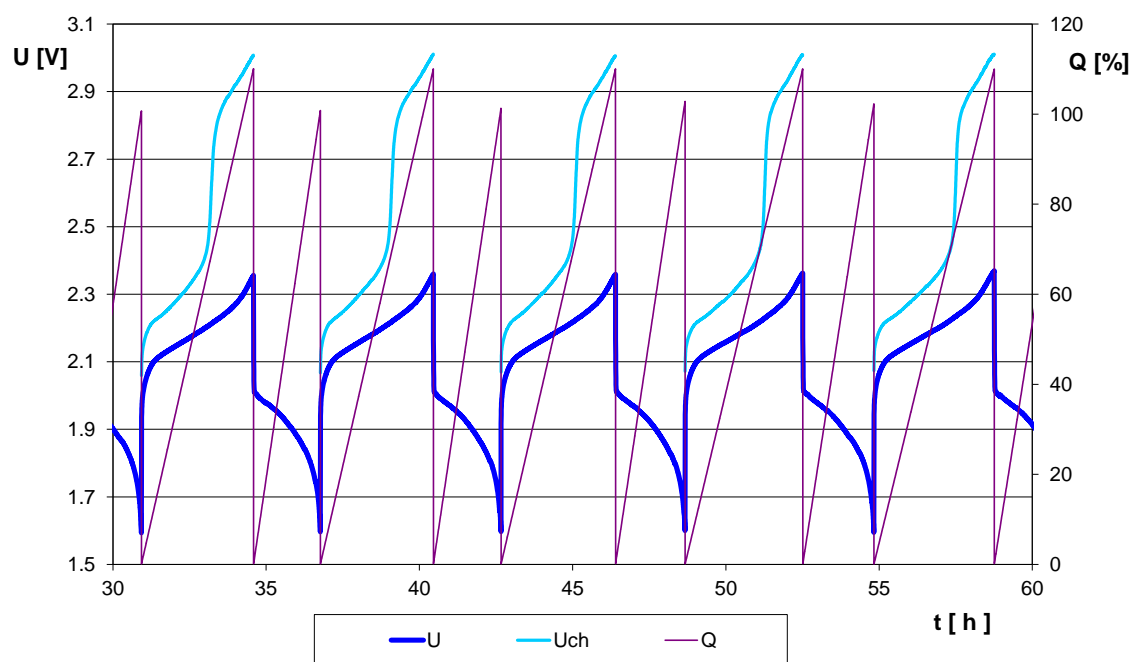


**Figure 1.** The dependence of voltage and charge during pulse charging.

$I = 0.4 \text{ A } t = 7 \text{ s}, I = 0 \text{ A } t = 3.5 \text{ s}, Q = 110\%$

The second cell was charged by constant current of 0.4 A with voltage limitation of 2.45 V. Charging was ended at 110% of the capacity obtained from the previous discharge.

As seen from Fig. 2, during the cycling there is a gradual lengthening of the charging time due to the gradual completion of electrode formation of electrodes originally not completely formed. This is also evident on the final current during charging that gradually declined during cycling. Thus, the cell lasted longer than charged to the 110% of the capacity.

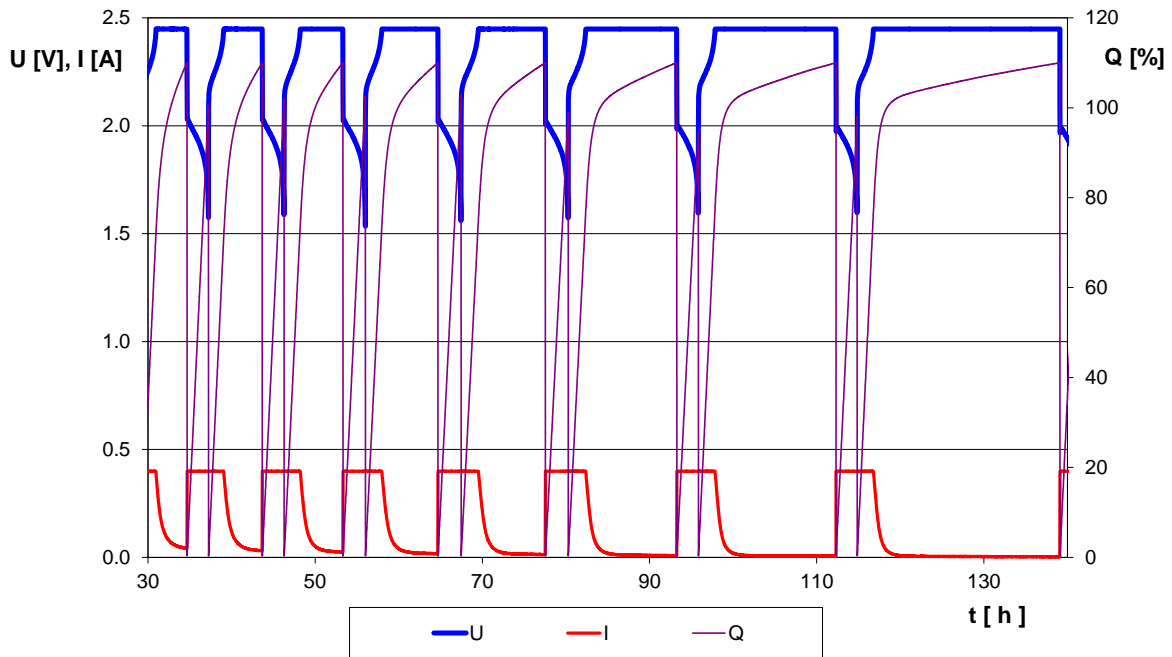


**Figure 2.** The dependence of voltage, current and charge during constant current charging with voltage limitation  $I = 0.4 \text{ A}$ ,  $U = 2.45 \text{ V}$ ,  $Q = 110\%$

Fig. 3 shows the comparison of capacity dependencies of the cells charging with the pulse current method and constant current method with the voltage limitation.

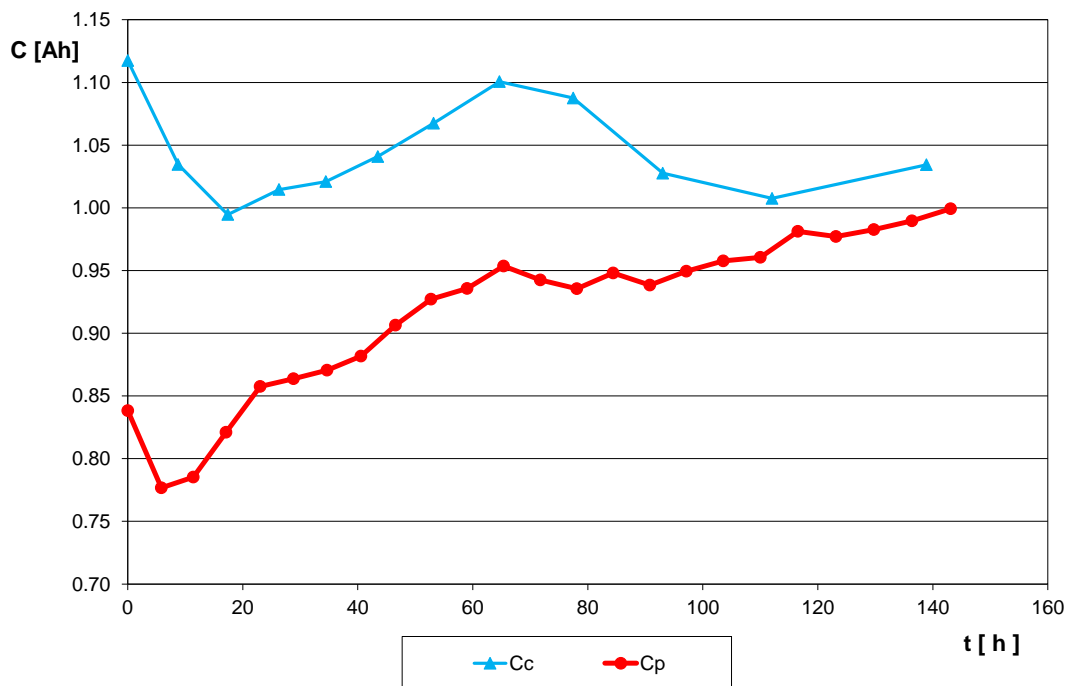


**Figure 3.** The resulting cell capacities, subjected to constant current charging method with voltage limitation ( $C_c$ ) and pulse current charging method ( $C_p$ )

During constant current charging with the voltage limitation the cell capacity is maintained around its original value at the end of the experiment with a slight decline. The decline in the capacity is 0.1 Ah in the course of the 12 cycles.

In contrast, during the pulse current charging it was achieved positive results in capacity dependence. Besides the initial decrease the cell capacity continued to grow. The increase was 0.17 Ah within 24 cycles.

Due to the differences in the number of cycles of two cells it is also seen that the pulse charging is possible to reach the state of full charge in the half time than in the case of constant current charging with the voltage limitation.

### Conclusions

Pulse charging method can lead both to a reduction in charging time and to increase or at least to maintain the capacity of the lead acid battery cell. It is necessary to test more pulse charging modes varying by length and size of pulses in order to find the optimal mode for charging the lead acid battery cell.

As an alternative it is possible add a short discharge pulses to pulse charging, possibly during charging it can be gradually reduced the height or length of pulses, depending on the battery state of charge.

### Acknowledgements

This work was sponsored by the internal grant No. FEKT-S-11-7 and by the EU project CZ.1.05/2.1.00/01.0014.

### References

1. L. Lam, H. Ozgun, O. Lim a J. Hamilton, Pulsed-current charging of lead/acid batteries-a possible means for overcoming premature capacity loss, *Journal of Power Sources* **53**, Issue 2, p. 215–228, Melbourne, Australia, ISSN: 0378-7753, 1995
2. D.A.J. Rand, J. Garche, P.T. Moseley and C.D. Parker, Valve regulated lead acid batteries, ISBN: 978-0-444-50746-4, 2004
3. A. Chih-Chiang Hua, B. Zong-Wei Syue, Charge and discharge characteristics of lead-acid battery and LiFePO<sub>4</sub> battery, The 2010 International Power Electronics Conference (IPEC), Taiwan, p. 1478 – 1483, ISBN: 978-1-4244-5394-8, 2010
4. G. Yifeng, H. Limin, The charging technology for lead-acid battery with a negative pulse, Power and Energy Engineering Conference (APPEEC), 2010 Asia-Pacific, Beijing, China, p. 1-3, ISBN: 978-1-4244-4812-8, 2010

## Alkali hydroxide doped PVA membranes

Kunovjánek, M.<sup>1</sup>, Musil, M.<sup>1</sup>, Trnková, L.<sup>2,3</sup>

<sup>1)</sup> Department of Electrotechnology, Brno University of Technology, Faculty of Electrical Engineering and Communication, Technická 3058/10 616 00 Brno, Czech Republic.

<sup>2)</sup> Department of Chemistry, Masaryk University in Brno, Faculty of Science, 753/5, Bohunice, Brno, Czech Republic

<sup>3)</sup> Central European Institute of Technology, Brno University of Technology, Technická 3058/10, CZ-616 00 Brno, Czech Republic, European Union

### Abstract

Membranes with high ionic conductivity are used in many branches of electrochemical industry. Electrolysis, fuel cells and moreover alkaline batteries can be mentioned. This paper is focused on polymer membranes made from polyvinyl alcohol (PVA), which were doped with alkali hydroxides (potassium hydroxide - KOH, sodium hydroxide - NaOH and lithium hydroxide LiOH). Using impedance spectroscopy the temperature dependence of electric resistance of membranes were studied and discussed. .

### Introduction

Polyvinyl alcohol is white powdered material, which exhibits its crystalline character. This material is excellent thanks to high tensile strength, flexibility, high thermal and chemical stability, solubility in water and moreover ability to form thin film layer. PVA properties are set not only by the length of the polymer chain, but by the orientation of syndiotactic and isotactic chain sequences too. This material can be assumed to be a mixture of vinyl alcohol and vinyl acetate polymers. This mixture is soluble in water thanks to vinyl alcohol dominance. In some cases reaches weight fraction of acetylene residues up to 11 %. It corresponds to 88 mol. % hydrolysis of the basal polyvinyl acetate.

Properties of PVA membranes were many times changed by addition of various additive types. For example, in [1] is Polyvinylchloride (PVC) into the volume of PVA added to improve thermal, mechanical and electrochemical properties of membranes. Resulting mixture was consequently crosslinked by glutaraldehyde. Thin PVA film forms after excesses water evaporation.

In reference [2] authors doped PVA solution with small amount of titanium dioxide (TiO<sub>2</sub>). Mixture was crosslinked using glutaraldehyde and weak sulfuric acid as a catalyst.

Borax crosslinking is described in [3]. This method is very prospective, because hydroxides doped PVA solutions cannot be crosslinked with glutaraldehyde (reaction with glutaraldehyde runs just in acid pH). PVA was as a water solution in desired concentration. Small amount of borax was added subsequently. Borax concentration affects reaction kinetics - crosslinking process can be finished in just several seconds.

According to [4], it is possible to prepare alkali hydroxides doped PVA membranes. The only disadvantage of this method was long time for preparation. PVA and KOH solutions must be stirred

for hours. If not, KOH releases from the bulk of resulting PVA membrane. Best results were achieved at concentration ratio of PVA and KOH set up 60:40. Membranes with this concentration ratio proved excellent properties.

### Experimental

PVA Mowiol purchased from Kuraray was dissolved in water into resulting 10 wt. % solution. Hydroxide solutions of KOH, NaOH and LiOH were prepared afterwards. According to [4], KOH was prepared in 10 wt. % water solution. Following hydroxides were prepared in such a molar concentration, that hydroxide content in every membrane would be the same. Mixtures of PVA and hydroxides (concentration rate 60:40) were stirred in during 24 hours. A small amount of glycerin was added to improve mechanical properties of membrane. Membranes treated with glycerin are more flexible.

Crosslinking process initiated by sodium tetraborate (borax) run at room temperature. 1 wt. % water solution of borax was prepared. Subsequently 2 grams of borax solution was added to the final 20 g mixture containing PVA, hydroxide and glycerin. Borax was very quickly stirred into the bulk of PVA mixture. This resulting solution was poured into Petri dish and let crosslink at room temperature (the crosslinking process takes just several seconds).

Membranes were in Petri dishes for three days. Subsequently were peeled off and dried at 50 °C for several hours to evaporate possible residual moisture. Some of them were swelled in 1 mol . l<sup>-1</sup> KOH solution.

To find out resistivity of membranes, 4 electrodes cell, which was designed for these purposes, was used. The cell contains two working Pt electrodes and two referent Hg/HgO electrodes, which indicate voltage differences on membrane. The membrane is placed in the annular middle of the cell.

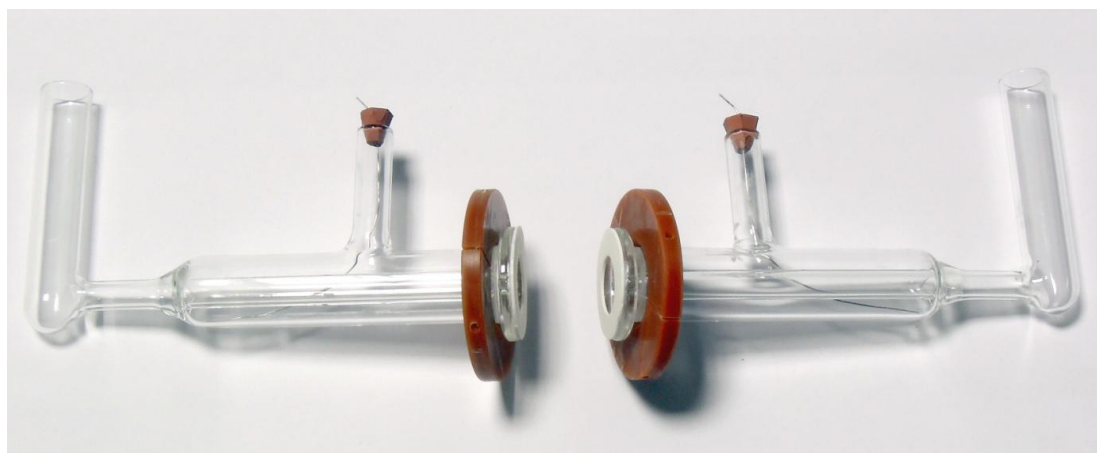


**Figure 1.** Four electrode cell designed for ionic resistivity measurements.

Impedance spectroscopy runs on potentiostat VSP Biologic. All samples were tempered in the climate chamber with set temperature. Measurement started at temperature 0 °C and finished at 50 °C with 10 °C step. Every set temperature was stabilized for 24 hours.

Empty cell filled with just electrolyte and then cell embedded with membrane were measured on resistance at every temperature. Membrane resistance was calculated as a difference between these two values. Measurement results are summarized below in Table 1.

**Table I.** Electric resistances of three PVA membrane types in KOH electrolyte

$v$ [°C]	Membrane electric resistance [ $\Omega$ ]		
	PVA+KOH	PVA+NaOH	PVA+LiOH
0	0.194	0.163	0.426
10	0.136	0.110	0.353
20	0.105	0.075	0.260
30	0.070	0.045	0.205
40	0.039	0.032	0.170
50	0.062	0.066	0.170

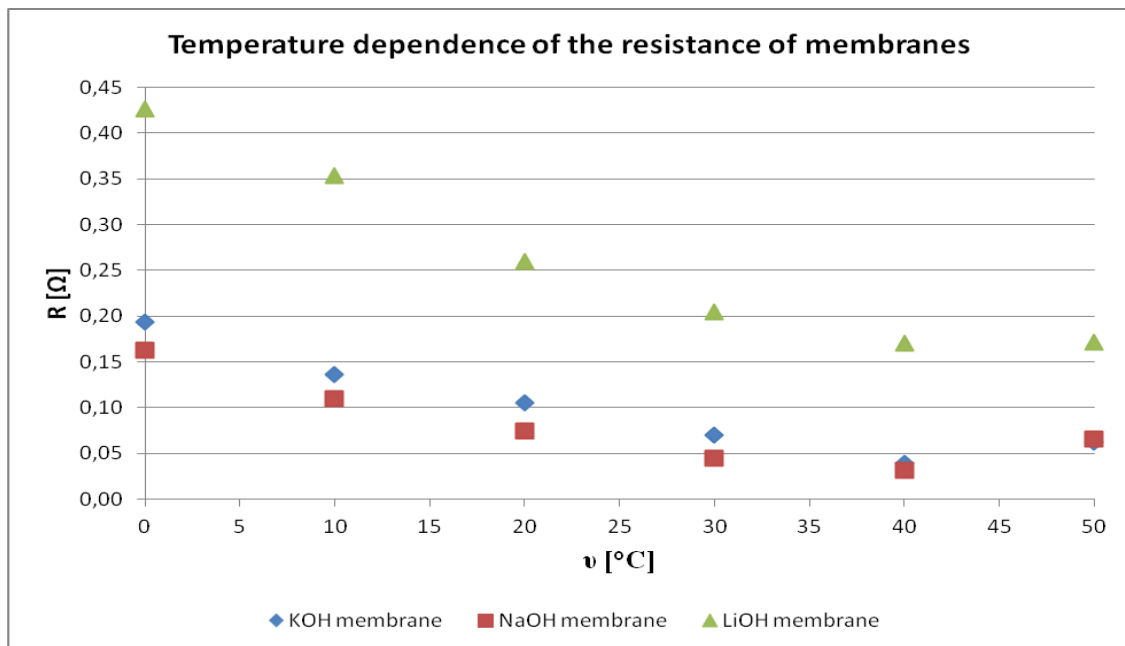


**Figure 2.** Temperature dependence of membrane resistances

LiOH doped PVA membrane demonstrates the highest electric resistance from all the samples. KOH and NaOH doped have similar resistance. It is obvious (Figure 2) that resistance is temperature dependent with minimum at 40 °C.

From the „mechanical“ point of view, the LiOH doped PVA membrane proved best results - high tensile strength and thin profile. KOH and NaOH doped membranes were flexible, but without sufficient tensile strength. It was easy to tear them. This problem could be solved by application of PVA and hydroxide mixture on the suitable under layer. For example nonwoven polypropylene textile could ensure strength and moreover, polypropylene is alkali hydroxides resistant.

For all membranes specific conductivity was calculated. For this calculation we need thickness of membrane and measured area. Measured area was the same for all membranes and is given by area of cell ( $S = 2,11 \text{ cm}^2$ ). Thickness of membrane ( $l$ ) was measured by digital micrometer (KOH = 0,826 mm, NaOH = 0,713 mm, LiOH = 0,34 mm). Specific conductivity ( $\gamma$ ) of membranes was calculated by equation:

$$G = \gamma \cdot \frac{S}{l}$$

Specific conductivities of membranes are in Table 2. As you can see, membranes doped by KOH and NaOH have similar results. Membrane doped by LiOH has lower specific conductivity.

**Table II.** Specific conductivity of three PVA membrane types in KOH electrolyte

$\nu$ [°C]	Membrane specific conductivity $\gamma$ [mS.cm <sup>-1</sup> ]		
	PVA+KOH	PVA+NaOH	PVA+LiOH
0	202	207	38
10	288	307	46
20	373	451	62
30	559	751	79
40	1004	1056	95
50	631	512	94

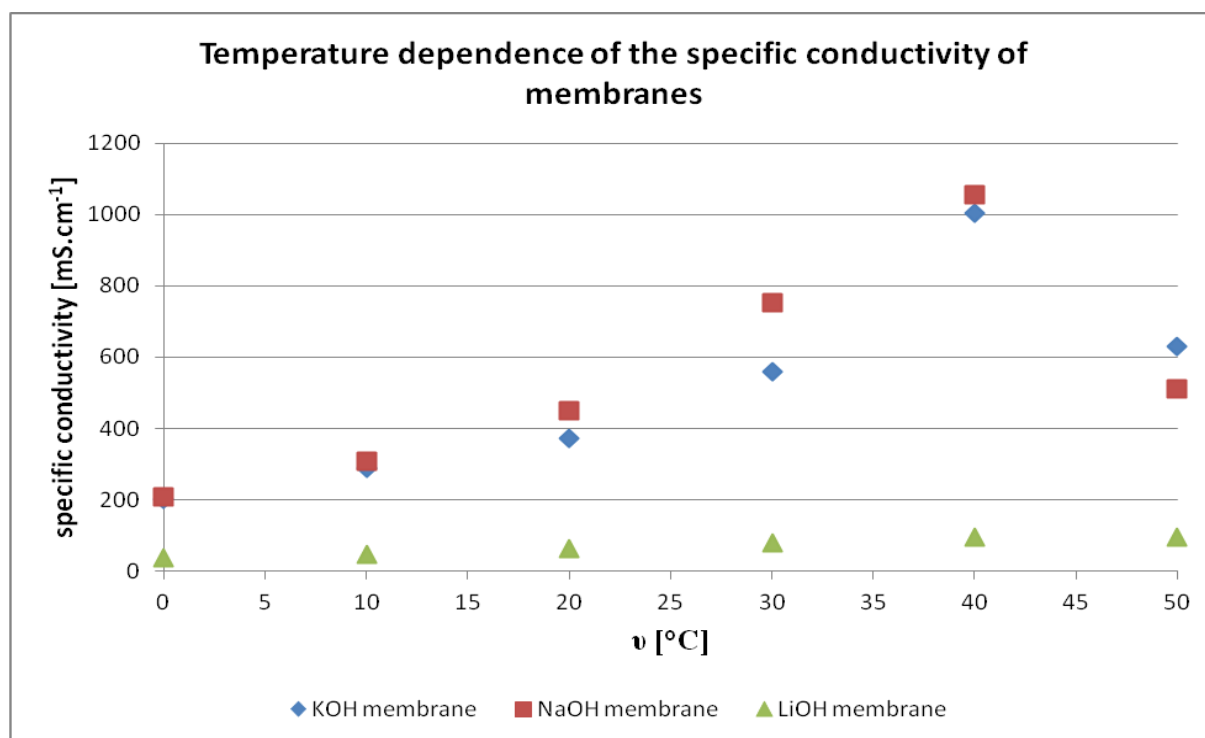


**Figure 3.** Temperature dependence of the specific conductivity of membranes

### Conclusion

Based on the literary researches, 3 alkali hydroxides doped PVA membrane types were fabricated. Electric resistance of these membranes was measured by impedance spectroscopy within four electrode cell. All the membranes prove high ionic conductivity, particularly these, which were doped with KOH and NaOH hydroxides. These membrane types will be further applied in fuel cells and electrolyser. Power and other characteristics will be determined.

### Acknowledgements

This work was supported by the grant FEKT-S-11-7 and CEITEC – Central European Institute of Technology Project CZ.1.05/1.1.00/02.0068.

### Literature

1. Chun-Chen Yanga, Jen Ming Yangb, Cheng-YeouWuc, Poly(vinyl alcohol)/poly(vinyl chloride) composite polymer membranes for secondary zinc electrodes, *Journal of Power Sources* 191 (2009) 669–677
2. Potočková, L., Stabilita kompozitních filmů polyvinylalkoholu s oxidem titaničitým, *Bakalářská práce*, Brno 2009, Fakulta chemická, VUT Brno
3. David A. Katz, *POLYVINYL ALCOHOL SLIME*, 2005
4. Saleem, M, Sayyad M.H., Karimov, Kh.S., Ahmad, Z., Fabrication and Investigation of the Charge/Discharge Characteristic of Zinc/PVA-KOH/Carbon Cell, *Acta Physica Polonica A*, Vol. 116 (2009)

## Temperature Dependence of the Electrical Properties of Nanocomposites

Polsterová, H.

Institute of Electrotechnology  
Faculty of Electrical Engineering and Communication  
Brno University of Technology, Czech Republic

Nanotechnology and nanomaterials have very good mechanical and electrical properties. Therefore, they are currently a rapidly growing field, which is used in many sectors (machinery, electronics, chemicals and pharmaceuticals, textiles, etc.). The properties of nanomaterials depend on the contents of nanofillers in the matrix. Ideal nanocomposites are a homogeneous matrix of uniformly dispersed filler particles with dimensions of the order of nanometers. The distance between the particles decreases with increasing concentration. When the particle diameter is small, the decrease is very fast already at low concentrations. Distance does not depend only on the particle concentration, but also on the ratio between the densities of the filler and the matrix (1).

In the area of contact with the matrix particles arises an interface. In this area there are gradual changes in properties of nanocomposites, which change gradually from the properties of particles to the properties of the surrounding matrix. Interface surrounds the particle within a distance of a few nanometers. Contact of the fundamental matrix with particles may lead to a formation of a new phase. It has properties different from those of matrix properties and the properties of aggregates, and could have a decisive influence on the properties of the nanocomposite.

### Experimental

A four-component casting epoxy resin that is used in the ABB Company, Brno, was selected for the matrix. As the filler, Al<sub>2</sub>O<sub>3</sub> nanoparticles, supplied by firm Sigma Aldrich, were used. Nanoparticles size of < 50 nm with a surface area > 40 m<sup>2</sup>g<sup>-1</sup> was guaranteed by the nanofiller manufacturer.

The nanofiller shares in samples were selected by percentage 0, 0.5, 1 and 2 (by weight). Casting was carried out by using a steel mould, which allowed to simultaneously prepare 10 samples in the shape of plane parallel plates with dimensions 110 × 110 mm and of thickness 2 mm. The surface of samples was sufficiently even, smooth and plane parallel, so that it was not necessary to use evaporated electrodes. In the course of measurements, samples were mounted in the three-electrode press-on system Tettex 2904. Measurements of electrical properties were carried out on dried samples at zero relative humidity. The closed space of the measuring capacitor was filled with molecular sieve. The sample was fetched from the desiccator to the measuring capacitor always the day before the measurement. Once the sample was transferred from the desiccator to the measuring capacitor, the temperature in the electrode system was raised for a short time to some 100 °C; in the course of the following night, the temperature was lowered to the value required for the experiment. The experiment was carried out the next day.

The samples were for the following dielectric properties measured: relative permittivity and dissipation factor in the frequency of range 50 Hz, internal and surface resistivity (using megaohmmeter Radiometer IM6).

## Results

The following figures (Fig. 1, 2 and 3) display the temperature dependence of internal resistivity, dielectric constant and dissipation factor for samples with filler containing 0, 0.5, 1, and 2 percent of nanoparticles of aluminum oxide ( $\text{Al}_2\text{O}_3$ ). From the graph in Fig. 1 –graphical dependence intrinsic resistivity  $\rho_v$  to temperature – it can be seen that the samples containing nanoparticulate fillers 0.5 % have lower internal resistivity in the entire temperature range. This value weight percent performance could be taken as the critical value. At higher weight percentage of  $\text{Al}_2\text{O}_3$  nanoparticles filling the inner resistivity higher than that of pure epoxy (0 % of nanofiller content).

The graph at Fig. 2 is a graphical display of the dependency of the dissipation factor  $\text{tg } \delta$  on the temperature. It is apparent that the samples with the performance of 1 and 2 %  $\text{Al}_2\text{O}_3$  nanoparticles exhibit significantly lower dissipation factor  $\text{tg } \delta$  at higher temperatures. In the area of higher temperatures and frequencies, the decrease dissipation factor  $\text{tg } \delta$  was observed and measured as in (3). Samples subsidized by nanoparticulate filled with  $\text{Al}_2\text{O}_3$  content of 0.5 weight percent showed a higher dissipation factor than pure epoxy. This may be due to the low volume fraction of the nanoparticles in the epoxy.

Waveforms of relative permittivity depending on the temperature are graphically depicted in Fig. 3. It is apparent that the samples, again with the performance of 0.5 %  $\text{Al}_2\text{O}_3$ , show a higher permittivity than pure epoxy. For samples with higher filler content of  $\text{Al}_2\text{O}_3$ , significant decline in permittivity against pure epoxy was recorded at higher temperatures. This could lead to a claim that a growing percentage of alumina nanoparticles filling the resulting nanocomposite dielectric constant will decline.

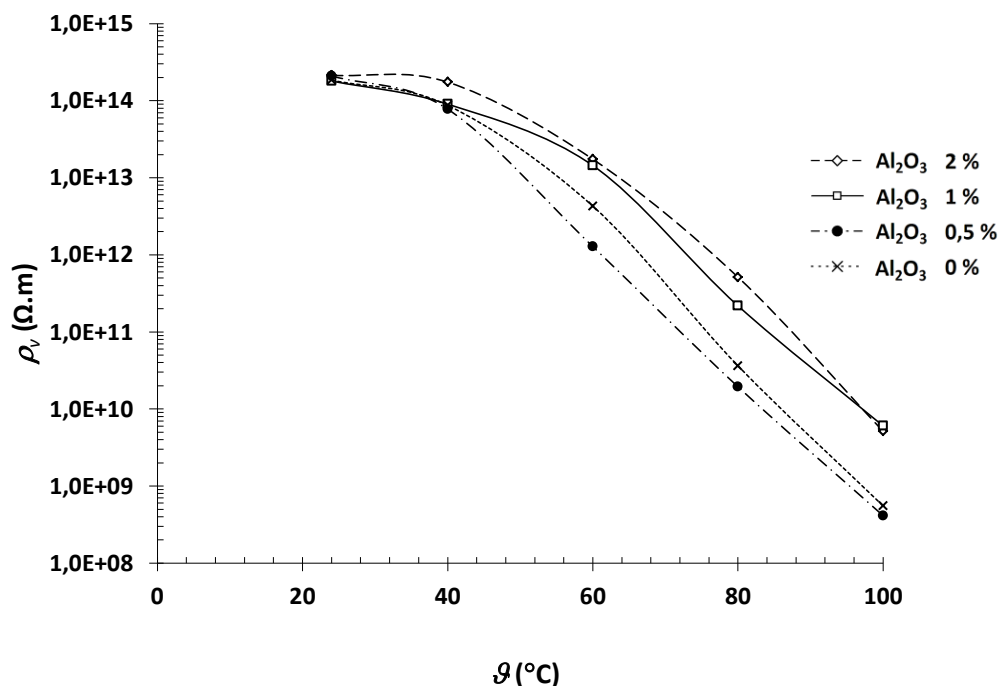


**Figure. 1** Graph of internal resistivity temperature dependence (parameter – content of  $\text{Al}_2\text{O}_3$  )

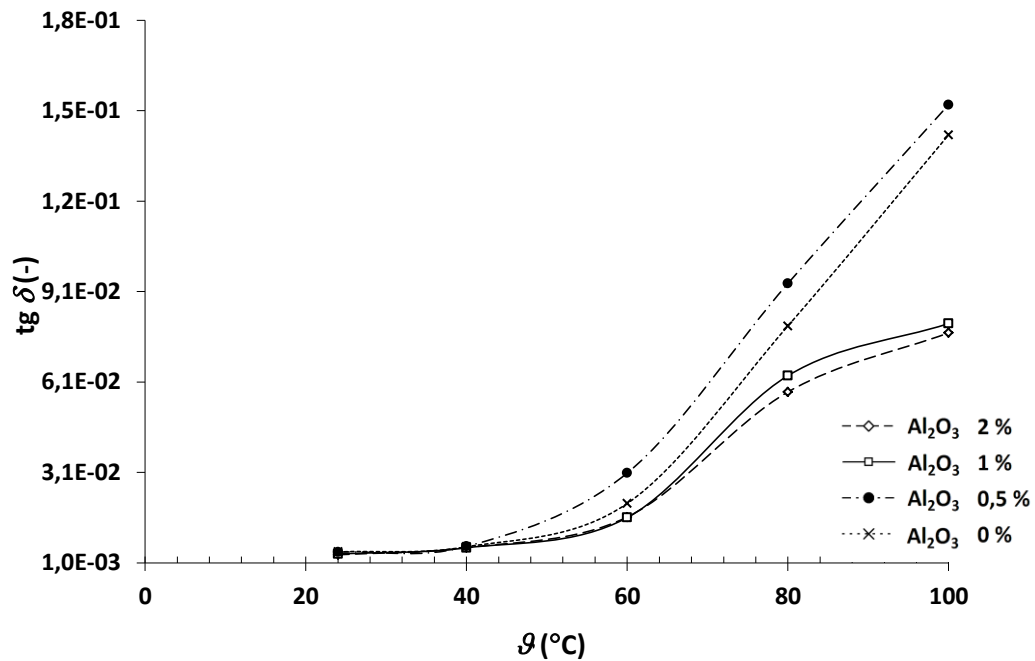


Figure 2. Graph of permittivity temperature dependence (parameter – content of  $Al_2O_3$ )

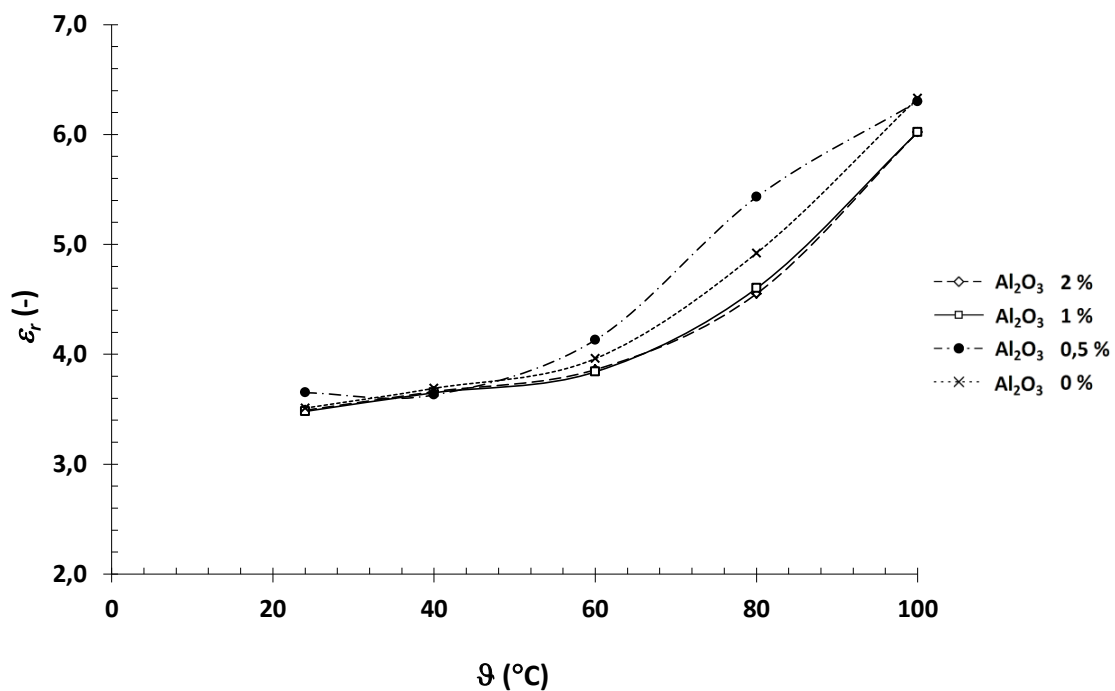


Figure 3. Graph of the dissipation factor temperature dependence (parameter – content of  $Al_2O_3$ )

### Conclusion

Electrical properties of epoxy resin itself, from which samples were made, are very good. Nevertheless, increase of the internal values of resistivity and a decrease in dielectric constant for samples with higher filler contents can be observed at higher temperatures. Volume of inside

resistivity increasing at higher temperatures can be attributed to stronger ties between the nanofiller particles in filler (2).

It can be stated that for samples with filler content of 1 and 2 %, decrease of the dissipation factor appears at higher temperatures.

### Acknowledgment

The work described in this paper was supported by the FEKT-S-11-7 project “Materiály a technologie pro elektrotechniku”. Its support is gratefully acknowledged.

### References

1. J.T.Lewis, "Nano-Composite Dielectrics," *The Dielectric Nature of the Nano-Particle Environment*, IEEE Trans. FM, vol. 126, no.11 pp. 1020–1030, 2006.
2. D.R. Paul, C.B. Bucknall, *Polymer Blends* [4]. Volume 1: Formulation. New York: John Wiley Sons, 600 p. ISBN 0-471-352-79-9, 2000
3. TANAKA, T. Dielectric Nanocomposites with Insulating Properties. In *IEEE Transactions on Dielectric and Electrical Insulation*. roč. 12, č. 5. Říjen 2005. ISBN 1070-9878/05
4. LIBRA, M. *Elektrické vlastnosti nanokompozitů* – diplomová práce. Brno, 2011. 52 s. Vedoucí diplomové práce Ing. Helena Polsterová, CSc. FEKT VUT v Brně

## Analysis of luminescence radiation interact by silicon defects

Stojan, R.<sup>1,\*</sup>, Vaněk, J.<sup>1</sup>, Malý, M.<sup>1</sup>, Gvritishvili, R.<sup>1</sup>, Šimonová, L.<sup>1</sup>, Frantík, O.<sup>1,2</sup>

<sup>1</sup> Department of Electrical and Electronic Technology, Brno University of Technology, 616 00 Brno, Czech Republic, \*e-mail: [xstoja00@stud.feec.vutbr.cz](mailto:xstoja00@stud.feec.vutbr.cz), \*phone: +420 54114 6168

<sup>2</sup> Solartec, s.r.o., Televizni 2618, 756 61 Roznov pod Radhostem, Czech Republic

### Introduction

Luminescence diagnostic methods of solar cells have still significant diagnostic potential. According to the excitation method of luminescence radiation from silicon solar cells we talk about electroluminescence or photoluminescence methods.

It is known that luminescence radiation is characterized as electromagnetic waves by intensity, spectrum, coherence, duration and polarization. This paper deals about new potential in to use one of those characteristics luminescence radiation for detection defects of solar cells. Polarization spectroscopy of defects in solar cells may be used to better characterization of solar cells. We used the existing electroluminescence technology and extend it about known polarization spectroscopy to yield the polarized luminescence light by defect in solar cells structure (in wavelengths area with peak about 1100 nm).

### Method

A fast surveying characterization tool providing spatially resolved information about electrical, optical and material properties of silicon solar cells is electroluminescence. It is technique that use a CCD camera. Bandgap luminescence of crystalline silicon solar cell in forward-biased is surveyed with a CCD grey-scale camera.

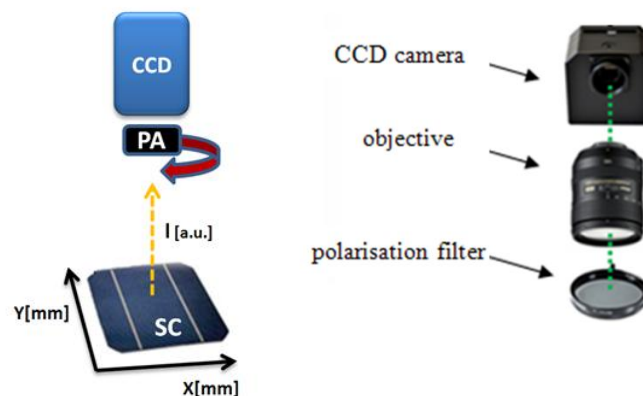


**Figure 1.** Electroluminescence with polarization spectroscopy of defects in solar cells.

The main idea of this paper is based on Malus' law and its using in wavelengths area of bandgap luminescence. Researching of the bandgap luminescence is due to used CCD detector (type G2-3200) that is displayed in Fig. 1. We assume that the linearly polarized light, which we expect to defined defect through an optical element that it is able to polarize light (polarization analyzer - PA).

The intensity of transmitted light by polarization analyzer is dependent on the relative angular position of the polarization plane of luminescence beam and polarizer. The result should be a theoretical sinusoidal dependence.

Luminescence of solar cell connected in forward bias and placed in a dark box was excited by a constant current density (with measuring temperature 23 °C) in our experimental measurements. Orientation of polarization analyzer PA to position of solar cell was changed by 10 °. Extent of polarization of luminescence radiation gives us the degree of polarization.

## Conclusion

The performed polarization analysis showed a slight degree linearly polarization of linearized bandgap luminescence by micro-crack polycrystalline solar cell defect. In graph shown in Fig. 2, is declared luminescence dependence of the defect in specific red square area. There was sinusoid dependence of the luminescence radiation intensity on the angle of rotation of the polarization analyzer. This research with extend measuring analysis can be one of the next steps to improving accuracy defect detection in silicon solar cells.

Our introduce experiment results will be continuing next research focused on linear polarization band-gap luminescence from another type of defects. We will be geared direct to circular luminescence polarization too because it's not investigated interesting field and may be technique to characterization silicon solar cell defects.

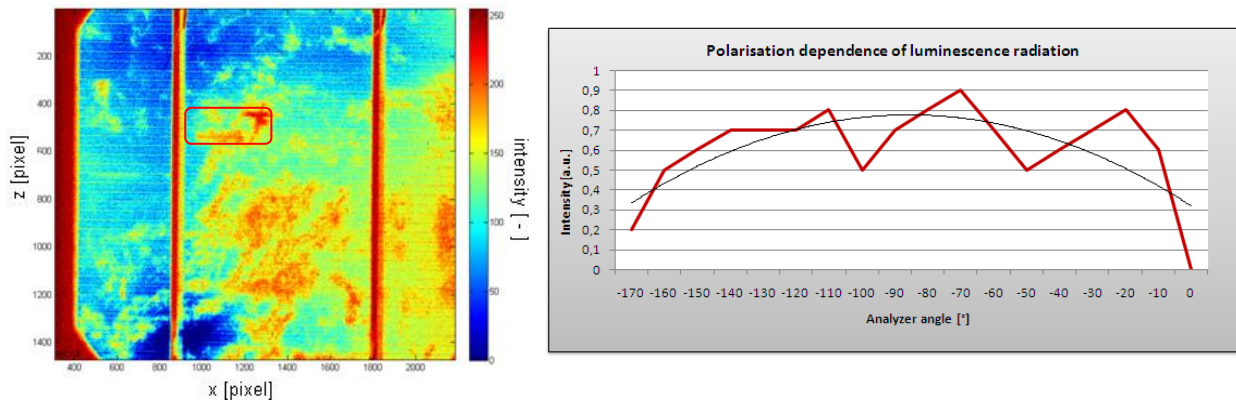


**Figure 2.** Characterization of poly-silicon solar defects intensity.

## Acknowledgement

This research was supported by R&D project FEKT-S-11-7 (Materials and technologies for electrotechnics) at Brno University of Technology.

### References

1. T. Fuyuki, H. Kondo, Y. Kaji, A. Ogane, and Y. Takahashi, "Analytic Findings in the Electroluminescence Characterization of Crystalline Silicon Solar Cells", *J. Appl. Phys.* 101, 2007, 023711.
2. TRUE, Bruce. Photoluminescence and Electroluminescence for Silicon Solar Cell Inspection [online]. Niederlassungen Deutschland : 2010 [cit. 2010-01-14]. *Laser 2000*,
3. Matthew P. Peloso; Bram Hoex; and Armin G. Aberle; Polarization analysis of luminescence for the characterization of silicon wafer solar cells. *Appl. Phys. Lett.* 98, 171914 (2011); doi:10.1063/1.3584857 (3 pages)
4. E. Collett, *Field Guide to Polarization*, SPIE Press, Bellingham, WA (2005).
5. KLIGER, David S.; LEWIS, James W.; RANDALL, Cora Einterez. *Polarized Light in Optics and Spectroscopy* . United States of America : ACADEMIC PRESS, INC., 1990. 304 s. ISBN 0-12-414975-8.

## AGM separator in VRLA batteries

Tošer, P., Bača, P.

Department of Electrotechnology, FEEC, Brno University of Technology, Technická 3058/10, Královo Pole, 61600, Brno, Czech Republic

### Introduction

There are three main critical factors associated with VRLA batteries in total. We have to take into consideration electrolyte supply, pressure of positive active mass growth and oxygen transport as well. In this paper are discussed properties of the AGM separators delivered from H&V UK company. The life-cycle of the experimental cells is tested based on different type of separator because we have to find out the best commercial type for our experiments.

### Experimental, Results and Discussion, Conclusions

The basic type of lead acid battery has a flooded design and there is a loss of water during charging. VRLA design based on absorbed glass mat separator has many advantages. In VRLA battery, sulfuric acid is either stored the pores of the plates and the separator. The cell is filled with only enough acid to coat the pores of the plates and partially saturate the separator.

When the cells are charged, big particles of  $\text{PbSO}_4$  have been dismissed and converted to Pb and  $\text{PbO}_2$ . These reactions produce oxygen gas and hydrogen gas with subsequent loss of water. One of the advantages of VRLA design is that an internal oxygen cycle runs and water loss is minimized. Due to these requirements we can describe the ideal separator for lead acid batteries. This separator should:

- Act as an electrical insulator
- Possess sufficient strength for processing
- Sustain a high level of pressure at the positive plate
- Conform to the surface of the plates
- Provide a sufficient supply of electrolyte to the plates
- Prevent acid stratification
- Allow effective oxygen transport to the negative plate

#### Influence of sulphuric acid density on wicking

The change in the relative density can be caused by the filling a battery with sulphuric acid. This density can influence the concentration gradient of the electrolyte (within the separator). The wicking time of separators was measured up to 6 and 12 cm at various acid densities (Figs. 1 and 2). The relative density was checked by the optical refractometer. The results demonstrated that as the relative density was increased up to 80 % the rate of wicking decreased. The impact of separator thickness is evident in Fig. 1. If the separator is thinner the wicking time is much shorter.

The separator is one of the keys components in a VRLA battery. An AGM separator which does not have right hydrophilic properties could cause battery failure. In a full paper will be discussed and shown experimental results. We can clarify the changes in the structure of whole separator and check properties of the best one.

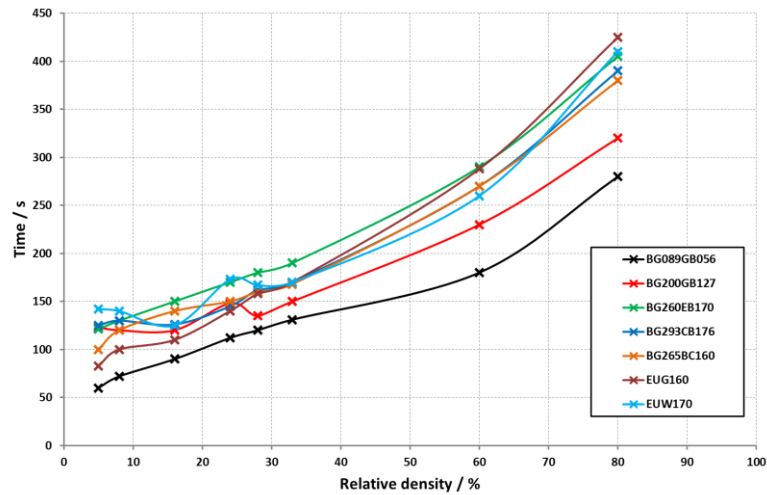


**Figure 1.** Wicking time to 6 cm vs. acid relative density for all separators

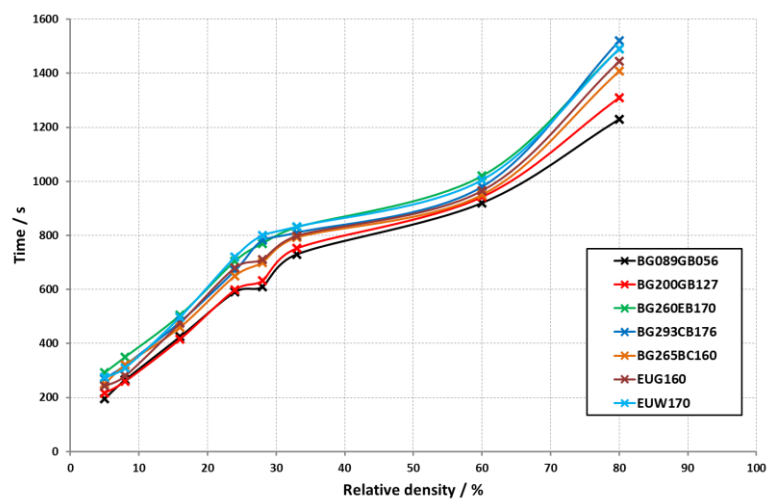


**Figure 2.** Wicking time to 12 cm vs. relative density of sulfuric acid for all separators

### Acknowledgements

This work was supported by the Support for human resources and transfer of knowledge in conditions of international cooperation of research teams no. CZ.1.07/2.3.00/20.0103 and by the specific graduate research of the Brno University of Technology No. FEKT-S-11-7.

### References

1. K.McGregor, H. Ozgun, A.J. Urban, G.C. Zguris, Journal of Power Sources 111 (2002) 288-303.
2. R.J. Ball, R. Evans, R. Stevens, Journal of Power Sources 104 (2002) 208-220.
3. G.C. Zguris, Journal of Power Sources 88 (2000) 36-43.
4. R.J. Ball, R. Kurian, R. Evans, R. Stevens, Journal of Power Sources 104 (2002) 234-240.

## The Influence of Temperature in Curing Processes in the Manufacturing of Electrodes of Lead-Acid Batteries

Vaculík, S.<sup>a</sup>, Zimáková, J.<sup>b</sup>, Bača, P.<sup>a</sup>

<sup>a</sup> Brno University of Technology, Antonínská 548/1, 601 90 Brno, Czech Republic

<sup>b</sup>Institute of scientific instruments of the ASCR, Královopolská 147, 612 64 Brno, Czech Republic

### Introduction

Lead-acid batteries are the oldest type of rechargeable battery, invented in 1858 by French physicist Gaston Plante. Batteries have changed little since 19<sup>th</sup> century although improvements in materials and manufacturing methods continue to bring improvements in energy density, life and reliability. All lead-acid batteries consist of flat lead plates immersed in a pool of electrolyte (solution of sulfuric acid). The main advantages are well mastered technology, relatively low cost of manufacture and high power. The lead-acid battery has become one of the main portable sources of electric power with wide applications in man's everyday life (telecommunications, information technologies, ect.). Relative good specific power has enabled its widespread use for starting, lighting and ignition of engine purpose for vehicular applications.

Resulting properties of lead-acid batteries are affected by the parameters set in manufacturing of electrodes:

- composition of the active mass
- temperature and humidity during the process of curing
- formation

[1,2]

### Pastes

There are two kinds of pastes for lead-acid batteries: positive and negative. Each is composed of lead powder (lead oxide - PbO), water and sulfuric acid (H<sub>2</sub>SO<sub>4</sub>). It's properties are influenced by additives which can be added to the mixture.

*Paste preparation* – lead powder is charged in a mixing machine and then water and sulfuric acid solution (30 %) are added under constant stirring. During this stage are formed basic lead sulphates (1BS).

### Curing

During the process of curing, paste particles are interconnected to form an uninterrupted strong porous mass (skeleton) which is tightly bound to the grid.

Basic processes during the process of curing:

- paste particles interconnected into skeleton
- corrosion layer forms on the grid surface which is bonded to the skeleton
- oxidation of free Pb in the paste

Depending on the values of ambient temperature and the humidity are on the surface of the electrodes produced two kinds of sulfate particles: tribasic lead sulphate (3BS) and tetrabasic lead sulphate (4BS).

Tribasic lead sulphate particles are obtained when the paste preparation is performed at temperature from 30 °C to 60 °C and plate curing is conducted within same temperature. These particles are 1 – 2 μm long and tightly interconnected.

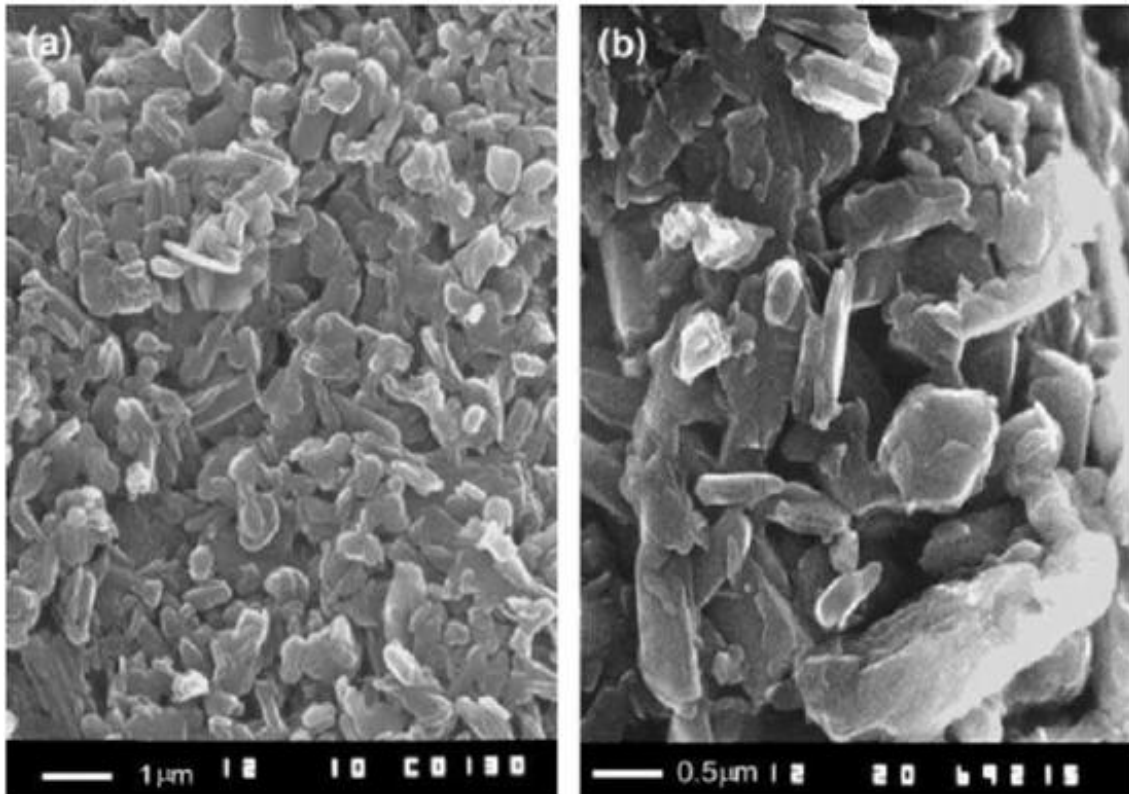


*Figure 1. SEM micrographs of structure of cured pastes 3BS [3]*

Tetrabasic lead sulphate particles are performed at the temperature from 80 °C to 95 °C. Length of these particles is 15 – 20 μm and 4 – 5 μm in diameter. [3]

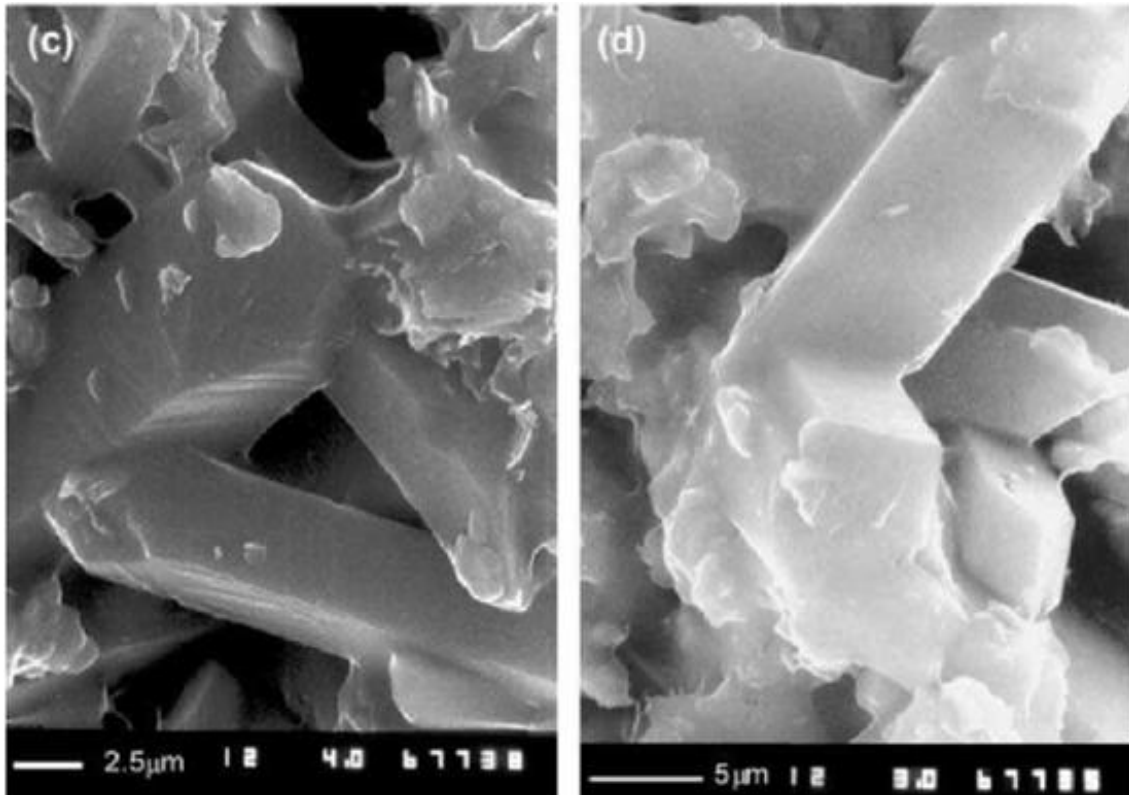


**Figure 2.** SEM micrographs of structure of cured pastes 4BS [3]

The aim of our work is investigate the effects of temperature on the crystallographic structure of sulphades formed by proces of curing.

### Acknowledgements

This work was supported by the specific graduate research of the Brno University of Technology No. FEKT-S-11-7 and by the Grant Agency of the Czech Republic: grant No. GAP 102/10/1410.

### References

1. H. Karami, M. Shamsipur, S. Ghasemi, *Journal of power sources*, 164, 2007
2. R. Kiesling, Lead acid battery formation techniques, Digatron firing circuits
3. D. Pavlov, Lead-acid batteries: Science and technology, A handbook of lead-acid battery technology and its influence on the product, Elsevier, 2011

## Snail tracks phenomenon on photovoltaic modules

Vanek, J., Gvritishvili, R., Strnadel, J.

<sup>1</sup>Department of Electrotechnology, Brno University of Technology, Faculty of Electrical Engineering and Communication, Technicka 10, 616 00 Brno, Czech republic

### Abstract

This paper presents results of analyses of the polycrystalline silicon photovoltaic modules with phenomenon emerging recent years on the surface of cells working at least one half of year in duty called as “Snail tracks” or “Snail trails” typical by optical color changing on surface in accident shape like trails made by snails. We have undergone these modules extensive testing and analyses. The output operation performed in laboratory by flash tester and also in situ on operation field reveals no significant drop in wattage, and the drop exhibited by a very small number of modules was due to cell breakages in some cases corresponding with the shape of snail trails. We have also focused on thermal analyses of modules which we are bringing in this article.

### Introduction

After a period of time ranging from several months to several years after initial installation, solar modules show some discoloration on the cells (fig. 1), and crisscrossing narrow dark lines about the thickness of a finger begin to appear on the surface of the modules. We have undergone these modules extensive testing and analyses. The detail study of snail tracks phenomenon shown no visible damages of the silicon surface of solar cell (fig. 2).

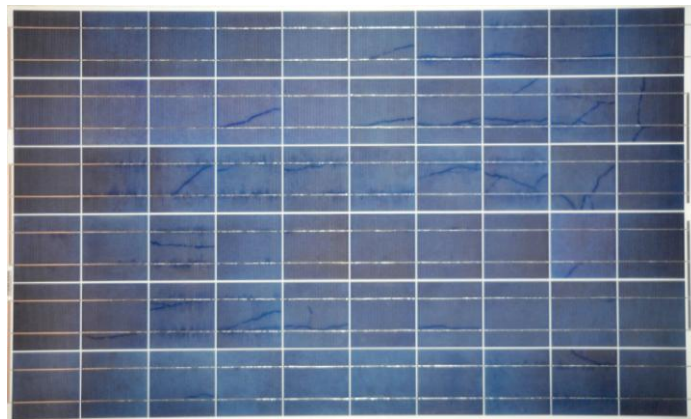


**Figure 1.** Sample of photovoltaic module no. 1 with visible “snail tracks” defects

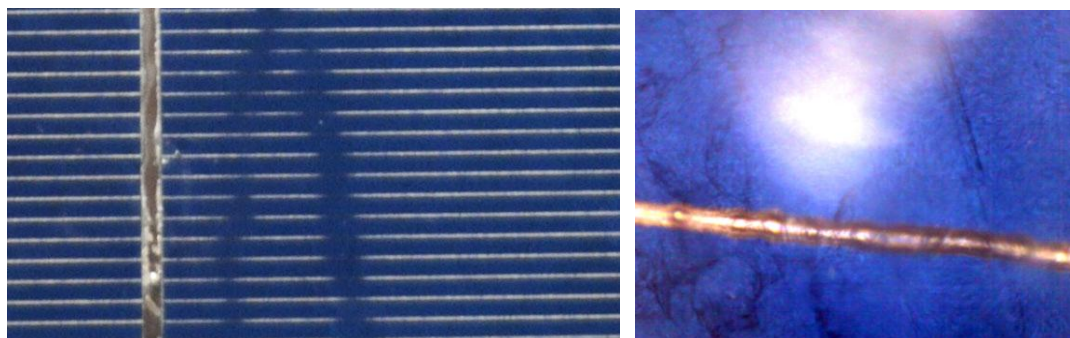


**Figure 2.** Detail of “snail track”

The phenomenon of snail tracks is made by local color changing of silver surface of metal collector's contacts of neighboring contacts so the results of optical observation looks like connected lines. The surface of the metal contacts is changed to dark brown or black color. By optical observation there are no visible damages of silicon substrate. Also the output of thermovision (fig. 3) and operation performed in laboratory by flash tester and also in situ on operation field reveals no significant drop in wattage.

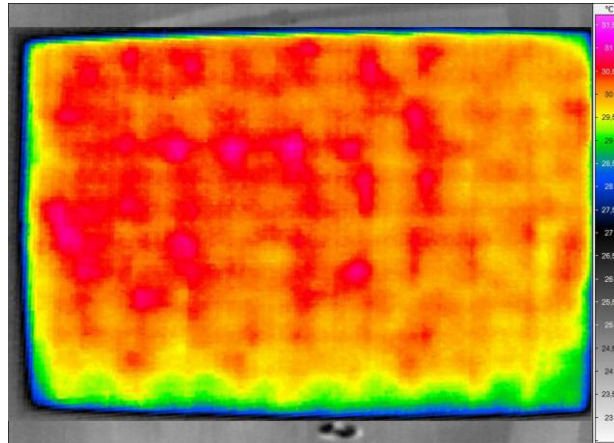


**Figure 3.** Temperature distribution of PV module no. 1 taken by thermocamera

**TABLE I.** Parameters of PV module no. 1 taken by flash tester.

$T_p$	25.0°C
$G_{(i)}$	1.0kW/m <sup>2</sup>
$I_{sc}$	8.493 A
$U_{oc}$	36.764 V
Eff.	13.80%
FF	73.00%
$P_{mpp}$	227.919 W
$U_{mpp}$	28.974 V
$I_{mpp}$	7.866 A
$R_{ser}$	0.6 Ohm
$R_{sh}$	369.3 Ohm

The output of 220Wp module taken by flash tester can be seen on figure 3 and table 1. The peak power of the new panels under standard measuring conditions declared by the manufacturer is 230 W  $\pm$  3% at STC. Even for other electrical parameters, the manufacturer guarantees maximum difference of  $\pm$  3%. To all of these tolerance limits the tested panels have fit.

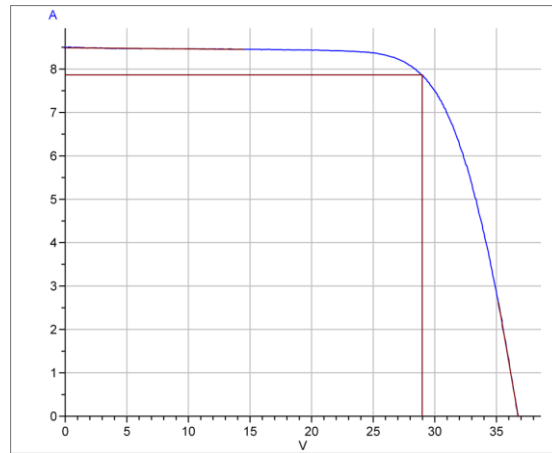


**Figure 3.** VA characteristic of sample photovoltaic module no. 1

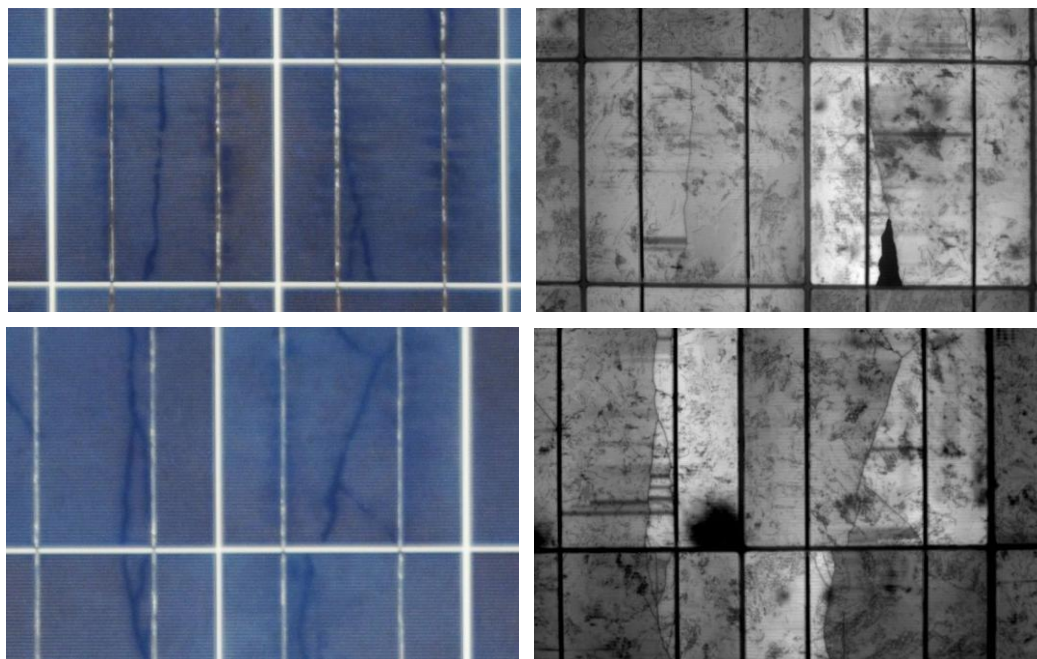


**Figure 4.** Comparing of visible „snail tracks“ defect and the same place shown by electroluminescence method

The standard diagnostic method have not shown any signs of the appearance of phenomenon “snail tracks” and not to be the optical change of silver surface contact color there was no reason for usage of more diagnostic method.

The first method showing the correlation with the snail tracks phenomenon is electroluminescence (fig. 4). On the electroluminescence output figures are shown the microcracks corresponding with the snail tracks lines. For the most microcracks shown by electroluminescence also holds the rule that the metal contacts over the microcracks of silicon substrate is not disconnected. This is the reason while there is no drop of wattage.

### Color changing of Ag

There are several theories explaining the discoloring of Ag metal paste grids. Peng et al. in [1] is trying to explain the color change of grid by reaction Ag with CO<sub>2</sub> accounts for the formation of

Ag<sub>2</sub>CO<sub>3</sub> nanoparticles. Koentges et al. in [2] is trying to explain the color change of grid by halogens reaction with Ag.

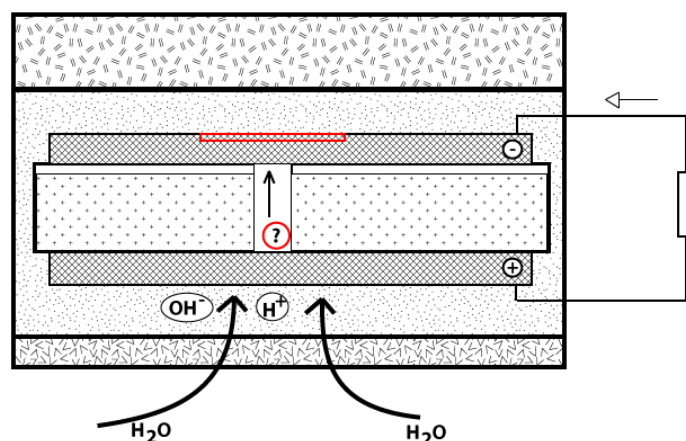


**Figure 5.** The transport mechanism of ion in solar module structure with microcracks

The possible transport mechanism of ion radical responsible to the color changing of front side metallization over the microcracks is shown on fig. 5.

### Conclusion

The main origin of snail trails on photovoltaic modules, have been observed and confirmed on Ag grid surfaces, which can absorb and scatter light resulting in dark discolorations on the Ag surface. There is correlation with cell cracks, but these aren't the origin of snail tracks make the cell cracks visible. Ag tests on the discolored modules suggest there is no significant power degradation or discolored area enlargement after performing the aging tests against standardized protocols. Collectively, the results of this study provide insights into future research needs addressing the discoloration issue associated with snail trails in solar cells.

### Acknowledgement

This paper is also based on the research supported by research center CVVOZE CZ.1.05/2.1.00/01.0014 and the project FEKT-S-11-7.

### References

1. M. Koentges, et al., Snail Tracks (Schnecken Spuren), worm marks and cell cracks, 27<sup>th</sup> EU-PVSEC, WIP, Frankfurt, Germany, (2012)
2. P. Peng, et al., Microscopy study of snail trail phenomenon on photovoltaic modules, RSC Advances, 11359-11365, 2, 2012
3. Paul SCHISSEL and A. W. CZANDERN A, Reactions At The Silver/Polymer Interface: A Review, Solar Energy Materials 3 (1980) 22, 245
4. Tauš, P, and M., Taušová. Economical analysis of FV power plants according installed performance, Acta Montanistica Slovaca 14, no. 1 (2009): 92.
5. J. Berghold, et al., Electrochemical corrosion within solar panels, 27th EU-PVSEC (WIP, Frankfurt, Germany, 2012) 4BV.3.37

## Synthesis the graphene from carbon nanotubes, based on the electrochemical approach and the effects of oxidizing and reducing agents on its electrochemical performances in oxygen electrodes.

Danilov, M.O.\*, Slobodyanyuk, I.A., Rusetskii, I.A., Kolbasov, G.A.

V.I. Vernadskii Institute of General and Inorganic Chemistry of the Ukrainian National Academy of Sciences, prospekt Palladina 32/34, Kyiv 142, Ukraine.

\*Corresponding author: Danilov M.O. E-mail: danilovmickle@rambler.ru

Graphene is a planar polynuclear aromatic macromolecule with two-dimensional order of carbon atoms, which corresponds to the order of atoms on the basal face of graphite crystal, i.e. it consists of carbon hexagons  $C_6$  formed by the carbon atoms that are in the  $sp^2\pi$ -hybridized state. Based on the Van der Waals radius of carbon atom, the graphene thickness is 0.34 nm. In view of this, the study of the dependence of electrochemical properties on the method for the preparation of reduced graphene oxide (RGO), which is used as a catalyst support for fuel cell oxygen electrodes, is of great interest.

Chemical oxidation of multiwall carbon nanotubes (MWCNTs) with reagents of different oxidation power was studied. The functionalization yield, namely the density of carboxyl and hydroxyl functional groups on the graphitic network, was quantified by different methods (1). Let us consider the standard potentials (2) of the reactions of possible carbon oxidation in the acidic and alkaline mediums:

	acidic		alkaline
$C, H^+ / CH_3OH$	- 0.32 V	$C, / CH_3OH, OH^-$	- 1.48 V
$HCHO_2, H^+ / C$	+ 0.528 V	$CHO_2^- / C, OH^-$	- 0.603 V
$CO, H^+ / C$	+ 0.518 V	$CO_3^{2-} / C, OH^-$	- 0.766 V
$H_2CO_3, H^+ / C$	+0.207 V		

In accordance with these potentials for the chemical oxidation the oxidants should be taken with potentials more electropositive than + 0.528 V. The most famous oxidants in the acidic medium are:  $KMnO_4$  +1.69 V, ozone +2.075 V,  $Cr_2O_7^{2-}$  + 1.36 V,  $OsO_4$  +1.02 V; in the alkaline medium:  $FeO_4^{2-}$  + 0.81 V, and a number of others. So, for the chemical oxidation in an alkaline medium can be used oxidant with potentials more electropositive than - 0.603 V. More suitable oxidants are  $KMnO_4$  +0.588 V, ozone +1.247 V and others. In the Ref. (3) the electrochemical oxidation of carbon nanotubes was achieved by potential cycling in acid solution between +1.00 and +2.00 V. They said that the electrochemical oxidation of MWNTs produce the quinoidal functional groups at the surface of nanotubes. The value of potential depends of the electrode material on which the anodic oxidation of MWCNT is carried out. In an alkaline medium, the value of electrode potential for the electrochemical oxidation of carbon nanotubes must be more + 0.8 V. Let us consider the standard potentials of reactions (2) of possible reduction of epoxy, phenol and carboxyl groups in the acidic and alkaline mediums:

	alkaline		acidic
$C / CH_3OH, OH^-$	- 1.148 V	$C, H^+ / CH_3OH$	- 0.320 V
$CHO_2^- / C, OH^-$	-0.603 V	$HCHO_2, H^+ / C$	+ 0.528 V
$CO_3^{2-} / C, OH^-$	-0.766 V	$H_2CO_3, H^+ / C$	+0.27 V

Therefore, the reductants with potentials of under  $-1.148$  V must be used for the chemical reduction of oxidized graphene in alkaline medium. Such reductants can also be hydrogen, zinc, magnesium, etc. The value of this potential fully corresponds to the standard potential of the reductants reported in Ref (2). A typical reductant for graphene oxide is hydrazine (4), whose standard redox potential of electrochemical reaction in alkaline solution  $E = -1.16$  V. We have also shown in Ref (5) that to obtain reduced graphene oxide, sodium hypophosphite can be used ( $E = -1.51$  V). In acid medium reductants with potentials of under  $-0.320$  V must be used for the chemical reduction of oxidized graphene. Such reductants can also be hydrogen, zinc, magnesium, etc. In our opinion, a potential of under  $-1.3$  V is required for the electroreduction of graphene oxide obtained from MWCNTs in alkaline medium. For acid medium, this potential is lower than  $-0.4$  V. This potential depends on the current tap material, on which the cathodic reduction of oxidized graphene in electrolyte is performed. To synthesize oxidized graphene, a modified Hammers method (4) using multi-walled carbon nanotubes (MCNTs) of a bulk density of  $25\text{-}30$  g/dm<sup>3</sup> was employed. The outside diameter of nanotubes was  $\sim 10\text{-}30$  nm, the specific surface area was  $230$  m<sup>2</sup>/g. As oxidant we used  $\text{KMnO}_4$  ( $+1.69$  V) and  $\text{K}_2\text{Cr}_2\text{O}_7$  ( $+1.36$  V). A typical reductant for graphene oxide is hydrazine, whose standard redox potential of electrochemical reaction in the alkaline solution is  $E = -1.16$  V (2). So to reduce the graphene oxide we choose reducing agents which have the standard redox potentials of the electrochemical reactions in an alkaline environment a little more electronegative or more electropositive than  $E = -1.148$  V. Such reductants can be sodium hypophosphite ( $E = -1.51$  V) and sodium sulfite ( $E = -0.936$  V) (5). These reductants are nontoxic, which is their advantage. The electron micrographs have been obtained with the aid of a JEM-100 CXII electron microscope. The X-ray phase analysis was performed with the aid of a DRON-4 X-ray diffractometer with  $\text{CuK}_\alpha$  radiation. An X-ray phase analysis and the studying absorption spectra and photoluminescence spectra of dispersion of the obtained product was carried out for the identification of reduced graphene oxide. Fig. 1 and 2 show micrographs of RGO, which was obtained using different reductants from carbon nanotubes oxidized by heptavalent manganese. Fig. 3 shows micrographs of RGO, which was obtained using sodium hypophosphite as the reductant from carbon nanotubes oxidized by  $\text{K}_2\text{Cr}_2\text{O}_7$ .

Oxygen electrodes, where RGO was used as an active layer, have been made by pressing. A mockup and the method for the testing of gas-diffusion electrodes is described in Ref. (6). Electrodes with an active layer of starting MCNTs and carbon nanotubes with deposited Pt in amount 10 mass % have been made for comparison. On the oxygen electrodes made, current-potential curves were measured. Fig. 4 shows plots of potential against current density for oxygen electrodes based on graphene oxide reduced from MCNTs oxidized by  $\text{KMnO}_4$  and  $\text{K}_2\text{Cr}_2\text{O}_7$ . As we can see from Fig. 4 the RGO obtained by the reduction with sodium hypophosphite (RGO-SH) (curve 1 in Fig. 4) from nanotubes oxidized by  $\text{KMnO}_4$  give the best results. Reduced graphene oxide obtained from nanotubes oxidized by  $\text{K}_2\text{Cr}_2\text{O}_7$  by reduction with sodium hypophosphite (curve 1 in Fig. 4) give not so good characteristics. When we consider the reductants, RGO obtained by the reduction with sodium hypophosphite (RGO-SH) (curve 1 in Fig. 4) from nanotubes oxidized by  $\text{KMnO}_4$  give the best results then the RGO obtained by the reduction with sodium sulfite (RGO-SS) (curve 1 in Fig. 4) from nanotubes oxidized by  $\text{KMnO}_4$ . In this figure, characteristics of electrodes with starting MCNTs are presented for comparison (curve 3 in Fig. 4). These results can be explained by the fact that, as follows from the above reasoning given for the selection of reducing agents has to use a reducing agent with the potential to more electronegative than  $-1.148$  V, which sodium hypophosphite is. For the selection of oxidant agents has to use an oxidant such as  $\text{KMnO}_4$  ( $+1.69$  V) with the potential to more electropositive than  $\text{K}_2\text{Cr}_2\text{O}_7$  ( $+1.36$  V). It has been found that the characteristics of RGO-SH electrode in oxygen reduction reaction are 3 - 4 times higher than those of electrode of starting MCNTs. RGO-based electrodes are also superior to MCNTs- $\text{MnO}_2$  nanocomposite in characteristics, which follows from

comparison with the data presented in Ref. (7). As seen from the figure 4 voltage-current density curves for the reduced graphene oxide close to the parameters of electrodes from platinum deposited on the multi-walled carbon nanotubes. The characteristics of RGO-based oxygen electrodes were stable in the course of six-month tests.

Consequently, for the oxidation of carbon nanotubes and other carbon materials and for its reducing to obtain the reduced graphene oxide for selection oxidizing and reducing agents should be used the standard redox potentials. It is shown that the obtained electrode materials are promising catalysts for oxygen electrodes of power cells, which can substitute for catalysts containing noble metals.

### Reference

1. V. Datsyuk, M. Kalyva, K. Papagelis, and et al, *Carbon*, **46**, 833 (2008).
2. S. G. Bratsch, *J. Phys. Chem.*, **18**, 1 (1989).
3. J.-Sh. Ye, X. Liu, H. F. Cui, and et al, *Electrochemistry Communications*, **7**, 249 (2005).
4. D.V. Kosynkin, A.L. Higginbotham, A. Sinitskii, and et al, *Nature*, **458**, 872 (2009).
5. M.O. Danilov, I.A. Slobodyanyuk, I.A. Rusetskii, and et al, *Russian J. Appl. Chem.*, **86(6)**, 858 (2013).
6. M.O. Danilov, G.Ya. Kolbasov, I.A. Rusetskii, and et al, *Russian J. Appl. Chem.*, **85(10)**, 1536 (2012).
7. M.O. Danilov, A.V. Melezhyk, *J Power Sources*, **163(1)**, 376 (2006).

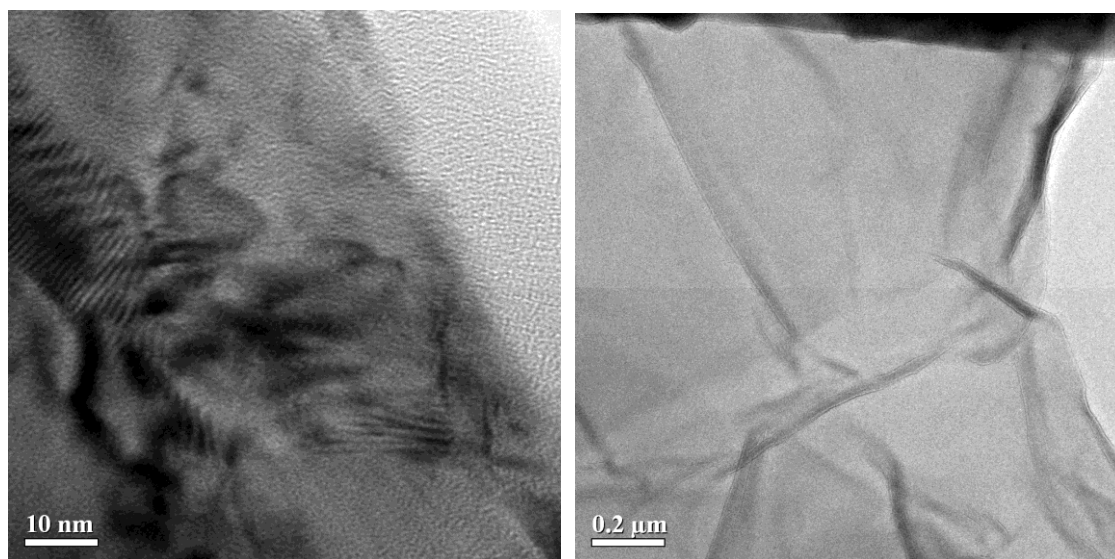


**Figure 1.** (left) Micrograph of a sample of RGO obtained from MCNT oxidized by  $KMnO_4$  and reduced with sodium sulfite.

**Figure 2.** (right) Micrograph of a sample of RGO obtained from MCNT oxidized by  $KMnO_4$  and reduced with sodium hypophosphite.

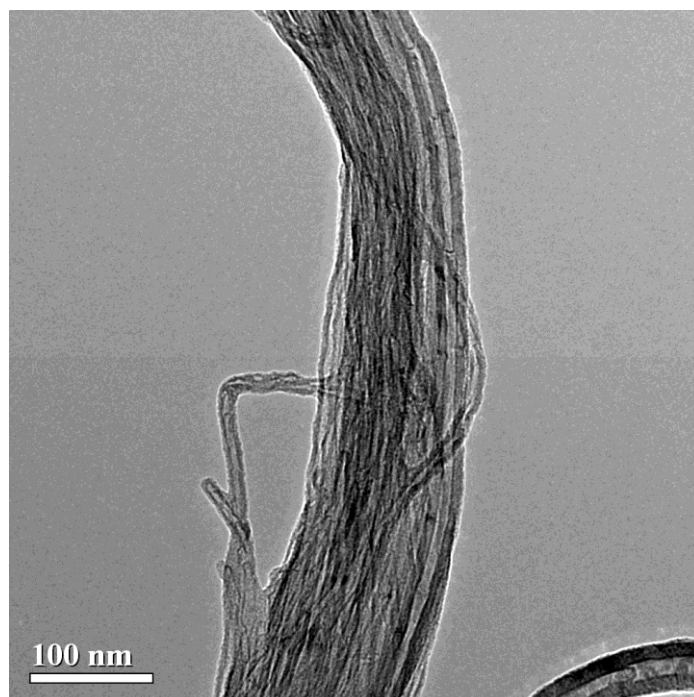


**Figure 3.** Micrograph of a sample of RGO obtained from MCNT oxidized by  $K_2Cr_2O_7$  and reduced with sodium hypophosphite

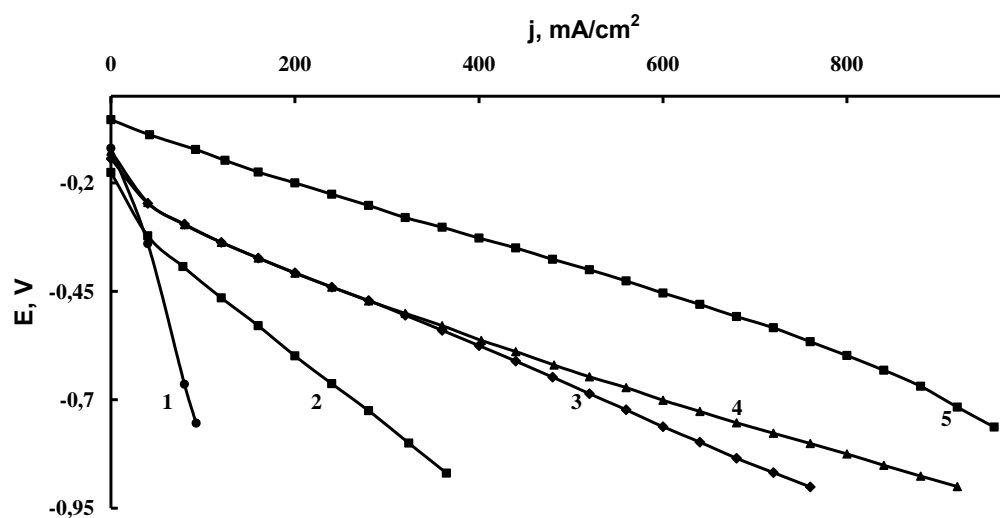


**Figure 4.** Voltage-current density curves for oxygen electrodes with 0.02 g/cm<sup>2</sup> of an active layer based on graphene oxide obtained from MCNT oxidized by  $KMnO_4$  and reduced to the RGO with: (4) sodium hypophosphite, (2) sodium sulfite. Curve 1: initial multiwall carbon nanotubes. Curve 3: RGO obtained from MCNT oxidized by  $K_2Cr_2O_7$  and reduced with sodium hypophosphite. Curve 5: MCNT contained 10 mass % of the deposited Pt.

## Review on gel polymer electrolytes for lithium ion batteries and supercapacitors

Musil, M., Dvořák, P.

Department of Electrical and Electronic Technology, Brno University of Technology,  
Faculty of Electrical Engineering and Communication, Technická 3058/10 616 00 Brno,  
Czech Republic.

This paper is a brief review of gel polymer electrolytes appropriate for electrochemical power sources such as Lithium ion batteries, supercapacitors and electrochromic components. Predominantly are mentioned polymers based on polyethylene oxide (PEO), polyacrylonitrile (PAN), polymethyl methacrylate (PMMA) and Polyvinylidene fluoride (PVdF).

### Introduction

Electrolytes are used in solid, gel, or liquid state. These electrolytes allow the movement of ions and are called ion conductors. Polymer electrolyte can be generally defined as a membrane, which allows the movement of charged particles. Gels are appropriate for lithium ion batteries, supercapacitors and electrochromic devices.

Although first polymer electrolyte type was introduced in 1973 (Fenton and co.), in the industry field are gels applied since early 1980.

Polymer electrolytes are sorted into dry, solid polymer electrolytes and gel polymer electrolytes. Solid polymer electrolytes are represented by PEO. These electrolytes prove very low ionic conductivity at room temperature ( $\sigma \approx 10^{-8} \text{ S}\cdot\text{cm}^{-1}$ ). Low ionic conductivity is caused by the fact, that PEO creates solid polymer matrix and solvent at the same time. Due to his fact, ionic mobility is very limited and PEO based electrolytes are not practicable for electrochemical power sources. [1, 2, 3]

### Gel polymer electrolytes

Gel polymer electrolytes employ cohesive properties of solid materials and ionic diffusion in liquid simultaneously. These electrolytes aren't neither in solid, nor in liquid state. Thanks to these properties, gels are used in many branches of industry; especially in electrochemical power sources. Ionic conductivity  $\sigma$  usually reaches values about  $10^{-3} \text{ S}\cdot\text{cm}^{-1}$ .

Gel polymer electrolytes consist of polymer, inorganic salt and organic liquid (solvent). Polymer matrix prevents from the liquid electrolyte (solvent + salt) escape and makes gel rigid. Organic liquid functions as plasticizer and adds to the matrix fluid properties.

Polymer electrolytes in contrast to liquid ones prove advantages - internal short circuit prevention, electrolyte leakage and lower self-discharge.

### Fundamental gel polymer electrolytes requirements:

- a) high ionic conductivity in wide temperature range
- b) adequate mechanical properties
- c) high transference number
- d) thermal and electrochemical stability
- e) compatibility with electrode materials
- f) long lifetime

### Preparation methods

The most usual preparation is based on polymer dissolved in the organic solvent. Anorganic salt and organic liquid with high boiling point are added subsequently. Evaporated solvent from the mixture results in gel polymer electrolyte. This method is widely spread in the majority of published papers. This method is used because of its preparation simplicity; nevertheless, modifications in gel composition are limited.

Another method is based on polymerization process of monomer in mixture consisting of monomer, crosslinking agent, polymerization initiator, inorganic salt and organic liquid. In dependence on initiator type, monomer polymerization is initiated by heat, or by UV radiation. GPEs prepared by this method can be optimized in many ways.

### The most commonly used polymers

Main roles of polymer matrix in gel polymer electrolyte are retaining as much electrolyte (organic liquid solvent containing dissolved inorganic salt) as possible and simultaneously retaining solid state material properties.

#### *Poly(ethyleneoxide) PEO*

As was written previously in text, first experiments were done with dry solid state electrolytes in early Nineteen Seventies. PEO are usually applied in LI-pol accumulator types.

#### *Poly(acrylonitrile) PAN*

Proves comparatively high ionic conductivity and electrochemical stability.

#### *Poly(methyl methacrylate) PMMA*

First experiments with methyl methacrylate appeared in 1985. It was observed, that enormous number of lithium ions is necessary to reach high number of battery cycles. Ions „vanished“ within cycles.

#### *Poly(vinylene fluoride) and Poly(vinylidene fluoride-co-hexafluoropropene) PVdF-HFP*

Thanks to high chemical stability were PVdF membranes soaked into electrolyte. This application does not represent typical gel polymer electrolytes.

*Poly(2-ethoxyethyl methacrylate) PEOEMA*

Ethoxyethyl methacrylate contains oxygen atom, which enables macromolecule backbone to bend. These ethoxyethyl methacrylate chains are more flexible and allow ions flow through the electrolyte easier.

*Poly(3-(Trimethoxysilyl)propyl methacrylate) TSPMA*

This polymer macromolecule containing silyl group proves higher fire safety. It's disadvantage is brittleness of polymer. To optimize resulting gel polymer electrolyte properties, TSPMA is usually used in copolymer systems (EOEMA-TSPMA e.g.).

**TABLE I.** Representative polymer properties [1, 2]

Name	Formula	Glass transition temperature [°C]	Melting point [°C]
PEO	- (CH <sub>2</sub> -CH <sub>2</sub> O) <sub>n</sub> -	-64	65
PAN	- (CH <sub>2</sub> -CH(-CN)) <sub>n</sub> -	125	317
PMMA	- (CH <sub>2</sub> C(-CH <sub>3</sub> )(-COOCH <sub>3</sub> )) <sub>n</sub> -	105	160
PVdF	- (CH <sub>2</sub> -CF <sub>2</sub> ) <sub>n</sub> -	-40	171
PVdF-HFP	- (CH <sub>2</sub> -CF <sub>2</sub> ) <sub>n</sub> (CF <sub>2</sub> -CF(CF <sub>3</sub> )) <sub>m</sub> -	-90	135
TSPMA	- (CH <sub>2</sub> =C(-CH <sub>3</sub> )-CO <sub>2</sub> -(CH <sub>2</sub> ) <sub>3</sub> -Si-(OCH <sub>3</sub> ) <sub>3</sub> ) <sub>n</sub> -	-48	110
PEOEMA	- (CH <sub>2</sub> =C(-CH <sub>3</sub> )-CO <sub>2</sub> -CH <sub>2</sub> -CH <sub>2</sub> -O-C <sub>2</sub> H <sub>5</sub> ) <sub>n</sub> -	-	-

Polymers with low glass transition temperature prove higher ionic conductivity.

Conventional electrolyte composition

Liquid electrolyte makes gel ionic conductor and affects mechanical stiffness. Liquid electrolyte consists of organic liquid and inorganic salt. Liquid and salt are chosen according to intended usage. Electrolyte for li-ion accumulators must contain lithium salt, while in supercapacitors not. In general, it is necessary to prepare electrolyte with high ionic conductivity and wide potential window.

In Table 2 are representative organic liquid properties, such as melting and boiling points, density, permittivity and viscosity. It is necessary to follow these parameters. Usually are chosen liquids (or liquid mixtures) with low melting point, high boiling point, low density, and viscosity and high permittivity. Proper component selection ensures operability (at high ionic conductivity) in wide temperature range. In the electrochemical industry are commonly used binary and even ternary organic liquid mixtures. (e.g. EC/DMC 1:1 mixture.)

**TABLE II.** Representative organic liquids properties [4]

	T <sub>m</sub> [°C]	T <sub>b</sub> [°C]	ρ [g/ml]	ε [-]	η [cP]
Dimethyl-carbonate (DMC)	2.4	90	1.06	3.12	0.59
Diethylene-carbonate (DEC)	-43	126	0.97	2.82	2.80
Gamma-butyrolactone (γBL)	-43.3	204	1.13	39.00	1.73
Propylene-carbonate (PC)	-48.8	242	1.20	66.14	64.92
Ethylene-carbonate (EC)	36.4	248	1.32	89.78	4.61 <sup>1</sup>

T<sub>m</sub> ... melting temperature

T<sub>b</sub> ... boiling temperature

<sup>1</sup> At temperature 40 °C

Electrochemic reactions ensure anorganic salts - LiClO<sub>4</sub>, LiPF<sub>6</sub>, LiAsF<sub>6</sub>, LiBOB or LiCF<sub>3</sub>SO<sub>3</sub> for li-ion accumulators and electrochromic devices. In supercapacitors can be employed lithium salt too, but even higher ionic conductivity ensure ammonium salts such as TEABF<sub>4</sub>, TEAClO<sub>4</sub>, TEAPF<sub>6</sub>, TBAPF<sub>6</sub>, TBABF<sub>4</sub> and TBAClO<sub>4</sub>.

Conventional electrolyte compositions are in Table 3. Aprotic electrolytes are compared there with acidic and alkali electrolytes used in lead-acid and alkaline batteries.

**TABLE III.** Ionic conductivity of selected electrolytes [4]

Ionic liquids	Ionic conductivity [mS/cm]
EMImNTf <sub>2</sub>	9.5
EMImBF <sub>4</sub>	15.5
Aprotic electrolytes	
1M LiBF <sub>4</sub> v PC	3.4
1M LiBF <sub>4</sub> v EC/DMC	4.9
1M LiPF <sub>6</sub> v PC	5.8
1M LiPF <sub>6</sub> v EC/DMC	10.7
1M LiClO <sub>4</sub> v PC	5.6
1M LiClO <sub>4</sub> v EC/DMC	8.4
1M TEABF <sub>4</sub> v PC	12.7
1M TEABF <sub>4</sub> v EC/DMC	24.7
Water-based electrolytes	
H <sub>2</sub> SO <sub>4</sub> (30 wt. %)	750
KOH (29 wt. %)	540

### Ionic conductivity of gel polymer electrolytes

Gel polymer electrolyte ionic conductivity is composed from the liquid electrolyte ionic conductivity and ionic ability to move through the polymer matrix. Unfortunately, GPE ionic conductivity is approx. ten times lower than liquid electrolyte conductivity. Ionic conductivity properties in GPEs are improved by lowering crystallinity of the polymer. Amorphous polymer parts are more passable for ions. Crystallinity is usually lowered by nanoparticles addition (Al<sub>2</sub>O<sub>3</sub>, CuO, TiO<sub>2</sub>, BaTiO<sub>3</sub> or SiO<sub>2</sub>), reating co-polymers or by liquid electrolyte addition. [2, 4, 5]

### **Conclusion**

In this review are summarized basic properties and demands on gel polymer electrolytes appropriate for electrochemical power sources such as Li-ion batteries, supercapacitors and electrochromic devices. Properties and influence of polymer and liquid electrolyte types on the resulting gel polymer electrolyte ionic conductivity and potential window range were discussed. Although, gel polymer electrolytes prove lower ionic conductivity in comparison with liquid electrolytes, gels are used because of its mechanical stability (resist dimension electrode changes, prevents from Whisker propagation. Moreover, there is no electrolyte leakage risk.

### Acknowledgements

This work was supported by the grant FEKT-S-11-7 and project CVVOZE CZ.1.05/2.1.00/01.0014.

### References

1. Cesar Sequeira, Diogo Santos, *Polymer electrolytes: fundamentals and applications*. Cambridge: Woodhead Publishing, 2010. ISBN 18-456-9772-3.
2. Jeffrey W. Fergus, Ceramic and polymeric solid electrolytes for lithium-ion batteries, *Journal of Power Sources*, Volume 195, Issue 15, 1 August 2010, Pages 4554-4569, ISSN 0378-7753
3. S. K. Tripathi, Ashish Gupta, Manhu Kumari, *Studies on electrical conductivity and dielectric behaviour of PVdF–HFP–PMMA–NaI polymer blend electrolyte*, *Bull. Mater. Sci.*, Volume 35, No. 6, November 2012, Pages 969–975
4. Kang Xu, Nonaqueous Liquid Electrolytes for Lithium-Based Rechargeable Batteries, *Chemical Reviews*, Volume 104, 2004, Pages 4303-4417
5. A.K. Arof, M.Z. Kufian, M.F. Syukur, M.F. Aziz, A.E. Abdelrahman, S.R. Majid, Electrical double layer capacitor using poly(methyl methacrylate)–C<sub>4</sub>BO<sub>8</sub>Li gel polymer electrolyte and carbonaceous material from shells of mata kucing (*Dimocarpus longan*) fruit, *Electrochimica Acta*, Volume 74, 15 July 2012, Pages 39-45, ISSN 0013-4686

## Polymer gel PMMA based electrolytes containing Li<sup>+</sup> salts

Dvořák, P., Musil, M.

Department of Electrical and Electronic Technology, Brno University of Technology,  
Faculty of Electrical Engineering and Communication, Technická 3058/10 616 00 Brno,  
Czech Republic.

In this paper, we report the synthesis and characterization of novel methacrylic based polymer electrolytes containing different lithium salts (LiClO<sub>4</sub>, LiPF<sub>6</sub>, LiBF<sub>4</sub>) in EC:DMC (1:1 wt) suitable for lithium batteries and supercapacitors. The gel polymer electrolytes were prepared by UV irradiation and temperature initiation processes. Electrolytes were studied using electrochemical methods and they exhibit good ionic conductivity (up to 9 μS/cm at 20 °C). The accessible electrochemical window (EW) of gel electrolytes was estimated about 4 V.

### Introduction

Polymer electrolytes are an essential part of modern power sources. Their electrochemical and mechanical properties have been investigated since 1980. Liquid electrolytes as the medium for ion transport between electrodes of a device are being replaced by solid or gel (semi-solid) electrolytes. This is because electrochemical power sources based on liquid electrolytes are usually associated with problems of leakage, self-discharge, corrosion, bulky design etc. Application of the gel electrolytes includes lithium batteries, supercapacitors and electrochromic devices. [1-3]

Polymer gel electrolytes are generally prepared by immobilizing the electrolyte in polymer matrix. Commonly used polymers in the synthesis of polymer gel electrolytes are polyacrylonitrile (PAN), polymethacrylate (PMMA), polyvinylidene fluoride (PVDF) and polyethylene oxide (PEO). There are two general methods of the gel electrolyte preparation. The first method – solvent casting is based on mixture of polymer, salt and aprotic solvent in a volatile co-solvent followed by partial or complete removal of the co-solvent. The second is in using direct polymerization of monomers mixed with the aprotic solvent. [4-8]

The gel polymer electrolytes investigated in this paper were prepared by direct polymerization. Our gel electrolytes are PMMA-based with EC:DMC (1:1) based electrolyte mixed with different kind of Li<sup>+</sup> salt. This paper brings comparison of both direct methods of gel preparation.

### Experimental

#### Materials

All chemicals were purchased from Sigma-Aldrich. Monomer methyl methacrylate (MMA) was distilled under reduced pressure. Cross-linking agent ethylene glycol dimethacrylate (1-2, EDMA) and both polymerization initiators benzoine ethylether (BEE) and 2,2'-Azobis (2-methylpropionitrile) (AIBN), ethylene carbonate (EC; 99,0 %, anhydrous) and dimethyl carbonate (99,9 %, water content under 0,005 %) were used as received. Lithium salts LiClO<sub>4</sub>,

LiBF<sub>4</sub> and LiPF<sub>6</sub> were dehydrated by vacuum heating at 110 °C for 24 hours. All chemicals were stored at 4 °C in the glove box refrigerator.

### Gel polymer electrolyte preparation

The initial mixture was prepared in the glove box under argon atmosphere and contains monomer MMA, cross-linking agent EDMA (0,5 mol % of monomer), polymerization initiator BEE (0,75 wt % of monomer) in the case of UV irradiation and AIBN (0,75 wt % of monomer) for temperature initiation. Furthermore, 30 wt % of monomer (in the case of UV irradiation) or 40 wt % of monomer (in the case of temperature initiation) of 1 M lithium electrolyte (LiClO<sub>4</sub>, LiBF<sub>4</sub> or LiPF<sub>6</sub>) EC/DMC (1:1 wt%) was added.

Different amount of 1M electrolyte was chosen for the reason of getting similar mechanical properties.

#### *Gel electrolytes prepared by UV radiation*

Polymer electrolytes were prepared using direct radical polymerization initiated by UV 500 W light and took 20 minutes at room temperature. The procedure was carried out in mold formed from PTFE plate, packing distance PTFE frame and glass plate. Mold was closed using screw clamps.

#### *Gel electrolytes prepared temperature initiation*

Prepared cells were filled with initial mixture and placed into an oven for 2 h at 65 °C. The design of the cells prevents MMA evaporation. The whole procedure was made in glove box to avoid of oxygen and water contamination.

Obtained samples of GPEs with area 4 cm x 4 cm and thickness corresponding with type of used PTFE seal (UV radiation 1,0 ± 0,1 mm, temperature initiation 2,0 ± 0,1 mm ) were more or less elastic and transparent.

### Equipment and measurements

Potentiostat VMP3 (Biologic) was used for electrochemical measurements. Samples of gel polymer electrolytes were putted into cells (type ECC-Std, El-Cell). Cells were placed into the conditioned chamber (CLIMACELL, BMT MMM Group).

Conductivity measurements were performed by using impedance spectroscopy, whereby the influence of temperature was studied in the range 0 to 80 °C in the frequency range from 100 kHz to 0,1 Hz. The resulting ohmic resistance was converted to specific conductivity values using the equation:

$$\sigma = \frac{d}{RS}, \quad (1)$$

where  $d$  is the thickness,  $S$  is the area of the sample and  $R$  is ohmic resistance.

The transference number was determined by DC polarization/AC impedance combination method and calculated according the following equation:

$$t_{Li^+} = \frac{I_{SS}(\Delta U - I_0 R_0)}{I_0(\Delta U - I_{SS} R_{SS})}, \quad (2)$$

where  $\Delta U$  is applied DC potential difference,  $I_0$  and  $I_{ss}$  are values of current obtained from DC polarization curves, represent the initial and steady state current flowing through the cell.  $R_0$  and  $R_{ss}$  obtained from AC impedance spectra, represent the initial and steady state resistance.

The applied DC potential difference was 10 mV. The frequency range of AC impedance was from 100 kHz to 0,01 Hz.

Electrochemical window (EW) of GPE was measured by cyclic voltammetry. Transference number and CV measurements of prepared polymer gel electrolytes were performed in ECC-Std cells in conditioned chamber at 20 °C.

## Results and discussion

All prepared electrolytes were elastic and homogenous membranes of a thickness 1 mm or 2 mm depending on the thickness of PTFE seal in the preparation cell. All used chemicals are colorless; therefore the prepared membranes are highly transparent.

As shown in Fig. 1, ionic conductivity increased with temperature increase. This is a typical behavior of gel polymer electrolyte. This is because increasing temperature results in the expansion of the polymer. This expansion produces local empty space and expands the free volume, which promotes the polymer segments and carrier ions to move.

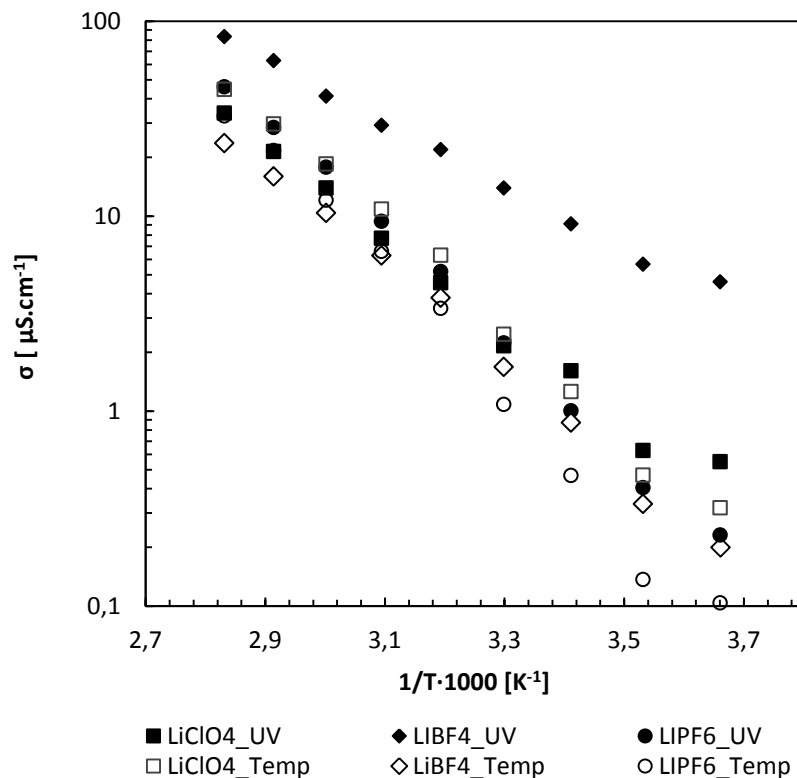


**Figure 1.** Arrhenius plot of the specific conductivity vs. temperature in the temperature range from 0 °C to 80 °C

Ionic conduction in the GPEs obeys the Arrhenius relation:

$$\sigma = A e^{\frac{-E_a}{RT}}, \quad (3)$$

where  $T$  is temperature,  $A$  is pre-exponential factor,  $E_a$  is the activation energy and  $R$  is the Universal gas constant

The transference number of an ion reveals how much of the total conductivity is contributed by the ion. It is the ratio of the conductivity due to ions to the total conductivity of the material. Transference number of an electrolyte is important as it determines the number of charge–discharge cycles the electrolyte can sustain. Charge–discharge cycles can give rise to concentration gradients in polymer electrolyte. This can eventually result in localized changes in conductivity of the electrolyte. A large transference number can reduce concentration gradient in the electrolyte during charge–discharge processes, thus sustain its power density and increase cycle life of the electrolyte.

**TABLE I.**  $E_a$  and  $t_{Li^+}$ , specific conductivity and electrochemical window values of prepared gel polymer electrolytes

Polymerization	salt	$E_a$ [kJ/mol]	$t_{Li^+}$	$\sigma$ [ $\mu$ S/cm]	EW [V]
UV	LiClO <sub>4</sub>	43	0,98	1,6	4,8
	LiBF <sub>4</sub>	30	0,71	9,1	3,2
	LiPF <sub>6</sub>	55	0,98	1	5,6
Temperature	LiClO <sub>4</sub>	52	0,68	1,3	4,3
	LiBF <sub>4</sub>	49	0,73	0,9	3,9
	LiPF <sub>6</sub>	62	0,69	0,5	4,3

$t_{Li^+}$ ,  $\sigma$  and potential window values at 20 °C

(a) limit cut off current density 0,8  $\mu$ A/cm<sup>2</sup>

(b) limit cut off current density 0,3  $\mu$ A/cm<sup>2</sup>

For a practical lithium ion battery, the cell potential can reach up to 4 V. This implies that the polymer electrolyte should be electrochemically stable up at least 4 V. The electrochemical stability window (EW) of polymer electrolytes is shown in Figure 2 and values are in Table 1.

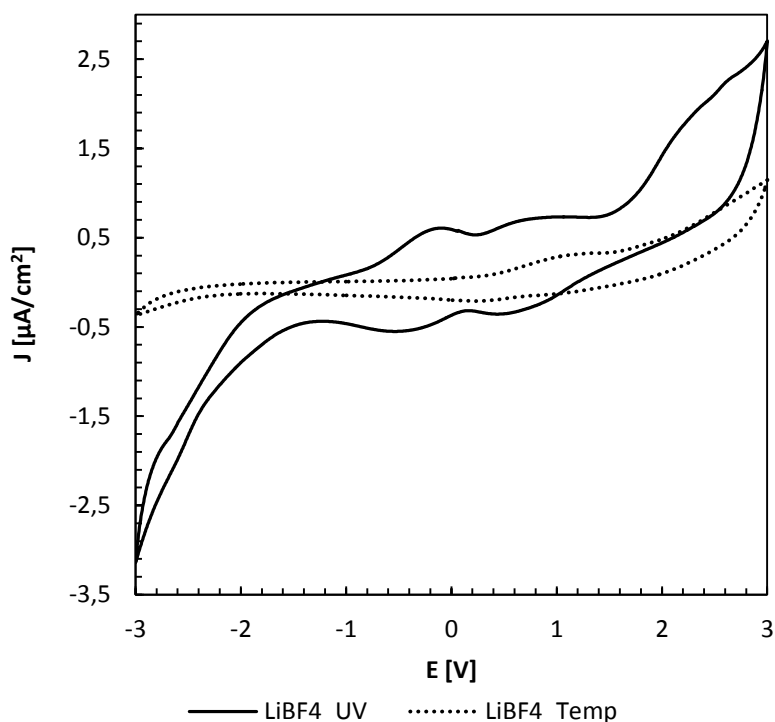


**Figure 2.** The electrochemical window of 1M LiBF<sub>4</sub> EC:DMC (1:1 wt) gel electrolyte at 20 °C

## Conclusion

PMMA-based gel polymer electrolytes were successfully prepared by two methods of direct polymerization processes and their electrochemical properties were investigated. The maximum ionic conductivity was found to reach 9,1  $\mu\text{S}/\text{cm}$  at 20 °C. The temperature dependence of the conductivity could be related to Arrhenius equation over the temperature range of 0 – 80 °C. The electrochemical window was stable up to 4 V width.

## Acknowledgements

This work was supported by the grant FEKT-S-11-7 and project CVVOZE CZ.1.05/2.1.00/01.0014.

## References

1. Cesar Sequeira, Diogo Santos, *Polymer electrolytes: fundamentals and applications*. Cambridge: Woodhead Publishing, 2010. ISBN 18-456-9772-3.
2. Jeffrey W. Fergus, *Ceramic and polymeric solid electrolytes for lithium-ion batteries*, Journal of Power Sources, Volume 195, Issue 15, 1 August 2010, Pages 4554-4569, ISSN 0378-7753
3. S. K. Tripathi, Ashish Gupta, Manhu Kumari, *Studies on electrical conductivity and dielectric behaviour of PVdF–HFP–PMMA–NaI polymer blend electrolyte*, Bull. Mater. Sci., Volume 35, No. 6, November 2012, Pages 969–975
4. Jakub Reiter, *Poly(ethyl methacrylate) and poly(2-ethoxyethyl methacrylate) based polymer gel electrolytes*, Journal of Power Sources, Volume 158, 2006, Pages 509–517
5. Jakub Reiter, Ondřej Krejza, Marie Sedlářiková, *Electrochromic devices employing methacrylate-based polymer electrolytes*, Solar Energy Materials & Solar Cells, Volume 93, 2009, Pages 249 – 255
6. S.A Agnihotry, P Pradeep, S.S Sekhon, *PMMA based gel electrolyte for EC smart windows*, Electrochimica Acta, Volume 44, Issue 18, 1 May 1999, Pages 3121-3126, ISSN 0013-4686
7. S. Ramesh, Khoo Ne Bing, *Conductivity, Mechanical and Thermal Studies on Poly(methyl methacrylate)-Based Polymer Electrolytes Complexed with Lithium Tetraborate and Propylene Carbonate*, Journal of Materials Engineering and Performance, Volume 21, January 2012—89
8. Jiří Vondrák, Jakub Reiter, Jana Velická, Marie Sedlářiková, *PMMA-based aprotic gel electrolytes*, Solid State Ionics, Volume 170, May 2004, Pages 79-82, ISSN 0167-2738

## Operation of E-Octavia fleet

Kristl, P., Vaněk, M., Poupa, P.

SKODA AUTO a.s.

Course of SKODA AUTO – emission targets, alternative powertrain solutions, electromobility. Introduction of E-Octavia fleet – technical specification for battery version of Octavia, vehicle development, user operational concept. Gaining and analysing data from vehicle run. Objective and subjective data – interesting findings from running fleet of electric vehicles.

Keywords: e-Octavia; electric drive; consumption; operational range; emissions

### Fuel consumption, emission

SKODA AUTO devotes great effort to reduce fuel consumption and emissions of whole model range, especially in cars GreenLine versions and Green tec. For example, a new generation Skoda Octavia in GreenLine version will be the most economical Octavia of all time - consuming just 3.3 l of diesel per 100 km, corresponding to CO<sub>2</sub> emissions of 87 grams per km.

Currently, 48 models ŠKODA AUTO achieves CO<sub>2</sub> emissions of less than 120 g/km, ten of them even gets below 100 g CO<sub>2</sub>/km.

SKODA AUTO offers environmentally friendly cars not only during the operation, but also in the production. Strategy GreenFuture SKODA clearly and concretely measurable committed to protecting the environment. GreenFuture is part of a growth strategy for 2018, and at the same time an important contribution to achieving the objectives of the Volkswagen Group, to become by 2018 the greenest automaker in the world.

SKODA AUTO will be further reducing the average amount of CO<sub>2</sub> emissions of all its models.

To achieve this objective, SKODA AUTO cooperates with Volkswagen to develop advanced technologies that contribute to the economical operation and to reduce the burden on the environment. For example further improvement and development of efficient turbo engines with direct injection, known under the abbreviation TDI and TSI.

Development of alternative drive trains is an important part of future strategy.

The first project in the field of alternative drives was the implementation of SKODA AUTO fleet of vehicles with purely electric-powered (BEV).

### Development of Octavia Green E Line

Development BEV is not only the development of the traction motor, power electronics, battery, but includes a wide range of development of new components, processes and activities.

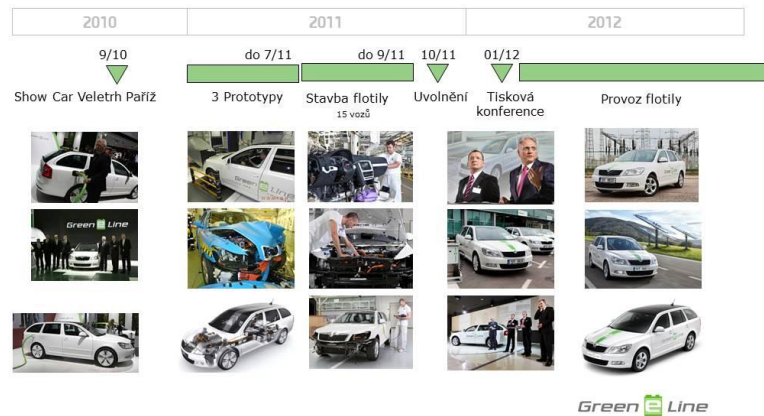


**Figure 1.** Development schedule of E-Octavia

Development and testing was focused primarily on high-voltage battery including charging, as well as the power electronics and motor control and peripheral systems such as heating and air conditioning. Great emphasis was placed on the safety of the car, from the perspective of both active and passive safety. Considering the greater weight of the vehicle (1595 kg) and change its centre of gravity, all brake systems including ESP were checked. Moreover, crash tests were conducted: front impact according to EC 96/79, rear shock according to ECE 32 and the side impact pole by Euro NCAP. Successful development was completed homologation car in September 2011.

### Description of car technique

Front-wheel drive ensures water-cooled synchronous motor with permanent magnets with a maximum output of 85 kW and a torque of 270 Nm. Transmission of the car is the gearbox, with a single gear (constant ratio 1: 9.81).



**Figure 2.** Technique of E-Octavia

Lithium-ion battery with a total energy capacity of 26.5 kWh consists of 180 cells. The battery has a total weight of 315 kg and is located at the rear of the vehicle. Its influence on the boot

capacity is minimal. It is water-cooled and rated voltage is 324V. Charging time three-phase voltage (400V) to 80% of battery capacity is 2.5 hours. Charging sockets are two, one in front of the vehicle (flip logo), the other at the rear of the sides missing fuel filler cap. The reason is simple: during the operation, clear feedback about preferred location is expected from the drivers. Operation range of the vehicle is 150 km by standard measurement methodology NEFZ.

Technical advantage for drivers is choice of one of two forward driving modes.

“The gear shift” can be set to position B, where the deceleration of the vehicle is permanently set on the maximum recovered in power or in position D, which is the default “gliding” in the case when the driver lifts his foot from the accelerator and does not brake with hydraulic circuit. In this setting (D) the driver can in addition choose one of the sub-level recovery D1 to D3 via paddles on the steering wheel. Another driver option is setting level of ride comfort. With new button in the center console can choose the level of normal, eco or range. Present basic level provides all the normal functions and performances without limitation, the level of eco range is limited and some features and reduced power available, such as top speed or maximum speed of electric AC compressor. These are guarantee of extended driving range.

All relevant customer information are displayed in the instrument cluster or on-screen navigation system RNS. In addition to standard information, it is all about the power consumption. It is possible to see consumption as comfort systems or battery capacity or current flows of energy.

In city traffic, the car is almost silent, it was necessary to protect pedestrians with artificial sound of engine. So-called sound generator with speakers mounted in the engine compartment generates at speeds up to 50 km/h synthesized sounds.

### **Findings from the field**

10 fleet E-Octavias has been in continuous operation since January 2012. During the first four months the opportunity to try car was given to the internal employees of SKODA AUTO in various professions and levels and from different departments. Since May 2012, cars have operated together with selected external partners as well as SKODA AUTO to actively build and develop competence in the field of electromobility.

After more than a year of operation, E-Octavia fleet has operated more than 255,000 kilometers, with a strong dominance of urban traffic (70%) than non-urban. Regarding the length of single drive, 85% of all journeys are to 21 km. E-Octavia are used practically without significant limitations, which confirms the average speed 45 km/h, but also the fact that 86% of all journeys are in normal mode (only 10% range). 75% of users use three-phase charging (400 V).

Other interesting information includes operating power consumption and especially range. The average annual consumption is less than 19 kWh/100km, while in the summer months the consumption is significantly lower because there is no need to temper interior and own traction system.

Each E-Octavia is equipped with recording equipment, during operation captures and transmits hundreds of individual variables. These data are processed in classification tasks. The measured values vary according to external conditions (eg. outside temperature), eventually are progressing evolves according to experience of the driver. Results are technically interpreted and reflected in new solutions.

### Operating range

Operating range is given according to standard NEFZ cycle. In this case, operating range is measured on “rolling road” (measurements on the reels) and there are precisely defined acceleration, deceleration during measurement, heating and air conditioning of the car is turned off. In this case, the car reaches operating range 150 km (which is specified in the technical documentation).

### Subjective users ratings

E-Octavia users are regularly asked about the findings, both positive and negative comments from service. Users highly appreciate the quietness and calm of e-car. Driving is not too stressful, control is classified as intuitive and convenient. E-Octavia drivers are enjoying acceleration and recuperation. Cars and their performance always evoke great interest in the area. The biggest limitations of E-Octavia users are operating range, charging time, and a small possibility of public charging points. Enlarge operating range and building of adequate charging infrastructure is a major challenge for next period.

### **Reference**

1. Perspektivy elektromobility, Mgr. Petr Kristl, ŠKODA AUTO a.s., magazine annex Electro and Automatization 2013

## **Secondary cells and Energy Accumulation in Energetic Applications and Transportation.**

Hladík, M.

The contribution will introduce shortly the main reason for the use and deployment of the energy accumulation and deployment in Energy Sector and Transportation. Part of this introduction will be also the list of main requirements on the secondary cells / accumulators for the energetic applications, transportation and explanations of the main pro and con for the single kind of the secondary cells technologies, BMS (Battery Management Systems) and relevant HES (Head End Systems). In the second part the presentation will be concentrated on related battery / accumulation electronics, software explaining the main prerequisites of the functional system especially equivalent voltage on all cells, protection mechanism against overload, high temperatures and charging / discharging regimes.

The third part analyses the issues oriented on some details of balancers (load optimization and control), BMS and HES incl. standardized data protocols for the successful integration with EMS (Energy Management System) and remote management. All technical issues are introduced not only from the technical point of view, but also with the respect to the economics and price / performance ratio. Last chapter of the contribution presents the new technologies and trends in energy accumulation and its outlook in near and long term future.

## Fast-charger for electric plane

Vorel, P.<sup>a</sup>, Procházka, P.<sup>a</sup>, Huták, P.<sup>a</sup>, Pazdera, I.<sup>a</sup>, Červinka, D.<sup>a</sup>

<sup>a</sup> Department of Power Electrical and Electronic Engineering, Brno University of Technology, Technická 12, 616 00 Brno, Czech Republic

### Introduction

A complete electric drive, battery pack, battery monitoring system (BMS) and fast-charger co-operating with this BMS was developed and realized in the Department of power electrical and electronic engineering. The whole system was designed for an electric plane VUT 051 RAY. A synchronous motor with permanent magnets (55kW) is used. The battery pack consists of 3060 pieces of Li-ion cells PANASONIC NCR18650-A. 90 serial blocks per 34 parallel cells are used. The nominal parameters of one cell are 3.6V/2.9Ah. Therefore the total battery pack nominal parameters are approx. 324V/98Ah. The total weight of the pack is 137.7kg (pure cells without construction components and BMS circuits). This paper describes the developed fast-charger for the mentioned battery pack. Power and also control circuits are introduced briefly. The charging algorithm and over-charging protections are discussed.

### Basic description

A power switching supply source (converter) of a progressive non-traditional conception represents the core of the charger. Power switching transistors Cool-MOS and ultra-fast power silicon-carbide diodes (both from INFINEON) are used in the power circuit. Very low dimensions and weight of the device were achieved using a non-usually high switching frequency of 100kHz. The basic parameters are in Tab.1.

**TABLE I.** Basic technical parameters of the fast-charger

Max. steady output power	16kW
Max. output DC voltage	ca 380V
Max. steady output DC current	42A
Supply	3x400V/50Hz
Weight	ca 23kg
Dimensions	37x35x26cm

### Charging method

The control circuits of the charger together with the BMS circuits of the accumulator pack ensure a cascade voltage control with a slave current loop. The charging process is following:

a) While the accumulator is so discharged that the voltage from neither one of 90 serial blocks reaches its maximum value (final cell voltage) the BMS requires full charging current (42A). This information is transferred from BMS to the slave current control loop included in the charger. Then the accumulator is charged with this constant current (the internal current control loop ensures it). However the value of the charging current can be limited manually to a lower value with a switch placed on the front panel of the charger.



**Figure 1.** Total view of the charger device (without upper cover)

b) If the charging process continues and the voltage on any (at least one) of the serial blocks (cells) reaches the final value then the BMS starts to decrease the desired current value for the slave current controller just to keep the voltage of the incriminated cell on the final level – no over-voltage (too high current) but also not to decrease the voltage (too low current). This means the charging process in the described phase b) continues always more slowly – more charged cells need lower charging current not to exceed the final voltage of any cell. Globally the phase b) represents a regime with constant voltage (if all the cells are identical then they react synchronously). Let 's point out that not only the pure control of the total pack voltage is performed but each of serial blocks is taken into consideration – so when the block capacities or state of charge will differ each other no over-charging of any cell can appear – even if no balancing circuits in the BMS were used. (Presence of balancing circuits only makes the charging process shorter if some irregularities if the cells appear).

Note: The used charging method is often called CC/CV (constant current/constant voltage). However in our conception the regime CV is improved taking into consideration separately the voltages of all the serial blocks (all cells of the pack).

After ending the first phase a) (CC – constant current) the accumulator is charged to approx. 80% of its nominal capacity (whether the initial state of charge and capacity of all cells are approximately identical). The identical state of charge of the cells ensure the balancing circuits of BMS, the identical capacity is expected. However, during the accumulator aging some capacity irregularities among the cells can appear – then the charging process takes a longer time because the phase a) ends sooner thanks to the weakest cell and the phase b) with lower charging current comes.

It is clear from the description that the charging process runs automatically till the end, no over-charging can appear. So the charger need not be switched-off after the accumulator is fully charged. The state of charge can be observed in detail (display of the charger). Approximately it can be observed also watching the signal LEDs.

### **Safety system of protections against the over-charging**

Li-ion accumulators and related types are very sensitive to over-charging (as well known). The lifetime decreasing and even sudden damaging with a fire risk can appear. Therefore the voltage control and additional over-voltage protections must be solved really precisely to ensure the safe user operation.

As mentioned above the co-operation of BMS and the internal slave current controller ensures in proper operation that no cell of the accumulator can be over-charged. The used logic of control signal from BMS (required current for the charger) ensures that when the control cable is interrupted or short-cut (mechanical damage, connector failure etc.) this state represents in the charger anyway the requirement of zero charging current.

An additional hardware analogue internal master voltage controller is included in the charger – for a case when the external BMS circuits would fail (they would require a non-zero charging current in a situation with an over-voltage). This controller is certainly able to control only the total accumulator voltage (not each cell separately). The set required voltage for this controller is 385V. If BMS works properly then the total voltage can not exceed 378V. This is why the additional voltage controller is normally always saturated what means out of order from the user standpoint (the BMS performs the voltage control).

Further a software one-shoot over-voltage protection is used for a case of a failure of the before mentioned protective voltage controller. If the output voltage exceeds 400V then the required charging current is internally set to zero (independently on the BMS requirement). A LED signalises this situation.

Finally a very fast hardware one-shoot protection is used. If the output voltage exceeds 450V then the power circuit of the charger is blocked. This is used not to protect the accumulator (the voltage of 450V is anyway fatal for the accumulator) but it serves as a protection for the charger device and its human operator. For example when operating with no load (accumulator disconnected, power cable failure etc.) a high output voltage can appear on the output terminals being dangerous for the device itself. The transfer delays of the internal protective voltage controller (385V) and software protection (400V) cause that the device could be damaged meanwhile. Moreover the presence of voltage (385V) on the damaged power cable would be unwanted.

### Charger circuits

The global internal connection of the charger is in Fig. 2. A power switching supply source is used. A DC/DC converter with a pulse transformer creates the core of the device.

Due to the high output power (16kW) the device must be supplied from a 3-phase network. The net voltage is lead through the main switch OT25FT3 (3x25A) to the input net filter. This eliminates the interference of the converter to the distribution network. A 3-phase input rectifier follows. Its output DC voltage represents the DC link of the following DC/DC converter. The converter is represented with blocks Converter primary circuits, Pulse transformer (with a serial coil and current measuring transformer), Output rectifier, Choke. These parts create the power circuit of the charger. The block “Drivers” represents an interface between the control circuits generating the PWM signal and power circuit, whose transistors are switched with this PWM signal.

All the circuits described further create the control circuits of the charger. The PWM signal is created in the block PWM modulator according to the input control voltage  $U_c$ . An over-current protection is implemented in this block too. The over-current is detected with current transformers (galvanic separation). Further a protection against over-voltage in the split DC-link is implemented. The information of the over-voltage is transferred to the block via optical fibres.

A cascade control structure is used. The existence of the slave current control is advantageous because of the reachable dynamics of the control processes (system stability problems).

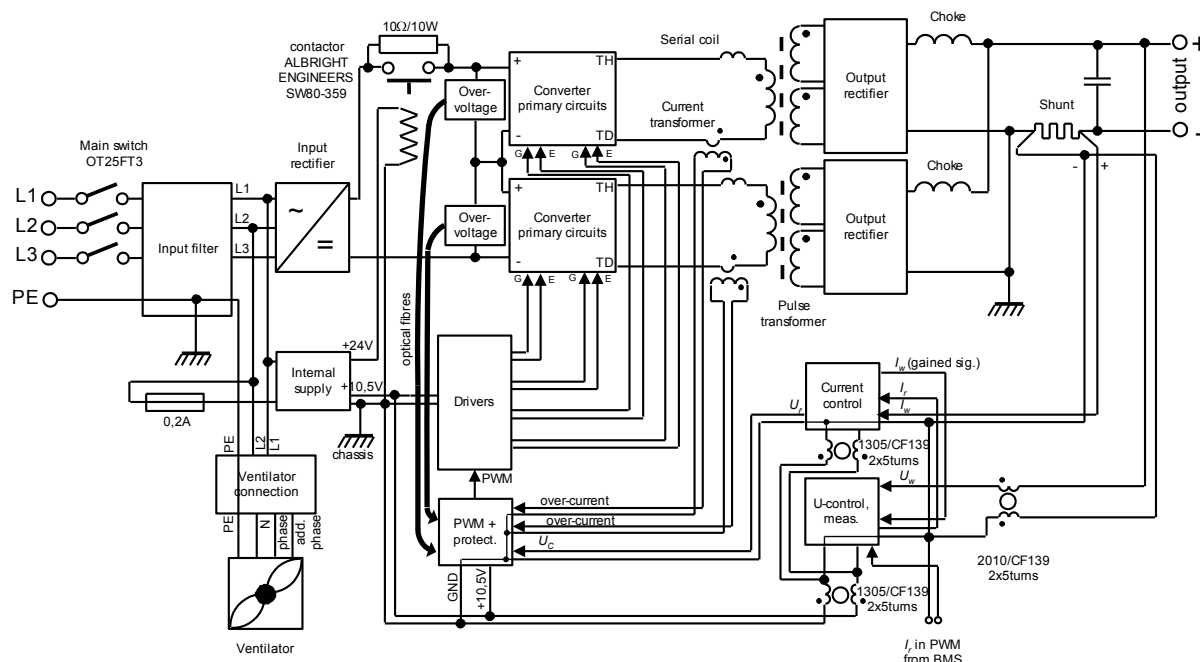


**Figure 2.** Internal connection of the fast-charger

The voltage control in the charging process is performed with the BMS circuits of the accumulator. These BMS circuits are not present inside the charger. BMS provides the information of the required charging current to the charger via a one-bit logical signal – the information is coded with a PWM (certainly this PWM is another one that the PWM switching power transistors). The block “U-control, measurement” in Fig. 2 demodulates this PWM information so it creates an analogue signal  $I_r$  (required current). The mentioned block includes also an over-heating protection, protective internal voltage controller (385V), software over-voltage protection (400V) and the fast hardware over-voltage protection (450V).

The current controller gets the required current value  $I_r$  from the described block “U-control, measurement”. The true value of the current  $I_w$  is obtained from a shunt at the output of the charger. The output signal of the current controller represents the control voltage  $U_c$  for the PWM modulator.

### Acknowledgement

This research has been supported with a grant project MPO FR-TII/061 “Application of VUT 001 Marabu for hydrogen fuel cells propulsion“. Partially the development was supported by the faculty project FEKT-S-11-14 “Utilization of new technologies in the power electronics”.

### References

1. P. Vorel, P. Procházka, V. Minárik, “Powerful fast charger 16kW for electric vehicle,” Proceedings of ABAF Brno 2011. ISBN 978-80-214-4310-5, (September 2011)
2. G. Kovacevic, A. Tenconi, R. Bojoi, “Advanced DC–DC converter for power conditioning in hydrogen fuel cell systems,“ International Journal of Hydrogen Energy, Volume 33, Issue 12, ISSN 0360-3199, (June 2008)

## Electric Drive of Propeller for Battery-Powered Aircraft

Červinka, D., Knobloch, J., Klíma, B., Huták, P., Kadlec, J., Fajkus, P.

Brno University of Technology,  
Faculty of Electrical Engineering and Communication,  
Department of Power Electrical and Electronic Engineering,  
Technická 3058/10, 616 00 Brno, Czech Republic,  
www.uvee.feec.vutbr.cz

Described drive is designed for battery-powered aircraft of category VLA. The design focuses on compactness and especially on weight of whole system. Although it looks like a common solution of electric drive for an independent traction, this application has its own specifics that we want to show.

Nominal power of drive is approx. 55kW. No-load voltage of batteries is 378V in fully charged state, with nominal load voltage decreases to 324V. Final voltage under load is 297V at battery discharge mode. (1)

Figure 1 shows the structure of system. Drive consists of four main subsystems:

- Li-Ion accumulator system with BMS
- Central unit with main computer, fuses and contactors
- Traction DC/AC inverter with permanent magnet synchronous motor (PMSM)
- Control system with onboard monitoring panel (cockpit unit)

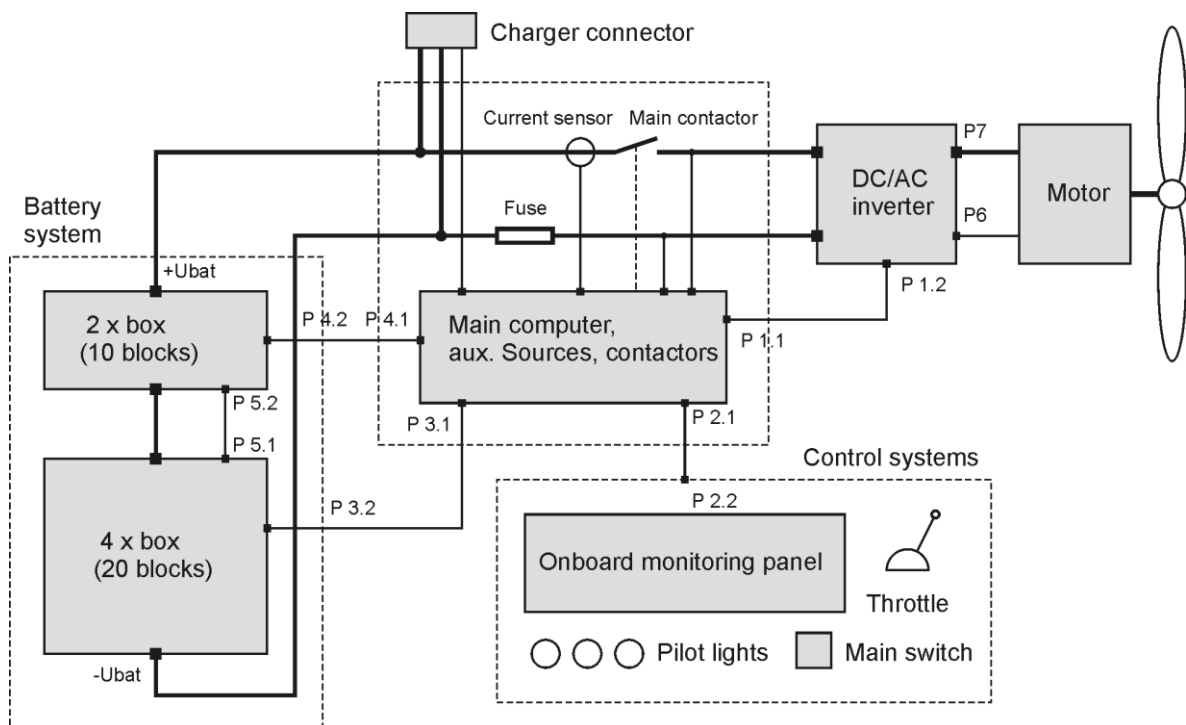


**Figure 1.** Overview of the drive system

Communication between all subsystem is ensured via CAN Bus. Central unit evaluates all measured signals (temperatures, voltages, currents, speed) and processes error messages from all subsystems. The central unit contains power parts as a fuse and contactors too.

Control system is installed in the center of plane dashboard, and handles communication with pilot. The most important part of control instruments is throttle lever for setting desired power of motor. Touchscreen provides only monitoring functions, as a displaying selected parameters of battery system, inverter and motor.

The PMSM was chosen due to best ratio between power and mass. Construction of motor shield with holes allows to airflow inside motor directly to winding, which ensures sufficient cooling. Nominal torque of motor is allowed only during the plane flight with nominal speed. The motor cooling is not sufficient during the plane taxi. Therefore motor is equipped by temperature sensors and control system inform the pilot.

Traction DC/AC three phase inverter is based on Semikron IGBT module. To meet demanding requirements to reliability the industrial SKiM606GD066HD module was chosen. This module is intended for demanding automotive applications. This module contains no soldered connections, which can ensure module shock resistance. Driver and control board of inverter are mounted directly on IGBT module. This configuration is ideal in terms of consumed space. Traditional vector control algorithm with resolver position feedback is used for motor control. Control signal gained from the throttle lever sets desired power. This simulates behavior of throttle well-known from traditional combustion engine.

IGBT module is mounted on aluminum heatsink, which is exposed to air stream during flight. As in the case of motor, the cooling problem arises during airplane taxi. Therefore the inverter is equipped with four small ventilators to ensure sufficient airflow.

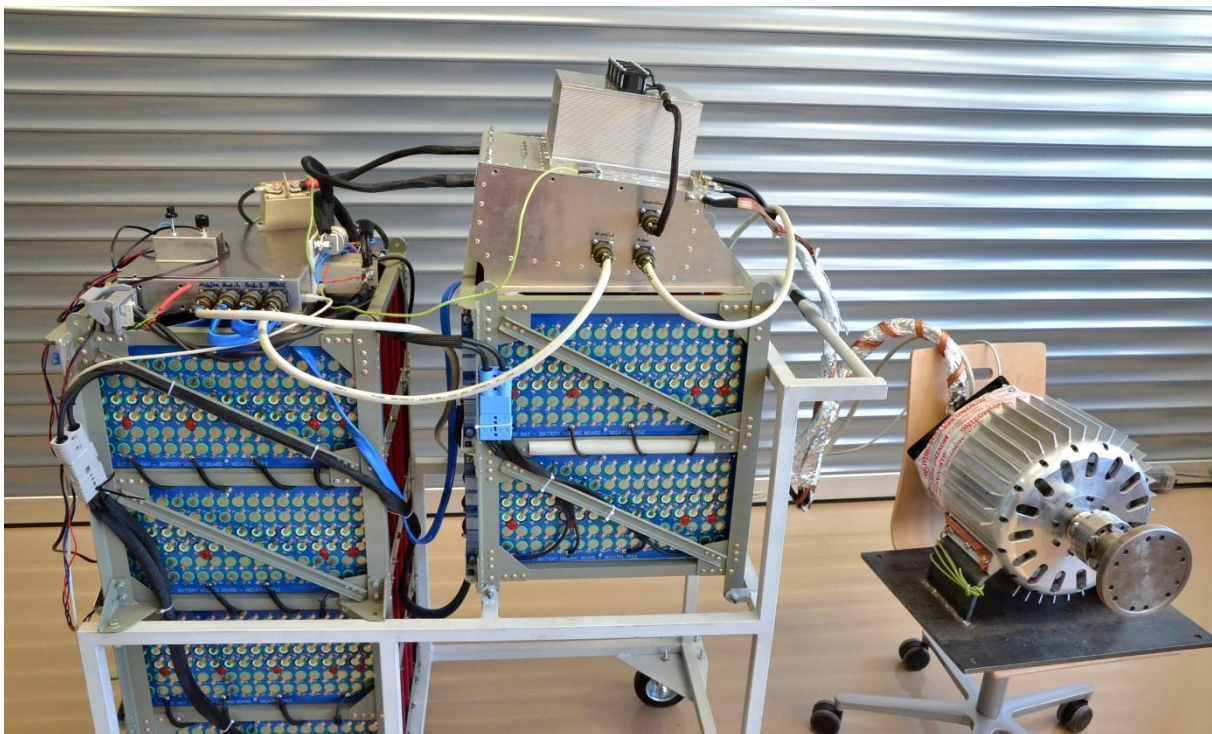


**Figure 2.** Traction drive during laboratory tests

Traction system is equipped with backup control circuitry to ensure safety operation of the plane. This hardware mode can be activated only by pilot only in the case of fatal communication failure. All complicated communication and safety systems in central unit are bypassed. Power of

propeller is in this case controlled only by simple potentiometer connected directly into inverter. This function can't be used in common operation of plane, it can be enabled only in the high risk of the plane crash. The possible damage of inverter, motor and battery by high temperature are only secondary matters.

### Acknowledgement

This work has been prepared under the support provided by research projects FEKT-S-11-14, FR-TII/061 Ministry of Industry and Trade of the Czech Republic and Center for Research and Utilization of Renewable Energy no. CZ.1.05/2.1.00/01.0014.

### References

1. Klíma, B., Červinka, D., Pazdera, I., Píštěk, A., Hlinka, J., *Battery System of Electric Airplane VUT 051 RAY*, Advanced Batteries, Accumulators and Fuel Cells ABAF 12, ISBN 978-80-214-4357-0, Brno, (2011)
2. Cipin R., Kadlec J., Klíma B., Hutak P., *Battery System for the Airplane VUT 051 RAY*, Advanced Batteries, Accumulators and Fuel Cells ABAF 13, ISBN 978-80-214-4610-6, Brno, (2012)

## Li-ion accumulators for propulsion system of electric Airplane VUT 051 RAY

Kadlec, J.<sup>1</sup>, Cipin, R.<sup>1</sup>, Klima, B.<sup>1</sup>, Cervinka, D.<sup>1</sup>, Vorel, P.<sup>1</sup>

<sup>1</sup> Brno University of Technology, Department of Power Electrical and Electronic Engineering, Technicka 12, Brno, Czech Republic

### Abstract

This paper describes battery system for the airplane VUT 051 RAY and description of the whole airplane battery.

Required battery parameters are divided into two aspects:

The first one is power. There are important requirements on the motor power and total energy of the battery for safe flight:

- Motor power 52 kW
- Battery output power 60 kW
- Stored energy for one flying cycle 34 kWh

The second aspect is total mass of whole electric drive system:

- Whole system mass max. 230 kg
- Allowed battery mass max. 150 kg
- Motor mass 40 kg

From previous aspects, the battery has to have energy density minimally 227 Wh/kg. Other requirement is minimal discharge rate 2C.

Recently, Lithium-ion (Li-ion) accumulators have better capacity/weight ratio of all accumulators' types. Due to this fact, they could be successfully used for some mobile applications, because these applications need high accumulated energy with maximally low weight – for example automotive industry or aerospace.

Following chapters present the Li-ion accumulators system (includes a monitoring system) that is designed as an energy source for the airplane VUT 051 RAY. DC-line (the battery), composed of this kind of accumulators, will feed mainly a synchronous motor (about 52 kW). Similar projects of electric airplanes are HK36 Super Dimona, Antares DLR H2 and ENFICA-FC, see lit. (1), (2).

Whole battery consists of 3060 Li-ion cells Panasonic NCR18650A (3). Connection grid contains 90 cells in series and 34 cells in parallel.

Important parameters of Li-ion accumulators Panasonic and whole battery are shown in Tab. 1.

**TABLE I.** Important parameters the Li-ion accumulator Panasonic and the battery.

Parameter	one cell	whole battery
Nominal voltage [V]	3.6	324
Maximal voltage [V]	4.2	378
Nominal capacity [Ah]	3	102
Mass [kg]	0.0455	150
Maximal current [A]	6	204



**Figure 1.** Battery transport carriage.

### Acknowledgements

This work was solved in the frame of the faculty project FEKT-S-11-14 “Utilization of new technologies in the power electronics”; of the projects CZ.1.07/2.3.00/30.005 and CZ.1.05/2.1.00/01.0014; and of project MPO FR-TI1/061 “Application of VUT 001 Marabu for hydrogen fuel cells propulsion”.

### References

1. Bencalík, K.: Předběžný návrh koncepce vodíkového pohonu letounu VUT 051 RAY, Brno 2011, report number: LU33-2011-RAY.SY
2. Romeo, G. - Borello, F. - Cestino, E.: Design of Inter-City Transport Aircraft Powered by Fuel Cell & Flight Test of Zero Emission 2-Seater Aircraft Powered By Fuel Cells, Torino 2012, ISBN: 978-1-4673-1370-4
3. Electronic text available at address: <http://industrial.panasonic.com/www-data/pdf/ACA4000/ACA4000PE3.pdf>

## Possibility of using the advanced battery systems in the Polish mining industry

Polnik, B.<sup>a</sup>, Miedziński, Z. B.<sup>b</sup>, Kozłowski, A.<sup>c</sup>

<sup>a</sup> Division of Drives and Control Systems, Institute of Mining Technology KOMAG,  
Pszczyńska Str. 37, 44-101 Gliwice, Poland

<sup>b</sup> Institute of Electric Power Engineering, Wrocław University of Tehcnology,  
Wybrzeże Wyspiańskiwego Str.27, 50-370 Wrocław, Poland

<sup>c</sup> Institute of Innovative Technologies EMAG, Leopolda Str.31, 40-189 Katowice, Poland

Mining industry is currently one of the biggest industries in the world. All mines produce “indispensable” minerals, starting from fuels such as coal and ending with noble metals such as gold or copper. Mines in the world compete in the volumes of mined minerals what requires use of state-of-the-art, more efficient and, and what is more important, safer machines. Such trend favours development of technology and mobilize engineers to adapt the technologies that were used so far in easier environment to the needs of the mining industry.

Machines and equipment used in hard coal mines, which are supplied from packs of batteries, are reviewed. Trends in development of mining technologies are given, formal requirements for use of machines in underground mining plants are discussed and state-of-the-art solutions for the mining industry, which are developed in Polish research centres, are presented.

### Formal requirements.

When it comes to hard coal mines in Poland 99% of all mining plants are the mines with methane or coal dust explosion hazard. Thus, each machine designed for operation in mines undergrounds within the European Union should meet the requirements of the following directives:

- Directive 94/9/EC of the European Parliament and the Council of 23 March 1994 on the approximation of the laws of the Member States concerning equipment and protective systems intended for use in potentially explosive atmospheres.

- Directive 2006/42/EC of the European Parliament and the Council of 17 May 2006 on machinery, amending 95/16/EC Directive.
- Directive 2004/108/EC of the European Parliament and the Council of 15 December 2004 on the approximation of the laws of the Member States relating to electromagnetic compatibility and repealing Directive 89/336/EEC.
- Directive 2006/95/EC of the European Parliament and the Council of 12 December 2006 r. on the approximation of the laws of the Member States relating to electric equipment designed for use within a certain voltage limit.
- Directive 2006/95/EC of the European Parliament and the Council of 16 September 2009 concerning the minimum safety and health requirements for use the work equipment by workers at work (second individual Directive within the meaning of Article 16 (1) of Directive 89/391/EEC).

Additionally, there are also the standards harmonized with the above mentioned directives, which specify the requirements for each type of machine and equipment.

### Sample applications:

Machines – until now these are only of Lea (mainly mono-drive) and Ldag (dual-drive) battery locomotives – Fig. 1.

a)



b)



**Figure 1.** Mine battery locomotives manufactured in Poland. a) – Lea BM-12, b) – Ldag 05M

These locomotives were manufactured in 1960s and they are still in operation. They are supplied by pack of lead-acid batteries of different capacity.

In 2012 Polish company IzolPlast in collaboration with the Institute of Innovative Technologies EMAG developed and manufactured new mine battery locomotive ELA-44 (Fig. 2).



**Figure 2.** ELA-44 mine battery locomotive

It has state-of-the-art drive system (DC motors were replaced with asynchronous motors), but it is still supplied by lead-acid batteries.

KOMAG Institute of Mining Technology was the first company in Poland, which suggested the mining machines with the cells of new generation. In collaboration with other manufacturers from mining and automotive industries, KOMAG developed two types of suspended monorails – GAD-1 (Fig. 3) and PCA-1 (Fig. 4).



**Figure 3.** (left) GAD-1 battery drivetrain of suspended monorail

**Figure 4.** (right) PCA-1 suspended battery drivetrain

The above machines were positively verified during attestation tests and they were approved for periodical operational tests.

Among other use of batteries in underground mining industry, two of them are used now: present mine lamps (Fig. 5) and optical-and-acoustic signalling device (Fig.6). In the solutions given in Fig. 5 and 6 the same pack of batteries are used, but of different capacity. In such a situation, devices can be recharged from the same charger.



**Figure 5.** (left) SMARTLIGHT-05/M1 mine helmet lamp

**Figure 6.** (right) SOA-1 optical-and-acoustic signalling device

Detailed information on the developed solutions is given in the paper and the problems, which were faced by designers during work on innovative solutions, are discussed. In addition, the trend in development of mining machines, which would require state-of-the-art sources of energy, is presented.

## Comparison of fuel cell and Li-ion accumulators for using in electrical airplane

Prochazka, P., Cipin R., Pazdera, I., Knobloch, J., Fajkus, P.

Affiliation – Brno University of Technology, Faculty of Electrical Engineering and Communication, Department of Power Electrical and Electronic Engineering, Technicka 3082/12, 616 00 Brno, Czech Republic, [www.uvee.feec.vutbr.cz](http://www.uvee.feec.vutbr.cz)

The article deals with a comparison of a fuel cell and Li-ion accumulators for utilization in an electrical propulsion system of the airplane VUT 051 RAY. The measurements were done on a stack Heliocentris HyPM<sup>®</sup> XR 8. This stack contains the fuel cell (8.5 kW) manufactured by company Ballard with maximal output current 380 A and voltage from 20 to 40 V. (1)



**Figure 1.** Stack Heliocentris HyPM<sup>®</sup> XR 8. (2)

Properties of the fuel cell are compared with a battery block, which consist of Li-ion accumulators Panasonic NCR18650A. This battery block is actually used for the propulsion system of the airplane VUT 051 RAY.

### Fuel cell measurements

The measurements ere firstly done for step changes of the load. The main airplane drive is very often loaded in this way (the pilot ascends to the desired height with a full power; he switches off the engine and he glides with airplane to lower level where the whole process is repeated). It is very important to be able to turn on and off the drive very quickly. Fig. 2 ÷ Fig. 5 shows transient curves of the voltage and the output current of the fuel cell during its turn (on/off) state. The output currents are about 60 A, 100 A, 150 A and 250 A.

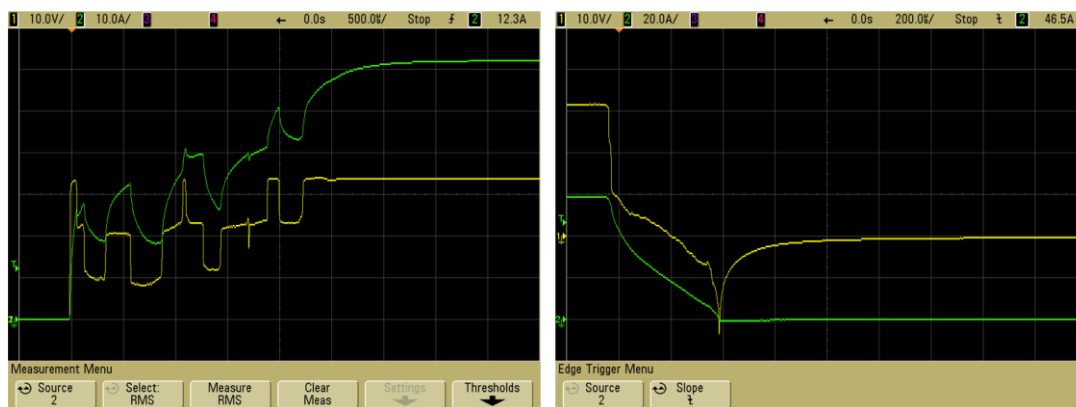


**Figure 2.** Switch on and switch off the fuel cell into load 60 A.

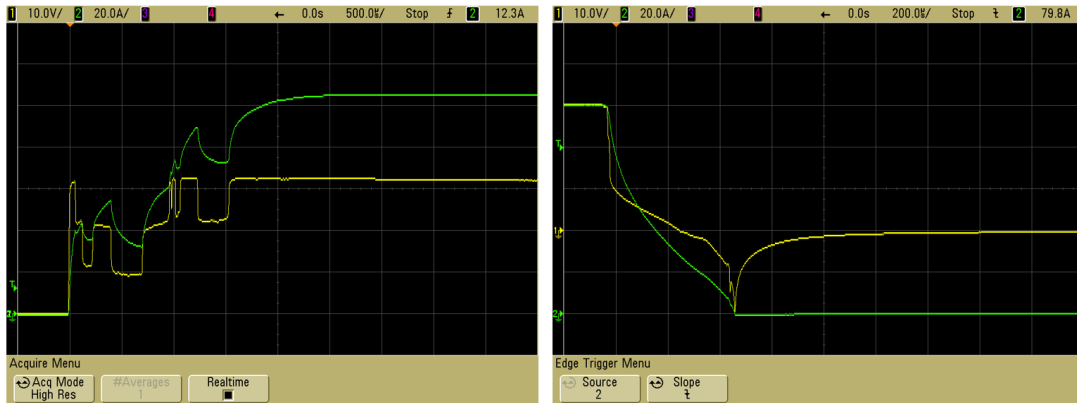


**Figure 3.** Switch on and switch off the fuel cell into load 100 A.

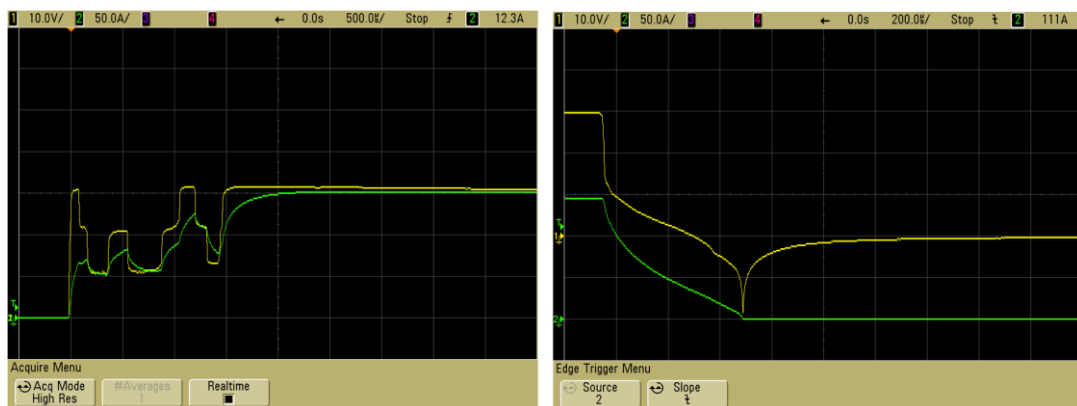


**Figure 4.** Switch on and switch off the fuel cell into load 150 A.

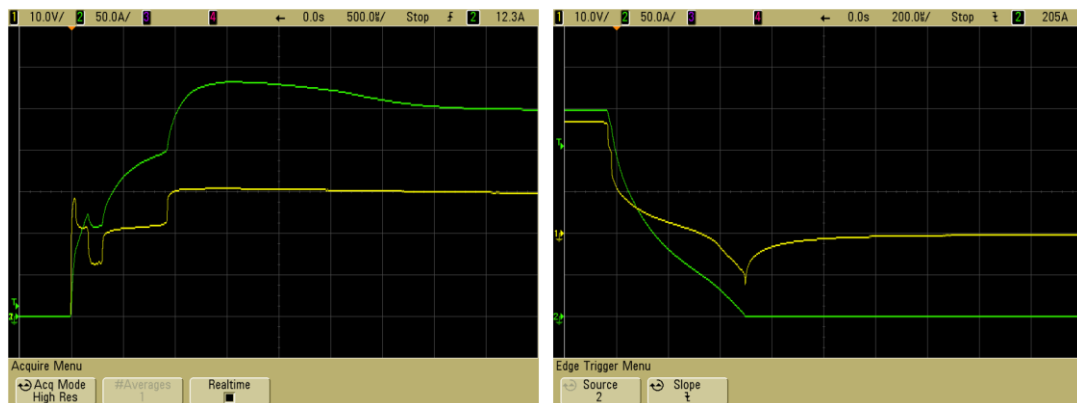


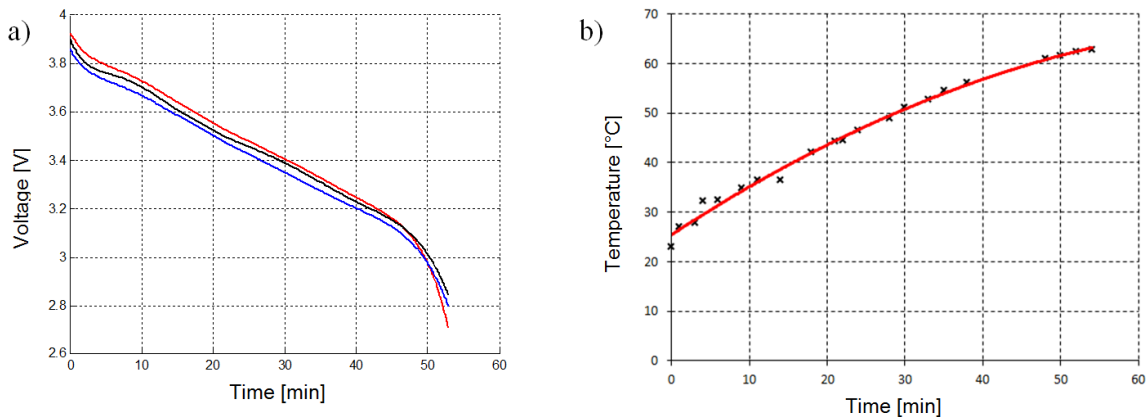
**Figure 5.** Switch on and switch off the fuel cell into load 250 A.

### Battery pack measurements

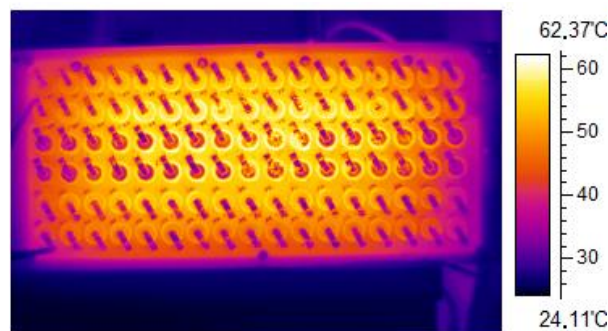
The battery block was firstly discharged with constant current 116 A (3.4 A per one accumulator), see Fig. 6a). This current level is equivalent to current load during horizontal flight of the airplane. Total measuring time was 53 min. After this time, the battery block was completely discharged, i.e. consumed energy was about 102 Ah. Ambient temperature before the measurement was 23 °C. The temperature course is shown in Fig. 6 b).

Fig. 7 shows battery block temperature in the end of discharging. The warmest accumulators are at the second row from the top side because warm air moves up. Accumulators at the edge of the battery block are cooled with ambient air. The point of maximal temperature has about 62 °C. (3)

The second discharging was done with average value of the current 180 A. Fig. 8 shows discharge curves. The battery block was completely discharged after 35 min, i.e. consumed energy was about 104 Ah.



**Figure 6.** a) Discharging curves (constant current 116 A). b) Temperature course.



**Figure 7.** Figure 7: Thermo-figure of battery block after discharging by constant current 116 A.

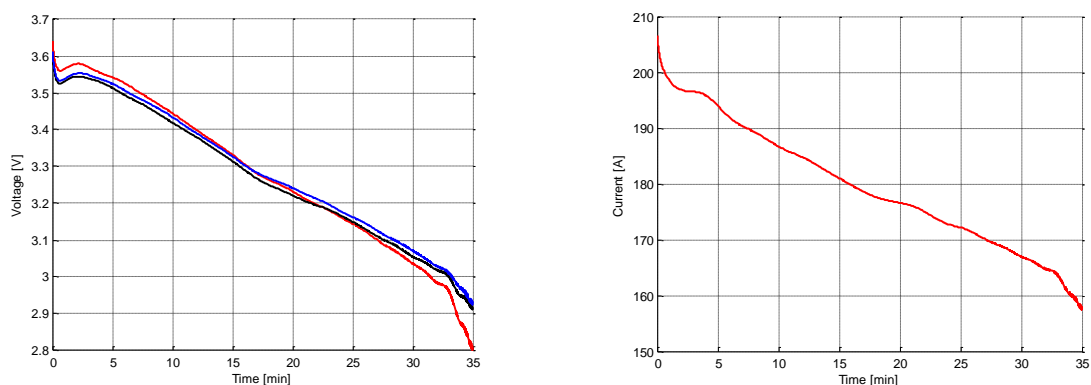


**Figure 8.** Discharging curves for average current 180 A.

## Conclusions

The full paper will contain additional details of the fuel cell measurements. And it will be done full comparison of the stack Heliocentris HyPM<sup>®</sup> XR 8 a battery block with Li-ion accumulators Panasonic NCR18650A used in the airplane.

### Acknowledgements

This work was solved in the frame of the faculty project FEKT-S-11-14 and the project No. CZ.1.07/2.3.00/30.005 funded by European Regional Development Fund; and Center for Research and Utilization of Renewable Energy No. CZ.1.05/2.1.00/01.0014.

### References

1. Prochazka P., Pazdera I., Bencalik K., *Usage of the Fuel Cell Powered Electric Drive in Aviation*, Advanced Batteries, Accumulators and Fuel Cells ABAF 13, ISBN 978-80-214-4610-6, Brno, (2012)
2. Electronic text available at address:  
<http://www.technovolt.ro/cataloge/heliocentris/CATALOG%20SISTEME.pdf> (2013)
3. Cipin R., Kadlec J., Klima B., Hutak P., *Battery System for the Airplane VUT 051 RAY*, Advanced Batteries, Accumulators and Fuel Cells ABAF 13, ISBN 978-80-214-4610-6, Brno, (2012)

# INFORMATION ABOUT THE ELECTROCHEMICAL SOCIETY



ABAF 2013 is co-sponsored by the Electrochemical Society, Inc (ECS). ECS is an international non-profit, educational organization concerned with a broad range of phenomena relating to electrochemical and solid-state science and technology. It has over 8,000 member scientists and engineers in over 70 countries worldwide, as well as roughly 100 corporations and laboratories, which hold corporate membership. The objectives of ECS are:

- to advance the theory and practice of electrochemistry, solid-state science, and allied subjects;
- to encourage research and dissemination of knowledge in these fields;
- and to assure the availability of adequate training and education of fundamental and applied scientists and engineers in these fields.

First founded as the American Electrochemical Society in 1902, the name of the Society was changed to The Electrochemical Society already in 1930 to more accurately reflect its international activities and membership. Presently, more than 50 % of members reside outside USA. ECS has grown and continued to respond to the changing technical needs and interests of its members; and in 2000, adopted the official acronym of ECS. The tag-line name of ECS is "The society for solid-state and electrochemical science and technology," encompassing its long tradition to advance these fields. ECS continues to disseminate information through individual membership, corporate membership, student services, four technical journals, a quarterly news magazine, books, technical meetings, and awards; and to provide networking contacts through ECS thirteen Divisions. Geographically, members can also associate with Sections. For example, most members in Europe are members of the European Section.

ECS bridges the gaps among academia, research, and engineering—bringing together scientists from around the world for the exchange of technical information. This unique blend provides an unparalleled forum for the integration of these areas of science and technology. The ECS staff can provide support to you in learning more about ECS and its many activities. Full information can be obtained at [www.electrochem.org](http://www.electrochem.org).

The Society actively recruits students and gives them the opportunity to get organized in Student Chapters. One of the active chapters is also in Brno, the site of this year's ABAF meeting. Student membership can be obtained at significant discount.

ECS maintains digital library of its collection of publication, including *ECS Transactions*, where some of the ABAF presentations are presented as well. Access to the library, with certain number of downloads, is part of the membership benefits package.

(Contributed by Petr Vanýsek, [pvanysek@niu.edu](mailto:pvanysek@niu.edu))



Bochemie Group is a leading Central European manufacturer and a significant Czech producer of various products used in disinfection, wood preservation, accumulator materials, metal surface treatment and other segments. On a global scale it is a successful manufacturer of specialty chemicals for market niches.



Bochemie has been developing its know-how for more than 100 years. Management team privatized the company in 1994 and in mid-1990's created Bochemie Group which was sold to Benson Oak Capital. At the end of 2007 Bochemie s.r.o. merged with acquisition vehicle Bochemie a.s. The group headquarter is located in the Czech Republic, the branches are in the Slovak Republic, Poland, Hungary, Bulgaria, Romania and Russia.

*Bochemie performs its business activities in four strategic business units:*

**SBU DEZI** – range of disinfection products primarily for healthcare market as well as agriculture

**SBU FUNGI** – range of fungicidal and insecticidal products for wood protection and masonry

**SBU ACCU** – various products for Ni-Cd and Ni-Fe accumulators, perforated bands, accumulator masses and electrodes

**SBU Feropur** – production of Feropur, a unique chemical for pre-pickling of the stainless steel long products (wire rod, bars)

*Our commitment to future*

**SBU Green projects** – developing new strategic competences in the area of green economy and focusing on: recycling, new materials and new technology.

Bochemie is seeking projects in diverse areas of „GREEN ECONOMY“

- Green buildings
- Green transportation
- Green energy
- Agriculture, Forestry, Water Management, Air pollution and others

**Feropur**®



**Chloramin**



[www.bochemie.cz](http://www.bochemie.cz)

[www.savo.eu](http://www.savo.eu)

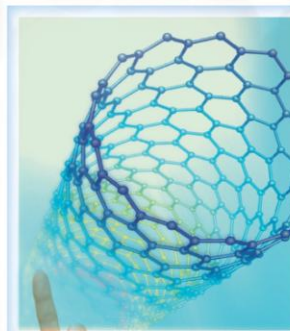
Bochemie a.s., Lidická 326, 735 95 Bohumín Tel: 596 091 111, e-mail:  
bochemie@bochemie.cz



## Aldrich Materials Science — Your Materials Chemistry Partner

**8000+ products for research in:**

- Alternative Energy
- Biomaterials
- Metal & Ceramic Science
- Micro/Nano Electronics
- Nanomaterials/Technology
- Organic and Printed Electronics
- Polymer Science



### **Your Materials Matter**

- Material Matters™  
A quarterly technical periodical
- Technology Spotlights & Tutorials
- Expert Technical Support
- Online Product Catalogue

[aldrich.com/matsci](http://aldrich.com/matsci)

**SIGMA-ALDRICH**



**pragolab**

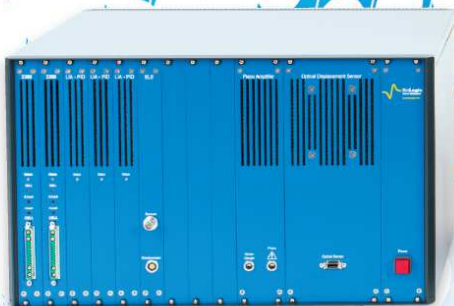
laboratorní přístroje a zařízení

hmotnostní spektrometrie • separační techniky  
elementární analýza • atomová spektroskopie  
elektrochemie • uv-vis spektrometrie  
reologie • analýza povrchů • spotřební materiál  
laboratorní vybavení • servis



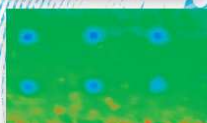
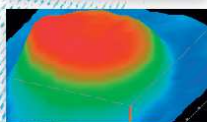
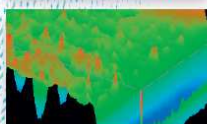
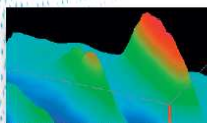
www • pragolab • eu  
pragolab@pragolab • cz  
Nad Krocínkou 55, 190 00 Praha  
Jamborova 25, 615 00 Brno

**NEW  
product**



**Application areas:**

bio-sensors,  
biochemistry,  
corrosion,  
coatings,  
catalysts...



# M470

## Introducing the 4<sup>th</sup> generation of scanning probe electrochemical workstations

- **9 available techniques:**  
SECM, LEIS, SVP, SDS, SKP, OSP, ic-SECM, ac-SECM, ac-SDS
- High performance scanning stage:  
**0.09 nm** ultimate z-resolution,  
**20 nm** resolution on all axes,  
**100 mm** scan range on all axes,  
**10 mm/s** max scan speed
- New innovative techniques:  
**ic-SECM** offering true simultaneous imaging of topography and reactivity,  
**ac-SECM** offering measurement of surface conductivity without a mediator.
- Fully integrated potentiostat/galvanostat/FRA:  
**±10 V** potential range, current ranges from **1 A to 1 nA**,  
**1 MHz to 1 μHz** EIS capability

Product designed and manufactured by Uniscan Instruments Ltd,  
a Bio-Logic SAS company

[www.bio-logic.info](http://www.bio-logic.info)



**pragolab**  
laboratorní přístroje a zařízení

# AFM mikroskopie Agilent Technologies

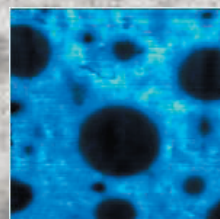
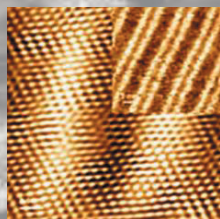
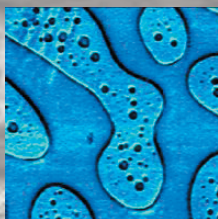


AFM/SPM systémy Agilent jsou používány v celé řadě oborů jako jsou například:

- výzkum a vývoj materiálů
- mikroelektronika
- nanolitografie
- aplikace s polymery
- biotechnologie
- medicína

Technologie AFM/SPM mikroskopů umožňuje zobrazování v atomárním měřítku s rozlišením až na desetiny nanometrů. Zásadní výhodou těchto mikroskopů je, že vzorky lze zobrazovat v libovolných podmínkách. Je možné měřit při různých teplotách nebo i přímo v kapalinách. Konstrukce AFM mikroskopů Agilent umožňuje přímý optický přístup ke vzorkům - mikroskopy jsou vybaveny videokamerou.

Základním principem je snímání povrchu miniaturním hrotem, který měří konkrétní vlastnosti povrchu. Vyhodnocovací jednotka měří signál z fotodetektoru dle polohy hrotu. Držáky snímacích hrotů (tzv. nose cone) urychlují a zjednodušují změny zobrazovacích režimů. Modulární koncepce přístrojů umožňuje rozšířit schopnosti mikroskopického systému dle aktuálních potřeb.



Společnost H TEST a.s. je výhradním distributorem Nanomeasurement Division Agilent Technologies, která zahrnuje AFM a SEM mikroskopii.



H TEST a.s.  
Šafránkova 3  
155 00 Praha 5  
Tel: 235 365 207  
info@htest.cz



**Agilent Technologies**

Authorized Distributor

[www.agilent.com/find/nano](http://www.agilent.com/find/nano)

**Title:** Advanced Batteries Accumulators and Fuel Cells – 14<sup>th</sup> ABAF  
**Edited:** Jiří Vondrák  
Marie Sedlaříková  
Vítězslav Novák  
Petr Bača  
**Publishing Office:** Jiří Vondrák  
Marie Sedlaříková  
Vítězslav Novák  
Petr Bača  
**Deadline:** July 14<sup>th</sup> 2013  
**Publisher:** Brno University of Technology  
Faculty of Electrical Engineering and Communication  
Department of Electrical and Electronic Technology  
**Year:** 2013  
**Number of Copies:** 100

The authors are fully responsible for the content and language of their contribution

**ISBN 978-80-214-4767-7**